STUDY OF NEUTRON-RICH SODIUM ISOTOPES NEAR THE N=20 ISLAND OF INVERSION THROUGH β-DELAYED γ-RAY SPECTROSCOPY

By

Amelia Anne Doetsch

A DISSERTATION

Submitted to
Michigan State University
in partial fulfillment of the requirements
for the degree of

Physics—Doctor of Philosophy

2026

ABSTRACT

The existence of nuclear magic numbers, evidence of the nuclear shell structure, is one of the most quintessential nuclear phenomena. Despite decades of study, a complete description of the forces which drive the evolution of nuclear shells is elusive. In the $N \sim 20$, $Z \sim 11$ region, known as the "island of inversion", phenomena associated with the conventional nuclear shell closure at $N = 20$ suddenly disappear. Current understanding of this shell evolution is complex, highlighting the importance of residual interactions in allowing "intruder states" dominated by single- and multi-neutron excitations across the shell gap to become favored over normal states. ^{32}Na was one of the first nuclei identified in this region of deformation [1]; however, over five decades later, spectroscopic information on this isotope is sparse, and, where it does exist, much ambiguity remains. The present study attempts to expand spectroscopic knowledge of ^{32}Na and resolve ambiguity in excited state energies, spins, and parities, as well as underlying structural characteristics.

The β decay of ^{30,32}Ne was studied at the Facility for Rare Isotope Beams (FRIB), leveraging the FRIB Decay Station initiator (FDSi) to extract detailed, high-resolution spectroscopic information about the child isotopes. Previous studies [2–4] of ^{30}Ne β decay are well-reproduced by the present measurements, allowing a high level of confidence in the present methodology. Four γ rays were observed following the β decay of ^{32}Ne, three of which were newly identified transitions which could be placed within the ^{32}Na level scheme. Based on selection rules and previous theory calculations presented in Ref. [5], tentative spins and parities were proposed for five states, including both isomers and the ground state. The known microsecond isomer [5] was not observed, but the present results indirectly support the interpretation of Ref. [5] in which the microsecond isomer is a deformed spin isomer. The known isomer around 120 keV [6] was deduced to be populated based on energy summing relations. Despite dedicated search, its γ decay was not observed; keeping in mind its expected long half-life ($\gtrapprox$ ms), this suggests that this state may β decay. Further study is needed to make definitive conclusions regarding the decay of the 120 keV isomer. Theoretical interpretation of the deduced level scheme was carried out, utilizing the FSU interaction, the SDPF-

M interaction, and the Nilsson model. All model calculations well reproduce the experimental data and suggest that the low-lying level scheme is dominated by intruder states, with no trace of the normal configuration to be found.

ACKNOWLEDGMENTS

First and foremost, to Hannah. I struggle to put into words how much you mean to me. Throughout this journey, you are the person who has been at my side most consistently, steadily cheering me on. There were many times I questioned whether I was good enough to finish this work, and you were always there to remind me that I am. As we look forward to this next chapter in our lives, I will never forget what your encouragement has meant to me, and I will strive to provide you the same level of support that you have always given to me.

To my parents, who have championed my education since I was a child. I would not be where I am today without your encouragement. You have always believed in my ability to achieve great things, and you have helped me discover the path I needed to take to get there.

To my sister. You have been my best friend since we were kids, and you understand me in a way that few people do. You may not realize it, but I will always look up to you, and your advice these past few years has helped me understand more clearly my path in life.

To Andrew and Caitlin. Seeing you two hard at work every day inspired me to push myself to work harder, even on the days I lacked motivation. Having a second and third pair of eyes on my spectra and playing "Peak or No Peak" always gave me good ideas and helped drive my research forward.

To Rebeka. Even when you were super busy, you always made time for me when I asked. I appreciate the way you would carefully explain nuclear structure concepts to me when I found them very confusing. Research would've been much harder than it already was without you there to teach me and give me advice.

To the rest of the Beta Group — Aaron, Adam, Dustin, Ellie, Jessica, Mejdi, Tawfik, and Timi — and the rest of the nuclear chemistry group as a whole. Not only were you great teammates when it came to analysis meetings and experiments, you have been great friends to me. I will miss spending time with you all at bowling, beach day, and parties at Sean's.

To my committee: Alex, Alyssa, Heiko, and Ty. I could not have picked a better group of scientists to advise me. During my committee meetings, you have always asked me thoughtful

questions which have pushed me to a more thorough and complete understanding of my research. Your advice and ideas, not only on research but also on life after grad school, have been immensely helpful.

Most importantly, to Sean. You took a chance on me at a time when I felt lost and overwhelmed as a first-year graduate student. Under your guidance, I know I've grown leaps and bounds from where I started, not only in my technical skills but also in my confidence as a scientist. No matter where life takes me, I will always remember to examine the data closely, from all angles, before making any judgment, as you always encouraged me to do.

TABLE OF CONTENTS

LIST OF FIGURES

LIST OF TABLES

CHAPTER 1

INTRODUCTION

1.1 Nuclear magic numbers

The structure of atomic nuclei exhibits rich and complex patterns which scientists have studied since the early 1900s and continue to explore in the current day. One of the earliest observed patterns is that of the "nuclear magic numbers." Nuclear isotopes with certain numbers of protons and/or neutrons — 2, 8, 20, 28, 50, 82, 126 — exhibit enhanced stability relative to neighboring non-magic nuclei, similar to the way atoms with certain numbers of electrons are especially non-reactive. As will be discussed later in this section, this is taken as evidence of a "shell structure" in nuclei, similar to the atomic shell structure which is well-known [7].

Some nuclear isotopes are semi-magic (i.e. they exist along either a proton or a neutron magic number, like ${}^{38}_{18}\mathrm{Ar}_{20}$ or ${}^{18}_{8}\mathrm{O}_{10}$) whereas others are doubly-magic (i.e. they exist at both a neutron and a proton magic number, like ${}^{48}_{20}\mathrm{Ca}_{28}$ or ${}^{208}_{82}\mathrm{Pb}_{126}$). Both semi-magic and doubly-magic nuclei exhibit special properties that distinguish them from non-magic nuclei. When compared systematically, the presence of a shell closure can be signaled by changes in nuclear properties such as mass, charge radius, and electromagnetic transition probability [8].

To emphasize the prevalence of nuclear magic numbers, one can explore the Liquid Drop Model. This is a simple, semi-empirical model which predicts nuclear binding energies by modeling the nucleus as a drop of liquid. There are four simple parameters: volume, surface area, Coulomb repulsion, and isospin asymmetry. An optional fifth term related to nucleon pairing can be added. The Liquid Drop Model binding energy prediction is expressed in Equation 1.1 [7]. A is the nuclear mass number, N is the neutron number, Z is the proton number, and a_X are fit parameters which are optimized based on nuclear data.

$$B_{LD} = a_V A - a_S A^{2/3} - a_C \frac{Z^2}{A^{1/3}} - a_A \frac{(N-Z)^2}{A} \tag{1.1}$$

Figure 1.1 shows the difference between experimentally-derived binding energies and Liquid Drop Model predictions. There is a clear pattern: the discrepancy between the experimental value

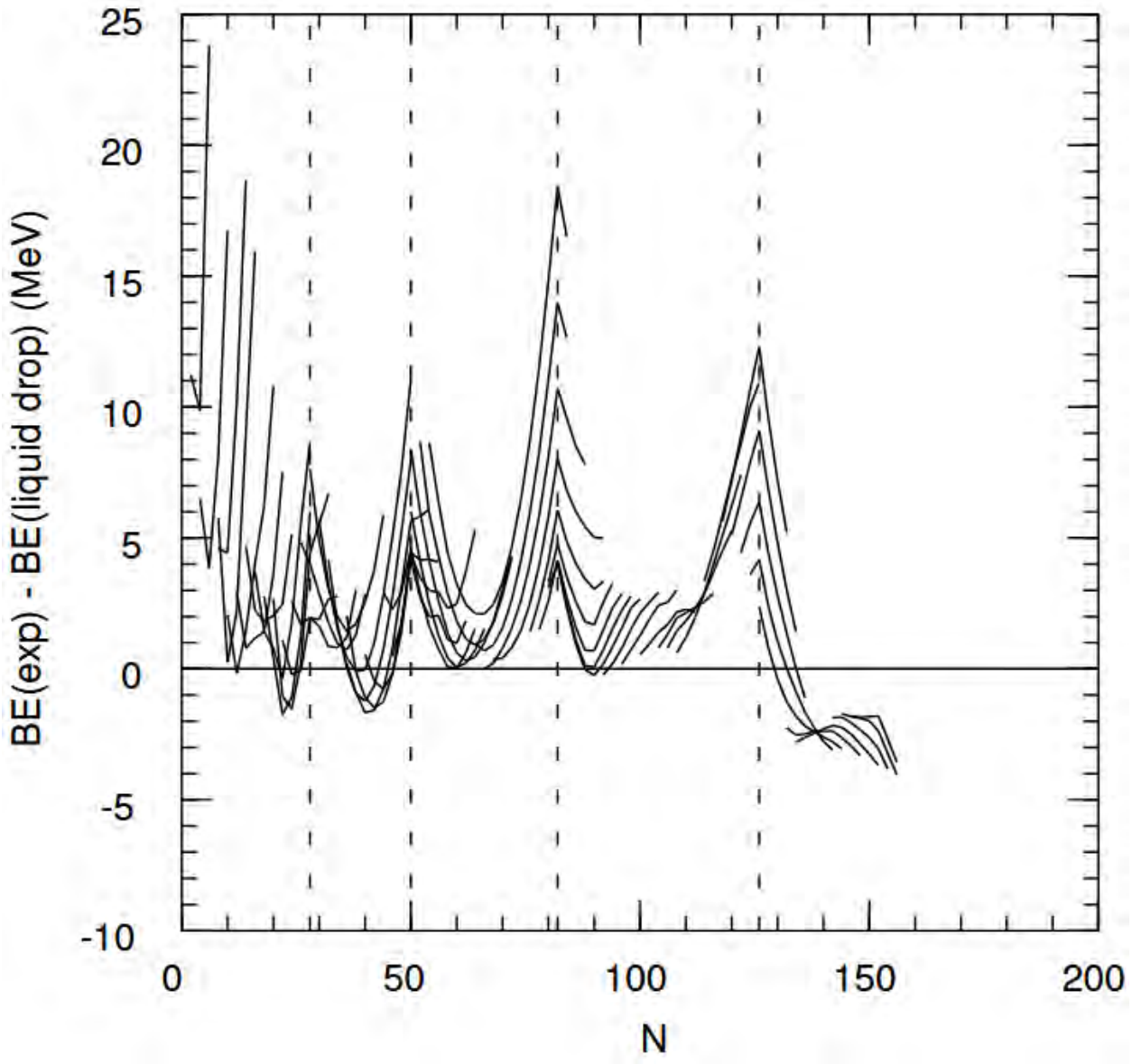

Figure 1.1 Difference in binding energy between experimental observation and Liquid Drop Model prediction. A distinct pattern is seen, with sharp peaks occurring at the neutron magic numbers. Image credit: [7]

and the Liquid Drop Model value tends to be much larger near the magic numbers, compared to neighboring non-magic nuclei. This indicates that magic nuclei tend to be more tightly bound than the Liquid Drop Model predicts. These systematic discrepancies are attributed to the existence of nuclear shell closures at the magic numbers, which are not treated within the Liquid Drop Model [7].

Spectroscopically, a simple indication of a shell closure in an even-even nucleus is a high excitation energy of the first excited 2^+ state paired with a low E2 transition strength between the 0^+ ground state and the first excited 2^+ state, (often denoted as B(E2; $0^+ \rightarrow 2^+$)) [9]. The 2_1^+ excitation energy is plotted in Figure 1.2, first for stable and long-lived nuclei and again for all nuclei measured as of 2016. In stable and long-lived nuclei, deviations are again observed at the conventional nuclear magic numbers. Here, it is shown that the 2_1^+ excitation energy is enhanced at the magic numbers, suggesting that the 2_1^+ excitation energies are also sensitive to the existence of shell closures [9]. It is important to note that the interpretation of values such as 2_1^+ excitation energies is not always simple, as they can be impacted by a multitude of interactions; however, in general, as evidenced in Figure 1.2, systematics of 2_1^+ excitation energies can be a good signal of the presence of a shell closure [9]. The picture becomes a bit more complex when adding more exotic nuclei into the picture (see the bottom panel of Figure 1.2); this will be discussed in detail in Section 1.3.

1.1.1 The Spherical Shell Model

The simplest model which reproduces the phenomena associated with shell structure starts with placing each individual nucleon into a spherically-symmetric mean-field potential produced by the rest of the nucleons in the nucleus. The simplest assumption that can be made is that the interactions between smaller pairs or groups of nucleons are insignificant; hence, the structure is driven by the interactions between each nucleon and the mean field [8]. The simplest choice of mean-field potential is a harmonic oscillator potential. Single-particle energies for neutrons filling this harmonic oscillator potential for the ^{208}Pb nucleus are shown in the far left column of Figure 1.3 [7]. Levels with equivalent $N = 2n + l$ are degenerate [10]; this quantity shall be referred to as the major harmonic oscillator shell number. This is a good starting point; as is apparent, shell gaps are reproduced at numbers 2, 8 and 20. However, beyond this, the following shell gaps exist at 40, 70, 112, and 168, which are inconsistent with what is experimentally observed.

Another simple form of the potential which can be considered is a Woods-Saxon potential, shown in Figure 1.4 (labeled "Central"). This has a similar shape as the harmonic oscillator

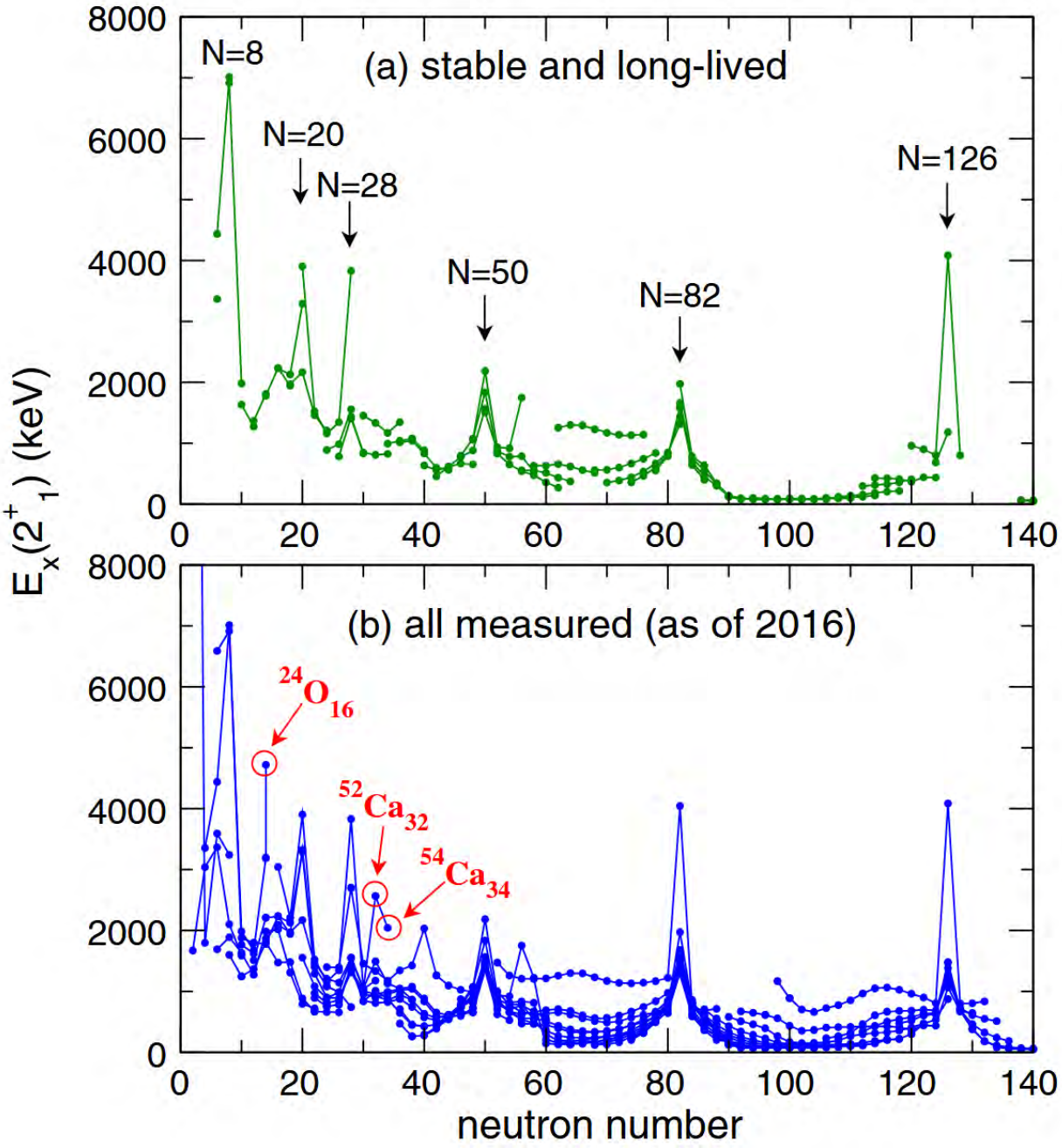

Figure 1.2 Excitation energy of the first excited 2^+ state for a) stable and long-lived nuclei and b) all measured (as of 2016). Reprinted figure with permission from T. Otsuka, A. Gade, O. Sorlin, T. Suzuki, and Y. Utsuno, Rev. Mod. Phys. **92**, 015002 (2020). Copyright 2020 by the American Physical Society.

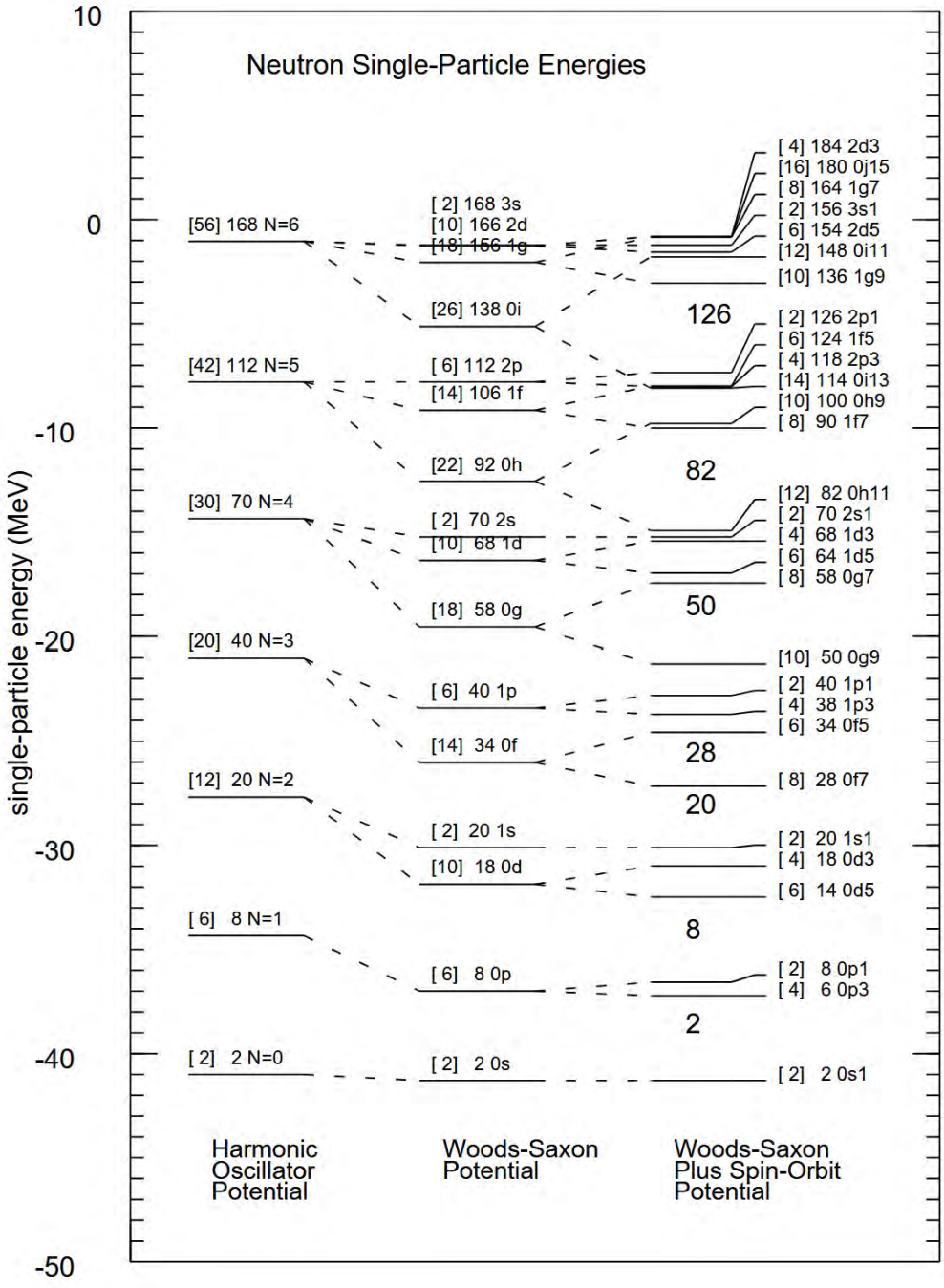

Figure 1.3 Single-particle energies for ^{208}Pb for a harmonic oscillator potential, a Woods-Saxon potential without the spin-orbit interaction, and a Wood-Saxon potential including the spin-orbit interaction. For harmonic oscillator levels, each level is labeled [occupation number] [cumulative occupation number] [major harmonic oscillator shell number, $N = 2n + l$]. For Woods-Saxon alone levels, each level is labeled [occupation number] [cumulative occupation number] [nl]. For Woods-Saxon plus spin-orbit levels, each level is labeled [occupation number] [cumulative occupation number] $nl(2j)$. Image credit: [7]

potential, but with a flattened bottom. The functional form of this potential is given in Equation 1.2, where V_0 is the potential depth and R_0 and a_0 are geometrical parameters [7, 8]. As shown in the middle column of Figure 1.3, when applying this nuclear potential, the $2n + l$ degeneracy is broken [10]. The light shell gaps remain, but the magic numbers above 20 are still not reproduced.

$$V_0(r) = V_0 f(r) = \frac{V_0}{1 + e^{(r-R_0)/a_0}} \tag{1.2}$$

In 1949, Mayer and Haxel, Jensen, and Suess independently identified the missing piece required to reproduce nuclear magic numbers: a strong spin-orbit potential term [11, 12]. This is also shown in Figure 1.4 (labeled "Spin-orbit"). This spin-orbit term is proportional to $\vec{l} \cdot \vec{s}$ [8].

As is shown in the rightmost column of Figure 1.3, the correct magic numbers are accurately reproduced when combining the Woods-Saxon potential with the spin-orbit coupling term. The spin-orbit term causes levels to split further, where the spin-orbit aligned $j = l + 1/2$ level drops lower in energy and the anti-aligned $j = l - 1/2$ level raises higher in energy. Upon examination of Figure 1.3, it appears that the magic numbers above $N = 20$ are produced primarily due to this splitting, where an $l + 1/2$ level splits so low in energy that it drop down into the previous harmonic oscillator shell, shifting the magic number from the harmonic oscillator result by the number of nucleons in the split level [7].

The form of the total nuclear potential is shown in Figure 1.4. One can note the central Woods-Saxon component, the spin-orbit component, and the additional Coulomb and centrifugal components which are included here. From this simple description of nuclear forces, the seminal spherical shell model emerges. The mean-field potential creates discrete orbitals distinguished by their orbital angular momentum l and total angular momentum j; orbitals are labeled l_j where $j = l \pm 1/2$ and $l = s, p, d, f, ...$ for $l = 0, 1, 2, 3, ...$ Proton orbitals may be labeled πl_j and neutron orbitals may be labeled νl_j, where the π and ν symbols simply indicate what species of nucleon is considered. The parity of the orbital is $(-1)^l$. Each orbital can hold $(2j + 1)$ protons or neutrons, in accordance with the degeneracy of l_j states with different values of m [7, 10].

A simple approximation which can be made to the non-interacting spherical shell model includes

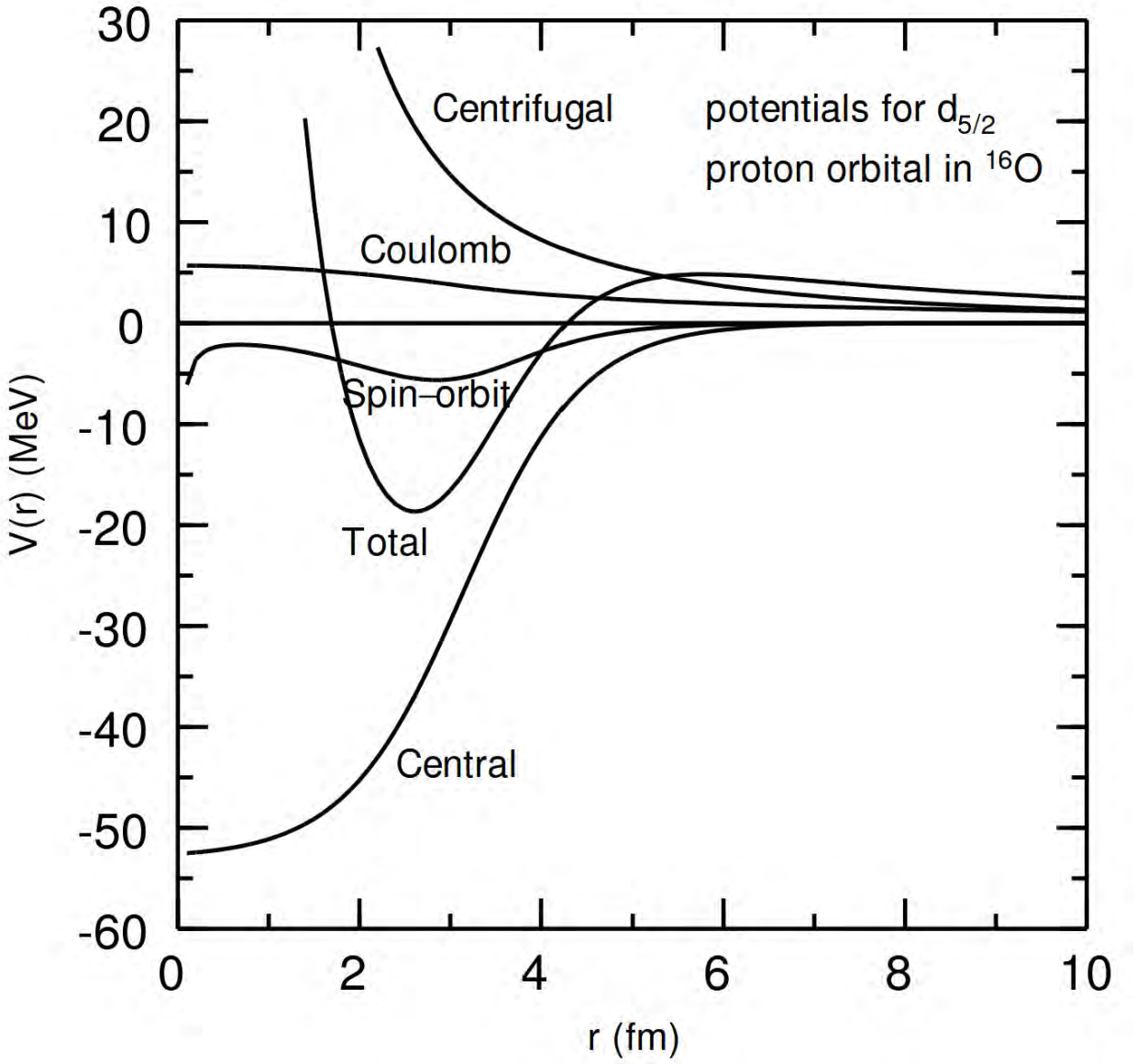

Figure 1.4 The nuclear potential as a function of distance from the center of the nucleus, and its components: centrifugal, Coulomb, spin-orbit, and central (Woods-Saxon). The potential is shown for a $d_{5/2}$ proton orbital outside of an ^{16}O core. The functional form of the central term is given in Equation 1.2. Image credit: [7]

the addition of a so-called "pairing" interaction. Simply put, this interaction causes like nucleons to form pairs which couple to a total spin and parity of $J^\pi = 0^+$. This provides a simple explanation for the observation that all even-even nuclei have 0^+ ground states [10]. In odd mass nuclei, where one nucleon is left unpaired, this formalism can be extended in order to greatly simplify the nuclear configuration, resulting in an extreme single-particle picture. From this perspective, the properties of the nucleus, such as spin and parity, are determined solely by the properties of the unpaired nucleon. This is to say that the nucleus is modeled as a lone nucleon coupled to an inert $J^\pi = 0^+$ core. The spin and parity of a nuclear level is then taken directly from the spin and parity of the orbital containing the unpaired nucleon. The ground state is expected to include no "holes", and all nucleons are expected to occupy the lowest available orbital according to the Pauli Exclusion Principle. If the unpaired nucleon is excited from the lowest available orbital into a higher-lying orbital, an excited state is formed. A "cross-shell excitation" involves the excitation of the unpaired nucleon across one of the major shell gaps. In this simplified picture, this excitation would produce an excited state with an excitation energy equal to the size of the shell gap [10]. These shell gaps are, conventionally, quite wide, so such excited states would be expected to appear at high excitation energies.

While there are cases in which this simple model is sufficient in predicting experimental observables, the characteristics of nuclear states are often more complex than what can be described in the non-interacting spherical shell model. In reality, it is often necessary to consider degrees of freedom for more than just one single nucleon outside of an inert core. In practice, theoretical shell model codes choose a valence space, consisting of a number of selected orbitals, and the outermost nucleons can fill those orbitals in different configurations that result in different nuclear structures. Moreover, shell model codes may choose an appropriate set of additional interactions between pairs or groups of valence nucleons, often referred to as "residual interactions." While the non-interacting spherical shell model makes the simple assumption that residual interactions are too weak to effect the nuclear structure, this assumption is usually not true. Fortunately, the nuclear shell model can be extended in various ways to encompass a greater degree of complexity

of nuclear interactions, which has allowed it to remain among the most successful nuclear models.

1.2 Nuclear shapes and collectivity

A complete understanding of nuclear phenomenology is not possible without the consideration of collective degrees of freedom. While most strongly necessitated in mid-shell medium-mass and heavy nuclei, collective features have been suggested in nuclei even as low as the neutron-rich $N \sim 8$ region [13]. The concept of nuclear collectivity may seem at odds with the spherical shell model, but they are not necessarily mutually exclusive. The inclusion of residual interactions can result in the manifestation of collectivity within a shell model framework [10].

The development of nuclear deformation is an inherently collective phenomena. While a number of exotic shapes are possible, most nuclei take on a quadrupole deformation — prolate or oblate. Prolate nuclei are stretched along the z-axis (also referred to as the symmetry axis), while oblate nuclei are compressed along the z-axis. Prolate deformation is more common than oblate deformation. The β parameter is typically used to indicate the degree of quadrupole deformation of a nucleus, with $\beta > 0$ corresponding to a prolate deformation and $\beta < 0$ corresponding to an oblate deformation. The γ parameter gives further detail on the axial asymmetry of the nucleus, with γ values of 0° and 180° corresponding to axially symmetric prolate and oblate deformations, and values in between representing some level of axial asymmetry. Deformation can also be characterized in terms of a rigid body moment of inertia I, or an intrinsic quadrupole moment Q_0 [10].

Practically speaking, collectivity can be inferred by the presence of a sequence of excited states with energies following some characteristic pattern. These sets of states may be referred to as "bands." The two most common forms of collective excitations are rotations and vibrations. Nuclear vibrations are characterized by oscillation in the nuclear shape.

In even-even nuclei, a rotational band can be inferred based on the presence of a set of states with energies that increase proportionally with $J(J+1)$. For a rigid, symmetric rotor, the spin dependence of the excitation energy is given by Equation 1.3, for even values of J and moment of inertia I. From this equation, it is apparent that the characteristic ratio $E(4_1^+)/E(2_1^+)$ for a

rigid rotor is equal to 3.33. The $E(4_1^+)/E(2_1^+)$ ratio for an even-even nucleus can be deduced from experimental data, making it a convenient quantity to use in order to infer rotational motion. Beyond rigid rotors, an $E(4_1^+)/E(2_1^+)$ ratio can span values roughly between 2 and 3.33. Values less than 2.0 are typical of conventional spherical shell model behavior, and values around 2 or slightly greater can indicate vibrational behavior. There is a transitional region between $\sim$ 2.5–3, which can indicate some level of axial asymmetry, and anything beyond $\sim$ 3 can be considered rotational. This ratio is plotted across the nuclear chart in Figure 1.5. The pattern is clear in medium-mass and heavy nuclei: there is a gradual transition from vibrational behavior near magic numbers, to strong rotational characteristics in midshell nuclei. While the systematic evolution is less clear in light nuclei, what is clear is that, even at low mass, collective features are abundant.

Another key experimental indicator of rotational motion in even-even nuclei is a large reduced transition probability between the 0^+ ground state and the first excited 2^+ state, (denoted $B(E2; 0^+ \rightarrow 2^+)$), typically on the order of tens of Weisskopf units. This quantity will be discussed further in Section 2.2. While the $E(4_1^+)/E(2_1^+)$ ratio may be a more easily accessible experimental quantity, both $E(4_1^+)/E(2_1^+)$ ratio measurements and $B(E2; 0^+ \rightarrow 2^+)$ measurements can be instrumental in the identification of collective motion in nuclei.

$$E_{\mathrm{rot}}(J) = \frac{\hbar}{2I} J(J+1) \tag{1.3}$$

Collectivity in nuclei is quite a broad topic; for the purposes of this work, the remainder of this discussion will be limited to the Deformed Shell Model, or the Nilsson Model, an extension of the spherical shell model that deals more directly with nuclear deformation. Unlike the spherical shell model, the Nilsson model allows nucleons to interact with a deformed potential. Similar to the spherical shell model, the resulting structure involves discrete orbitals which nucleons gradually fill. In this case, the orbitals are now deformation-dependent. K is defined as the projection of the $\vec{j}$ total angular momentum of the orbital onto the symmetry axis of the nucleus. Splitting of spherical shell model orbitals is introduced as the $\vec{j}$ vector can now have several non-degenerate alignments relative to the nuclear symmetry axis. For a given orbital with total angular momentum

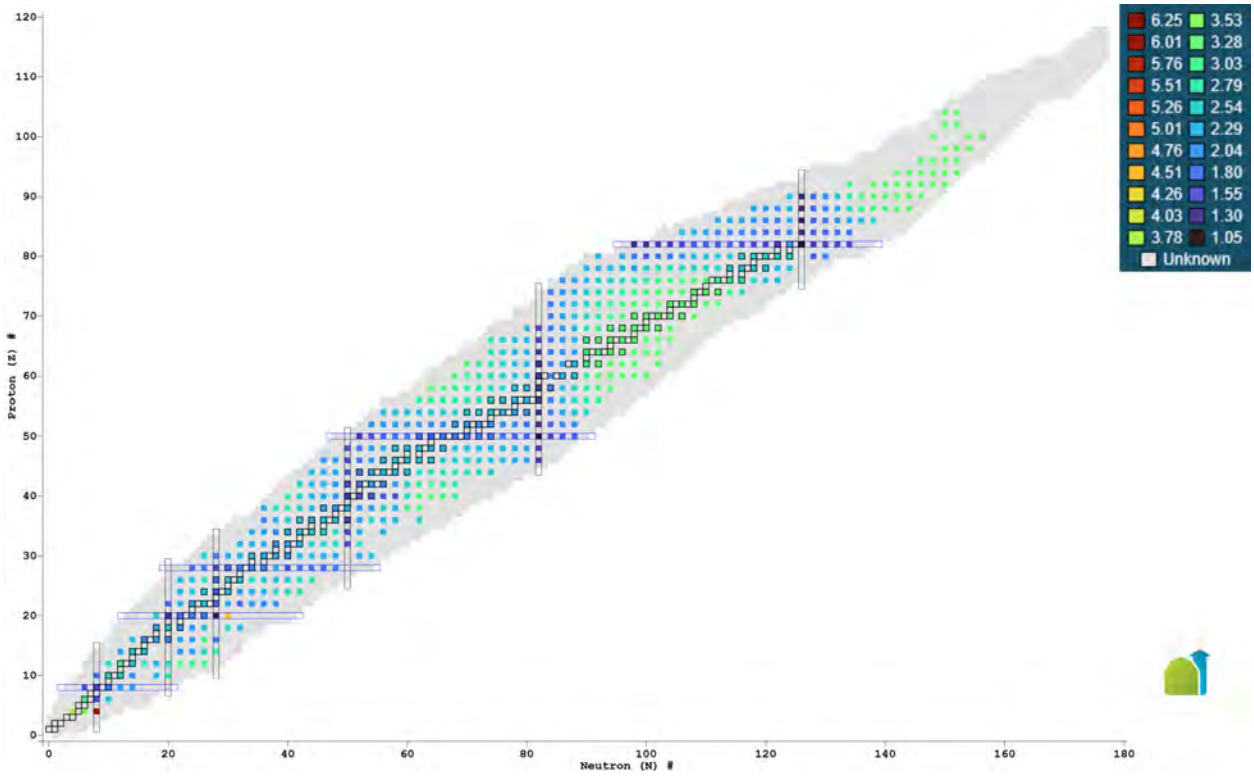

Figure 1.5 The ratio $E(4_1^+)/E(2_1^+)$ plotted for even-even nuclei as a function of proton number (y-axis) and neutron number (x-axis). Image credit: [14]

j, K ranges from 1/2 up to j. The maximum K value indicates that $\vec{j}$ is completely aligned with the symmetry axis; in contrast, $K = 1/2$ indicates minimum alignment between the symmetry axis of the nucleus and the $\vec{j}$ vector [10].

Nilsson model orbitals are typically labeled $K^\pi[Nn_z\Lambda]$. K has been discussed in the previous paragraph, and π is the parity of the orbital (the same as the parity of the corresponding spherical shell model orbital, given as $(-1)^l$). N corresponds to one of the major harmonic oscillator shells. n_z is the number of nodes of the wave function in the z direction. Intuitively, Nilsson orbitals with the minimum K value have the maximum wave function component in the direction of the z-axis, and will thus have the highest values of n_z. For a prolate nucleus, these orbitals will lie lowest in energy, as the orbit of the nucleus is closely aligned with the nuclear body. As the orbital becomes less aligned with the z-axis (the symmetry axis), n_z decreases, as the wave function will have a smaller z component. Finally, the Λ quantum number is the projection of the orbital angular momentum $\vec{l}$ along the symmetry axis. By definition, $\Lambda = K \pm 1/2$ [10].

A sample Nilsson diagram is shown in Figure 1.6 for both protons and neutrons in ^{32}Mg. The splitting of spherical shell model levels is apparent as the nucleus becomes more deformed; analogously, it is apparent that the Nilsson levels stemming from a shared spherical shell model level become degenerate at $\beta = 0$ (indicating spherical symmetry). In this way, the onset of nuclear deformation can be intrinsically linked to the single-particle picture of nuclear structure.

1.2.1 Shape coexistence

As the previous section suggests, the level structure of a nucleus can be quite dynamic, involving the existence of collective bands and deformed shapes. Along these lines, different nuclear shapes can coexist within the same nuclear isotope; this phenomenon is, not surprisingly, referred to as "shape coexistence." Of particular interest is nuclei where coexisting shapes are nearly—but not quite—degenerate. The evolution of the energies of coexisting states as nucleons are added or removed from the nucleus can be a key indicator of underlying structural evolution. Shape coexistence has been observed across the Chart of Nuclides. Figure 1.7 depicts some of the major regions of the nuclear chart where identified instances of shape coexistence are abundant. Notably for this work, the neutron-rich region around $N \sim 20$ has been identified as one such region.

The development of shape coexistence near $N \sim 20$ is related to two concepts: the presence of the $N = 20$ shell gap, and the presence of strong residual interactions across that shell gap. Cross-shell residual interactions can lower the energies of intruder states; these intruders can be interpreted as deformed states. If multiple states with different configurations exist within the same level scheme — say, one state in which no neutrons are excited past the shell gap, and another state in which a pair of neutrons is excited past the shell gap — these configurations may be related to different nuclear shapes, as one may involve strong cross-shell residual interactions, whereas the other may not. As will be discussed in Section 1.3, the presence of these cross-shell residual interactions in the island of inversion is critical to the understanding of shell evolution in this region of the nuclear chart.

^{30}Mg is a well-studied example of shape coexistence and collectivity in light nuclei. In a 2009 study by Schwerdtfeger et al. [15], shape coexistence was unambiguously determined for this

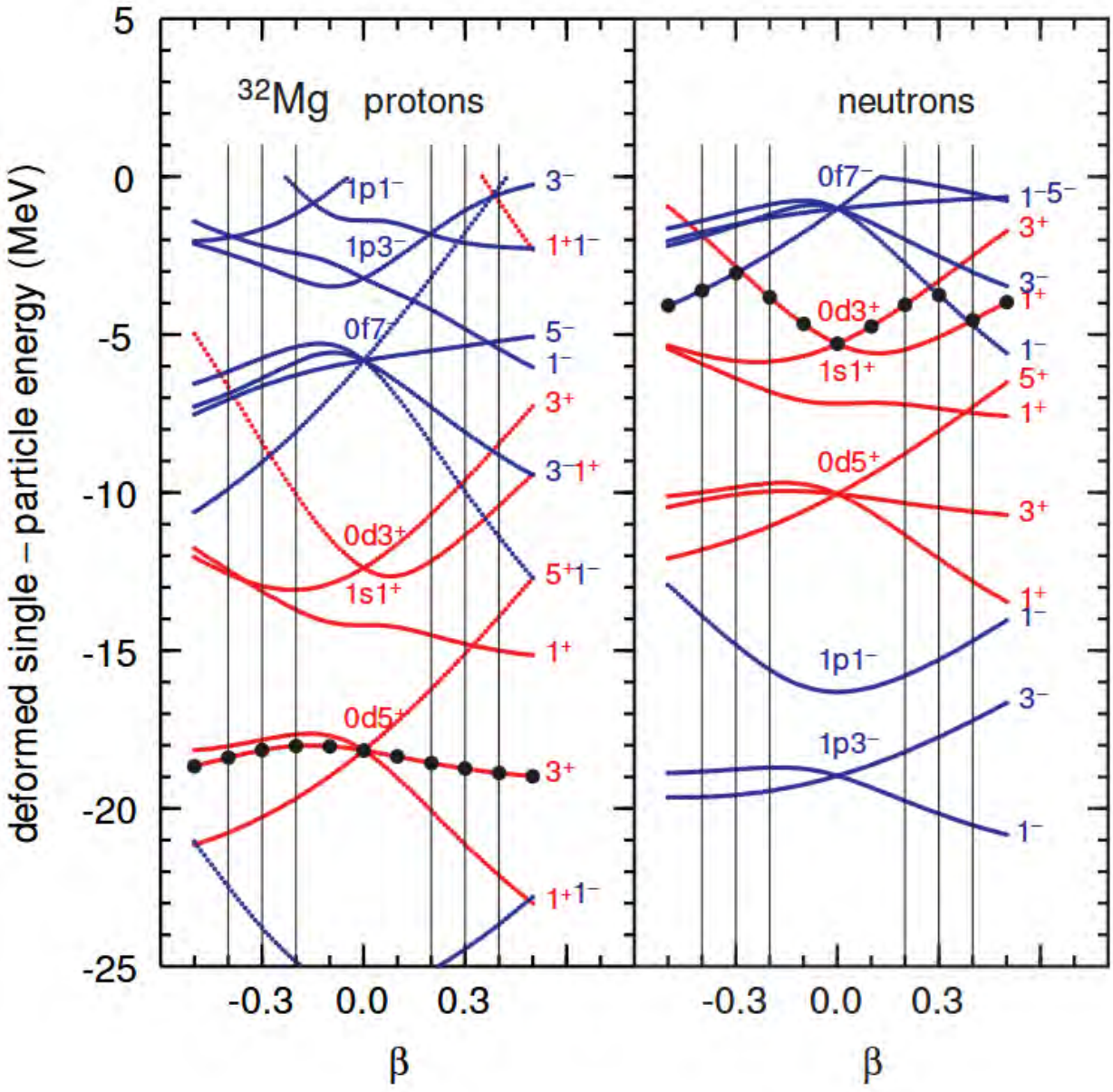

Figure 1.6 Sample Nilsson diagram for ^{32}Mg. The single-nucleon energies are shown for evolving deformation β. Each red (positive parity) or blue (negative parity) line represents a single Nilsson orbital, with its $2K^{\pi}$ value labeled on the rightmost end of the line. Orbitals are also labeled by their $Nl(2j)^{\pi}$ values. The black circles represent the highest filled orbital for ^{32}Mg as a function of deformation. Image credit: B. A. Brown

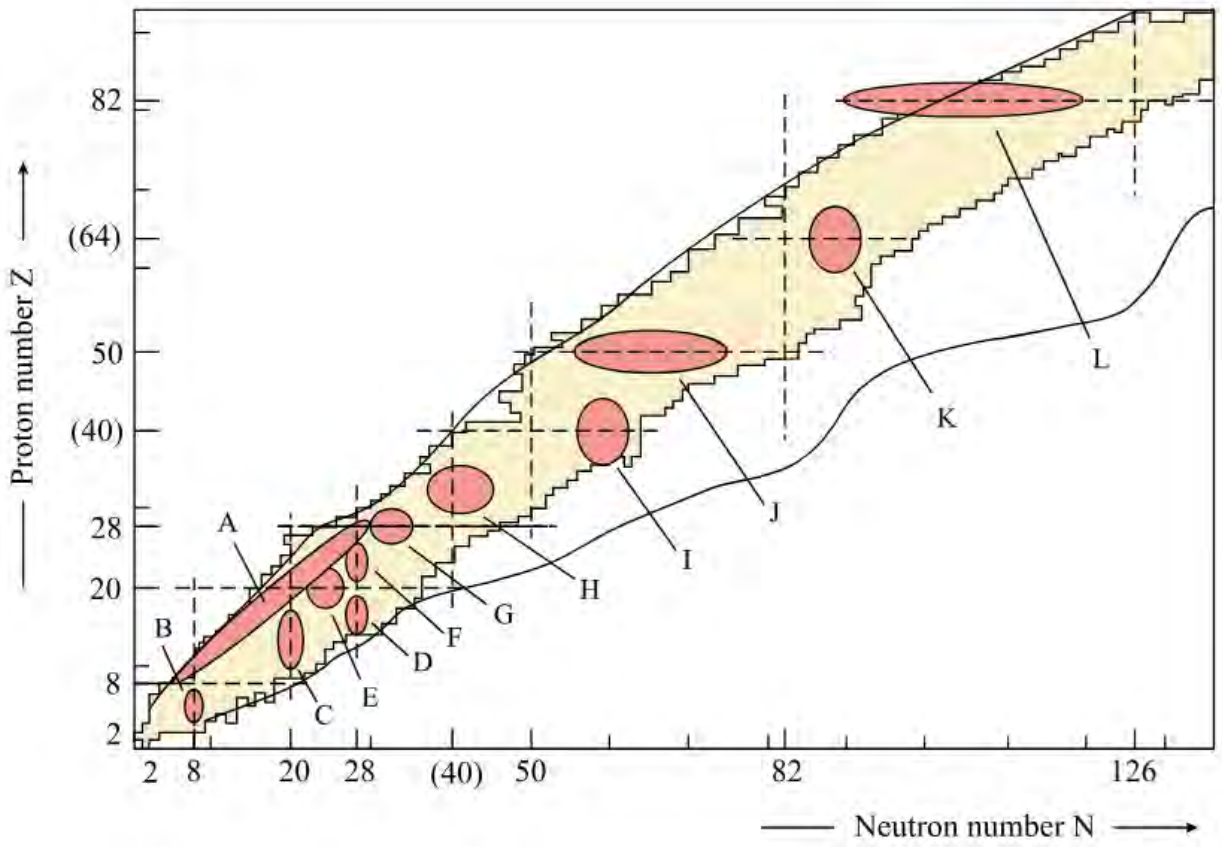

Figure 1.7 The Chart of Nuclides, with regions highlighted in pink depicting major regions where shape coexistence has been observed, as of 2011. Letters are assigned to each major region, and a full discussion of each lettered region can be found in Ref. [13]. Reprinted figure with permission from Kris Heyde and John L. Wood, Rev. Mod. Phys. **83**, 1467 (2011). Copyright 2011 by the American Physical Society.

nucleus by the conversion electron spectroscopic measurement of the E0 decay from the 0_2^+ state at 1789 keV to the 0_1^+ ground state. Comparison of theoretical calculations using the Gogny force with experimental data indicated average values of $\beta = 0.16$ for the 0_1^+ state and $\beta = 0.59$ for the 0_2^+ state. While weak mixing was inferred, the two states were relatively distinct, with the 0_1^+ state dominated by the nearly spherical configuration and the 0_2^+ state dominated by the deformed configuration [15]. For this region of the nuclear chart, the correspondence between deformed states and "intruder" configurations—configurations characterized by cross-shell excitations—is of critical importance [13]. For ^{30}Mg, the spherical state is related to the normal-order $\nu d_{3/2}$ configuration and the deformed state is related to the intruder $\nu f_{7/2}$ configuration, formed by exciting neutrons across the

$N = 20$ shell gap [15].

Two later studies of ^{30}Mg—Kitamura et al. (2020) [16] and Nishibata et al. (2020) [17]—both come to similar conclusions, affirming the presence of a shape coexisting excited 0^+ state in ^{30}Mg. While it is emphasized that the low E0 transition strength measured by Schwerdtfeger et al. (2009) is a strong indicator of low shape mixing between the ground and excited 0^+ states [15], Kitamura et al. (2020) note that their SDPF-M and EEdf1 model calculations present different interpretations of the underlying structures of these two states, and the authors suggest that measurements of spectroscopic factors could shed some insight into the models' discrepancies [16]. This is an excellent example of how a variety of different measurements of the same nuclear states can be critical in unraveling complex structures.

Nishibata et al. (2020) [17] identify several new states and transitions following the β decay of spin-polarized ^{30}Na, reporting comprehensively on several collective band structures in the ^{30}Mg nucleus. The experimentally-deduced band structures are shown in Figure 1.8. A vibrational ($E(4_1^+)/E(2_1^+) = 2.28$) ground state band is pictured alongside a deformed band based on the 0_2^+ state. Assuming the β parameter calculated in Ref. [15], the level spacing of the 0_2^+ and proposed 2_2^+ states is shown to be consistent with a rigid-body rotor. An axially asymmetric vibrational γ band is inferred above the proposed 2_3^+ state based on energy systematics and the intensity of the transition between the 3_1^+ state and the proposed 2_3^+ state. Another well-deformed collective band is proposed above the 1^+ state at 4.967 MeV, based on enhanced β-decay feeding from the deformed ^{30}Na ground state to these states. Finally, two states, perhaps somewhat mixed but with large spherical components, are suggested around 5 MeV [17]. The results and interpretations of Ref. [17] are compared with three theoretical models: CHFB + LQRPA, AMD + GCM, and EEdf1. Overall, interpretation of the ground state vibrational band, the deformed band, and the γ band agree fairly well with the calculations [17].

It is emphasized here that, based on the works of Refs. [15], [16], and [17], the ^{30}Mg level scheme exhibits varying and complex structures which require the coexistence of multiple different nuclear shapes, belonging to different collective bands, within one level scheme. Nuclear shape

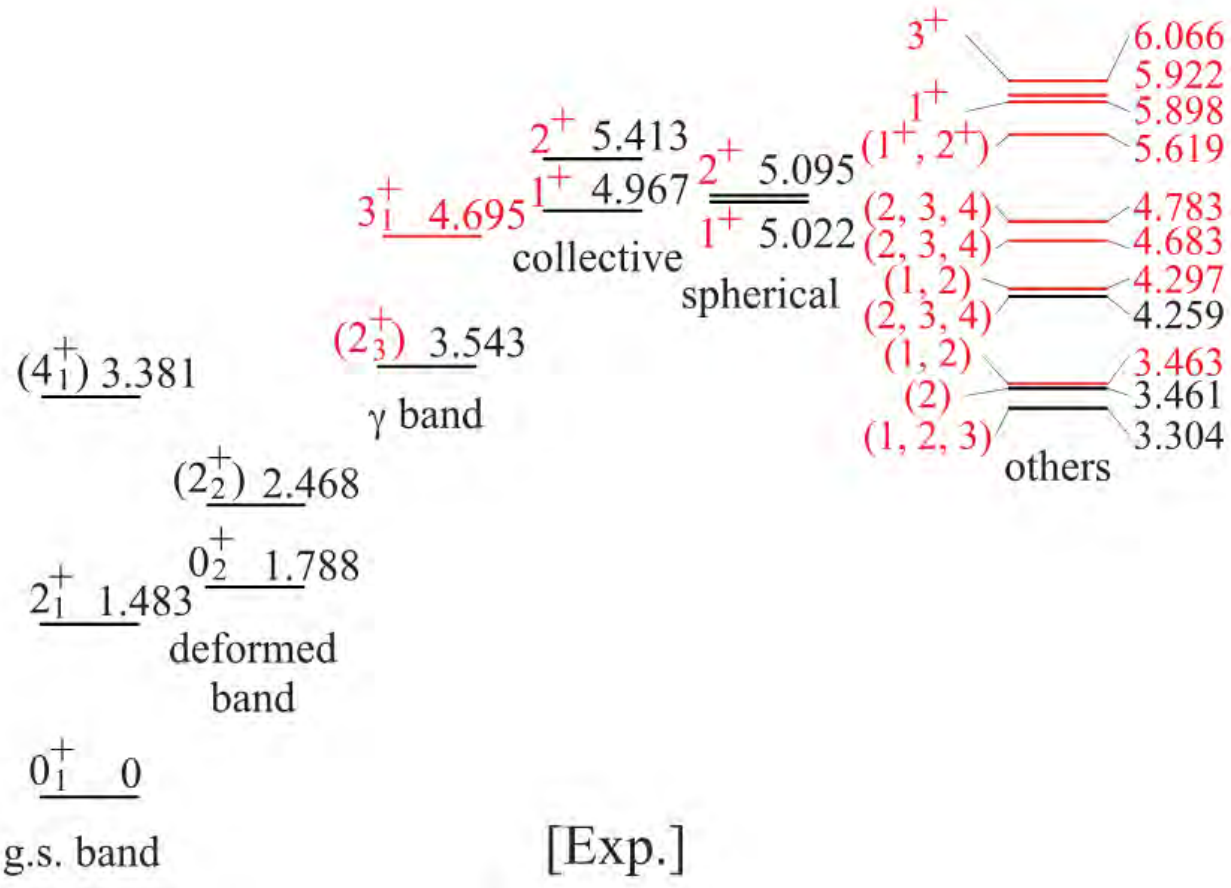

Figure 1.8 The level scheme of ^{30}Mg as observed in Ref. [17], broken into several structures, most of which are collective. See full text for details. Reprinted figure with permission from H. Nishibata et al., Phys. Rev. C **102**, 054327 (2020). Copyright 2020 by the American Physical Society.

coexistence in the neutron-rich $N \sim 20$ isotopes is an active area of research; as will be discussed in the next section, a complete description of this phenomenon in the region of interest requires the consideration of residual interactions which allow deformed intruder states to become energetically favored over spherical normal states.

1.3 The N=20 Island of Inversion

As has been suggested in the previous sections, the conventional spherical shell model is powerful in its ability to predict the locations of nuclear magic numbers, but its description of nuclear forces is incomplete in many areas of the Chart of Nuclides, particularly in midshell regions far from the valley of stability. In these cases, some discrepancies observed between

experimental results and the non-interacting spherical shell model can be resolved by explicitly introducing residual interactions to the shell model.

One phenomenon which has been observed in several exotic regions of the nuclear chart involves the apparent disappearance of a conventional magic number. This unique form of shell evolution has been observed in exotic neutron-rich isotopes near the neutron shell closures at N = 8, 20, 28, and 40 (see, e.g., Refs. [1, 18–24]). These regions are referred to as "islands of inversion," due to the inversion in the ordering of normal, spherical states and deformed intruder states in the level scheme [25]. Close inspection of Figure 1.2 hints at the existence of nuclei in which a conventional magic number disappears. In heavier nuclei, some theoretical models have suggested the existence of an $N = 50$ island of inversion [26, 27].

A comprehensive understanding of nuclear forces requires characterization of the microscopic interactions driving this type of shell evolution. Of particular interest is an understanding of the residual interactions that allow intruder states to become favored in the low-lying level scheme. The appearance of shape coexistence within and surrounding the islands of inversion is a key feature which can be used to track this unique form of shell evolution, as nuclear shapes and configurations can be intrinsically linked. While a thorough investigation of these topics is certainly beyond the scope of the present work, the remainder of this section will present a brief synopsis of some critical work which has elucidated nuclear properties in the $N = 20$ island of inversion.

Experimentally, anomalous behavior of the isotopes near $N \sim 20$, $Z \sim 11$ has been observed since a 1975 study by Thibault et al. identified that ^{31,32}Na were more tightly bound than expected by several theoretical models, suggesting the onset of deformation in these isotopes [1]. Soon after, Détraz et al. measured the unexpectedly low 2^+_1 excitation energy (885.7(20) keV) of ^{32}Mg [28]. Additional evidence for the onset of deformation in ^{32}Mg came with the measurement of its high B(E2) value between the ground state and the 2^+_1 state [20].

Systematic comparison of 2^+_1 excitation energies for even-even isotopes, $16 \leq N \leq 24$, $10 \leq Z \leq 20$, is shown in Figure 1.9. For the less exotic Silicon, Sulfur, Argon, and Calcium isotopic chains, there is an enhancement in 2^+_1 energy at $N = 20$. This enhancement is most notable for the

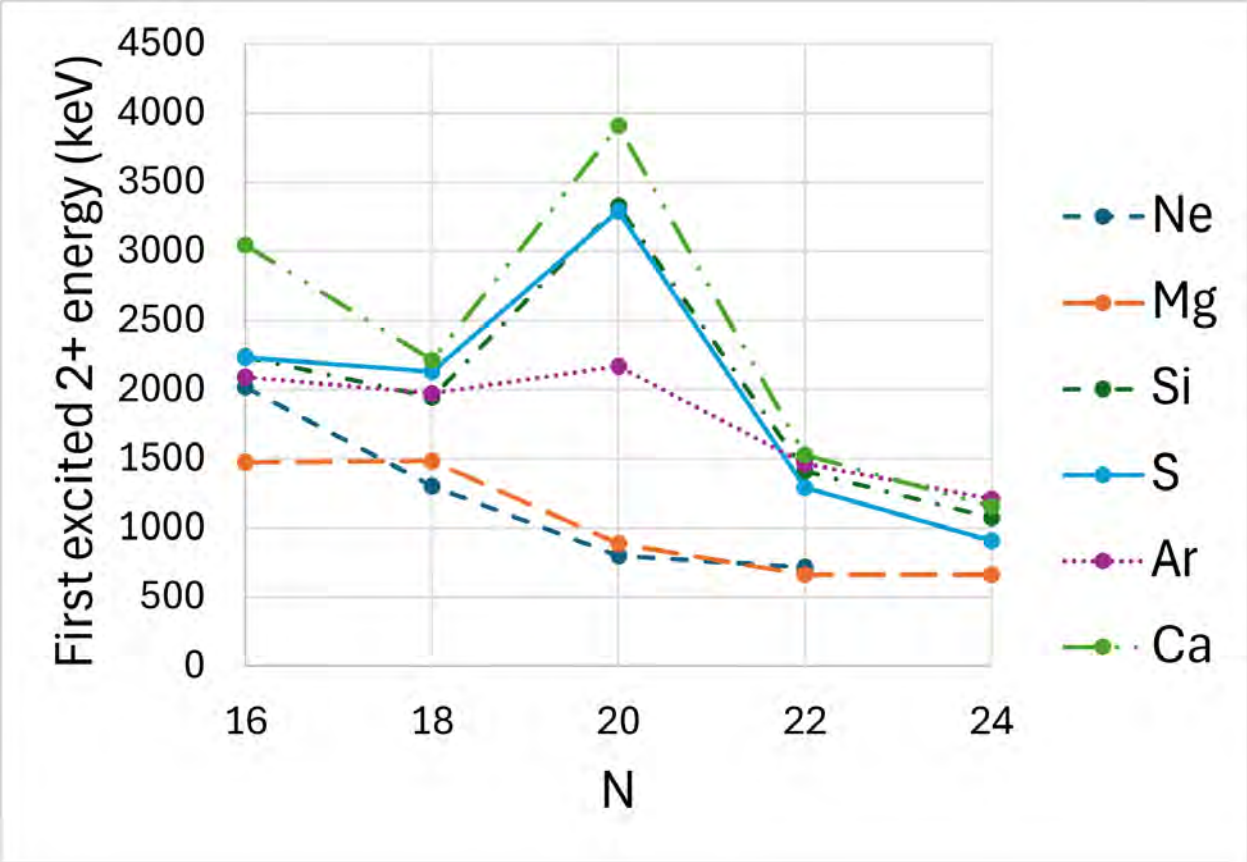

Figure 1.9 Excitation energy of the first excited 2^+ state for the neutron-rich even-even isotopes, $16 \leq N \leq 24$, $10 \leq Z \leq 20$. Neon: dark blue short dash. Magnesium: orange long dash. Silicon: dark green dot-dash. Sulfur: light blue solid. Argon: purple dotted. Calcium: light green dot-dot-dash. Data are from the Evaluated Nuclear Structure Data Files, Adopted Levels and Gammas. See Ref. [29] and references therein.

doubly-magic ^{40}Ca. However, there is no trace of enhancement in the 2_1^+ energies along the Neon and Magnesium isotopic chains. This deviation from the expected spherical shell model behavior can be taken as evidence for the inclusion of the $N \sim 20$ Neon and Magnesium isotopes within the island of inversion.

^{30}Mg lies just outside of the western border of the island of inversion [16, 17, 30]; ^{34}Si lies just outside of the northern border [31–33]. Eastward and southward extension remains a topic of discussion, with some studies noting low-lying intruder character as far south as the Fluorine isotopic chain and predicting shell quenching in the unbound, doubly-magic ^{28}O isotope [34, 35]. It has been suggested that the dominance of intruder states in the low-lying level scheme persists

along the Magnesium isotopic chain from ^{32}Mg all the way through the $N = 28$ island of inversion, constituting a merging of the two regions [36, 37]. As improvements in radioactive beam facilities allow scientists to reach closer to the neutron dripline, further exploration of these boundaries becomes possible.

The mechanism driving the dominance of intruder states in the $N = 20$ island of inversion is thought to result from the interplay of two effects. First, residual interactions can cause shifts in the standard spacing of the nuclear orbitals presented in the conventional nuclear shell model. As an example, emptying of the $\pi d_{5/2}$ orbital can push the $\nu d_{3/2}$ orbital higher in energy, towards the fp shell, high enough that the $N = 20$ shell gap is reduced. Due to the properties of certain residual interactions, particularly attractive or repulsive forces between pairs of orbitals can appear as the number of valence protons and neutrons evolves, resulting in dramatic shifts that accompany the addition of just a few nucleons. In the island of inversion, the summed effect of these residual interactions amounts to a reduction in the size of the $N = 20$ shell gap [9].

Conventionally, the $N = 20$ shell gap is large. Therefore, the excitation of neutrons across the shell gap should be energetically expensive, forcing states dominated by these cross-shell excitations to exist at high excitation energies. With a reduced (but not fully quenched) $N = 20$ shell gap, the excitation of neutrons from the sd shell into the fp shell requires less energy, making it easier for states dominated by cross-shell excitations to appear at lower energies. This effect is compounded, as these configurations dominated by cross-shell excitations gain additional correlation energy due to residual interactions across the shell gap. This allows these states to become even more energetically favorable. As these effects become more extreme near the center of the island of inversion, intruder states dominated by cross-shell excitations drop low enough in energy that there is an "inversion." The low-lying level scheme—including the ground state—can become completely occupied by intruder states, while states dominated by the normal configuration now lie at high excitation energies [13].

Of course, while this description of nuclear forces has had success in reproducing experimental observables within the $N = 20$ Island of Inversion, many outstanding questions remain. Of

particular interest is the degree to which specific residual interactions (such as tensor forces, 3N forces or continuum coupling) must be treated in order to reproduce experimental data, as well as the balance of the strength of different residual interactions in different nuclei. In particular, nuclei near the neutron dripline are only very recently beginning to be experimentally studied in detail, and testing of theoretical models against such nuclei is critical to the refinement of the nuclear interactions driving shell and shape evolution. Furthermore, recent studies have suggested a high degree of configuration and shape mixing in several nuclei near the island of inversion, emphasizing that the simple picture of the inversion of pure spherical and deformed states may be more complex than initially thought [16, 38–40]. More definitive delineation of the boundaries of the island of inversion is of particular interest, especially along the southern and eastern borders. Finally, it is notable for the current study that spectroscopy of the island of inversion is far from complete, particularly when approaching the neutron dripline. As will be discussed in Section 1.5, the level scheme of ^{32}Na — a critical member of the island of inversion — leaves many questions unanswered. Expanding the spectroscopy of this region of the nuclear chart provides opportunities to test and refine the description of the nuclear forces governing observed phenomena in the island of inversion.

1.4 Previous studies of ^{30}Ne β-decay

^{30}Ne is one of the two isotopes whose β decays are studied in the present work. The main child isotope of interest populated in this decay is ^{30}Na, although neutron emission branches (P_{1n} =12.6(35)% and P_{2n} =8.9(23)% [3]) allow exploration of the ^{28,29}Na level schemes as well. A variety of studies of the ^{30}Na level scheme have been published, using population mechanisms including inelastic scattering [41–43], Coulomb excitation [44–46], and nucleon removal [41, 47]; however, the focus of this section will be the population of excited states in ^{30}Na following ^{30}Ne β decay.

Two previous studies of this decay exist: a 1999 study by Reed et al. [2] and a 2007 study by Tripathi et al. [3]. As is evident in Figure 14 of Ref. [2], the study by Reed et al. was fairly limited in statistics, although it provided first indication of the intense 150.6(2) keV γ ray populating the

ground state of ^{30}Na [2]. As is seen in Ref. [3], the 150 keV level is the most intensely populated state following the β decay of ^{30}Ne, and it is also indirectly fed through γ decays of higher lying states which are fed in β decay. Reed et al. observed this transition to have an intensity of 95(10)% [2].

The later study by Tripathi et al. [3] significantly expanded the level scheme beyond what was seen in Ref. [2], identifying not only the 150 keV transition but also six additional higher-lying transitions. Figure 1.10 depicts the expanded level scheme deduced from Ref. [3]. Notable measurements include γ-ray and excited state energies, β-decay and γ-ray intensities, log(ft) values, neutron emission percentages, and β-decay half-life. A third study [4], although not focused on ^{30}Ne decay, reports good reproduction of the ^{30}Na level scheme as reported in Ref. [3], including observation of the same seven γ rays.

Beyond β-delayed γ rays, the half-life and neutron emission probabilities have been measured several times for ^{30}Ne β decay. The half-life measurements are given as follows: 7(2) ms [48], 5.8(2) ms [49], 7(2) ms [2], 7.5(15) ms [50], 7.3(3) ms [3], 7.18(22) ms [4]. Overall, there is good consensus among these multiple measurements. Excluding the outlying result of Ref. [49] puts a weighted average of the half-life around 7.2 ms, with a standard deviation of about 0.3 ms. There are three measurements of the one-neutron emission probability P_{1n}: 9^{+17}_{-9}% [2], 9(17)% [50], and 12.6(35)% [3]. While the first two measurements are much less precise than the third, there is good agreement among all three. Finally, the two-neutron emission probability has been measured once by Tripathi et al., resulting in a measurement of P_{2n} = 8.9(23)% [3].

The main goal of the study of ^{30}Ne decay in the present work is to validate the present methodology, which will be used in the study of the unknown ^{32}Ne β decay. If the present study achieves a much higher level of statistics for the ^{30}Ne isotope, the identification of new, weaker γ-ray transitions is possible, but it is not the primary focus.

1.5 Previous studies of ^{32}Na

The β decay of ^{32}Ne into ^{32}Na is not as well studied as the β decay of ^{30}Ne into ^{30}Na. Only two measurements of its half-life exist: 3.5(9) ms [49] and $4.5(4)_{\text{stat}}(6)_{\text{sys}}$ ms [51]. These can be

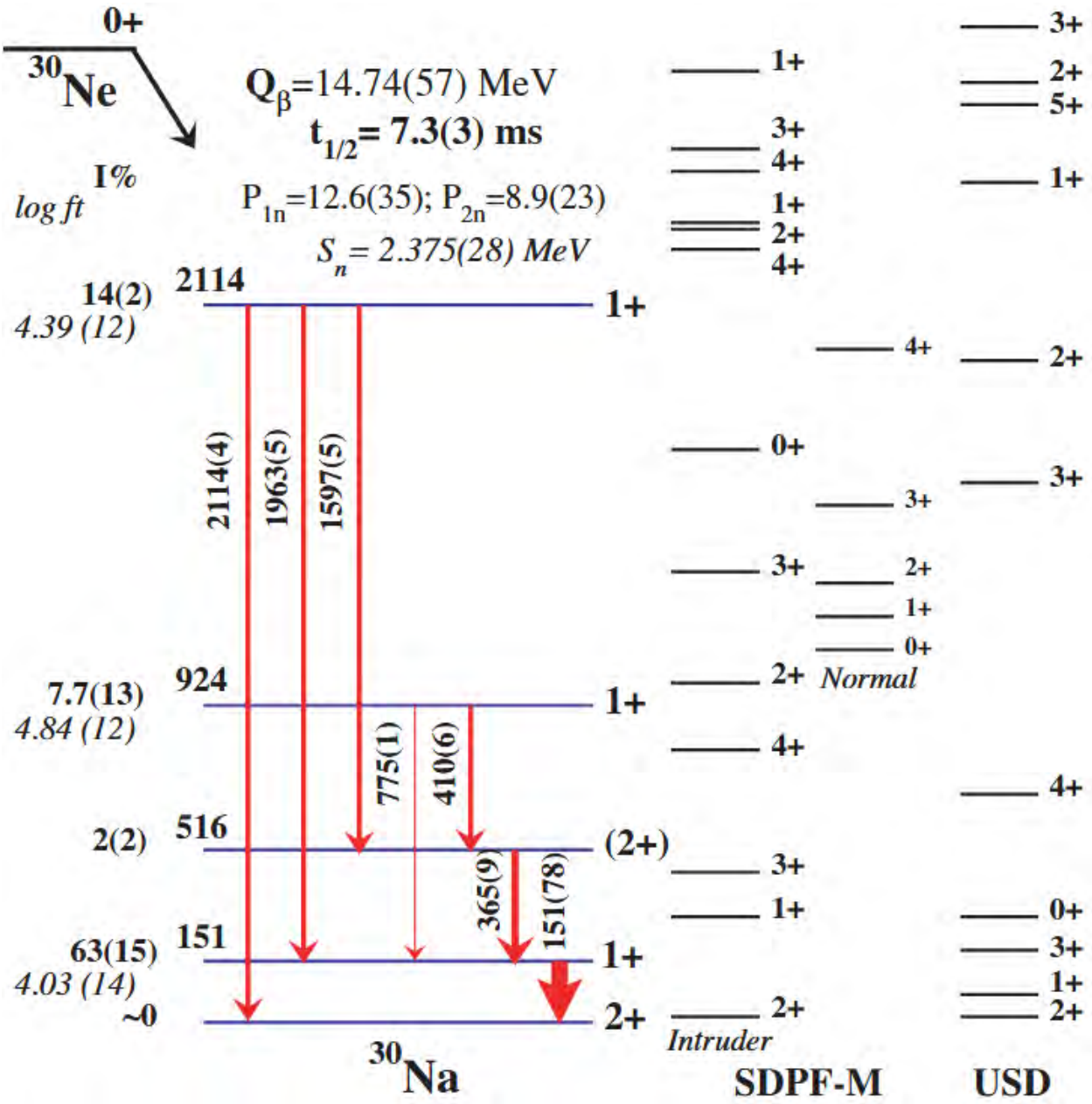

Figure 1.10 Diagram of the ^{30}Na level scheme populated in ^{30}Ne β-decay, as observed in Ref. [3]. Reprinted figure with permission from Vandana Tripathi et al., Phys. Rev. C **76**, 049902 (2007). Copyright 2007 by the American Physical Society.

$E_{x,i}$ (keV)	J_i^π	$T_{1/2}$	E_γ (keV)	$E_{x,f}$ (keV)
0	$(0^-, 3^-, 4^-)$	13.2(4) ms	n/a	n/a
117.6(64)		$\gtrapprox$ ms		
401 + x	$(4^-, 2^-)$		401	x
569(12) + y			569(12)	y
625 + x	$(6^-, 0^+)$	24(2) μs	224	401 + x

Table 1.1 Excitation energies of known states in ^{32}Na along with their de-exciting γ-ray energies, half-lives, and spin-parity assignments. Data are from Refs. [5, 6, 52, 54–56]; see text for details.

combined to produce a weighted average of 4.1(7) ms [52]. Neutron emission probabilities for this isotope have never been measured; with an estimated Q_β value of 18.360(500) MeV and a child neutron separation energy of 1.680(40) MeV [53], there is a large window for one-neutron emission. Furthermore, the child two-neutron separation energy is 5.980(40) MeV [53], which also allows a large window for two-neutron emission. Finally, β-delayed γ-ray transitions in ^{32}Na have never been measured. This will be the focus of the present study.

While there are certainly gaps in the experimental study of ^{32}Na, specifically when populated in ^{32}Ne β decay, some experimental data do exist. They are summarized in Table 1.1. The first study to report on γ-ray transitions in ^{32}Na is from 2010, published by Doornenbal et al. [54]. ^{32}Na was produced in projectile fragmentation of ^{48}Ca on a Be target; the produced ^{32}Na was impinged on a natural Carbon target to populate excited states following inelastic scattering. One γ-ray transition was observed at 569(12) keV. Following calculations by Poves and Retamosa, multiple low-lying states below 150 keV are predicted in ^{32}Na [55]. As such low-energy γ-ray transitions were below the experimental sensitivity, Doornenbal et al. did not infer the energy of the state which emits the 569(12) keV transition. The spin and parity of this state also remain unknown [54].

The next study came 13 years later in 2023, published by Gray et al. [5]. ^{32}Na was produced in projectile fragmentation of a ^{48}Ca beam on a ^{9}Be target. A cocktail beam was selected and delivered to a yttrium orthosilicate (YSO) implantation detector. Two γ-ray transitions were observed at 224 and 401 keV directly following ^{32}Na beam implantation. These transitions were observed in coincidence, and they were observed to have the same 24(2) μs half-life. The γ-ray spectra from this study depicting this information are given in Figure 1.11. This suggests the existence of an

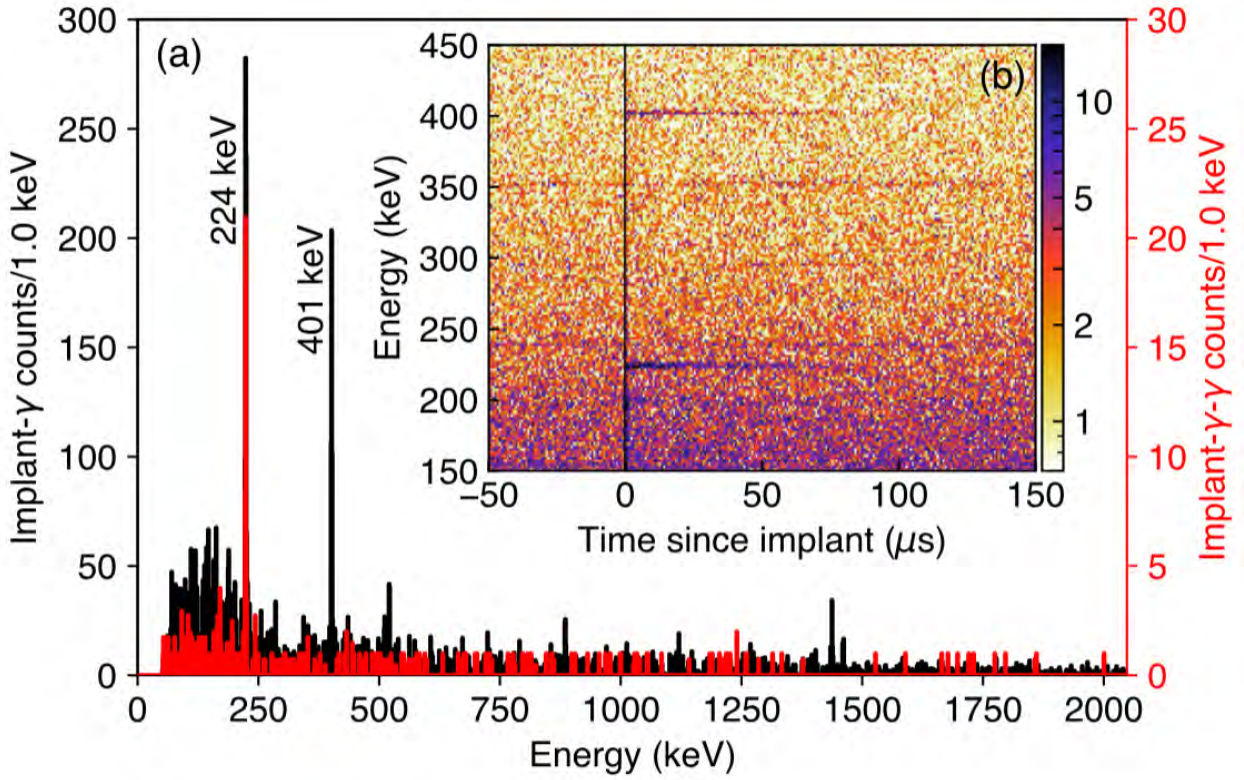

Figure 1.11 γ-ray spectra from Ref. [5], depicting the 224 keV and 401 keV delayed γ rays that were observed following implantation of ^{32}Na ions. The black plot is ^{32}Na implant-correlated, and the red plot adds on an additional 401 keV γ-ray gate. The inset expands the implant-gated γ-ray spectrum onto the time axis, emphasizing the isomeric nature of the initial state. Reprinted figure with permission from T. J. Gray et al., Phys. Rev. Lett. **130**, 242501 (2023). Copyright 2023 by the American Physical Society.

isomer with a 24(2) μs half-life which decays via a cascade of 224 and 401 keV γ rays. The 224 keV γ ray was placed above the 401 keV γ ray, directly depopulating the isomer. Gray et al. also recognized the potential existence of unobserved low-lying states, resulting in the ambiguity of the excitation energies of the isomeric state and the intermediate state populated in this study [5].

Based on electromagnetic transition strength estimates for the observed transitions, Gray et al. suggest that the isomeric state could be described in one of two ways: as a 6^- spherical shape isomer or a 0^+ deformed spin isomer. These two scenarios are depicted in Figure 1.12. In the first scenario, the isomeric state is spherical and decays into a deformed ground state band via a hindered E2 transition. This would indicate spherical-deformed shape coexistence in ^{32}Na. The spin-parity sequence of the three inferred states is $6^- \rightarrow 4^- \rightarrow 3^-$. In the second scenario, the

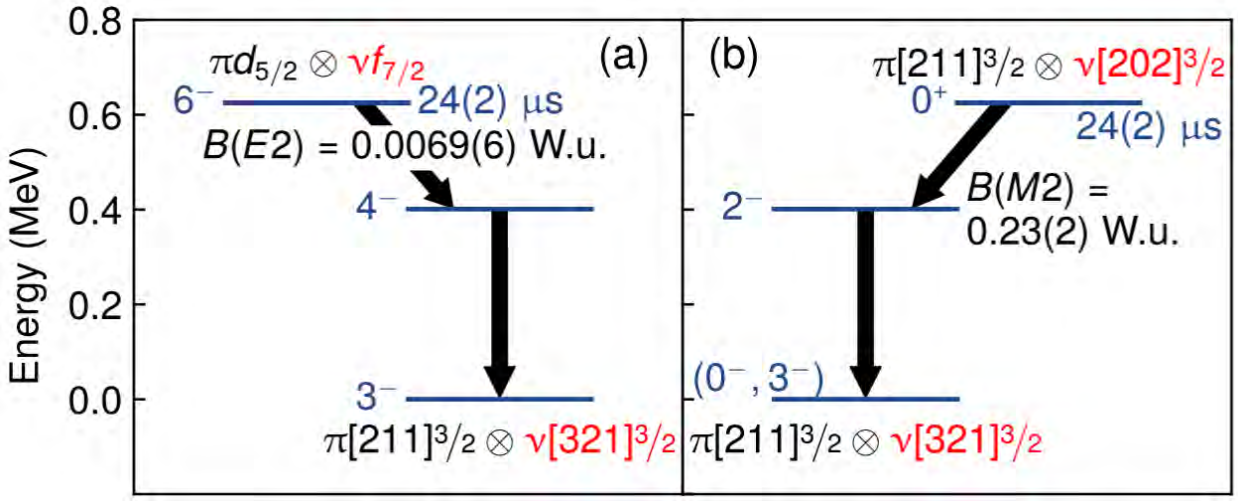

Figure 1.12 Two partial level schemes presenting the two scenarios for the isomeric state observed in Ref. [5]. (a) represents a 6^- spherical shape isomer decaying via a hindered E2 transition into a deformed ground state band, with spin-parity sequence $6^- \rightarrow 4^- \rightarrow 3^-$. (b) represents a 0^+ deformed spin isomer decaying via an M2 transition into a deformed ground state band with a different neutron configuration, with spin-parity sequence $0^+ \rightarrow 2^- \rightarrow (0^-, 3^-)$. Reprinted figure with permission from T. J. Gray et al., Phys. Rev. Lett. **130**, 242501 (2023). Copyright 2023 by the American Physical Society.

isomeric state is deformed and decays into a deformed ground state band via an M2 transition. The spin-parity sequence of the three inferred states is $0^+ \rightarrow 2^- \rightarrow (0^-, 3^-)$. Again, it is important to note that, while Figure 1.12 illustrates the final state as the ground state, it is also possible that the 401 keV γ ray could populate an unobserved low-lying state, possibly a long-lived isomer, a β-decaying isomer, or a low-energy γ-decaying state beyond the experimental sensitivity [5].

Ultimately, there are two scenarios for the set of states inferred in Ref. [5], both which involve very different underlying physics. It is interesting to note that the present study will utilize β decay to populate excited states in ^{32}Na. As will be discussed in Section 2.1, β decay is a very selective process, which will largely populate states with the same parity as the initial state and with a spin within one unit of the spin of the initial state [7]. With an initial spin-parity of 0^+ for the ^{32}Ne ground state, the 6^- and 4^- states of the first scenario would likely be inaccessible. On the other hand, the 0^+ state of the second scenario could be directly populated in β decay, and the 2^- state could be indirectly populated through E1 γ decay of a higher-lying 1^+ state populated directly

in β decay. Thus, observation or nonobservation of the γ rays observed in Ref. [5] following β decay of ^{32}Ne could very well provide the additional information needed to choose between the two scenarios suggested in Ref. [5]

A final study of ^{32}Na was published in 2025 by Lykiardopoulou et al. [6]. ^{32}Na was produced by impinging a proton beam onto a Uranium Carbide target. The mass of ^{32}Na was measured using a multi-reflection time of flight mass spectrograph (MR-TOF-MS), paired with a mass range selector (MRS) for additional beam purification. There are two clear peaks visible in the mass spectra (see Figure 2 of Ref. [6]), indicating the presence of a long-lived isomeric state alongside the ground state in the beam. This isomer is expected to live on the order of at least one millisecond, based on the experimental setup in which it is measured. Due to this long half-life, it would not have been feasible for Doornenbal et al. [54] or Gray et al. [5] to observe its decay. Based on the separation of the two mass peaks, the excitation energy of the isomer is 117.6(64) keV. No further comment is made on the spin and parity of the state or its decay mode [6].

A final matter is the ground state spin and parity. Ref. [5] suggests a spin and parity of either 0^- or 3^- for the ground state (see Figure 1.12). This is in line with the predictions of two previous works. Calculations in the β-decay study of Ref. [56] suggest spin and parity of either 3^- or 4^-. The theoretical study in Ref. [55] predicts a ground state multiplet with spins and parities of 0^-, 3^-, and 4^-.

As summarized in Table 1.1, what is known about ^{32}Na leaves many remaining questions. Only one excited state is firmly placed in energy, as it is unclear which final states any of the γ rays decay into. None of the states (excited or ground) have a firm spin-parity assignment. Several γ rays have been observed, but a decay from the 117.6(64) keV isomer has yet to be identified. Moreover, the 117.6(64) keV isomer does not yet have a firm half-life. As such, the construction of a level scheme for this isotope with any degree of certainty is nearly impossible. This leaves much room for the level scheme to be expanded. The present study of ^{32}Ne β decay aims to answer some of the outstanding questions regarding the ^{32}Na level scheme, as well as identify new γ-ray transitions and excited states in ^{32}Na.

CHAPTER 2

METHODS

2.1 β-decay

The vast majority of unstable nuclei decay via one of three very similar decay pathways: β^- decay, β^+ decay, or electron capture decay. These three processes are described schematically by Equations 2.1, 2.2, and 2.3, respectively. These decays are governed by the weak nuclear interaction [8].

$$(Z, N) \rightarrow (Z + 1, N - 1) + e^- + \overline{\nu}_e \tag{2.1}$$

$$(Z, N) \rightarrow (Z - 1, N + 1) + e^+ + \nu_e \tag{2.2}$$

$$(Z, N) + e^- \rightarrow (Z - 1, N + 1) + \nu_e \tag{2.3}$$

The β^- decay process presented a significant scientific puzzle during much of the early 20th century. Scientists observed that, in the α and γ decay processes, the energy spectra showed sharp peaks. This is easily understood in terms of energy conservation: the emitted α particle or γ ray must have a characteristic energy equal to the difference between the energies of the final and initial states. In contrast to the simple picture presented in α and γ decay spectra, the energy spectra of emitted β particles show broad, continuous distributions [8].

$$Q_{\beta^-} = [M(Z, N) - M(Z + 1, N - 1)]c^2 \tag{2.4}$$

It was later discovered that, as represented in Equation 2.1, a nucleus undergoing β^- decay emits two particles: the β particle itself (now known to be an electron), and a secondary particle, now referred to as an antineutrino. The energy released in the β^- decay process is defined by the decay Q-value, which is given in Equation 2.4 as the difference in the masses of the initial and final nuclei [7]. In the decay, this energy is imparted in the form of kinetic energy to the electron,

the antineutrino, and, nominally, the recoiling nucleus. Without the emission of the antineutrino, one would expect the decay electron spectrum to exhibit one or more sharp peaks, as with α and γ decay. The peak energies would depend on which final state in the child the decay proceeded to, with a maximum peak energy equal to the decay Q-value. However, the decay energy is indeed distributed probabilistically between the electron and the antineutrino, allowing electron energies to vary continuously up to the Q-value. It is now understood that the emission of the antineutrino is crucial; without it, conservation of lepton number is violated by Equation 2.1. Experimentally, the neutrino is not typically measured due to the difficulty of its detection [7, 8].

β^- decay and β^+ decay are mirror processes: in β^- decay, a neutron is converted to a proton, and in β^+ decay, a proton is converted into a neutron. Electron capture is similar to β^+ decay in that a proton is converted into a neutron; however, in this process, the nucleus captures an existing electron from the atomic orbitals. In order to satisfy charge and lepton-number conservation rules, no electron or positron need be emitted, unlike in β^- and β^+ decay [8]. The β^+ decay and electron capture decay processes are applicable mainly for neutron-deficient isotopes. For the rest of this work, "β decay" will refer to β^- decay unless otherwise noted.

There are two modes of β decay: Fermi and Gamow-Teller. In Fermi decay, the intrinsic spins of the emitted electron and antineutrino couple to $S = 0$; by conservation of angular momentum, the spin of the nucleus must not change. In Gamow-Teller decay, the intrinsic spins of the emitted electron and antineutrino couple to $S = 1$. The emitted particles may also carry away orbital angular momentum, but $L = 0$ ("allowed") decays are strongly favored [8].

β decays can be classified by the spin change (ΔJ) and parity change ($\Delta\pi$) from the initial to the final state of the decaying nucleus. These classifications are listed in Table 2.1. More orbital angular momentum carried away by the emitted particles corresponds to higher order forbidden transitions. Experimentally, forbidden transitions are rarely observed in light nuclei ($A \approx 70$ or less) [7]. $L = 0$ (allowed) Gamow-Teller β-decay transitions can involve a spin change of 0 or 1 units due to the $S = 1$ intrinsic spin coupling of the electron and the antineutrino, so the final state spin-parity J_f^π must be equal to $(J_i - 1)^\pi$, J_i^π, or $(J_i + 1)^\pi$. Allowed Fermi β-decay transitions must

Classification	ΔJ	$\Delta\pi$
Superallowed	0	no
Allowed	0, 1	no
First-forbidden	0, 1, 2	yes
Second-forbidden	1, 2, 3	no
Third-forbidden	2, 3, 4	yes
...	...	...

Table 2.1 β-decay selection rules, indicating level of forbidden-ness as a function of spin and parity change between the initial and final states.

proceed to a final state with spin-parity J_i^π.

A typical measure of the strength of a β-decay transition is its $ft_{1/2}$ value, where f is a phase space factor and $t_{1/2}$ is the partial half-life of the decay. The full theoretical formulation for the $ft_{1/2}$ value is unnecessary for the sake of the present discussion; what is significant is that $ft_{1/2}$ is inversely proportional to the β-decay transition matrix element. Thus, $ft_{1/2}$ values can provide unique insight into the underlying properties of the initial and final states.

Practically speaking, $ft_{1/2}$ values can span multiple orders of magnitude, so the reported values are often given as $\log_{10}(ft_{1/2})$ (often simplified to log(ft)). While computation of the phase space factor is complex, tabulated values exist in references such as Ref. [57]. More modern online tools also exist, such as the LogFT program, hosted online by the National Nuclear Data Center [58]. With the help of tools such as these, it is possible to calculate a log(ft) value for a β-decay transition by simply knowing the parent half-life, the energy of the decay, the intensity of the branch, and the charge of the child.

The different classifications of β-decay transitions given in Table 2.1 can be approximately characterized by their log(ft) values, with increasingly forbidden transitions having increasing log(ft) values. A systematic overview of log(ft) evolution for different orders of transitions is shown in Figure 2.1. As is apparent, most observed cases are allowed and first-forbidden, with more highly forbidden transitions occurring much less frequently. While sharp distinctions between the log(ft) values for different order transitions cannot be definitively drawn, a log(ft) value can often be a good indicator of the order of the transition, and thus can often be used to make tentative

spin-parity assignments or suggestions. Guidelines on using log(ft) values to assign the order of the transition are given in Refs. [59, 60], and some rules are suggested based on existing data.

In the case of $J_i^\pi = 0^+$, the final state spin-parity options are 0^+ and 1^+ (the $(J_i - 1)^\pi$ option is non-physical). $0^+ \rightarrow 0^+$ decays are special; for the case where both the initial and final states are members of an isospin multiplet, this decay is superallowed, and thus will have a low (3.1–3.6) log(ft) value [59, 60]. If the isospin changes from the initial to final state, the decay becomes hindered, with typical log(ft) values greater than 6.4 [59, 60]. For this reason, the observation of a β decay from an initial 0^+ state with a log(ft) between 3.6–6.4 typically suggests a spin-parity assignment of 1^+ for the final state [59, 60]. Indeed, as is evident in Figure 2.1, most $0^+ \rightarrow 1^+$ decays have log(ft) values in this region.

The Bateman Equations [61] describe the time dependence of the activities of decaying nuclei and their descendants. The decay rate λ is related to the half-life T as $T\lambda = \ln(2)$. For a given amount of radioactive material initially present (or, in this case, for an amount of radioactive material with initial activity A_0), the activity of the substance decreases exponentially over time. Equation 2.5 shows this time dependency, where $A_1(t)$ is the activity at time t. The subscript 1 indicates the first generation of decays, so $A_1(0)$ is the activity of the parent at time 0 and λ_1 is the decay rate of the parent.

$$A_1(t) = A_1(0)e^{-\lambda_1 t} \tag{2.5}$$

For the exotic isotopes analyzed in the present work, the child nucleus populated by the parent decay is often radioactive itself, and thus the material will continue to decay through multiple generations until a stable isotope is reached. The activity of child decays over time can be described by Equation 2.6. Note that this equation depends on the same variables as Equation 2.5, but with additional dependence on the child decay rate λ_2.

$$A_2(t) = A_1(0)\frac{\lambda_2}{\lambda_2 - \lambda_1}\left(e^{-\lambda_1 t} - e^{-\lambda_2 t}\right) \tag{2.6}$$

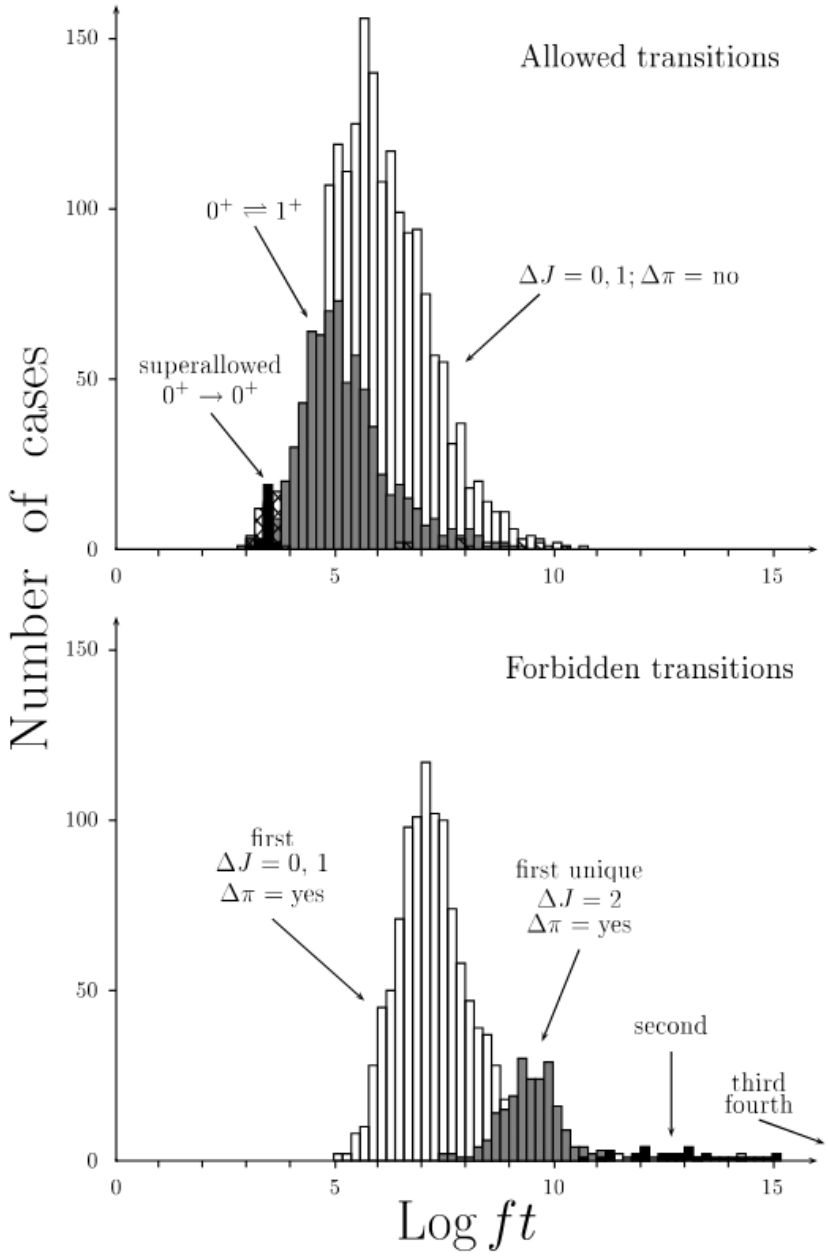

Figure 2.1 Systematic overview of log(ft) values for known β-decay transitions. Shaded regions indicate different orders of transitions. Reprinted from Nuclear Data Sheets **84**, B. Singh, J. L. Rodriguez, S. S. M. Wong, and J. K. Tuli, "Review Of Logft Values in β Decay," 487–583, Copyright 1998, with permission from Elsevier.

For this analysis, the latest generation of decays which will be considered are the 3rd generation (grandchild) decays. The time dependence of these decays is shown in Equation 2.7, which again depends on the same variables as Equations 2.5 and 2.6 but adds in a new dependency on the grandchild decay rate λ_3.

$$A_3(t) = A_1(0)\lambda_2\lambda_3\left(\frac{e^{-\lambda_1 t}}{(\lambda_2-\lambda_1)(\lambda_3-\lambda_1)} + \frac{e^{-\lambda_2 t}}{(\lambda_1-\lambda_2)(\lambda_3-\lambda_2)} + \frac{e^{-\lambda_3 t}}{(\lambda_1-\lambda_3)(\lambda_2-\lambda_3)}\right) \quad (2.7)$$

2.1.1 Delayed 1- and 2-neutron emission

Any β-decaying state (typically a nuclear ground state, but occasionally a long-lived nuclear excited state) can decay into a number of states in the child nucleus. Some decays may have large branches into only one or two states in the child, while in other nuclei, the decay strength may be more fragmented among different states. The final state populated by β-decay in the child nucleus may be the ground state, an excited state, or (if energetically available) a neutron-unbound excited state. In short, β decay may populate any state in the child which is lower in energy than the Q_β value. Therefore, if the neutron separation energy S_n of the child is smaller than the decay Q_β value, the decay can populate a neutron-unbound excited state. Similarly, if the two-neutron separation energy of the child is smaller than the decay Q_β value, the decay can populate a two-neutron-unbound excited state. Typically, excited states are depopulated by γ decay (which will be discussed in Section 2.2), but an additional decay channel opens up when the excited state is neutron-unbound: neutron emission. Thus, these states may emit one or two neutrons instead of simply γ decaying into the ground state [62]. This process is referred to as β-delayed neutron emission, or β_{xn} decay. A simplified schematic diagram of these processes is illustrated in Figure 2.2.

In the region of the nuclear chart explored in this study, Q_β values tend to be quite large (approximately on the order of 10-20 MeV) due to the exotic nature of these nuclei. For a similar reason, one- and two-neutron separation energies tend to be rather small. These properties are tabulated in the 2020 Atomic Mass Evaluation [53]; an interactive systematic overview is available

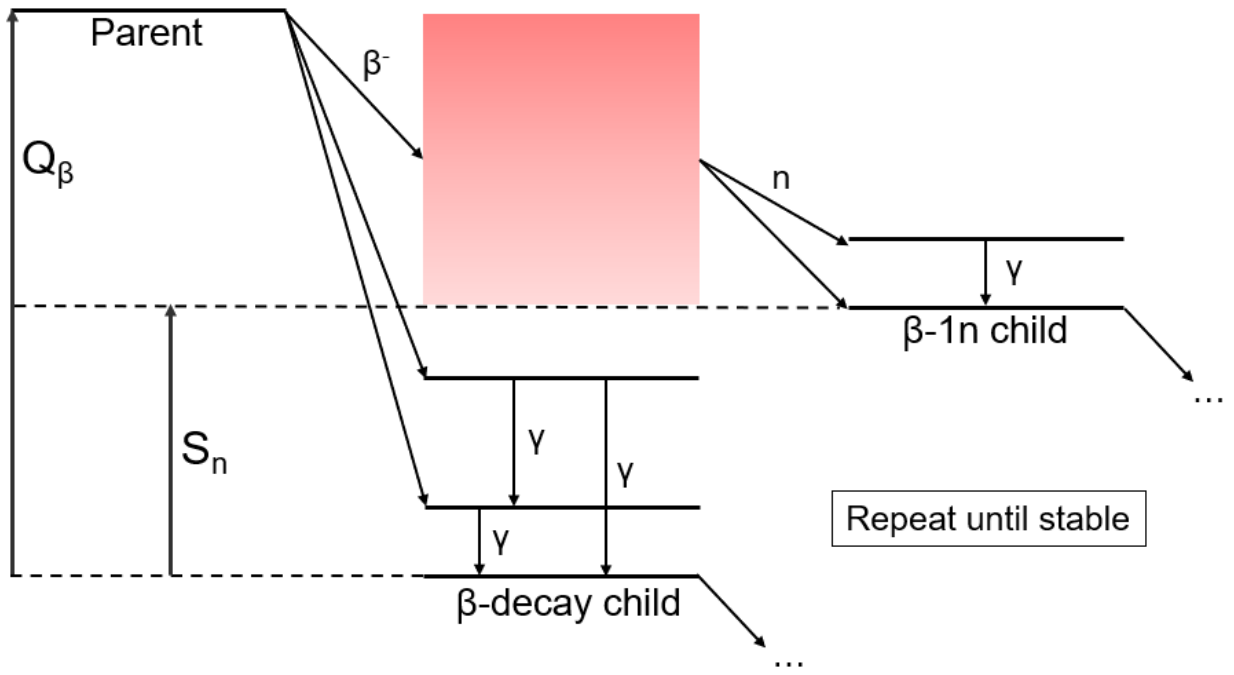

Figure 2.2 Cartoon schematic depicting energetics of the β-delayed neutron emission process.

via the NuDat 3.0 website [14]. Combining large Q_β values with small child neutron separation energies leaves a large window for neutron-unbound states to be populated in β decay, allowing for non-trivial one- and two-neutron emission branches in this region of the nuclear chart.

Experimentally, neutron emission probabilities (P_{xn}, with x referring to the number of emitted neutrons) can be calculated by measuring emitted neutrons. However, if neutron detectors are unavailable, the fingerprints of neutron emission processes can often be seen in β-delayed γ-ray spectra. Take, for example, the γ-ray spectrum produced following the decay of a parent nucleus ${}^{A}Z$. If known γ rays from the ${}^{A-1}(Z+1)$ child or ${}^{A-1}(Z+2)$ grandchild are seen, this can be indicative of one neutron emission. Neutron emission probabilities can be calculated by simply knowing the number of parent β-decays N_β, the γ-ray detection efficiency ε_γ, the number of ${}^{A-1}(Z+2)$ grandchild γ rays observed A_γ, and the branching ratio for production of that γ ray in the ${}^{A-1}(Z+1)$ child decay I_γ. See Equation 2.8 for details of this calculation, which will be used several times throughout this work. An identical calculation using population of the ${}^{A-2}(Z+2)$ grandchild γ rays can be undertaken in order to calculate P_{2n} values. When carrying out these types of calculations,

care must be taken to ensure the same grandchild γ ray is not produced substantially through competing decay paths, such as β-delayed neutron emission of the ${}^{A}(Z+1)$ child. This is to say that this calculation is only effective if the chosen γ ray isolates the ${}^{A}Z \rightarrow^{A-1} (Z+1) \rightarrow^{A-1} (Z+2)$ decay path and contains no contributions from, say, the ${}^{A}Z \rightarrow^{A} (Z+1) \rightarrow^{A-1} (Z+2)$ decay path.

$$P_n = \frac{A_\gamma}{I_\gamma \varepsilon_\gamma N_\beta} \tag{2.8}$$

Alternatively, a lower limit for the P_{xn} value can be computed using the amounts of β_{xn} child γ rays produced following the parent decay, if no viable grandchild γ rays are observed or the I_γ branching ratios of the grandchild γ rays are unknown. In this case, this measurement is only considered a lower limit, as this measurement does not account for alternate β_{xn}-delayed γ decay paths which do not involve the emission of the chosen γ ray, such as ground-state to ground-state β_{xn} decay.

2.2 γ decay

γ decay occurs when an excited nuclear state emits a high-energy photon in order to relax down to a lower excitation energy (or perhaps to the ground state). This type of decay is electromagnetic in nature. γ decays can occur with lifetimes as small as a femtosecond [8]; however, longer-lived states do occur and will be discussed in Section 2.3. The level schemes of nuclei are often complex, exhibiting many excited states than can γ decay to more than one final state. Unlike with β decay, the emitted γ-ray energy is characteristic, equal to the energy difference between the initial and final states. As aforementioned, if β decay populates an excited state in the child nucleus, this state will most likely γ decay towards the ground state. These γ rays may be referred to as β-delayed γ rays.

A classification system exists for γ decays, defining them by the spin and parity change between the initial and final states. These classifications are illustrated in Table 2.2. Electric transitions constitute a change in the charge distribution of the nucleus, while magnetic transitions constitute a change in the spin distribution of the nucleus [8]. Note that E0 $0^+ \rightarrow 0^+$ transitions are strictly forbidden to γ decay, as a photon must carry one unit of angular momentum. Such decays can

Multipolarity	ΔJ	$\Delta\pi$
Electric dipole (E1)	1	yes
Magnetic dipole (M1)	1	no
Electric quadrupole (E2)	2	no
Magnetic quadrupole (M2)	2	yes
Electric octupole (E3)	3	yes
Magnetic octupole (M3)	3	no
...	...	...

Table 2.2 γ decay multipolarity classifications as a function of spin and parity change between initial and final states.

occur through other internal electromagnetic transitions, such as internal conversion or internal pair production [62].

The transition probability for the EL(ML) γ decay between initial and final states i and j is given in Equation 2.9, where L is the angular momentum change, E_γ is the γ-ray transition energy, and $B(EL(ML); i \rightarrow f)$ is the reduced transition probability [8]. The reduced transition probability is a more complex quantity that is dependent on nuclear transition matrix elements [8]. Using Equation 2.9, the reduced transition probability can be experimentally determined from measurements of half-life and γ-ray energy, assuming the spin change of the γ decay is known. There are analytical ways to estimate reduced transition probabilities, which provide a means for interpretation of experimental results.

$$T(EL(ML); i \rightarrow f) = \frac{8\pi}{\hbar} \frac{L+1}{L[(2L+1)!!]^2} \left(\frac{E_\gamma}{\hbar c}\right)^{2L+1} B(EL(ML); i \rightarrow f) \tag{2.9}$$

Taking the approximation that the γ-ray transition is a single-particle transition, the reduced transition probability can be simply estimated as in Equations 2.10 and 2.11 [8]. r_0 is the nuclear radius parameter ($\approx$ 1.2 fm) and A is the nuclear mass number. The $e\hbar/2mc$ factor is equivalent to the nuclear magneton. These equations are referred to as "Weisskopf estimates" of reduced transition probabilities.

$$B_W(EL; i \rightarrow f) = \frac{r_0^{2L}}{4\pi} \left(\frac{3}{L+3}\right)^2 A^{2L/3} [e^2 \mathrm{fm}^{2L}] \tag{2.10}$$

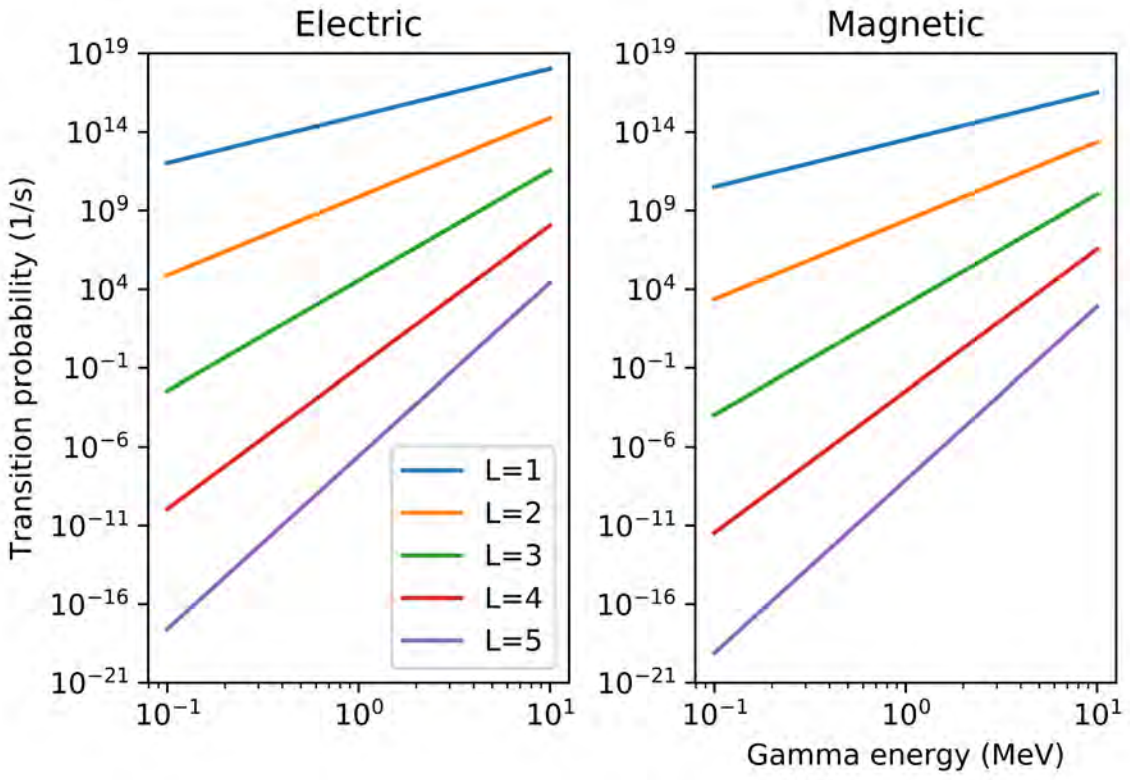

Figure 2.3 Weisskopf estimates of single-particle transition rates for (left) electric and (right) magnetic multipoles as a function of γ-ray energy. Several L values are shown. All are calculated for mass $A = 32$.

$$B_W(ML; i \to f) = \frac{10}{\pi} r_0^{2L-2} \left(\frac{3}{L+3}\right)^2 A^{(2L-2)/3} \left(\frac{e\hbar}{2mc}\right)^2 [\mathrm{fm}^{(2L-2)}] \tag{2.11}$$

Weisskopf estimates for electric and magnetic transitions for several values of L at mass $A = 32$ are shown in Figure 2.3. Notably, smaller L values are expected to have larger transition rates, indicating that lower multipolarities are favored. Comparing the two panels, for a given L value, electric transitions are expected to have higher transition rates than magnetic transitions, indicating that electric transitions are favored. Finally, the values increase with increasing γ-ray energy, indicating that higher-energy transitions are favored.

Experimentally-determined reduced transition probabilities are often compared to the Weisskopf single-particle estimates by dividing the experimental value by the corresponding Weisskopf estimate. The resulting value is also called the reduced transition probability, expressed in what are

known as Weisskopf units (W. u.). A reduced transition probability close to 1 W. u. may indicate that the observed transition is of a highly single-particle nature.

In reality, reduced transition probabilities are not always close to 1 W. u. Some typical values for light mass nuclei are tabulated in Ref. [63] and shown in Figure 2.4, where the x-axis represents the logarithm of the transition strength and the y-axis represents the number of cases observed. Notably, B(E1) strengths tend to be several orders of magnitude smaller than 1. In contrast, B(E2) values approaching 100 W.u. are common.

2.3 Isomeric states

As mentioned in Section 2.2, most excited nuclear states decay very quickly, with lifetimes as small as femtoseconds, via γ decay. However, this is not always the case, as Figure 2.3 suggests. Excited nuclear states with long half-lives are known as isomeric states, or isomers. Isomeric states may also sometimes be called metastable. A strict lower-limit for how long a state must live to be considered isomeric does not exist; different types of studies may take different limits depending on their sensitivity and purpose. For the purposes of this study, any state with a half-life greater than approximately 1 ns is considered isomeric.

There are many factors that can cause a decay to be hindered. As alluded to previously, high spin difference between the initial and final state or small transition energy are two such factors. In general, any significant difference in the initial state and final state wave functions can reduce the overlap of the nuclear transition matrix element, therefore reducing the transition probability. For example, differences in the shapes of the initial and final states can cause isomerism. This is significant in that the existence of a hindered transition can, in some (but not all) cases, be the result of shape coexistence; in the ^{30}Mg case, the $0_2^+ \rightarrow 0_1^+$ transition is shown to have a partial half-life of 396(113) ns [15].

Another type of transition which may be isomeric is a transition between states with very different K values (see Section 1.2). As a final example, a significant difference in shell model configuration can hinder a decay. This is not an exhaustive list of all possible types of isomers, but it covers many which are commonly observed. With such a wide variety of factors which can

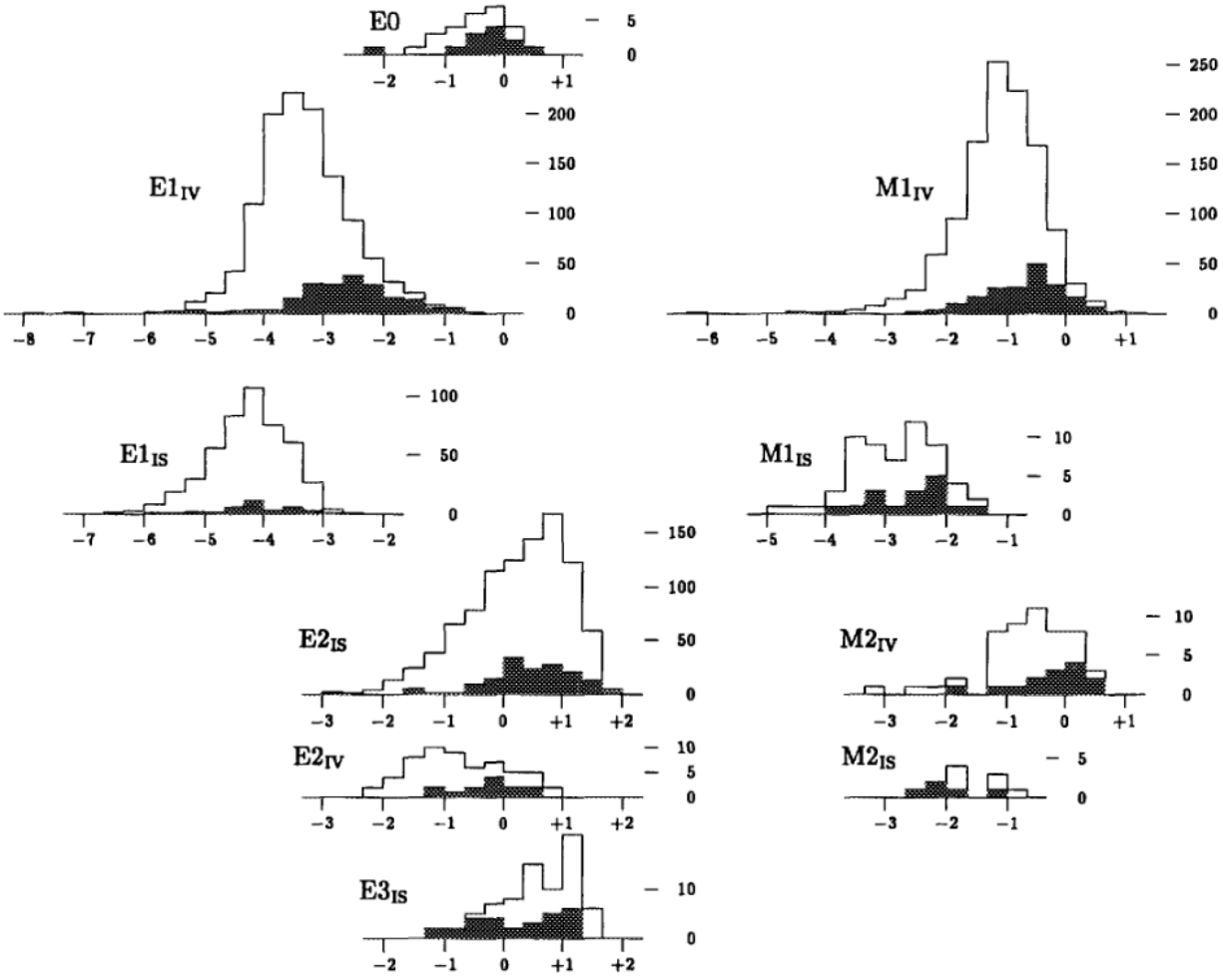

Figure 2.4 Systematic overview of experimentally measured γ-ray transition strengths for several different transition multipolarities, in Weisskopf units (or Wilkinson units for E0). The x-axis represents the logarithm of the transition strength. The white areas represent transitions for nuclei with A=5–44, and the shaded areas represent transitions for nuclei with A=5–20. The IS subscript stands for isoscalar, and the IV subscript stands for isovector. Reprinted from Atomic Data and Nuclear Data Tables **55**, P. M. Endt, "Strengths of Gamma-Ray Transitions in A = 5-44 Nuclei, IV," 171–197, Copyright 1993, with permission from Elsevier.

cause isomerism, the observation of an isomer can provide unique insight into the varied physical mechanisms driving evolution of nuclear structure.

An example of an isomeric state which exists near the region of interest is found in ^{32}Si, detailed in Ref. [64]. The 5^- excited state at 5505 keV decays via an E3 γ-ray transition to the 2^+ state at 1942 keV. Despite the large decay energy (3563 keV), the large spin difference between the initial and final states descreases the transition probability, resulting in a 46.9(5) ns half-life. The 4^+ yrast state lies higher in energy than the 5^- state, so the E1 $5^- \rightarrow 4^+$ decay cannot occur. A 3^- state lies just below the 5^- state, thus making an E2 $5^- \rightarrow 3^-$ decay possible; however, the small decay energy (217 keV) hinders this potential decay path. The ground state has 0^+ spin-parity, making a transition to this state highly unlikely due to the even larger spin difference. With no ideal low-multipolarity, high-energy decay paths available, the hindered E3 $5^- \rightarrow 2^+$ transition becomes the most viable decay path. Another key element to understanding this isomer is that the shell model configuration of this state is significantly different from the 2^+ and 3^- states, reducing the overlap in the initial and final state wave functions and further hindering the decay of the state. This simplified discussion is presented as an illustrative example; see Ref. [64] for a more detailed discussion of this isomeric state.

If a γ-decay is extremely hindered, its half-life can be pushed upwards into the regime of the ground state half-life. At this time scale, the β-decay transition probability may begin to rival the γ-decay transition probability, allowing these two decay pathways to compete. This is less common; an example of a β-decaying isomer is the excited 1^+ state at 46.6 keV in ^{34}Al on the border of the $N = 20$ island of inversion, with a half-life of 26(1) ms compared to the ground state half-life of 54.4(5) ms [31, 65].

CHAPTER 3

EXPERIMENTAL DESCRIPTION

3.1 Rare isotope production and separation

The experiment was performed at the Facility for Rare Isotope Beams (FRIB). At ground level, neutral atoms are heated into plasma, removing electrons and, thus, ionizing the atoms [8]. Nuclei are then directed underground where they are accelerated through the FRIB linear accelerator, which is made up of three parallel straight segments of around 150 m each connected by two bending segments [66]. Superconducting RF cavities create electric fields which are tuned to gradually accelerate the beam up to its desired energy [8]. The full FRIB beamline is depicted in Figure 3.1, from the ion source at the beginning to the experimental stations at the end.

In the present experiment, a primary beam of ^{48}Ca was accelerated to 200 MeV per nucleon (roughly half the speed of light) and impinged upon a rotating Carbon target of 8 mm thickness. Beam particles undergo in-flight projectile fragmentation, a process in which some number of protons and neutrons are removed from the incoming beam nuclei through collisions with the target. Fragments produced through this method will retain nearly the same velocity as the incoming beam [8, 62]. Following projectile fragmentation, a large range of isotopes are produced. This secondary beam is passed back up to ground level to the Advanced Rare Isotope Separator (ARIS) in order to select the ions of interest and discard the unwanted species. A diagram of ARIS is shown in Figure 3.2. Note the locations of DB1, DB2, DB3, DB4, and DB5. "DB" stands for "diagnostic box," and these are boxes containing elements such as detectors, slits, and wedges. Detectors allow for continuous monitoring of the transmission and purity of the beam, whereas slits and wedges (which will be discussed in detail later in this section) allow users to select which species of ions are transmitted through the separator and which are discarded.

It is noted here that two settings of ARIS were explored in the present experiment. One setting was optimized for the transmission of ^{37}Na, and the other setting was optimized for the transmission of ^{45}P. In both settings, the beam delivered to the experimental station was a cocktail beam composed of a variety of different ion species in the same mass region as the central species

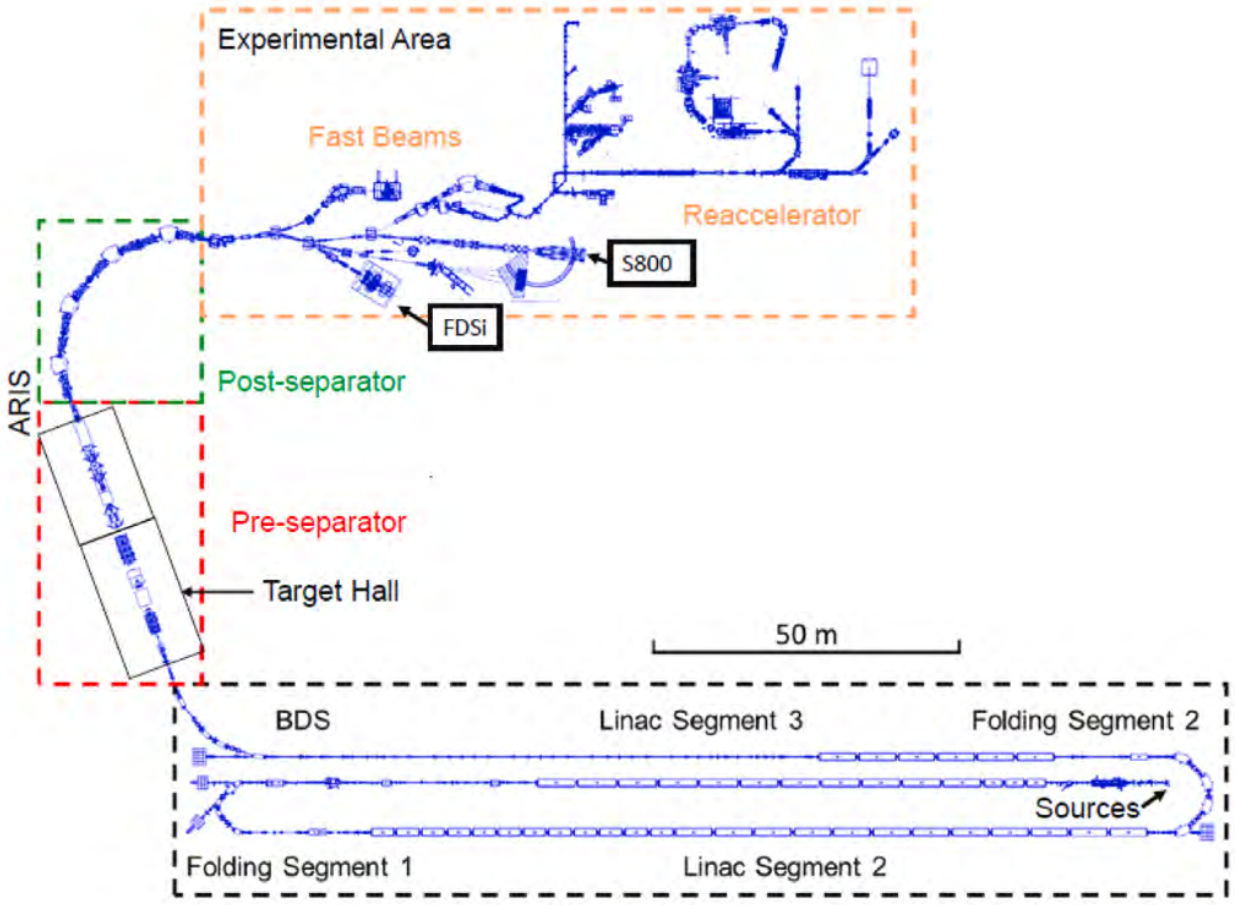

Figure 3.1 Diagram of the FRIB beamline, starting with the ion source, through the linear accelerator and fragment separation stages, and ending in the experimental areas. Note that, in the present experiment, the FDSi was not located at the labeled position in the Figure; it was located in the Transfer Hall, directly at the end of ARIS. Reprinted from Nuclear Instruments and Methods in Physics Research Section B: Beam Interactions with Materials and Atoms **540**, M. Portillo et al., "Commissioning of the Advanced Rare Isotope Separator ARIS at FRIB," 151–157, Copyright 2023, with permission from Elsevier.

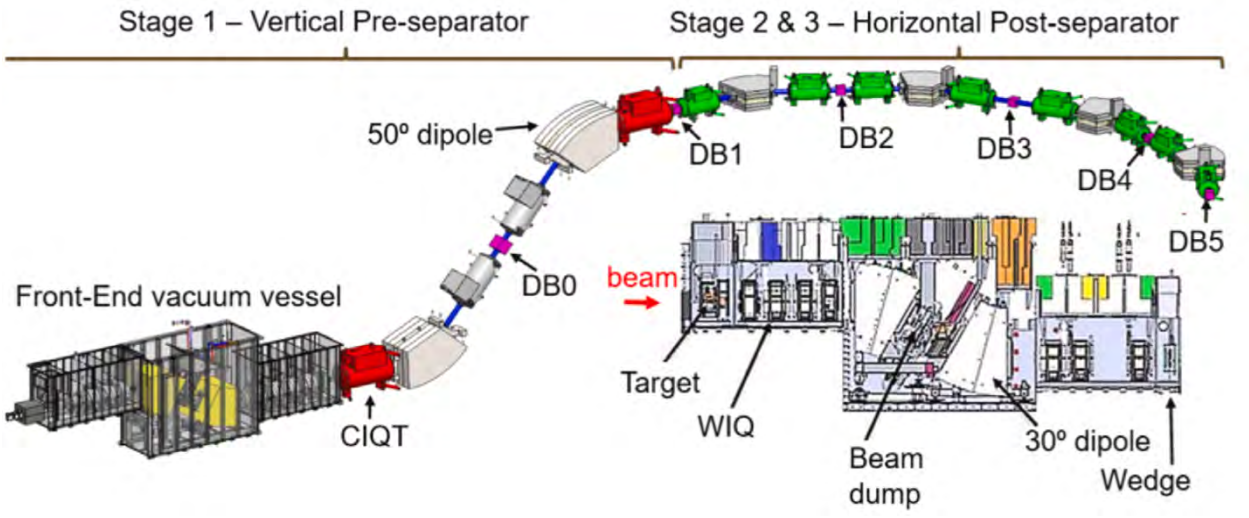

Figure 3.2 Diagram of the Advanced Rare Isotope Separator (ARIS) at FRIB. The inset shows a detailed diagram of the contents of the Front-End vacuum vessel. Reprinted from Nuclear Instruments and Methods in Physics Research Section B: Beam Interactions with Materials and Atoms **540**, M. Portillo et al., "Commissioning of the Advanced Rare Isotope Separator ARIS at FRIB," 151–157, Copyright 2023, with permission from Elsevier.

(^{37}Na or ^{45}P). Unless explicitly specified, all following details in this work pertain to the ^{37}Na setting.

There are multiple features within ARIS which can be tuned in order to optimize transmission and purity of ions of interest. These features include magnets in addition to slits and wedges. Magnets are used in several ways. Dipole magnets steer the isotopes of interest along the beam line, ensuring transmission of particles along a curved path. These magnets are tuned to the expected value of magnetic rigidity, $B\rho$, for the ion of interest. $B\rho$ is proportional to the momentum over charge of the ion, mv/q. Assuming a small velocity spread of the beam, this is nearly equivalent to the mass over charge, A/Z. In this way, ions with a selected A/Z can be chosen, as only those with the correct magnetic rigidity will be transmitted along the path of interest, and the rest will be lost. In addition to dipole magnets, quadrupole magnets are used to focus the beam into a smaller area to avoid losses due to spreading of the beam spot.

Wedges are special types of energy degraders which can be used to further select ions based on their charge. As described by the Bethe-Bloch equation, the energy loss as an ion travels through material is proportional to its charge squared, $-dE/dx \propto Z^2$ [8]. As a beam composed of many

ion species traverses through a degrader, more highly charged ions will lose more energy and, thus, velocity, effectively spreading out the ideal $B\rho$ values for the different species in the beam. A dipole magnet placed directly after a degrader can then be used to steer only the ions of interest along the beam path, eliminating contaminant ions. The geometry of the wedge-shaped degrader is unique in that some ions will pass through less material than others; this feature can be exploited to increase the displacement of contaminant ions from the ideal beam trajectory. There are two Aluminum wedges used in the present experiment: a 1.15 mm wedge positioned slightly downstream of the target and a 1 mm wedge positioned at DB2.

Slits were also employed in the present experiment in order to narrow the momentum spread of the beam. As slits work by introducing a physical cut on the ion's position in the x or y direction, it is important to note that the use of a slit requires a "dispersive" beam condition at the location of the slit. Here, "dispersive" means that the x and/or y position of the ion has some momentum dependence. In this way, the position cut can then correspond to a momentum cut. This helps to reduce the rate of transmission of contaminant ions. Slits were placed at DB1, DB2, DB4, and DB5. The widths of the slits, on the order of tens of millimeters, were varied throughout the experiment to optimize transmission of fragments of interest while minimizing contamination, based on evolving experimental goals. The slit widths employed corresponded to momentum acceptances between roughly 1% and 3%.

3.2 Particle identification

A cocktail beam was delivered to the experimental station. Due to the large number of species within the beam, the ability to distinguish between the different species is of utmost importance. This was achieved via the ΔE-ToF method. Given a small momentum spread, heavier species in the beam will have smaller velocities. Thus, over a fixed distance, heavier species will take longer to traverse the distance. Placing a fixed "start" and "stop" detector, time of flight can be calculated on an event-by-event basis. Similarly, assuming a fully-stripped beam, as charged ions travel through any material, they will lose energy according to the Bethe-Bloch equation, which gives a relationship $-dE/dx \propto Z^2$ [8]. From this, it can be determined that more highly charged

ions (i.e., nuclei with higher Z values) will deposit more energy in a given detector.

In this way, each species in the beam can be unambiguously identified in terms of its mass and charge. The time of flight "start" detector is the DB3 downstream PPAC anode, near the middle of the horizontal post-separator stage of ARIS (see Figure 3.2). The time of flight "stop" detector is a plastic scintillator in the diagnostic cross just upstream of the implantation point. The ΔE is measured through a 500 micron Si PIN diode in the same diagnostic cross.

An important note is that particles are separated by their mass and charge when using the ΔE-ToF method; however, explicit calculation of mass and charge are unnecessary. In this case, the assignment of ions can be performed by inspection of the particle identification plot given in Figure 3.3. This figure is derived by plotting ΔE versus time of flight on an event-by-event basis in a two-dimensional histogram. Note that a lower limit on the recorded energy loss was placed in order to remove the more intense Nitrogen ions, which are not of interest in the present study. In this figure, it is clear that each ion is well-separated into its own "blob"; this is to say that the boundaries of the areas which each species fills can easily be determined by inspection, and the areas filled by neighboring species are distinct. In a figure such as this, approximately horizontal lines of constant Z are expected. The lightest member of an isotopic chain appears furthest left, with mass increasing to the right. It is noted that A/Q should stay constant along a constant value of time of flight. In this region, with A/Q around three, in order to satisfy this condition, when moving directly upward by one blob, the A value should increase by three.

The region of isotopes present in the beam was known at the time of the experiment to include neutron-rich species of F, Ne, Na, and Mg, among other surrounding isotopic chains, nearing the neutron dripline. In the fluorine isotopic chain, it is known that ^{27}F is bound, ^{28}F is unbound, and ^{29}F is bound. This pattern is clearly observed in the second isotopic chain from the bottom of the plot, where the missing fourth blob from the left clearly indicates that this member of the isotopic chain is unbound and did not survive to the implantation point. From here, the ^{27}F blob can be identified as the third blob from the left in the second isotopic chain from the bottom, directly to the left of the missing blob. Moving down one row, one would expect to find the oxygen isotopic

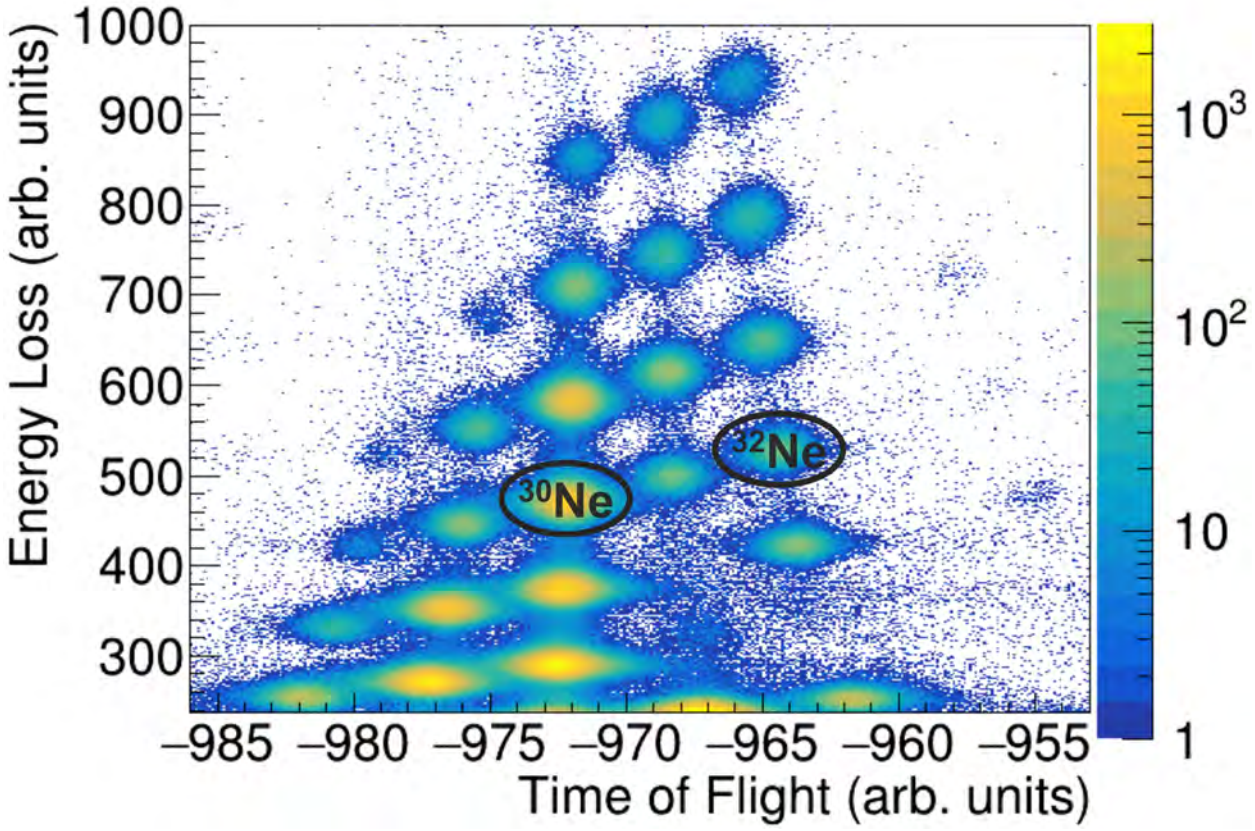

Figure 3.3 Particle identification plot of ions delivered to the first focal plane of the FDSi in the ^{37}Na setting. The locations of the ions of interest, ^{30,32}Ne, are labeled in the figure.

chain. Subtracting three from A, ^{24}O is expected to be directly below ^{27}F. This makes sense; ^{24}O is the last bound isotope of oxygen, and it is seen that this chain of blobs has a sharp cutoff after the suspected ^{24}O blob. With ^{27}F and ^{24}O reasonably identified, all other blobs could be tentatively assigned based on the rules given previously. This tentative assignment of isotopes was confirmed by gating on several isotopes with well-known decay schemes and confirming the presence of the correct β-delayed γ-ray transitions.

The ^{30,32}Ne isotopes of interest are assigned as labeled in the figure. There are 340,958 identified ^{30}Ne ions, and there are 34,547 ^{32}Ne ions. Of course, systematic error in the drawing of the gates cannot be eliminated; however, any imprecision in the drawing of gating regions will only impact the level of statistics of the desired isotope in the gate as well as the level of contaminant statistics in the gate. In the present analysis, when drawing PID gates, the preservation of statistics was

balanced with the elimination of contaminants. Any imprecision in the drawing of the gates will not impact any scientific conclusions made in the current work, as all plots will be made with equivalent PID gates. For the most part, the number of ions of each species is included in this work mainly to give the reader an idea of the level of statistics for each isotope; these numbers will not be used in a significant way in the analysis of these decays.

3.3 The FRIB Decay Station initiator

After fragment separation, the beam was delivered to the first focal plane of the FRIB Decay Station initiator (FDSi). The FDSi is the first stage of development of the eventual FDS. The FDSi is a modular system of devices which can be constructed to measure a number of types of decay radiation, including neutrons, electrons, and γ rays. There are two focal planes which make up the FDSi. The first, upstream focal plane is the discrete, high-resolution array. The primary detector arrays used at this focal plane are the Decay Germanium Array initiator (DEGAi) and the Neutron (Xn) Tracking Array initiator (NEXTi). A variety of implantation detectors can be used with this focal plane. The second focal plane is the high-efficiency total absorption spectrometer, the Modular Total Absorption Spectrometer (MTAS). It is emphasized that multiple detectors can be swapped in and out at each focal plane in order to optimize the desired measurement, making the FDSi a very adaptable system of devices [67, 68]. A computer rendering of the FDSi is shown in Figure 3.4, in the configuration with DEGAi on one hemisphere, NEXTi on the other hemisphere, and MTAS at the second focal plane. The optional second hemisphere of DEGAi is also shown.

At the time of the experiment, the FDSi was located in the Transfer Hall of FRIB, just at the end of the ARIS fragment separator. There were several detectors present. The primary implantation point was a Yttrium Orthosilicate (Y_2SiO_5, YSO) implantation detector, which will be discussed in Section 3.3.1. γ rays can be recorded in the fast-timing $LaBr_3$ array or the DEGAi Clover detector array. Finally, two sets of neutron detectors are present: the NEXTi array as well as the OGS detectors located near the implantation point in order to improve the angular coverage of neutron detection. This configuration is pictured in Figure 3.5, with the exception of NEXTi, which is out of frame and not used for the present analysis.

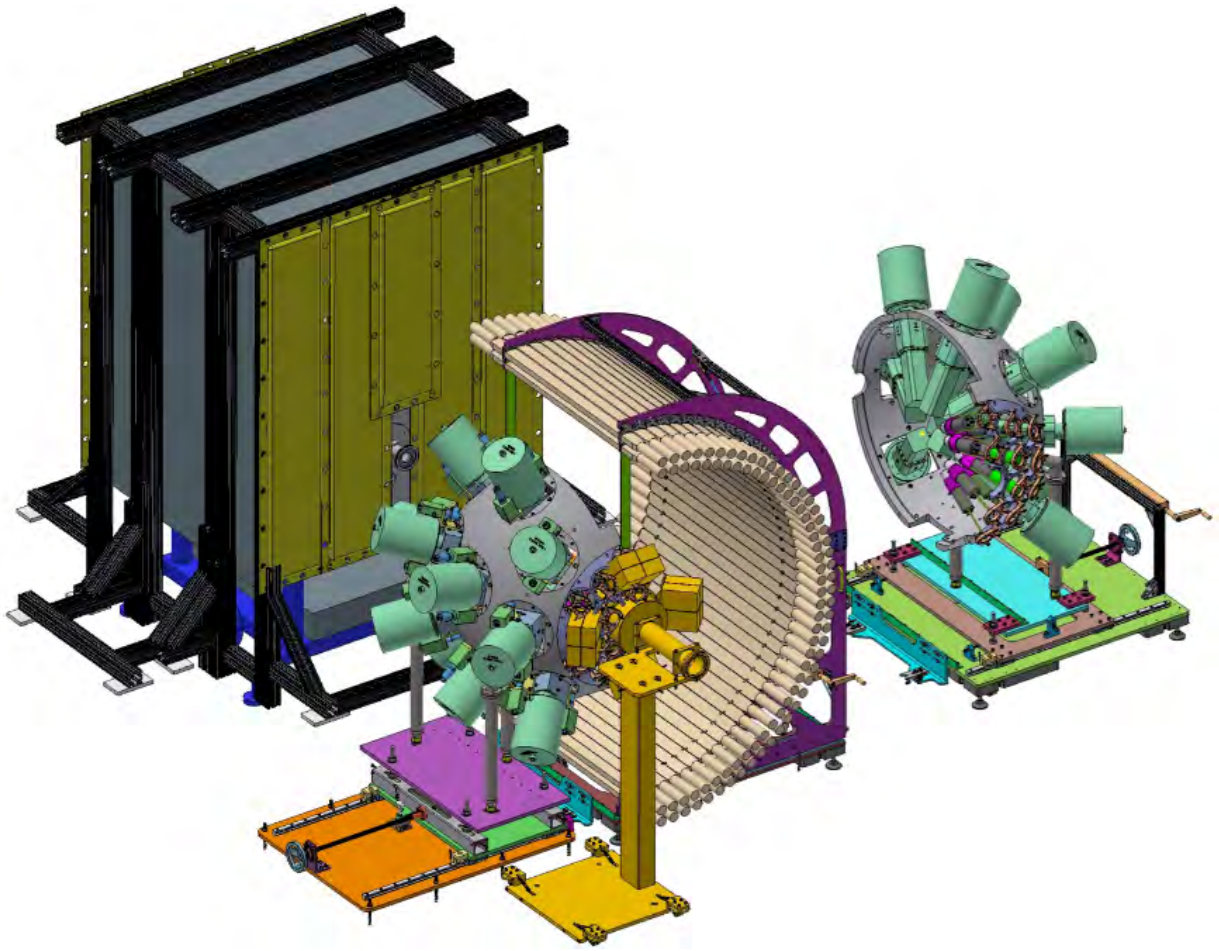

Figure 3.4 Computer rendering of the FRIB Decay Station initiator (FDSi). Pictured components are DEGAi (teal), NEXTi (beige), and MTAS (yellow and gray). Image credit: [68]

DEGAi is comprised of 11 Eurisys Two-Fold Segmented Clover detectors. Each Clover consists of four approximately cylindrical crystals of high-purity germanium [67]. Each crystal has diameter of 50 mm and a length of 80 mm. High-purity germanium is ideal for γ-ray detection, due to its superior energy resolution. Typical energy resolution for a coaxial germanium detector is approximately 1.7–2.3 keV FWHM at 1333 keV [69]. Some γ-ray detection efficiency is lost when using this type of detector, compared to, say, a scintillator. The DEGAi γ-ray energy and efficiency calibrations will be discussed in Sections 3.5 and 3.6.

A rotating Aluminum degrader was placed in the diagnostic cross upstream of the implantation point to ensure that the correct ions of interest came to a full stop near the center of the implantation detector. Rotation of the degrader allows variation of the effective thickness of the degrader, which

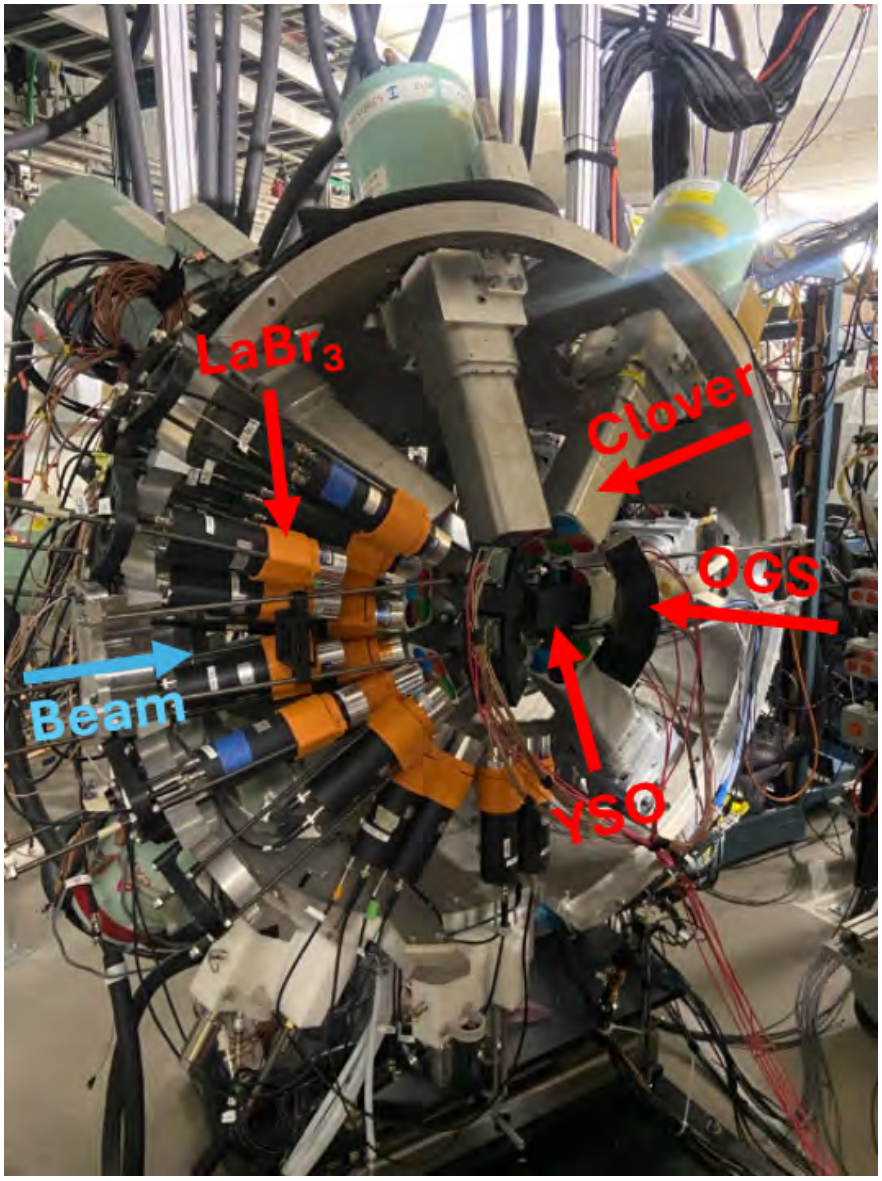

Figure 3.5 Picture of one hemisphere of the FDSi configuration used for the present study, located in the Transfer Hall of FRIB. Pictured components are DEGAi Clover detectors, the fast-timing $LaBr_3$ array, the YSO implantation detector, and the OGS neutron detectors. NEXTi was also present for this experiment as the second hemisphere, although its measurements are not discussed in the present work. The direction of incoming beam is also indicated in the figure. Image credit: Dustin Scriven.

allows fine-tuning of the implantation depth. The angle was varied a bit throughout the experiment, but, for the most part, the runs of interest have a 7 mm Aluminum degrader at 40 degrees. This amounts to an effective thickness of about 9.1 mm. Several detectors — a plastic scintillator coupled to a silicon photomultiplier tube (Si PMT), as well as two Si PINs — were also placed in this diagnostic cross.

Detector signals were digitized using 16 bit digitizers, with sampling rates of 250 MSPS. All interactions were recorded; no coincidence logic was required for events to be written. A constant fraction discriminator (CFD) was utilized in the processing of signals from the plastic scintillator in the diagnostic cross. CFDs were also used with the $LaBr_3$ array, but these detectors are not utilized in the present analysis.

3.3.1 The YSO implantation detector

In the center of the FDSi array is a YSO implantation detector. YSO (Yttrium orthosilicate, Y_2SiO_5) is an inorganic scintillator. Absorption of energy by an inorganic scintillator causes valence electrons to become excited; their subsequent de-excitation results in the emission of photons [69]. These photons can be measured with a photomultiplier tube (PMT). In this case, the YSO scintillator is segmented (24 x 24 2 mm pixels) to isolate signals in space, and it is coupled to a Hamamatsu 12700 position-sensitive PMT (PSPMT). The PSPMT has a high-gain and a low-gain output channel to optimize detection of both high-energy (implantation) signals and low-energy (β decay) signals. The YSO is 4.8 cm x 4.8 cm on its face, and it has a 1.2 cm thickness. Similar experiments may use thinner implantation detectors; the benefit of the relative thickness of the YSO used here is that a wide range of ion species with different dE/dx can be stopped in the same detector, increasing the number of isotopes which can be studied from a single experiment.

As suggested previously, the purpose of this detector is twofold. First, incoming beam comes to a full stop inside the YSO, leading to the implantation of radioactive ions within the detector. These implantations are recorded in the low-gain channel of the PSPMT. Some time later, these implanted ions β decay, and these decays, ideally, are recorded in the high-gain channel of the PSPMT. Due to the relatively high Q_β values in this region of the nuclear chart [14, 53], β-decay

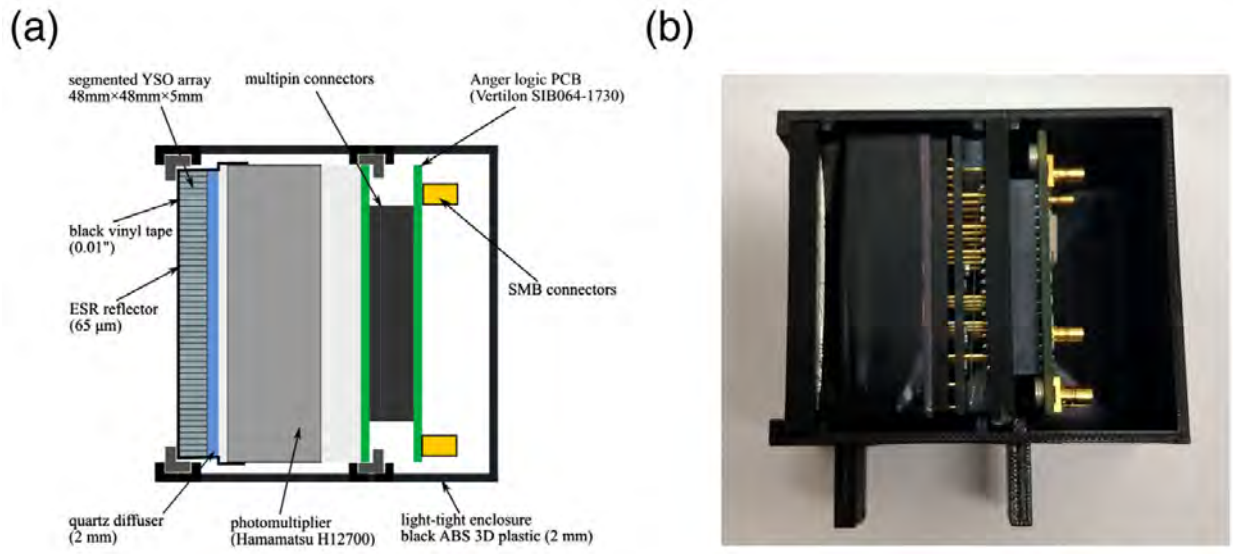

Figure 3.6 (a) Example schematic diagram of a YSO implantation detector and its required components, including a PSPMT and an Anger logic PCB among other parts. (b) Example photo of a YSO implantation detection setup. Note that this is not the exact configuration which was used in this study; namely, the YSO used in this study was 12 mm thick. These images are representative examples. Reprinted from Nuclear Instruments and Methods in Physics Research Section A: Accelerators, Spectrometers, Detectors and Associated Equipment **937**, R. Yokoyama et al., "Segmented YSO scintillation detectors as a new β-implant detection tool for decay spectroscopy in fragmentation facilities," 93–97, Copyright 2019, with permission from Elsevier.

electron energies may be quite high, and many of the observed β decays saturated the high-gain channel. In these cases, the low-gain channel was used to measure decay events.

Figure 3.6 shows both a diagram and a photo of a YSO implantation detection configuration used in a similar experiment. Note that this is a representative example, and is not exactly the same as the configuration used in the current experiment. Namely, a 1.2 cm YSO scintillator was used in the current experiment. Both the YSO and PSPMT are shown, alongside other components, such as the Anger logic PCB. Everything is enclosed within a light-tight plastic enclosure to isolate relevant signals. Additionally, front and rear veto detectors are placed within the plastic enclosure, before and after the YSO setup. These are also not depicted in Figure 3.6, and their application in the present analysis is minimal.

Position output is measured using Anger logic [70]. Rather than recording energy deposition in every pixel and determining the interaction position by, say, selecting the pixel with maximum

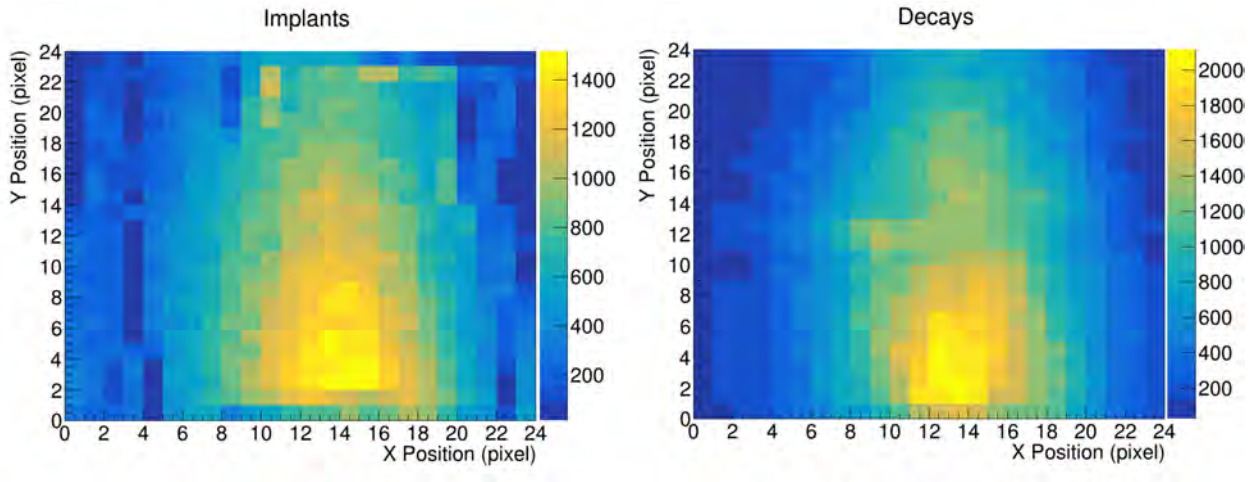

Figure 3.7 *x-y* position spectrum of (left) ^{30}Ne implants and (right) ^{30}Ne correlated β decays in the YSO detector. The correlation window used to make the plot on the right is 50 ms (temporal) and 2 pixels (spatial). See Section 3.4 for more details on the correlation procedure.

energy deposition, each pixel is read into the resistive network of the Anger logic PCB. Summed energies are recorded from each corner of the PCB. By taking averages of the four recorded energies, precise x-y coordinates can be determined for each interaction [71]. In this way, similar precision in position determination can be achieved, compared to if all pixel energies were recorded and written, but hardware requirements are reduced. Interaction positions are shown for ^{30}Ne implant and decay events in Figure 3.7. Unsurprisingly, these distributions look very similar, as would be expected both physically and as a result of the correlation procedure. More details on the correlation procedure can be found in Section 3.4.

It is significant to note that, as mentioned, the YSO is 1.2 cm thick. Radioactive ions are implanted roughly near the center of the YSO. This means that, when they undergo γ decay, the γ ray must travel through approximately 6 mm (half of the device's thickness) of YSO material before it can reach the DEGAi Clover detectors. If the implantation depth is off-center, it may travel through less material to escape in one direction and more material to escape in the opposite direction. Even if the implantation depth is exactly centered, path lengths longer than 6 mm are possible, depending upon the angle of emission of the γ ray. For this discussion, 6 mm is taken as the approximate path length for a γ ray to escape the YSO.

The fraction of photons transmitted through a material of density ρ and thickness t is given by

Equation 3.1, where C is the mass attenuation coefficient [69]. C depends on the material through which the photon is traveling and the energy of the photon, and it can be calculated using a tool such as the NIST XCOM database [72].

$$\frac{I}{I_0} = e^{-C\rho t} \tag{3.1}$$

The density of YSO is 4.4 g/cm^3 [71]. Based on the density and path length, the potential for attenuation of γ rays through this material is substantial, especially at low energies. γ-ray transmission through 6 mm of YSO as a function of γ-ray energy is shown in Figure 3.8. Indeed, it is seen that, below 75 keV, almost no γ rays would be able to escape the detector. There is a sharp increase in transmission between approximately 75 keV and 300 keV, after which the transmission begins to level off around 70%–90%. Two γ-ray energies of particular interest for the present analysis lie in the range of the sharp increase; these energies are 120 keV and 150 keV, and they are highlighted in red in Figure 3.8. It is seen that, for 120 keV and 150 keV γ rays, approximately 33% and 48% are expected to be transmitted through this thickness of YSO. This is a substantial amount of attenuation. This attenuation will be addressed in the present study so that measurements of these γ rays can be accurately understood; see Section 3.6 for more details.

3.4 Event correlation

One of the challenges to experimental studies of β decay is the (relatively) long half-lives. Even the shortest-lived β-decaying isotopes have half-lives on the order of milliseconds, which is much longer than typical experimental event windows. This is to say that the arrival of the unstable ion at the implantation detector will be categorized as a different event than the β decay of that ion. The challenge, therefore, is to connect an initial ion arrival event with its associated decay event that occurs in the future.

This can be further complicated by the existence of long-lived children and grandchildren which are populated after the initial parent decay of interest. These may create background in the detector, making it more difficult to identify the correct parent decays. In this study, a spatial and temporal correlation procedure is followed in order to identify which decays come from which ions with a

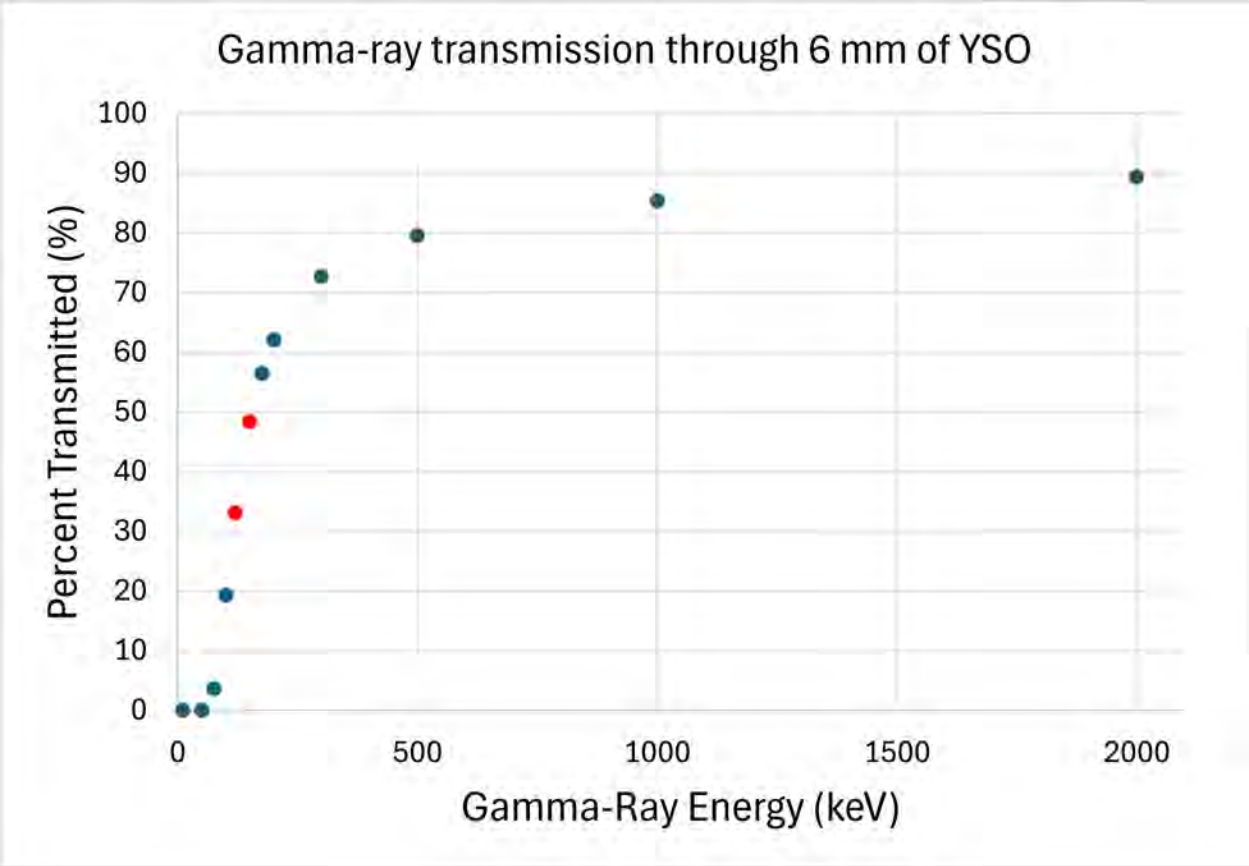

Figure 3.8 γ-ray transmission through 6 mm of YSO as a function of γ-ray energy. The 120 keV and 150 keV γ-ray energies which are relevant to the current analysis are highlighted in red. Attenuation coefficients were calculated using the NIST XCOM database [72].

relatively high degree of certainty.

Events are processed in a time-ordered fashion. As each event is processed, it is given a label. Implant events require both upstream PIN detectors to trigger above a certain threshold, and they also require the low-gain channel of the implantation detector to trigger. The rear veto is required not to trigger, in order to filter out events where an ion enters the detector, is not implanted, and exits the other side of the detector. Strictly speaking, the ToF detectors are not required to trigger, but, due to the application of PID gates in nearly every step of the analysis, implant events with missing ToF triggers will be implicitly excluded from most of the analysis. Decay events require only a trigger in either the high- or low-gain channel of the implantation detector. The upstream Si PIN detectors are required not to trigger, and the scintillator in the diagnostic cross, which is used

to veto light ion contaminants which may not trigger the Si PINs, is also required not to trigger. The final event type relevant to this analysis is called "Clover-only." As the label suggests, these are events where only a DEGAi Clover detector triggers, and there are no triggers in the upstream Si PIN detectors, cross scintillator, or implantation detector.

Every time the code encounters an implant event, the relevant event details — implantation position, implantation time, ion time of flight, and ion energy loss — are saved in a long-term storage vector. Then, when the code encounters a decay event, the parameters of that decay event are compared to all stored implant event parameters to determine if any implant events are correlated to that decay event.

In order for events to be correlated, there are two conditions which must be met. The first condition is that the decay must occur within a certain amount of time after the implant. This time window is called the "correlation window." The second condition is that the decay must be recorded within a specified distance of the implant; this distance may also be referred to as the "correlation window." For the rest of this work, the terms "temporal correlation window" and "spatial correlation window" may be used to avoid ambiguity. A conceptual depiction of the spatial correlation window is given in Figure 3.9. Note that, in this work, the spatial correlation window is defined as a circle with a chosen radius. The exact pixel in which the implant or decay occurs is not explicitly recorded, as the position is calculated by the Anger logic algorithm described in Section 3.3.1. Nevertheless, the convention of this work is to measure the correlation radius in units of pixel length; one pixel length corresponds to 2 mm.

The temporal correlation window can be set by the user. It is best determined based on the half-life of the desired parent decay. The child half-life (or half-lives, when β_{xn} decay is possible and there are multiple children) may also be considered, depending on whether the user wishes to suppress or collect child activity. A correlation window on the order of three to ten times the parent half-life is typically suitable. Analysis of the integrals of the Bateman equations (Equations 2.5, 2.6, and 2.7) can help determine the ideal window for maximum collection of parent (and potentially child) activity, along with minimum collection of background.

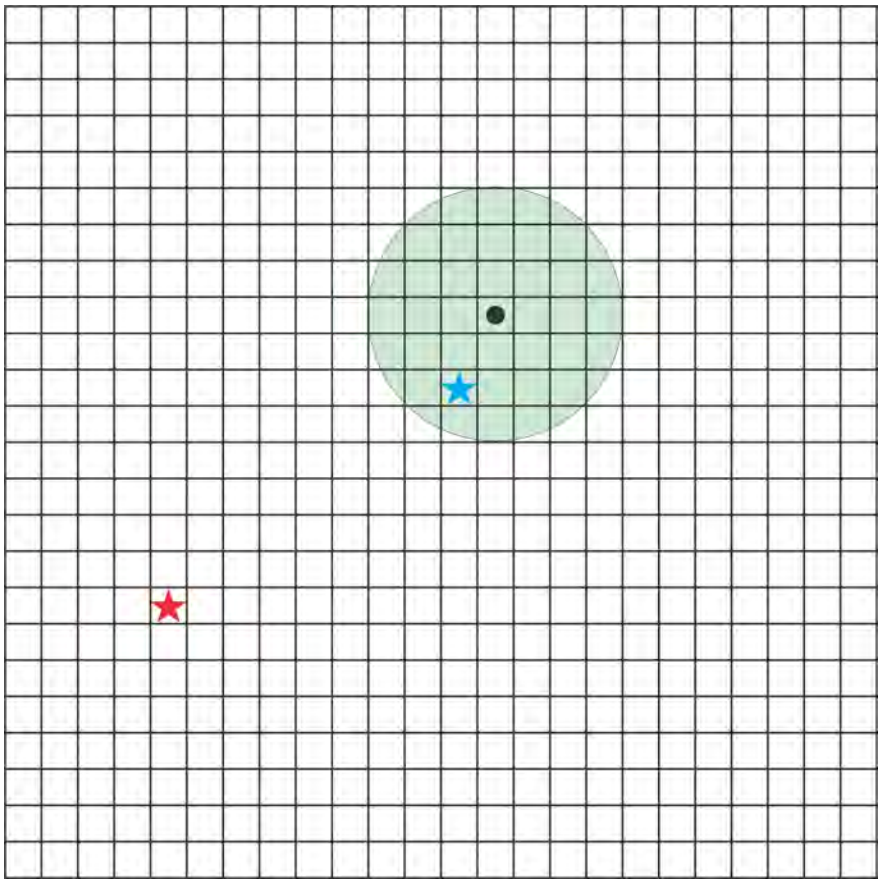

Figure 3.9 Cartoon depiction of the implantation detector, with a grid representing all 576 pixels of the PSPMT couple to the segmented YSO crystal. A sample decay position (small black circle) and its corresponding 3-pixel-radius correlation window (large light green circle) is shown. An implant correlated in space is shown as a blue star inside the light green circle, and an implant not correlated in space is shown as a dark red star outside of the light green circle.

The spatial correlation window can also be set by the user, although the optimized value is less clear-cut. For the purposes of this study, the ideal correlation window was determined by examining the timing properties of correlated decays as a function of the spatial correlation window. Conceptually, properly correlated decays will exhibit an exponential timing distribution, and they should occur close to the ion implantation site. As the distance from the decay increases, it becomes less likely to find properly correlated implants, thus making it more likely that any identified correlations are random. This is reflected in the timing distribution; increasing the spatial correlation window past the optimized threshold will mainly increase the constant background component, rather than the exponential component generated by proper correlations.

Figure 3.10 depicts the relationship between decay time and position as described above; the resulting decay curves are derived by making several different cuts on the decay distance. This is tested for the ^{32}Ne ion gate. It is clear that, for correlated decays observed close to the implant (within, say, 0–3 pixels), the decay curve takes on the characteristic exponential shape that would be expected for non-random correlations. However, as the distance is increased, the proportion of flat background starts to increase. Once the 4–5 pixel range is reached, there is no trace of exponential behavior visible.

This is taken as evidence that, for ^{32}Ne, most decays occurs within 2 or 3 pixels (4–6 mm) of the initial implantation. For the purpose of this study, the correlation window is set to 2 pixels unless otherwise noted. While 3 pixels also may have been an appropriate choice, the bulk of decays occur within 2 pixels, and not as many proper correlations are gained by increasing the correlation window to 3 pixels. By limiting the correlation window more strictly, a cleaner spectrum is prioritized, as the excess random counts from the 2–3 pixel gate onward are excluded. For the sake of completeness, data were analyzed with both 2 and 3 pixel correlation windows, and the limitation of the correlation window to 2 pixels was indeed found to provide cleaner spectra without sacrificing a large enough amount of properly correlated decays to significantly change experimental results.

A similar correlation procedure can be used to correlate delayed γ rays to ion implantations. This can be useful when long lived ($t_{1/2} \approx 10$ μs or greater) γ-decaying isomeric states are populated in the parent isotope which is delivered to the implantation detector. In this case, what may be observed is 1) an implant event, followed by 2) a Clover-only event, followed by 3) a decay event. The ion–β correlation described above will properly correlate the decay and the implant, but, unless further action is taken, the isomeric decay will be lost.

For this exercise of ion–γ correlation, another temporal correlation window — the ion–γ correlation window — must be chosen according to the expected half-life of the isomeric state. A spatial correlation window cannot be used, since the γ and ion are recorded in different detectors. Thus, any ion implanted anywhere in the detector can be correlated to any γ ray recorded in any of the Clover detectors. When a Clover-only event is identified, it is then compared to the long-term

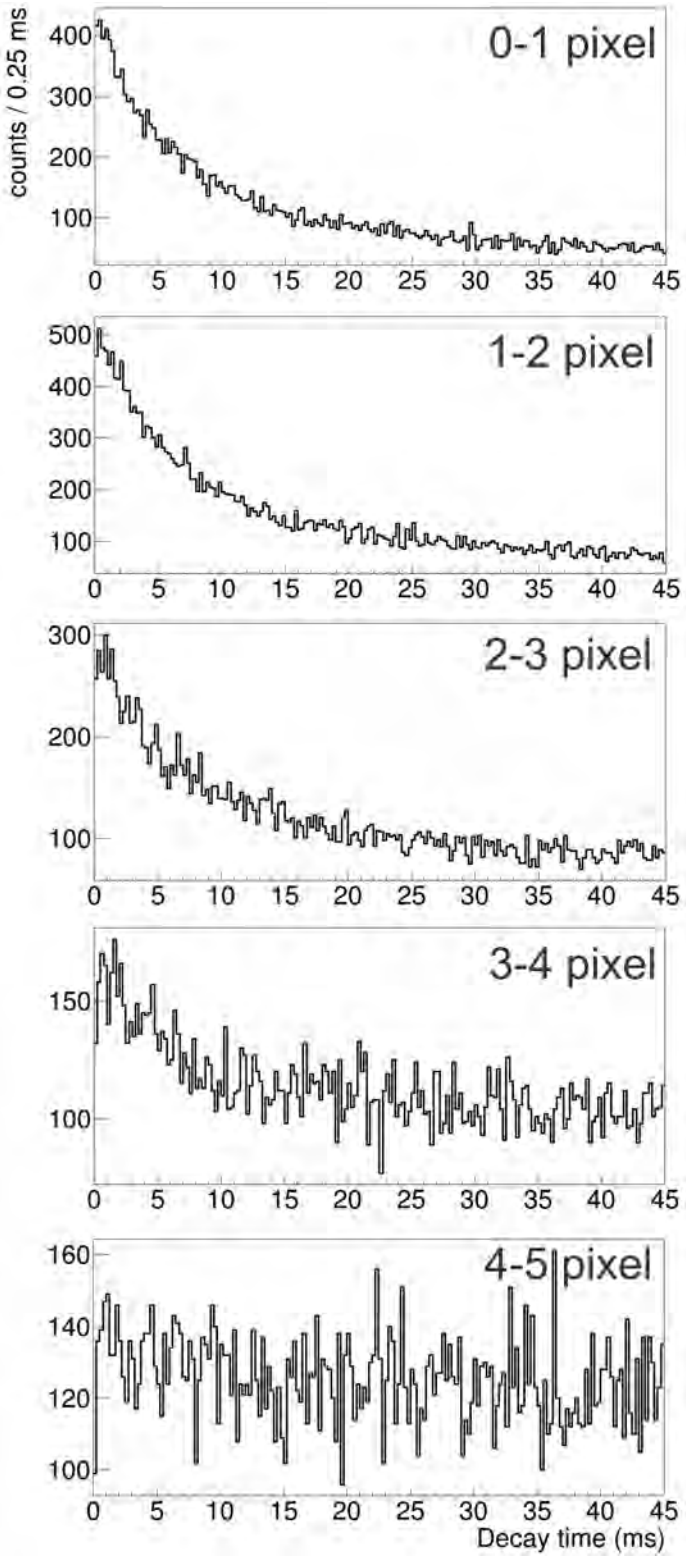

Figure 3.10 Decay curves for identified ^{32}Ne decays. Each panel shows a different cut on the distance between the implant and the decay. From top: 0-1 pixels, 1-2 pixels, 2-3 pixels, 3-4 pixels, 4-5 pixels.

ion storage vector and correlated to any ions which preceded it within the ion–γ correlation window.

The final scenario which may be encountered in this analysis occurs when an isomeric state is populated in the child nucleus following β decay of the parent. In this case, what may be observed is 1) an implant event, followed by 2) a decay event, potentially accompanied by one or more prompt γ rays, followed by 3) a Clover-only event. Practically speaking, the same correlation procedure described for ion–γ correlations may be followed; however, because the isomeric decay is β-delayed, a significantly longer ion–γ correlation window (order of 10 ms) would be necessary, and random background from the Clover detectors could easily dominate. To reduce this random background and further isolate events of interest, an ion–β–γ correlation procedure is defined.

Much like for the ion–β correlation procedure, a long-term storage vector is created to save the parameters of decay events which themselves have already been correlated to at least one ion. In this secondary long-term storage vector, the parameters of the correlated ions are also retained so that all three events — ion, β decay, and γ decay — can be related to each other with an appropriate level of detail. Then, as Clover-only events are encountered, they are compared to the β decay event storage vector. If the time difference between the β and the γ is less than some defined β–γ correlation window, this ion–β–γ correlation is saved for analysis. For an even cleaner correlation, if the level scheme suggests it, a gate can be placed around a γ-ray peak that promptly follows the β decay and precedes the isomeric γ decay.

Of course, even with these correlation procedures defined above, random correlations are inevitable, so it is important to quantify the impact of random correlations on the plots which are produced. There is a very simple way to quantify the impact of random correlations on the ion–β correlation procedure: by performing a reverse correlation. The reverse correlation procedure is illustrated in the diagram in Figure 3.11. In the ion–β correlation procedure described above (which will be referred to as "forward correlation"), for a given decay event, the code searches the events in a time-ordered fashion, from earliest to latest event in real time. Under the reverse correlation procedure, the code searches the events in reverse, from latest event to earliest event.

Practically, for forward correlations, when a decay is identified, the correlation search looks

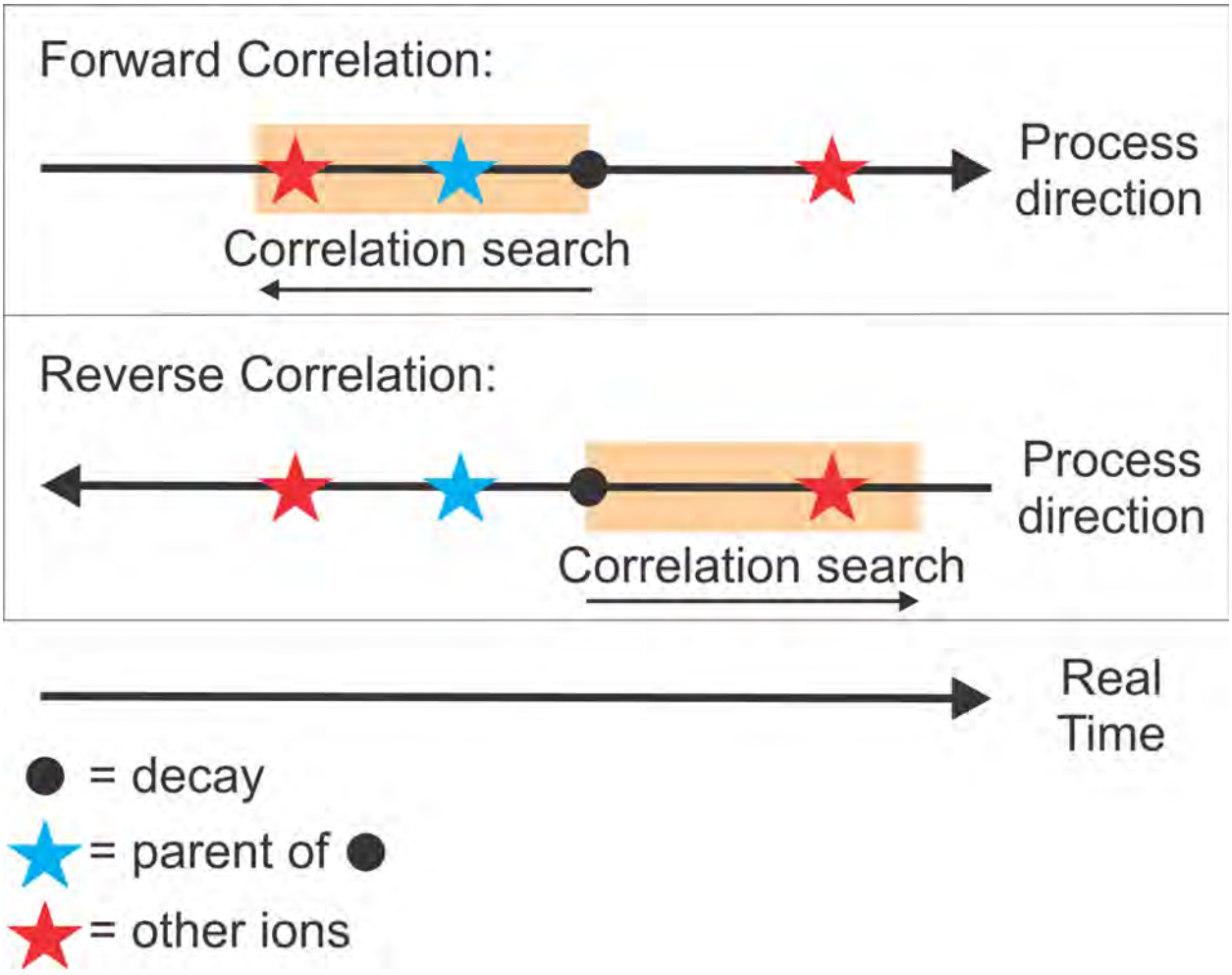

Figure 3.11 Timelines for (top) forward and (bottom) reverse correlations. Decay time is indicated by a black circle. The true parent implant is indicated by a blue star, and other nearby implants are indicated by red stars. The correlation window is indicated relative to the decay time as a light orange box. The thick arrows indicates the direction in which the code processes events; the thin arrows indicates the direction in which the code searches for correlated ions. The real time ordering of events progresses from left to right. See text for details.

backwards in time for correlated ions, while processing time-ordered events in the direction of increasing time. All correlated ions necessarily will have been implanted before the decay. For reverse correlations, the correlation search looks forward in time for correlated ions, while processing time-ordered events in the direction of decreasing time. All correlated ions necessarily will have been implanted after the decay. Of course, these correlations are non-physical; an ion must be implanted in the detector before the detector can detect its decay. Therefore, any correlations identified in the reverse correlation setting must necessarily be random. In this way, one can independently construct a spectrum that consists entirely of random correlations. For example, this can be used to identify the random component of a decay curve or of a β-delayed γ-ray spectrum. These reverse spectra can be subtracted from the forward spectra to remove random contributions from the experimental results.

It is important to note that, for β-delayed γ-ray spectra, this technique can be effectively used to remove background from random ion–β correlations. However, this is not the only type of background that exists. For example, this reverse correlation technique will not remove Compton scattering background.

3.5 γ-ray energy calibration

Each detector crystal in DEGAi is expected to have a unique calibration, so, when calibrating the data, each crystal must be treated separately. Figure 3.12 makes this evident. This two-dimensional histogram shows all recorded DEGAi counts during a single run as a function of γ-ray energy and the DEGAi crystal in which the count was recorded. The plot is zoomed in around the region in which the 1435 keV (produced following ^{138}La β decay, from intrinsic activity within the $LaBr_3$ array) and 1460 keV (produced following ^{40}K β decay) background peaks appear. For a well-calibrated detector array, two vertical stripes would appear, indicating that the 1435 keV and 1460 keV γ rays appear at the correct energy in each crystal. Not only does the uncalibrated spectrum show these peaks at arbitrary energies, these peaks are not at the same arbitrary energy in all crystals.

The simplest way to calibrate the array would be to use a standard radiation source, such as

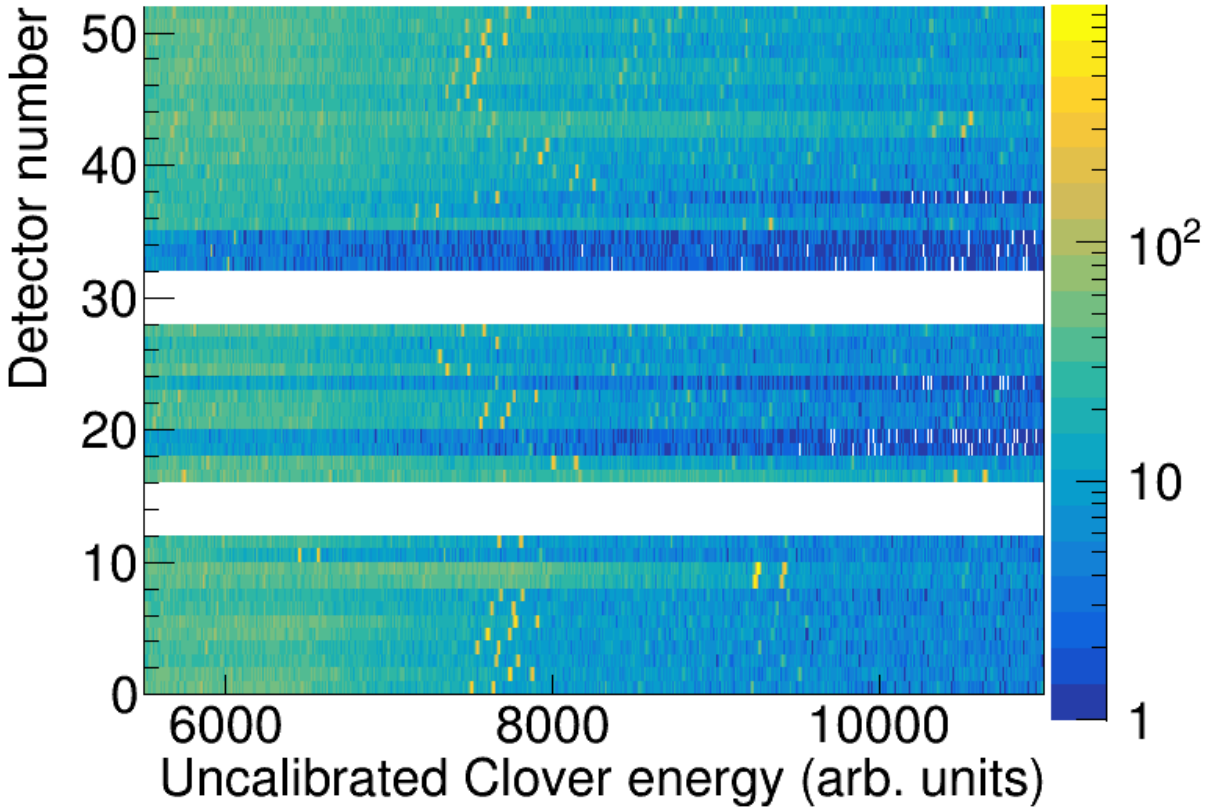

Figure 3.12 Raw energy recorded in DEGAi versus crystal number. This figure shows approximately one hour of data (run 1420), collected during the ^{37}Na setting and recording all interactions in DEGAi. Note that two Clovers were not present at the time of the experiment, as is made evident by the 2 white bands in this plot. The energy axis is focused around the region where the 1435 keV and 1460 keV background peaks appear in most crystals.

^{152}Eu. One source run would be recorded, and this run would be used to calibrate each crystal for the entire dataset. However, minor time-dependent calibrations shifts were observed throughout the experiment. This is evident in Figure 3.13, which shows γ-ray counts as a function of γ-ray energy and run number. Typical runs are approximately one hour in length, although there is some variation in the run length. In this figure, it is again expected that these two background γ rays create two vertical lines, indicating that the γ ray is recorded at the same energy in every run. However, there are notable deviations from the expected behavior. In this case, a single calibration for each crystal calculated at one point in time is not sufficient to accurately calibrate the array. While most of the time dependency observed was minor, the crystals were calibrated on a run-by-run basis in

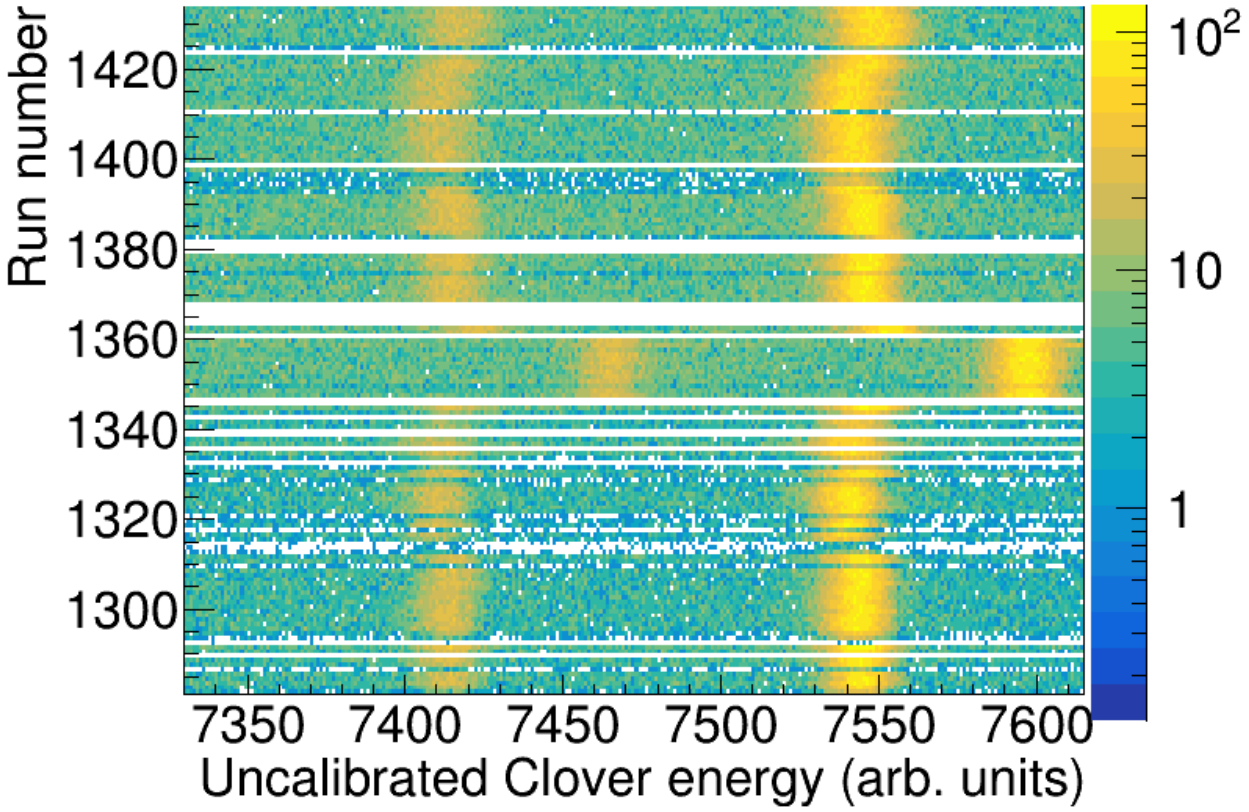

Figure 3.13 Raw energy recorded in crystal 47 of DEGAi versus run number. Runs collected during both the ^{37}Na and ^{45}P settings are shown, and gaps resulting from the any labeled "junk" runs are removed. All interactions in DEGAi are recorded with no gates applied. The energy axis is focused around the region where the 1435 keV and 1460 keV background peaks appear.

order to preserve resolution and ensure that all counts of a given γ-ray transition were captured within a single Gaussian peak shape.

In order to calibrate run-by-run, strong, evenly-spaced background lines throughout the entire dataset are required. Four background lines are chosen: 238.632(2) keV [73], from ^{212}Bi produced in the ^{232}Th decay series; 510.99895069(16) keV [74], produced following interactions of electrons and positrons; 1460.820(5) keV [75–77], produced following ^{40}K β decays; and 2614.511(10) keV [77], from ^{208}Pb produced in the ^{232}Th decay series.

The calibration process is automated and proceeds as follows. First, the TSpectrum class of the ROOT data analysis framework (see Ref. [78]) is used to identify peak-like structures in the

raw γ-ray energy spectrum. The identified peaks are fit to identify their centroids in arbitrary units. The peak with the highest centroid is set to an energy of 2614.5 keV. This method is largely effective, as the highest identified peak centroid does indeed usually correspond to the 2614.5 keV peak. In cases where this method fails and the wrong peak is identified, it is readily apparent in the calibration results, and that calibration is re-processed by hand.

The location of the 2614.5 keV peak is used to generate a rough, linear calibration, where the intercept is set to 0 and the slope is set to 2614.5 / [Peak centroid]. As the calibration is dominated by linear behavior, this rough calibration allows the centroid of the 511.0 keV peak to be easily identified. Combining the centroid of the 511.0 keV peak with the determined rough linear component of the calibration, a rough constant component is determined. With the constant and linear components of the calibration roughly determined, the remaining two calibration peaks can be easily identified. A quadratic fit of the four calibration points is performed to identify the exact, final calibration. Again, the linear term dominates, and the constant and quadratic terms contribute small corrections to the calibration. It is important to note that the inclusion of the quadratic term is necessary; when comparing the results of a linear calibration to those of a quadratic calibration, there were minor systematic downward shifts in peak energies for the linear calibration, which were improved with the addition of the quadratic term.

During calibration, it was noted that several crystals showed indication of disproportionate loss of efficiency at high energy. Specifically, the 2614 keV calibration peak became much smaller, so much so that TSpectrum could no longer identify the peak, no matter how the program was tuned. Hence, these crystals failed to calibrate for each run. These crystals were ultimately removed from the analysis so as not to introduce inconsistencies in detection efficiency, which could impact intensity measurements. These were crystals 18, 19, and 23. These three crystals were all from the "90 degree" set of crystals (the set of crystals whose normals are perpendicular to the beam direction). In addition, crystals 25 and 26 were also removed from the analysis. These crystals showed intermittent, extreme loss of resolution. This issue affected approximately 20% of runs; however, for the sake of consistency, they were removed from the entire analysis. These crystals

were also from the 90 degree set of crystals. Finally, Clovers 4 and 8 (crystals 12, 13, 14, 15, 28, 29, 30, and 31) were not present during the experiment. 39 total crystals were used for the final analysis.

The top plot in Figure 3.14 shows the ungated γ-ray energy spectrum for all crystals and runs after calibration. The calibration peaks are noted with red asterisks. The bottom plot of Figure 3.14 shows the calibration residuals for a set of known γ-ray transitions which appear in the spectrum, given as [Known γ-ray energy, from literature] − [Present γ-ray energy, after calibration]. The present values are determined by fitting the selected peaks in the top spectrum of Figure 3.14 to a Gaussian plus linear background peak shape and adopting the Gaussian centroid as the peak energy. Note that the error bars on the bottom plot of Figure 3.14 are given as the quadrature-summed errors of the known γ-ray energy and the presently-measured γ-ray energy. The error on the presently-measured γ-ray energy largely dominates, and it is taken as the σ value from the Gaussian fit. Despite the persistence of minor systematic shifts in the calibration (i.e., peaks below approximately 200 keV appear slightly lower in energy and peaks above approximately 200 keV appear slightly higher in energy), it is clear that the fit residuals are consistent with zero, well within the determined error bars. Thus, for all future peak fits in the present study, the Gaussian σ value is given as the error in the γ-ray peak energy centroid. The calibration results are summarized in Table 3.1.

3.6 γ-ray detection efficiency

The absolute γ-ray detection efficiency can be defined as in Equation 3.2. There is an intrinsic component relating to how radiation interacts with the properties of the material itself, and there is a geometrical component relating to the amount of solid angle subtended by the detector or detector array. Ultimately, combining these two components into an absolute efficiency defines the most readily useful efficiency quantity, which can be directly used in experimental computations.

$$\epsilon_{\text{abs}} = \epsilon_{\text{int}} * \epsilon_{\text{geom}} = \frac{\text{number of events recorded}}{\text{number of photons emitted by source}} \tag{3.2}$$

In practice, "relative" efficiencies are also useful quantities to work with. Relative efficiencies

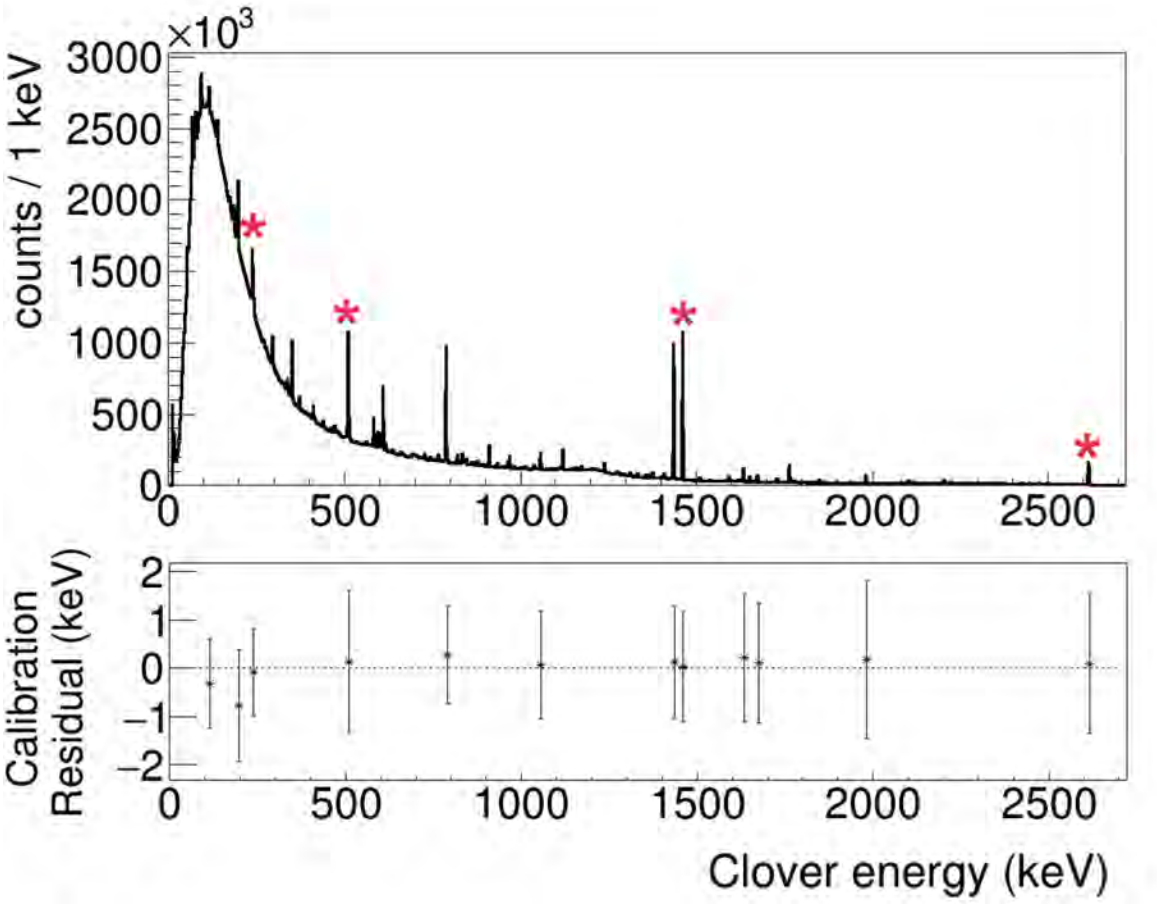

Figure 3.14 Top: γ-ray spectrum for all DEGAi events after energy calibration. The peaks marked with red asterisks were used as the calibration points. Bottom: Calibration residuals, calculated as [Adopted value] − [Present value], for several known γ rays in the spectrum.

can be calculated using measurements recorded with a standard radioactive source such as ^{152}Eu. A set of γ rays produced following β decay is selected; it is important that the absolute γ ray intensities are known as a percentage of the number of parent decays. The relative efficiency for this set of γ rays can then be calculated as in Equation 3.3. Optionally, an additional scaling parameter can be introduced such that a given γ ray has a relative efficiency of 100%, although this is not strictly necessary. Relative efficiencies are limited in how they can be used, as they cannot be used to calculate absolute quantities. In the present work, relative efficiencies for a set of ^{152}Eu reference peaks are calculated, and they are scaled with an appropriate external normalization to produce an absolute efficiency curve. Relative efficiencies may also be sufficient in situations where the desired quantity is the ratio of the efficiencies at two different γ ray energies.

Adopted energy (keV)	Present energy (keV)	Calibration residual (keV)
114.7(1) [79] (see [80–82])	115.0(9)	-0.3(9)
197.143(4) [83]	197.9(12)	-0.8(12)
238.632(2) [73]	238.7(9)	-0.1(9)
510.99895069(16) [74]	510.9(15)	0.1(15)
788.744(8) [84]	788.5(10)	0.3(10)
1056.78(3) [85]	1056.7(11)	0.1(11)
1435.816(10) [84]	1435.7(12)	0.1(12)
1460.820(5) [75–77]	1460.8(11)	0.0(11)
1633.602(15) [85]	1633.4(13)	0.3(13)
1673.60(15) [85]	1673.5(12)	0.1(12)
1981.933(90) [83]	1981.8(14)	0.2(16)
2614.511(10) [77]	2614.4(14)	0.1(14)

Table 3.1 Summary of calibration results, including the adopted values of the peak energies selected to validate the calibration, the presently-measured values of these peak energies after calibration, and the calibration residuals, calculated as [Adopted energy] − [Present energy].

$$\epsilon_{\text{rel}} = \frac{\text{number of } \gamma \text{ rays recorded}}{\text{absolute intensity of transition}} \tag{3.3}$$

For the sake of clarity, it is noted that all efficiencies considered in this work are "peak" efficiencies. This means that, when determining the number of events recorded by the detector (i.e., the numerator of Equations 3.2 and 3.3), only events where the full energy of the photon is absorbed are counted. For the remainder of this work, all quoted efficiencies are absolute peak efficiencies, unless otherwise stated.

A radioactive 2.4 μCi ^{152}Eu source was affixed to the upstream face of the plastic implantation box. Given the fairly high activity of the source, resulting in per-crystal γ-ray counting rates ranging from around 0.4 kHz to almost 2 kHz, it is noted that any losses accrued due to detector deadtime will not effect the final results, as the ^{152}Eu data is only used to determine the shape of the curve and not the absolute normalization, and deadtime losses are not expected to be energy-dependent. For the source measurements described in this work, intensity-calibrated SRM sources were not used, but sufficient data is available within the experimental dataset and within the literature such that this is not an issue. ^{152}Eu decays via electron capture/β^+ decay with a 72.08(13)% branching ratio, or decays via β^- decay with a 27.92(13)% branching ratio, with a half-life of 13.517(9) years [86].

E_γ (keV)	Child nucleus	Branching ratio (%)
121.8	^{152}Sm	28.53(17)
244.7	^{152}Sm	7.55(4)
344.3	^{152}Gd	26.6(2)
778.9	^{152}Gd	12.93(8)
867.4	^{152}Sm	4.23(3)
1212.9	^{152}Sm	1.415(8)
1299.1	^{152}Gd	1.632(11)
1408.0	^{152}Sm	20.87(10)

Table 3.2 γ rays produced in ^{152}Eu decay used to calibrate the relative γ-ray detection efficiency of the DEGAi array. γ-ray energies are from [77]; uncertainties are one to two orders of magnitude smaller than the precision listed here, and full precision is unnecessary for the present efficiency calibration. Branching ratios are evaluated weighted averages of measurements from 16–19 different works, taken from Ref. [86]. See the evaluation and references therein for further details.

When the stable ^{152}Sm or unstable ^{152}Gd child nucleus is populated, one of many characteristic γ rays may be produced. Several of these characteristic γ rays were selected to calibrate the relative efficiency of DEGAi. γ rays were selected to evenly cover a wide range of γ-ray energies from 121.8 keV up to 1408.0 keV, with preference given to γ rays with larger branching ratios where possible. The selected γ rays are shown in Table 3.2.

The ^{152}Eu decays were recorded for approximately eight minutes. The γ-ray spectrum produced is shown in Figure 3.15. Selected γ-ray peaks were fit to a Gaussian peak shape plus a linear background, and the number of counts inside the peak was calculated from the Gaussian fit parameters. From this, relative peak efficiencies were calculated using the branching ratios listed in Table 3.2. The data was fit with a function chosen to represent the expected behavior of the detection efficiency. The expected functional form of the curve is given by Equation 3.4, where $E_{\mathrm{mod}} = 0.05 * E_\gamma$ and p_x is a fit parameter.

$$\epsilon(E_{\mathrm{mod}}) = \exp\left(p_0 + p_1 E_{\mathrm{mod}} + p_2 \frac{\log(E_{\mathrm{mod}})}{E_{\mathrm{mod}}} + \frac{p_3}{E_{\mathrm{mod}}} + \frac{p_4}{E_{\mathrm{mod}}^2} + \frac{p_5}{E_{\mathrm{mod}}^3}\right) \tag{3.4}$$

This functional form is chosen because, as γ-ray energy increases, detection efficiency decreases exponentially. However, at low energy (around 100-300 keV), there is a peak in the efficiency, and, as γ-ray energy gets lower, the efficiency decreases again. This low energy behavior is described

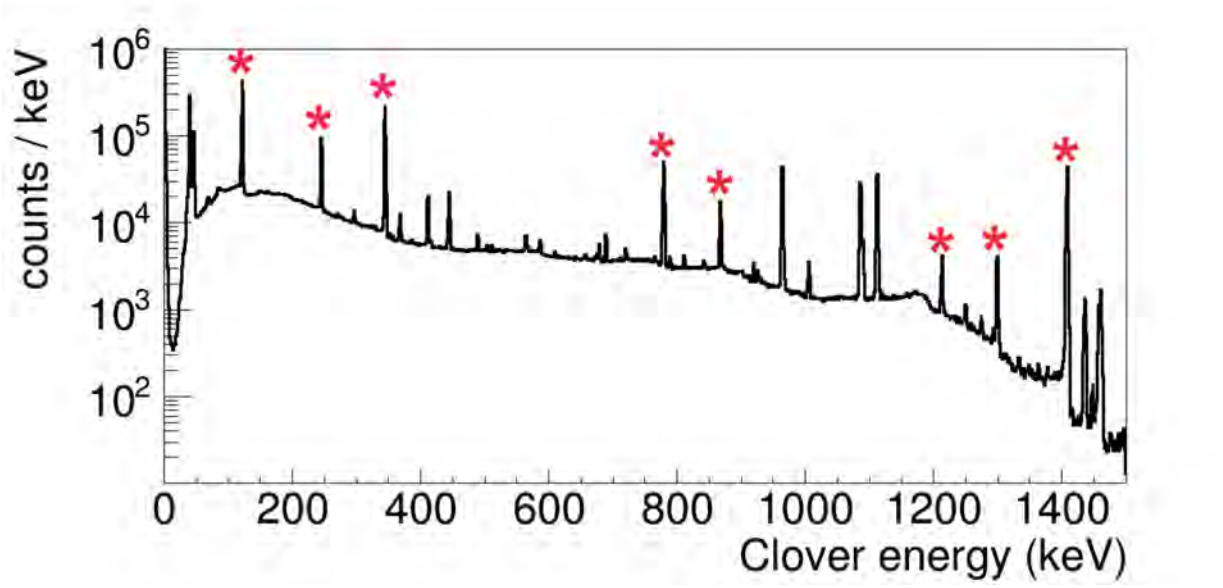

Figure 3.15 Eight minute recording of ^{152}Eu source γ-ray energy spectrum collected in DEGAi with the source affixed to the front face of the plastic implantation box.

by the last four terms of the sum, whereas the higher energy behavior is described by the first two terms of the sum. Figure 3.16 shows the calculated relative efficiencies of the eight ^{152}Eu reference peaks, as well as a fit of this data to the functional form described above. As is evident, there are too few low-energy data points to capture the expected behavior of the efficiency curve at low energy; thus, the curvature of this fit function is considered to be unreliable below approximately 500 keV. The solution to this problem will be discussed later in this section.

In order to extract absolute efficiencies, the relative efficiency curve must be normalized. This is achieved using data from another radioactive source: ^{60}Co. ^{60}Co undergoes β^- decay with a branching ratio of 100% and a half-life of 5.271 years [87], producing the stable ^{60}Ni isotope. With a 99.85% branching ratio, this decay will almost always be followed by a cascade of two γ rays: 1173 keV followed by 1332 keV [87]. Very rarely (with an approximately 0.13% branching ratio) will this ^{60}Co decay skip the 1173 keV γ ray and only emit the 1332 keV γ ray [87]. Other γ rays produced in this decay are produced in negligible amounts, and are irrelevant for this analysis.

A 0.10 μCi ^{60}Co source was affixed to the upstream face of the plastic implantation box, replacing the ^{152}Eu source. Decays from this ^{60}Co source were recorded for approximately two

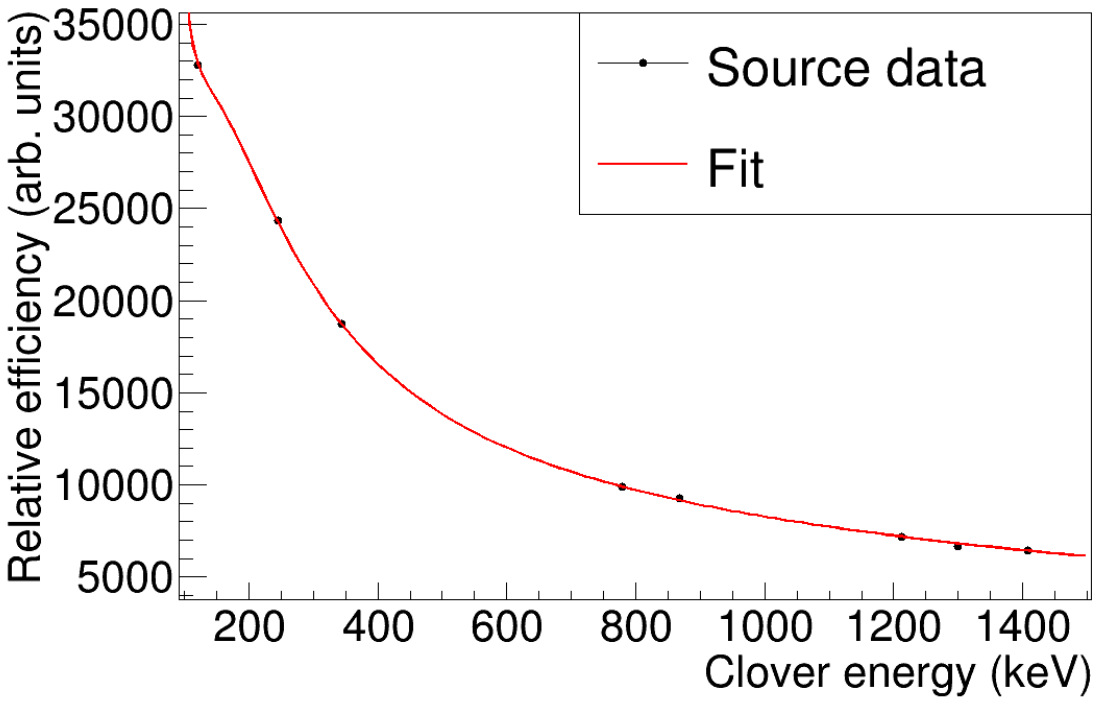

Figure 3.16 Relative efficiency of DEGAi array as a function of γ-ray energy. The data points are extracted from fits of the peaks in Figure 3.15 combined with known peak intensities, and the red line represents a fit of the data. Data was recorded in the configuration with the source affixed to the upstream face of the plastic implantation box.

hours. The γ-ray singles spectrum produced in this measurement is shown in Figure 3.17.

The probability of recording the 1173 keV and 1332 keV γ rays in coincidence is small, due to the small γ-ray detection efficiencies. The expected number of recorded coincidences is given by Equation 3.5. Note that the final factor multiplied in accounts for the fact that, if both γ rays are recorded by the same detector, a coincidence will not be recorded, and the energies will simply be summed. When considering all the detectors used in this analysis, this factor will be 38/39.

$$N_{\text{coinc}} = N_{\text{emitted}} * \varepsilon(1173\ \text{keV}) * \varepsilon(1332\ \text{keV}) * \frac{N_{\text{det}} - 1}{N_{\text{det}}} \tag{3.5}$$

Notably, N_{emitted} is simply the number of 1173 keV γ rays emitted, since every event of interest will always emit one of each 1173 keV and 1332 keV γ rays. The 1173 keV γ ray is chosen here because it feeds the 1332 keV state.

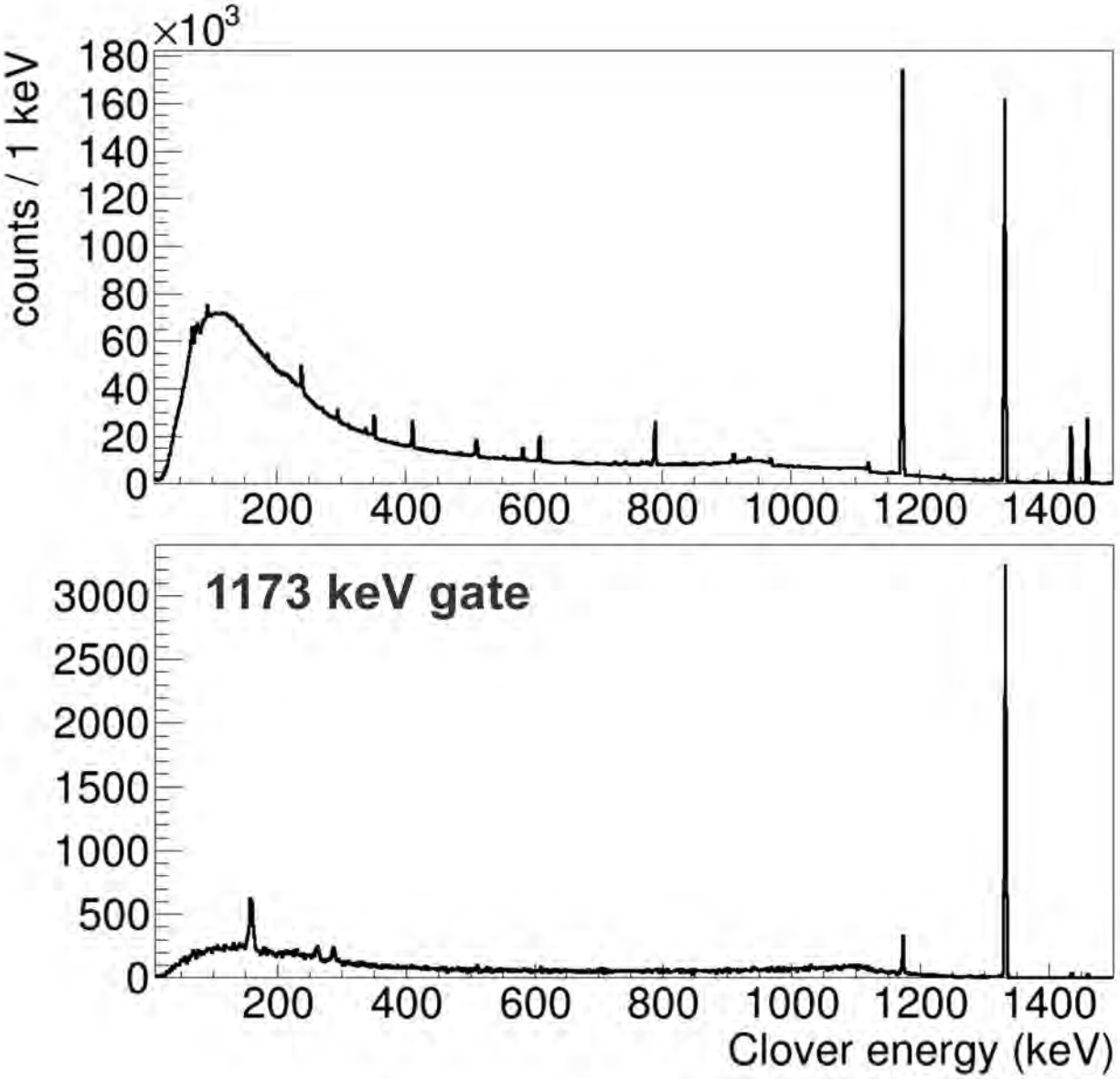

Figure 3.17 Top: ^{60}Co source spectrum collected in DEGAi with the source affixed to the front face of the plastic implantation box. Data were recorded for two hours. Bottom: The same spectrum, but with an 1173 keV γ-ray coincidence gate.

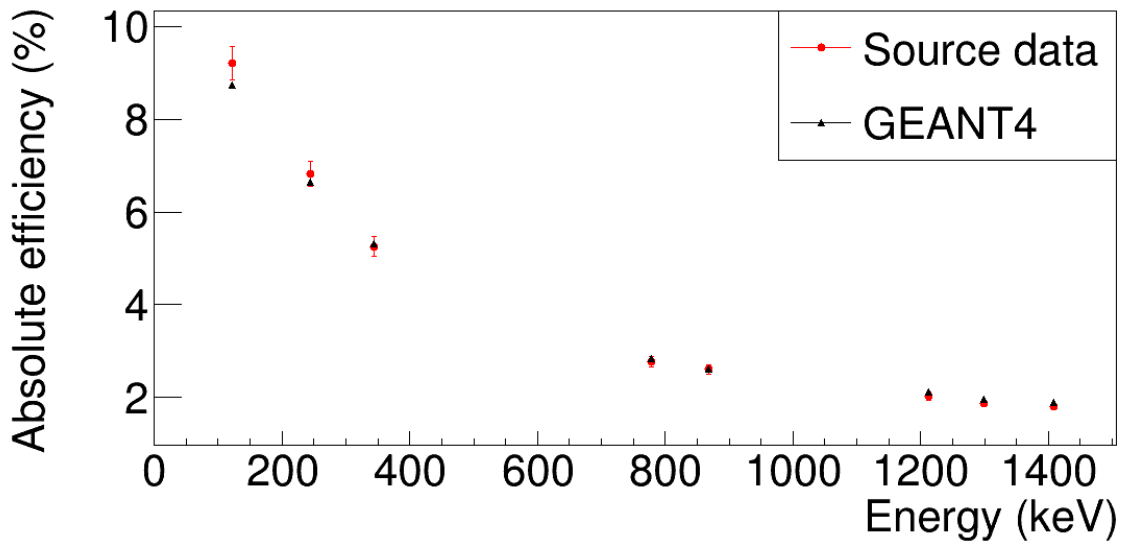

Figure 3.18 Absolute γ-ray detection efficiency in DEGAi as a function of energy. The black points are determined using ^{152}Eu and ^{60}Co standard sources affixed to the front face of the plastic implantation box (see Figures 3.15 and 3.17). The red points are determined using a GEANT4 simulation with the same configuration of source and detectors.

This allows for the substitution that $A(1173\text{ keV}) = N_{\text{emitted}} * \varepsilon(1173\text{ keV})$, where A denotes the area of the 1173 keV peak as recorded in the ^{60}Co γ-ray singles spectrum. With some rearranging of Equation 3.5, the absolute efficiency at 1332 keV can then be calculated as in Equation 3.6. Using the present data, this gives an absolute efficiency of 1.89(2)% at 1332 keV. Interpolating the relative efficiency curve fit from Figure 3.16 to extract the relative efficiency at 1332 keV allows the determination of a scale factor, such that the data points in Figure 3.16 can be scaled downwards to produce absolute intensities for the ^{152}Eu data points. As expressed before, while the accuracy of the low-energy region of the relative efficiency fit is uncertain, the fit is certainly reliable at 1332 keV. The scaled-down source data is shown in Figure 3.18, as the black data points labeled "Source data". The red "GEANT4" points will be discussed in the following paragraphs.

$$\epsilon(1332\text{ keV}) = \frac{N_{\text{coinc}}}{A(1173\text{ keV})} * \frac{N_{\text{det}}}{N_{\text{det}} - 1} \tag{3.6}$$

There are multiple problems with this approach to calibrating detection efficiency. As mentioned before, the low-energy behavior of the efficiency curve is expected to be fairly complex, and these

features are not adequately captured with only 3 low-energy (i.e. 121.8 keV, 244.7 keV, and 344.3 keV) calibration points. When looking at figure 3.18, the expected turnover in the efficiency curve is washed out, and the behavior appears simply exponential.

The second, more significant issue with this method is that the source data measured to calibrate the efficiency is not measured under the same conditions as the experimental data. Namely, the radioactive sources are affixed to the front face of the plastic implantation box, whereas experimental data is recorded with the radioactive ions implanted within the YSO crystal itself. In the experimental data, the effects of γ-ray attenuation as γ rays travel through the YSO crystal are expected to significantly change the observed efficiency curve. At high energy ($\gtrapprox$ 2000 keV), this effect may be minor; however, at low energy ($\lessapprox$ 300 keV), this effect is expected to be quite dramatic. Preliminary data analysis of the 150 keV γ ray produced in ^{30}Ne decay indeed showed dramatic disagreement with literature in γ-ray intensity when using the absolute efficiency curve calculated by fitting Figure 3.18. As discussed previously, it is expected that only 48% of 150 keV γ rays would be transmitted through 6 mm of YSO. Thus, it is reasonable to expect the efficiency curve to change significantly at low energies when the radioactive source configuration is moved from outside of the YSO to inside of the YSO.

It was not possible to record data with a standard reference source implanted within the YSO, and the experimental data recorded consisted mostly of exotic isotopes whose decay schemes are not well characterized in literature. Thus, in order to effectively characterize the efficiency of the DEGAi γ-ray detection array with the radioactive source implanted within the YSO, a GEANT4 simulation was performed. GEANT4 is a simulation toolkit designed to model the interactions of particles with matter [88–90].

Several significant components were identified which have the potential to impact the observed γ-ray efficiency. Most critical to the simulation is the implementation of the DEGAi Clover detector array itself. Eurisys 4x50x80 Two-Fold Segmented Clover Detectors comprise the DEGAi array. A class to model the geometry of this type of detector has been made publicly available within the UCGretina GEANT4 package [91]. This class was adopted with only minor changes, and 11 copies

of this Clover detector were created and placed at the angles and distances of the Clover detectors in the DEGAi array.

Along the beamline itself, the most critical piece of the detector construction is the YSO detector itself, as this contributes the most significantly to γ-ray attenuation. The 2 mm quartz light guide connecting the YSO and the PSPMT was included. Also implemented was the Hamamatsu 12700 PSPMT which is coupled to the YSO crystal [92]. As the modeling of the complexity of this device is beyond the scope of the current work, a 35 mm uniform solid box of 1 g/cm^3 density and atomic number 13 was used to approximate the PSPMT, its multipin connectors, and the Anger logic PCB. Ultimately, the results of the simulation were relatively insensitive to the specifications of the PSPMT, and the chosen volume resulted in satisfactory reproduction of source data, as will be shown in the following paragraphs. Finally, beamline components were contained within a sealed box made of 2 mm ABS plastic. This configuration described here is comparable to that which is detailed in Ref. [71] (see Figure 1). The main difference is that, in Ref. [71], a 5 mm YSO crystal was used, whereas in the present study, a 12 mm YSO crystal was used. The visualization of the geometry used in the GEANT4 simulation is shown in Figure 3.19.

In order to validate that the GEANT4 simulation could accurately reproduce DEGAi measurements, it was determined that the simulation must be able to reproduce the source data shown in Figure 3.18. Clover detectors were separated into four subsets, and each subset was compared to data separately to better understand the simulation. The subsets were upstream, 90-degrees, mid-downstream, and downstream, based on the positioning of the detectors along the beam axis relative to the central implant detector. A ^{152}Eu source was first placed on the front/upstream side of the implantation detector (outside of the implantation box), as it was placed for the source measurements made to create Figure 3.18. Several simulation parameters were tuned until the simulated efficiencies in this configuration matched the efficiencies shown in Figure 3.18. The tuned parameters included: dead layer thicknesses on the Clover detectors, the positioning of the YSO/quartz/PSPMT assembly within the ABS box, the positioning of the entire implantation setup along the beam axis, the density and atomic number of the PSPMT, and the distance between each

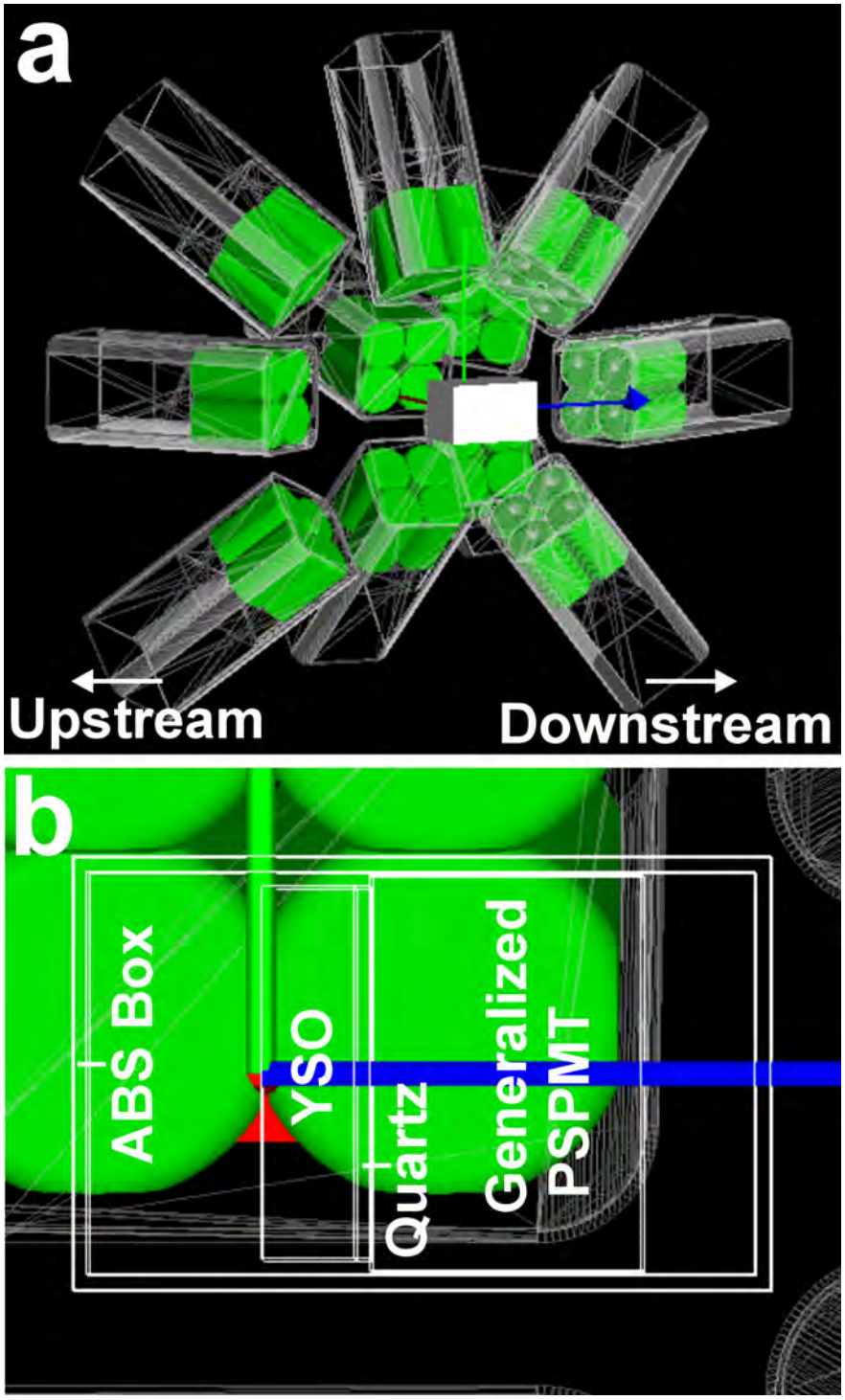

Figure 3.19 a) Rendering of DEGAi designed in GEANT4 with central implantation device in the center (white). The four crystals of each Clover are colored green, and the aluminum housing is shown as a grey wireframe surrounding the crystals. b) Expanded wireframe view of the central implantation box. Renderings produced with GEANT4; see Refs. [88–90] and Ref. [91].

Clover and the implant detector.

Ultimately, several parameters were changed to optimize the reproduction of data. 1 mm dead layers were included on the downstream detectors only. The 90-degree detectors (mid-downstream, downstream) were shifted 2 cm (2.5 cm, 1 cm) away from the implantation box relative to the expected positioning of the detectors. The YSO was centered at 0.625 cm along the beam axis, and a 2.25 cm gap was placed between the upstream inner face of the ABS box and the upstream face of the YSO. Figure 3.20 shows the results for the optimized simulation parameters for each of the four subsets of detectors, compared to the measured source efficiencies for each corresponding detector subset. The same comparison is shown for the entire array in Figure 3.18. Error bars on the GEANT4 efficiencies are statistical. Error bars on the source data include statistical errors, uncertainty in the fit of the relative efficiency at 1332 keV, uncertainty in ^{152}Eu and ^{60}Co peak fits, and uncertainty in literature I_γ values for ^{152}Eu. The dominant source of error comes from the ^{60}Co coincidence peak, both from its statistical error and its fitting error, although other sources of error are not insignificant.

Figure 3.20 shows good agreement between source data and the GEANT4 simulation. There are a few data points which do not agree within 1σ, particularly when looking at the 90 degree detectors separately; however, the majority of these discrepancies are resolved by increasing error bars to 2σ. Furthermore, when the entire array is summed in Figure 3.18, all points except the 122 keV point agree within 1σ, and the discrepancy for the 122 keV point is resolved by increasing errors to 2σ. There is a 5.3% relative difference between the GEANT4 result and the source data for the 122 keV point. This is taken as a measure of the systematic error of the simulation, and a 5.3% relative systematic error will be added to the final, experimental efficiency values. This systematic error is not included in Figures 3.20 and 3.18.

With the simulation sufficiently validated, the source position can be moved to the center of the YSO, the configuration in which experimental data are recorded. The source is changed from ^{152}Eu to a γ-ray source of a chosen energy. In this way, the γ-ray energy can be set as needed, and efficiencies can be directly extracted for several γ rays of interest. Figure 3.21 shows the

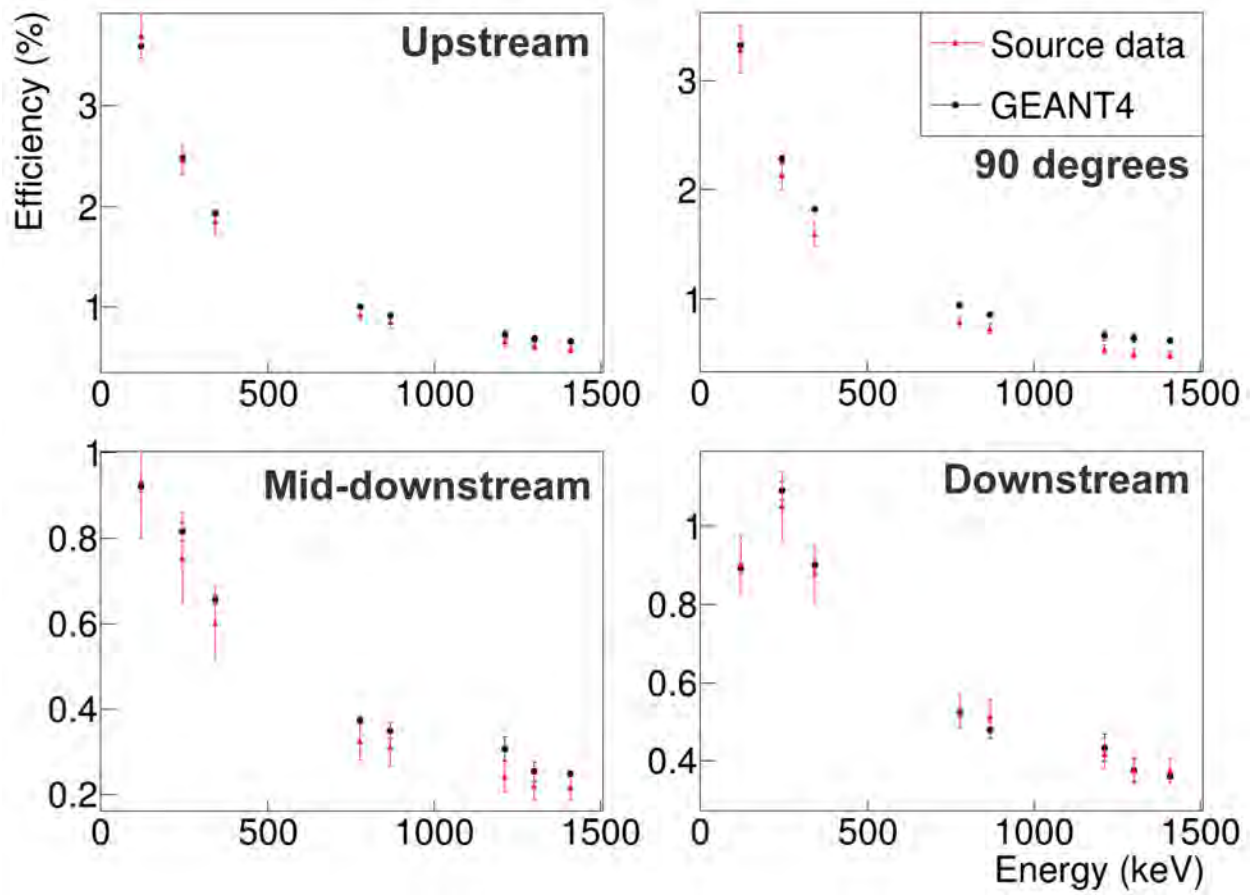

Figure 3.20 Validation of GEANT4 simulation for four subsets of detectors: upstream, 90 degrees, mid-downstream, and downstream. The data points are determined experimentally from ^{152}Eu and ^{60}Co source data. The simulated points are derived using GEANT4 with the same configuration of source and detectors.

results of the GEANT4 simulation in this configuration. A clear trend is observed, which the fit function given in Equation 3.4 well reproduces. Unlike in Figure 3.16, the low energy behavior is well characterized by several low-energy data points, with the turnover occurring around 250 keV. Notice that the lowest-energy data point at 120 keV has efficiency only slightly greater than 1%; in the source data (see Figure 3.18), the 122 keV data point has efficiency over 9%. Therefore, it is shown that the source configuration matters significantly at low energy.

As further proof of the efficacy of these efficiency calculations derived from GEANT4, preliminary γ-ray intensities for the known ^{30}Ne γ rays were calculated and compared to known quantities [3]. Preliminary results using the GEANT4-derived efficiencies showed satisfactory agreement be-

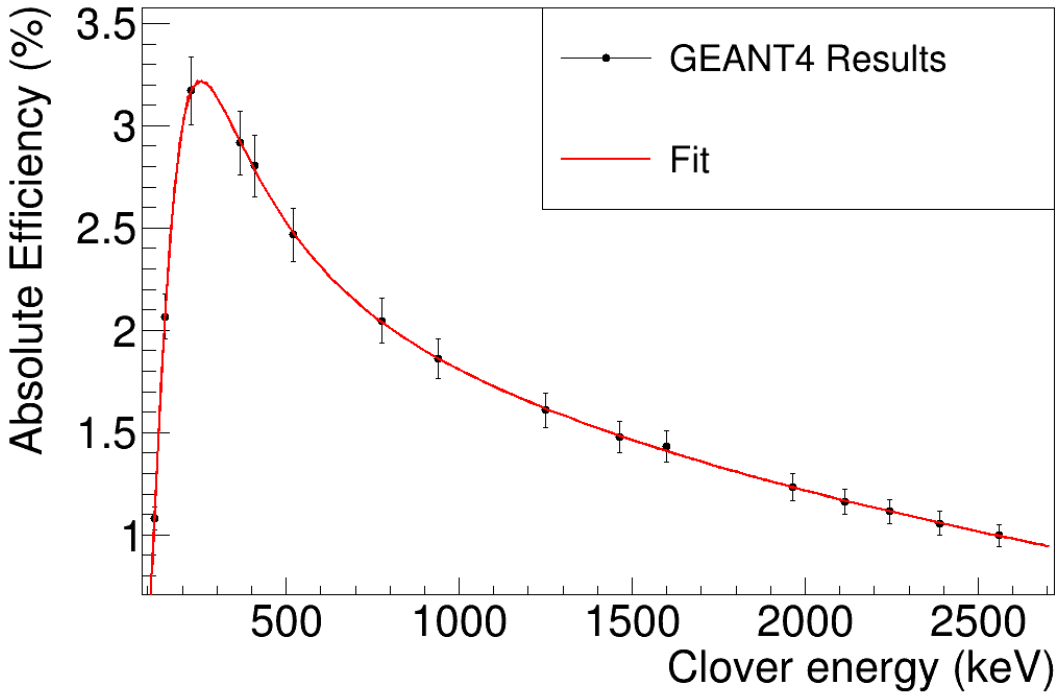

Figure 3.21 Efficiency of entire DEGAi array derived with GEANT4 under experimental conditions (i.e., the source is implanted within the implantation detector). The black points represent values directly extracted from GEANT4, and the red line represents a fit of the data to the functional form given in Equation 3.4. The error bars combine statistical errors with a 5.3% relative systematic error (see text for details).

tween the present work and known quantities. See Table 4.2 for the final results of this comparison, and the rest of Section 4.1 for more details.

CHAPTER 4

RESULTS

4.1 β-decay of ^{30}Ne

β-decay of ^{30}Ne was studied first. As Section 1.4 suggests, this decay is quite well studied. Therefore, the ^{30}Ne dataset in the present work will be mainly used to validate methodology.

To correlate ^{30}Ne ion implantations to β decays, the spatial correlation window of 2 pixels was selected as described in Section 3.4. Based on previous half-life measurements of ^{30}Ne β-decay (7(2) ms [48], 5.8(2) ms [49], 7(2) ms [2], 7.5(15) ms [50], 7(2) ms [93], 7.3(3) ms [3], 7.18(22) ms [4]), a sufficiently long temporal correlation window of 50 ms was chosen to optimize observation of ^{30}Ne parent decays. This is equal to approximately 7 half-lives; based on the exponential nature of β decay, less than 1% of parent β decays would occur beyond this window. Only roughly 45%-58% of $^{30,\,29,\,28}$Na children would have sufficient time to decay in this time window, so background due to child activity is slightly suppressed. A smaller correlation window from $3t_{1/2}$ to $5t_{1/2}$ may be appropriate in cases where the ratio of background activity (both from random correlations and child activity) to parent activity is high, and some percentage of parent decays can be neglected in favor of a cleaner spectrum. In order to preserve statistics and correlate as many parent decays as possible, a longer correlation window is chosen here.

A key step is the analysis of the decay curve of ^{30}Ne, given in Figure 4.1 as the black histogram. In order to extract useful information from this plot, it must be fit with a sum of multiple contributions whose functional forms are given by the Bateman equations (Equations 2.5, 2.6, and 2.7).

For this fit, there are many contributions which can be considered, including child decays, grandchild decays, and random background decays which may be correlated to the initial implantation. It is key to understand which contributions make a meaningful impact on the result of the fit. For example, the contribution from decays of the ^{30}Na child almost certainly will have an impact, as it has a half life of 45.4(11) ms ([94], see Appendix), slightly smaller than the correlation window used, and will be populated after 78.5% of parent decays, based on the neutron emission probabilities of P_{1n} = 12.6(35)% and P_{2n} = 8.9(23)% ([3], see Appendix). However, the decays

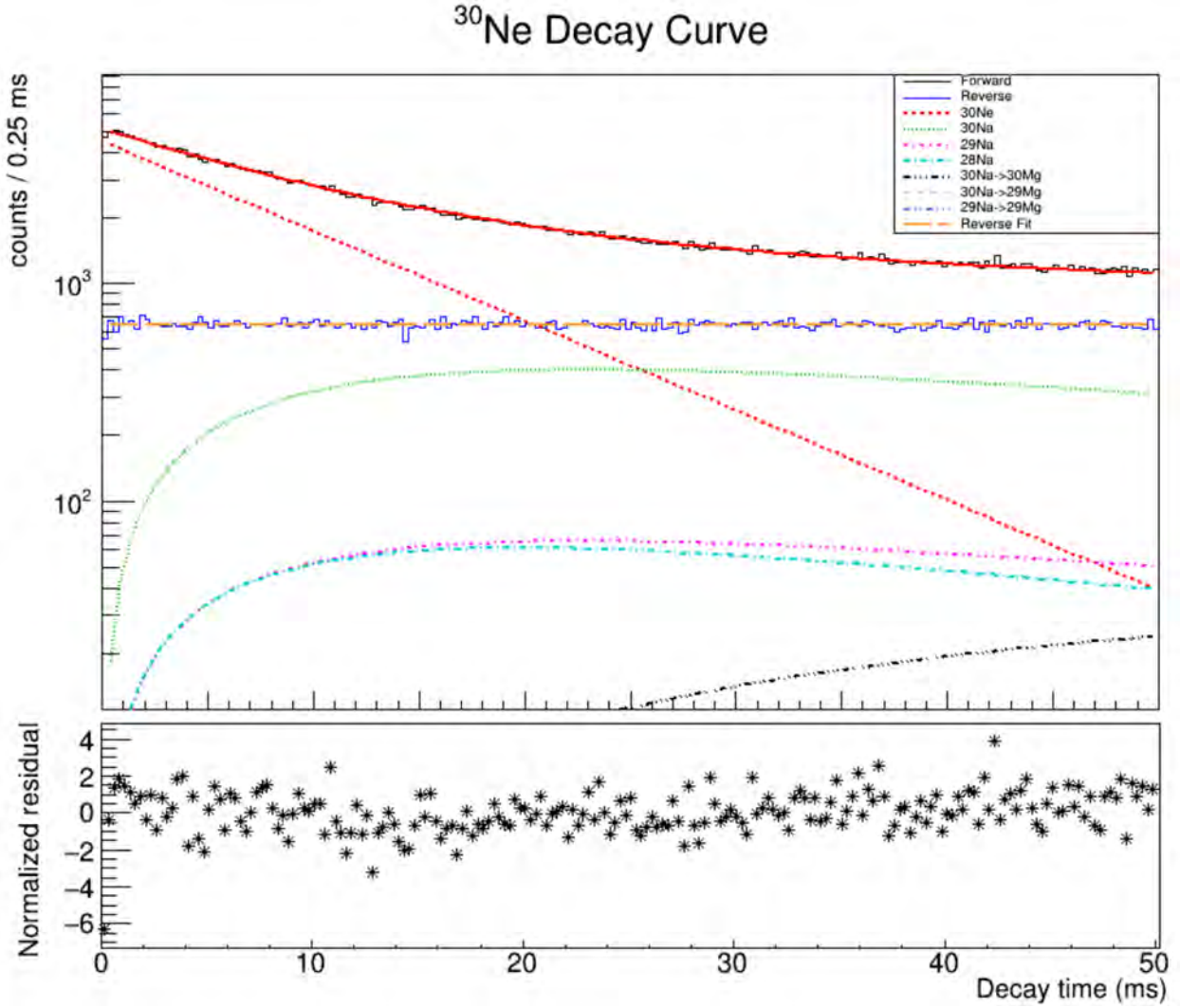

Figure 4.1 Decay time for all identified ^{30}Ne decays, fitted to a sum of Bateman equations. The black histogram represents the forward-correlated decay curve, and the blue histogram represents the reverse-correlated decay curve. The total fit is shown in solid red, the parent contribution is shown in dotted red, and the background fit is shown in dash-dot orange. The remaining fit contributions are descendant contributions which are labeled in the figure. Several granddaughter components do not contribute significantly to the fit, and thus their contributions are out of frame. The bottom panel shows normalized residuals of the total fit. See text for full description of fitting process.

Contribution	Half-life	P_{1n} (%)	P_{2n} (%)
^{30}Ne	varied	12.6(35) [3]	8.9(23)[3]
^{30}Na	45.4(11) ms [94]	30(5) [96]	1.27(25)^a [96]
^{29}Na	44.1(9) ms [97]	21.5(30)^a [98]	^{a}
^{28}Na	30.5(4) ms [99]	0.58(12)^a [99]	^{a}
^{30}Mg	319(6) ms [94]		
^{29}Mg	1.30(12) s [97]		
^{28}Mg	20.915(9) h^a [95]		

Table 4.1 Decay data used to perform fit of the histogram in Figure 4.1. Grandchild P_{xn} values are not listed because future generations are not included in the fit. See the Appendix for a more detailed compilation of previous measurements of these values. ^{a}: Decay pathway neglected in fit.

of the ^{28}Mg grandchild will have little effect, as its half life of 20.915(9) h ([95], see Appendix) is much longer than the correlation window. For this analysis, three generations of decays were considered. In order to be included in the fit, the given decay was required to have a significantly short half-life and to be populated in significant amounts through parent and child β_{xn} channels. Taking into account these considerations, the isotopes included in the fit were: ^{30}Ne, ^{30}Na, ^{29}Na, ^{28}Na, ^{30}Mg, and ^{29}Mg. Note that there are some grandchildren which can be populated through multiple channels. In this case, two decay channels are included which result in the decay of ^{29}Mg, one which involves β decay of ^{29}Na and another which involves β_{1n} decay of ^{30}Na. A constant randomly-correlated background component is also included in the fit.

In the fit, only two parameters are varied: the parent half-life and the initial parent activity. The constant background is fixed to the value given by a fit of the reverse-correlated decay curve (described in Section 3.4), and all other quantities (child and grandchild half-lives and parent and child P_{xn} values) are fixed to literature values. The chosen values for these fixed variables are shown in Table 4.1, and a detailed compilation of past measurements of these values is given in the Appendix. For β_{xn} channels which are neglected due to low P_{xn}, P_{xn} is forced to zero. In practice, this forces a small amount of extra decay strength into the β_{0n} channel, as the fitting code requires $\Sigma P_{xn} = 1$. A thorough examination of the impact of this practice on deduced quantities is conducted, and will be discussed later. The uncertainty resulting from the inclusion of fit parameters fixed to literature values will also be discussed.

The determined fit parameters give a parent half-life of 7.31(3) ms and an initial activity of 4499(19) counts / 0.25 ms, with a χ^2/NDF value of 1.3. Note that the errors on the varied parameters are not inclusive of all sources of error; they solely account for the uncertainty in the likelihood fitting procedure. The half-life is in good agreement with most previous measurements: 7(2) ms [48], 5.8(2) ms [49], 7(2) ms [2], 7.5(15) ms [50], 7(2) ms [93], 7.3(3) ms [3], 7.18(22) ms [4].

The main drawback of this method of half-life measurement is that the decay curve fit is subject to many sources of systematic error, due to the necessity of including fixed parameters derived from literature. When β-delayed γ rays are present, a gate on a strong transition in the child can significantly reduce the statistics of the histogram, but it can also greatly simplify the fit and eliminate these systematic errors. As ^{30}Ne does produce quite a few strong β-delayed γ rays, (see Section 1.4), which will be shown in Section 4.1.1 to be present in significant amounts in the data, this will be the preferred method of half-life extraction for this study. In practice, the measured half-life from the current fit is used in an approximate sense to validate the effectiveness of the fit.

The most significant quantity which is extracted from the fit of Figure 4.1 is the number of parent decays, determined by integrating the parent activity component. This quantity will be represented as N_β. Many derived quantities, such as β-delayed γ-ray intensities and P_{xn} values, depend on the number of parent decays observed within the correlation window. This quantity is not simply the number of correlations, as there is significant background from random correlations as well as subsequent generations of decays. This is evident in Figure 4.1. Thus, integration of the parent component of the fit is the best way to determine this value.

By analytically integrating Equation 2.5 and plugging in the determined fit values, the number of ^{30}Ne parent decays is determined to be 188,078 $\pm$ 434$_{\text{stat}}$ $\pm$ 1,124$_{\text{fit}}$ $\pm$ 6,143$_{\text{sys}}$. The statistical error is derived from the Poisson $\sqrt{N}$ statistical error. The fit error is determined by propagating the fit parameter errors given by the Standard Likelihood fitting algorithm which was used to fit the histogram. The systematic error is determined by individually varying each fixed parameter by $+1\sigma$ and -1σ and quantifying the change in the number of decays under these conditions. In determination of the systematic error, the decay channels which were neglected were individually

added back in to quantify the impact of these channels. They were found to be insignificant. The systematic error due to the fixed background height was examined by allowing the background height to vary and noting the change in the number of decays. The biggest source of systematic error comes from the fixed background.

Combining all sources of error in quadrature gives a final value of $N_\beta = 188,078 \pm 6,260$. This will be used in calculations going forward. As this is an intermediate value, it is not rounded. Final values are rounded according to the precision of the final errors.

Based on this number and the number of implants given in Section 3.2, a "correlation efficiency" can be extracted, as $N_\beta / N_{\text{implants}}$. This is the likelihood that an implanted ion will be properly correlated to its first-generation decay. This value is 55.2(18)% for ^{30}Ne. Losses in efficiency occur when parent decays are not effectively correlated during the correlation procedure, due to factors such as restrictions imposed by the correlation windows or mislabeling of events. Furthermore, while the β-detection efficiency is expected to be quite high (around 80% in a study with the same type of detector [71]), it is still not 100%, so some loss is accrued in β detection as well.

4.1.1 γ-ray transitions in ^{30}Na

The next key step is to look for γ rays observed in DEGAi in coincidence with correlated ^{30}Ne β decays. The same 50 ms, 2 pixel correlation window is used. This spectrum is shown in Figure 4.2. The forward-correlated and reverse-correlated spectra are compared. Peaks that exist in both spectra are likely due to randomly-correlated background, whereas peaks that exist solely in the forward-correlated spectrum are more likely the characteristic β-delayed γ rays produced following the ^{30}Ne parent and child decays.

Note that a condition was placed on Figure 4.2, such that only γ rays which appear promptly following the β decay are shown. This prompt γ-ray timing condition is introduced as a graphical cut on the γ-ray energy versus time spectrum, as the shape of the prompt distribution is energy-dependent. This energy dependence is largely the result of the timing pick-off method employed within the experimental electronics. The use of a graphical cut allows the width of the time cut to vary smoothly with γ-ray energy to match the shape of the prompt distribution. For reference, the

width of the cut is approximately 475 ns at 1 MeV, and the width is increased to approximately 850 ns at 100 keV. The same cut will be used in γ-ray analysis throughout this work, and it will only be removed when searching for β-delayed isomers. In the case of ^{30}Ne, no isomers are expected following the β decay, and, when removing the prompt timing condition, no delayed transitions emerge.

The background γ rays which are present in Figure 4.2 are mainly the result of random ion–β correlations. Many transitions from the A=18, 19, 20, and 22 decay chains are present. Exotic isotopes from these light-mass decay chains, mostly from Carbon, Nitrogen, and Oxygen parents, are present in the beam. Long-lived decay descendants (i.e., descendants with half-lives comparable to or greater than the implantation rate) of these exotic isotopes create a constant background in the implantation detector, thus resulting in random correlations between these decays and the ^{30}Ne implants of interest.

An interesting case is the presence of background γ rays, clearly visible in both the forward- and reverse-correlated spectra, belonging to the ^{43}Ca isotope, which is too heavy to be produced down the decay chains of any of the ions present in the ^{37}Na beam setting. As was mentioned in Section 3.2, two beam settings were explored during this experiment: ^{37}Na and ^{45}P. During the experiment, the ^{45}P setting was explored first, the ^{37}Na setting was explored second, the ^{45}P setting was then explored for a second time, and, finally, the ^{37}Na setting was explored for a second time. Several of the isotopes delivered in large amounts to the FDSi during the ^{45}P setting would indeed decay into ^{43}K, which itself β decays and produces these two ^{43}Ca β-delayed γ rays. ^{43}K has a half-life of 22.3(1) h ([100], see Appendix), which is long enough to create particularly long-lived background in the YSO. This background would exist long enough to continue to produce random correlations long after the beam setting was switched out of the ^{45}P mode and into the ^{37}Na mode.

To focus the γ-ray spectrum on the peaks which are properly correlated to the ^{30}Ne β-decay, the reverse-correlated spectrum is subtracted from the forward-correlated spectrum. No scaling factor is required, as the rate of random correlations is the same in both directions. Figure 4.3 shows the result of this background subtraction. Peaks attributed to the ^{30}Na child of interest are labeled with

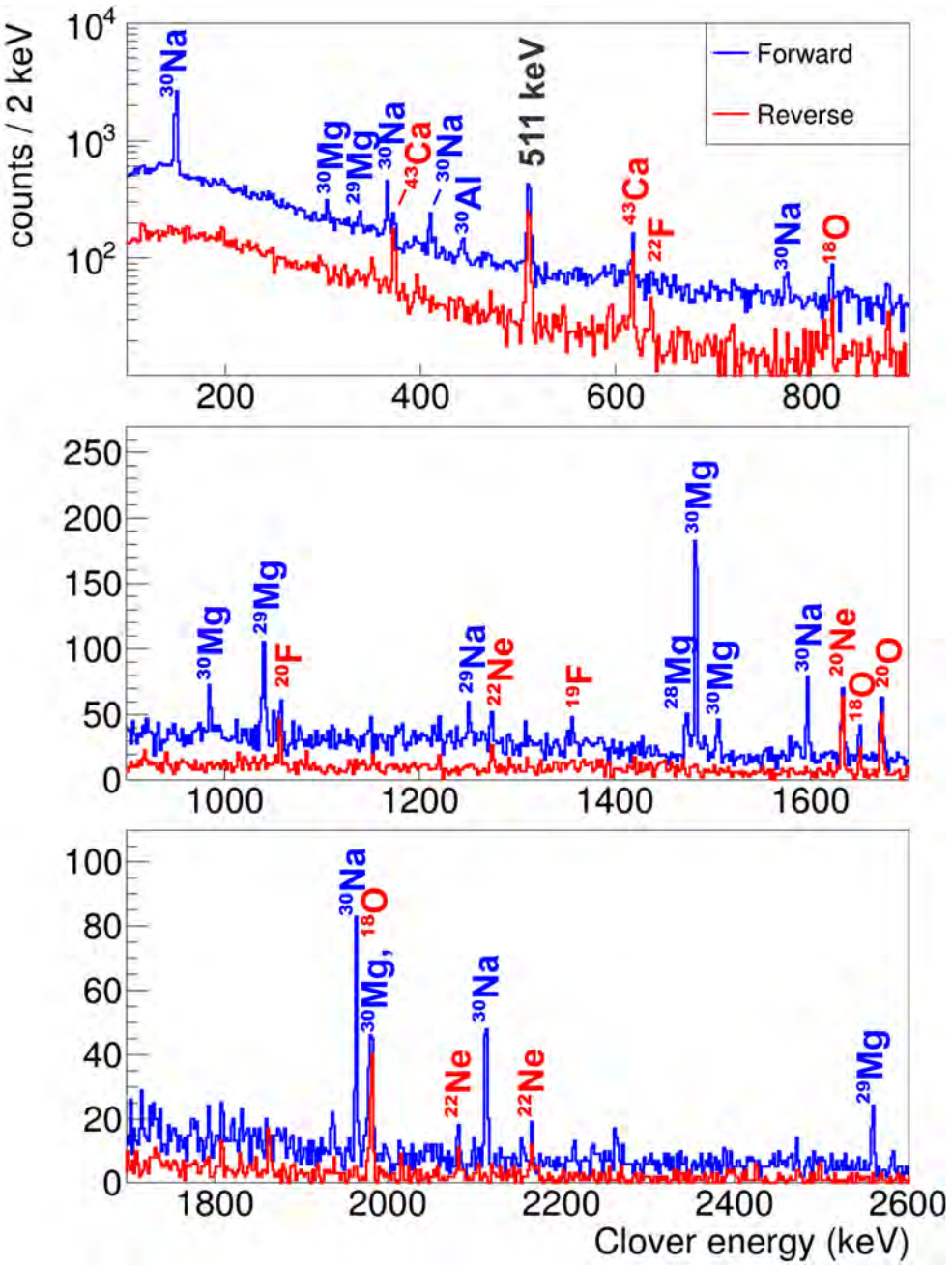

Figure 4.2 γ-ray spectrum in coincidence with identified ^{30}Ne β decays. A correlation window of 50 ms was used to optimize the observation of transitions in the ^{30}Na child. Peaks are labeled with the name of the isotope to which the transition belongs. The forward-correlated spectrum is shown in blue, and the reverse correlated spectrum is shown in red.

their energies in keV, and grandchild peaks are noted as well.

Assuming prior knowledge of the ^{29}Na and ^{29,30}Mg level schemes (^{29}Na: [2, 101, 102]; ^{29}Mg: [30, 56, 98, 99, 103–105]; ^{30}Mg: [15–17, 28, 56, 98, 104–113]), one can eliminate several of the peaks visible in Figure 4.3 as candidates for transitions in the ^{30}Na level scheme. The seven remaining peaks are 149.4(10) keV, 366.1(10) keV, 409.5(10) keV, 775.3(19), 1597.9(11) keV, 1963.9(9) keV, and 2113.3(15) keV. With these transitions in mind, a level scheme for the ^{30}Na child can be built. One reliable tool that can be used to do this is a γ-γ coincidence spectrum. While still gating on identified ^{30}Ne β decays, one can apply another gate on a narrow range of γ-ray energies in order to isolate cascading transitions in the child level scheme. An appropriate gating range is typically determined based on the width of the gating γ-ray peak observed in a plot like Figure 4.3. γ-γ coincidence spectra for several different γ-ray gates are shown in Figure 4.4. From the coincidence plots, one notes several coincidence relationships: 149 keV and 366 keV, 366 keV and 1598 keV, and 149 keV and 1964 keV. In addition, two small coincidence relationships are noted for granddaughter γ rays which correspond to cascades which have been identified in past studies: 338 keV and 1040 keV (^{29}Mg, [30, 104]), and 305 keV and 1483 keV (^{30}Mg, [16, 17, 56, 98, 104, 109, 113]). A small peak seems to appear at 242 keV in the 1483 keV coincidence spectrum. As this does not correspond to a know transition, does not appear in Figure 4.3, and is small enough that it could reasonably be considered to be a background fluctuation, this coincidence will be neglected for the rest of the analysis.

Another tool which can be helpful in the building of the level scheme is energy summing relations. This is to say that the observation of two γ rays whose energies sum up to the energy of a third observed γ ray can often imply the placement of one or more levels. From here, one can note the following relationships: 149.4(10) keV + 1963.9(9) keV = 2113.3(13) keV, 366.1(10) keV + 1597.9(11) keV = 1964.0(15) keV, and 366.1(10) keV + 409.5(10) keV = 775.6(14) keV. Based on the coincidence and energy summing relationships noted above, all of the seven identified transitions can be placed in a level scheme which matches that of Ref. [3]. The deduced level scheme is shown in Figure 4.5.

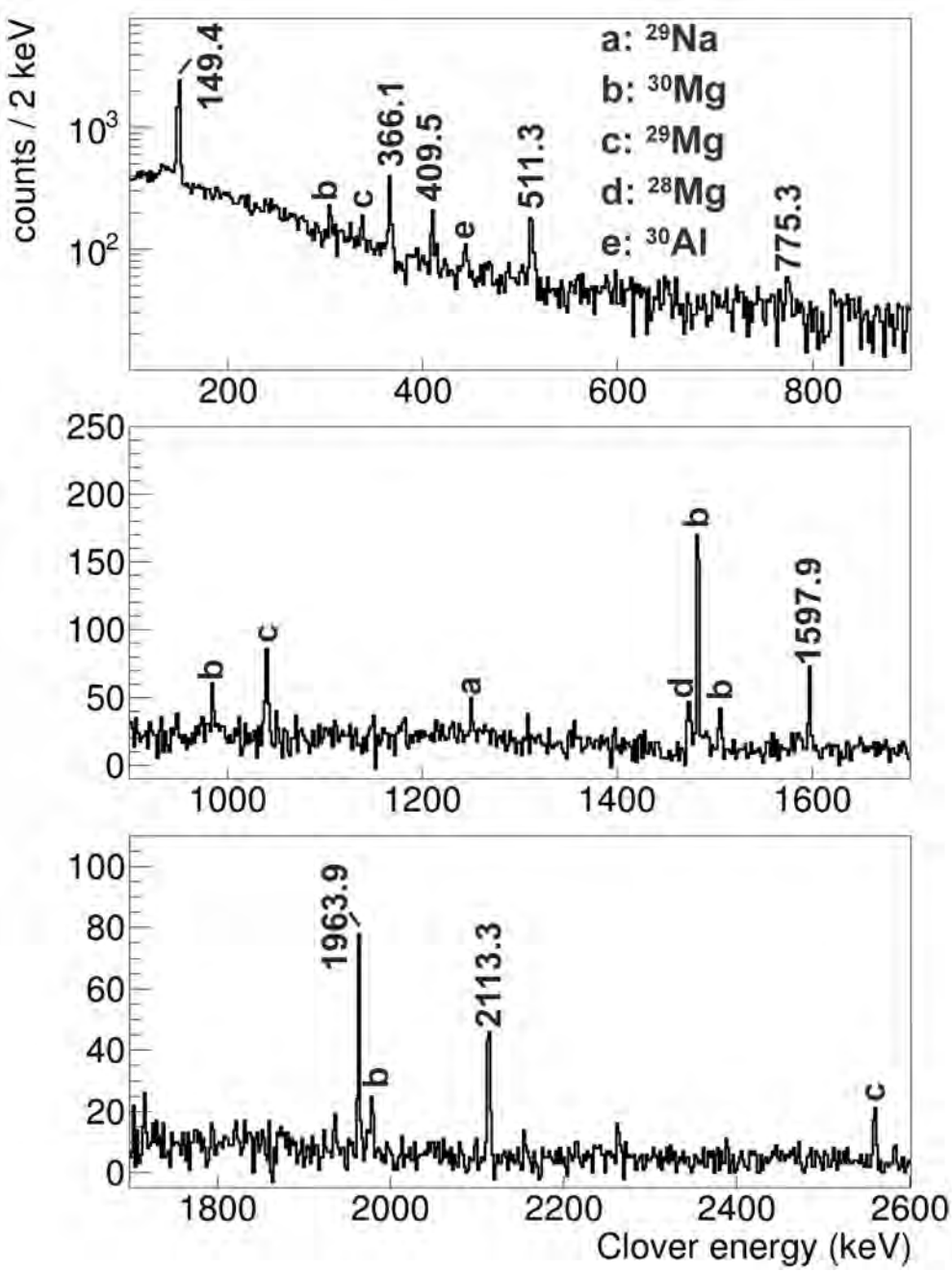

Figure 4.3 γ-ray spectrum in coincidence with identified ^{30}Ne β decays, with an ion-β correlation window of 50 ms. The spectrum is obtained by subtracting the reverse-correlated spectrum from the forward-correlated spectrum (see Figure 4.2). The 511 keV e^-e^+ annihilation peak is also labeled with its energy. a: Transitions in the ^{29}Na grandchild. b: Transitions in the ^{30}Mg grandchild. c: Transitions in the ^{29}Mg grandchild. d: Transitions in the ^{28}Mg grandchild. e: Transitions in the ^{30}Al great-grandchild.

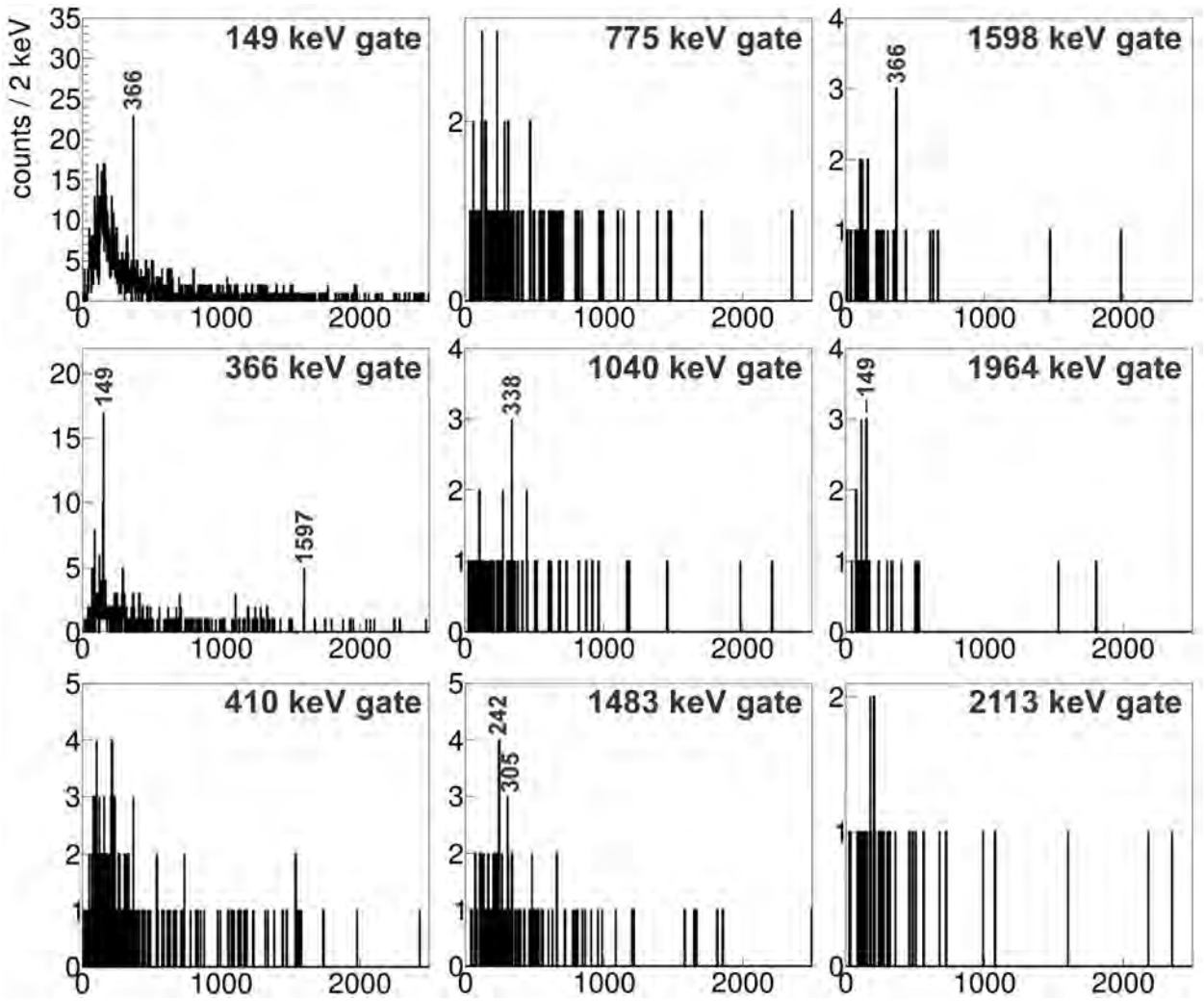

Figure 4.4 γ-ray spectrum in coincidence with identified ^{30}Ne β-decays, shown for several different γ-ray coincidence gates. Coincident γ-ray lines are identified by their energies in keV.

Table 4.2 shows the fitted γ-ray energy centroids from the ^{30}Na and ^{29}Na peaks in Figure 4.3, along with the absolute γ-ray intensity of each peak as a percentage of the number of parent β decays. Equation 4.1 shows how these intensity values are calculated, where A_γ is the area of the γ-ray peak in Figure 4.3, ε_γ is the γ-ray detection efficiency at that energy, and N_β is the number of parent decays as determined in Section 4.1. Both the determined γ-ray energy value and its absolute intensities are compared with measurements from Ref. [3].

$$I_\gamma = \frac{A_\gamma}{\varepsilon_\gamma N_\beta} \tag{4.1}$$

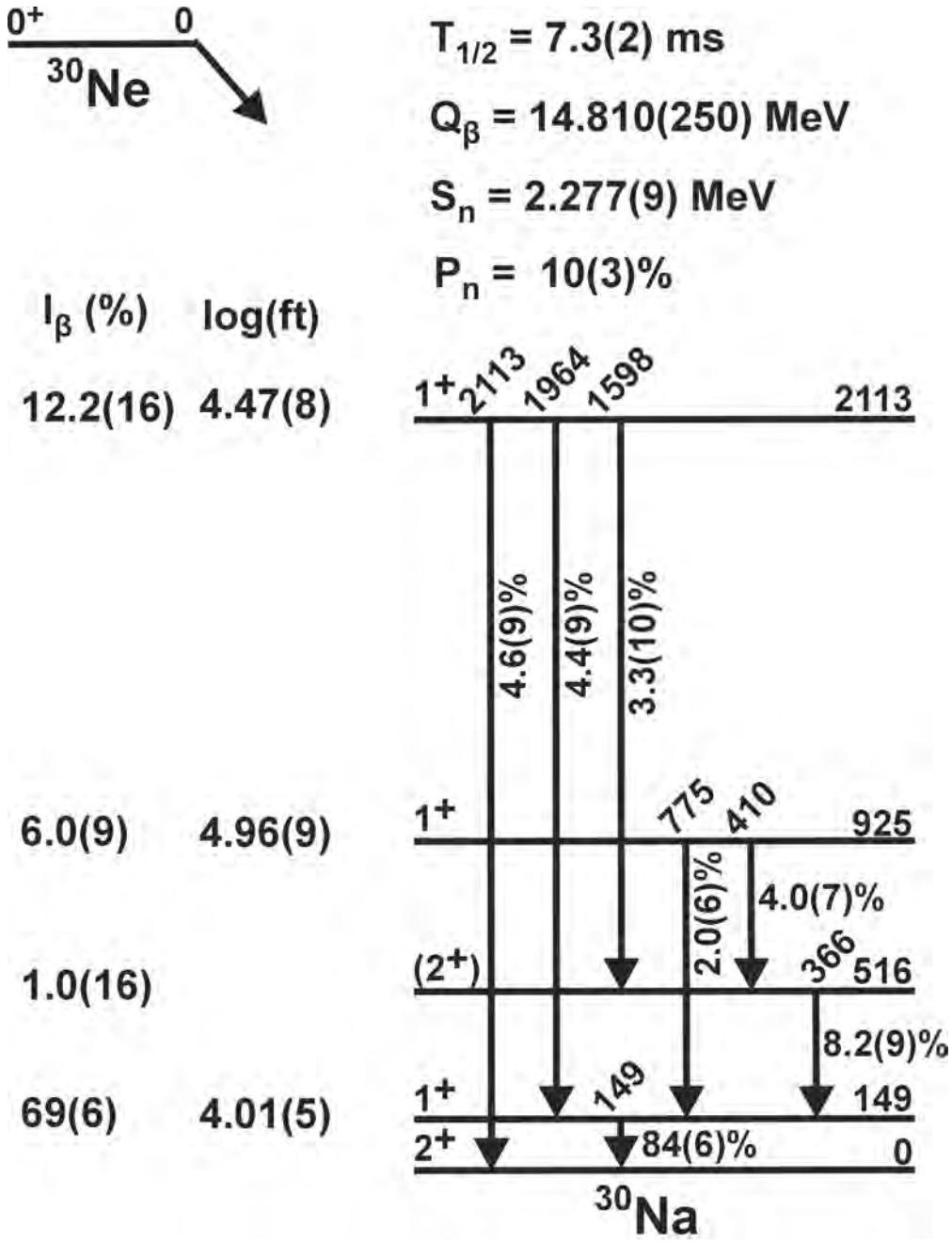

Figure 4.5 Level scheme of ^{30}Na inferred from the present work. See full text for discussion of calculations cited in this diagram. Excited state spin-parity assignments are taken from Ref. [3], as the present data do not contradict these assignments. The ^{30}Na ground state spin-parity is taken from Ref. [114]. Q_β and S_n are taken from Ref. [53].

Isotope	E_γ (keV)		I_γ (%)	
	Present work	Prev.	Present work	Ref. [3]
^{30}Na	149.4(10)	150.6(2) [2] (see [3, 47])	84(6)	78(10)
	366.1(10)	365.5(5) [3]	8.2(9)	9(2)
	409.5(10)	410.0(5) [3]	4.0(7)	6.3(10)
	775.3(19)	775(1) [3]	2.0(6)	1.4(5)
	1597.9(11)	1597(1) [3]	3.3(10)	5(1)
	1963.9(9)	1963(1) [3]	4.4(9)	5(1)
	2113.3(15)	2114(1) [3]	4.6(9)	4(1)
^{29}Na	1250.1(11)	1249 [115] (see [3, 101])	1.4(8)	

Table 4.2 γ-ray transition energies observed in Figure 4.3 along with their intensities as a percentage of the number of observed β decays. Present intensities are compared to previously measured values from Ref. [3]. Errors on values from Ref. [3] are from Ref. [94].

Good agreement within 1σ is seen for most of the determined values. The intensity of the 410 keV γ ray is reduced compared to the value given in Ref. [3], but agreement is still observed within 2σ. While the 1250 keV γ ray from ^{29}Na was observed in Ref. [3], its intensity was not previously reported, and is thus given here for the first time.

From the γ-ray intensity calculations, it is possible to deduce the β-decay feeding intensity to each inferred level. This is a simple calculation given in Equation 4.2. The β-decay feeding intensity into a level is equal to the difference in the sums of the γ-ray intensities of γ rays that feed into the level versus γ rays that depopulate the level. The deduced level energies, their β-decay feeding intensities, and the corresponding log(ft) values (calculated using LogFT [58]) are shown in Table 4.3. Again, these values are compared to those published in Ref. [3]. Good agreement within 1σ is seen with Ref. [3] for all of the deduced E_x I_β, and log(ft) values.

$$I_\beta(E_x) = \Sigma I_\gamma(\text{out of level}) - \Sigma I_\gamma(\text{into level}) \tag{4.2}$$

As mentioned previously, gating on a strong β-delayed γ-ray transition can simplify the β-decay curve seen in Figure 4.1. In this work, several γ-ray gates are employed. These γ-gated decay curves are shown in Figure 4.6. The γ-gated decay curves made while gating on γ rays which are produced following the parent decay are fitted with a weighted log likelihood fitting algorithm in order to extract the parent half-life. Note that the ion–β correlation window is extended to 73

E_x (keV)		I_β (%)		log(ft)	
Present work	Ref. [3]	Present work	Ref. [3]	Present work	Ref. [3]
149.4(10)	151(1)	69(6)	63(15)	4.01(5)	4.03(14)
515.5(14)	516(1)	1.0(16)	2(2)		
925.0(17)	924(1)	6.0(9)	7.7(13)	4.96(9)	4.84(12)
2113.3(15)	2114(2)	12.2(16)	14(2)	4.47(8)	4.39(12)

Table 4.3 Excitation energies of inferred states in ^{30}Na, along with their β-decay feeding intensities and calculated log(ft) values. Present values are compared to previously measured values from [3].

ms in order to capture the majority of the decay curve, as well as a significant extent of constant background. This improves the accuracy of the fit. Two γ-gated decay curves made while gating on γ rays which are produced following the child decays are shown for qualitative comparison: 1483 keV (^{30}Mg) and 2559 keV (^{29}Mg). For the seven identified γ rays belonging to the ^{30}Na level scheme, satisfactory agreement is seen in the extracted half-lives. The adopted value in this work is $t_{1/2}$ = 7.3(2) ms, choosing the fit value extracted with the 149 keV γ-ray gate, which has, by far, the highest level of statistics. Excellent agreement is seen between this value and the previously measured values of 7(2) ms [48], 5.8(2) ms [49], 7(2) ms [2], 7.5(15) ms [50], 7.3(3) ms [3], and 7.18(22) ms [4].

4.1.2 Descendant decays and delayed neutron emission

Figure 4.3 clearly shows the presence of γ-ray activity following the decay of ^{30}Ne descendants. To explore this activity further, the correlation window was increased to 200 ms. Effectively, 100% of parent decays will have occurred within this time window. Approximately 94-99% of ^{30,29,28}Na child decays will have occurred within this time window; thus, compared to the 50 ms correlation window, the 200 ms correlation window captures the majority of child decays in addition to all parent decays.

The background subtracted β-delayed γ-ray spectrum with a 200 ms correlation window is shown in Figure 4.7. γ rays produced following the parent decay are labeled according to the isotope to which they belong, and γ rays produced following the child and grandchild decays are labeled with their energies in keV. There are a few places where incomplete background subtraction

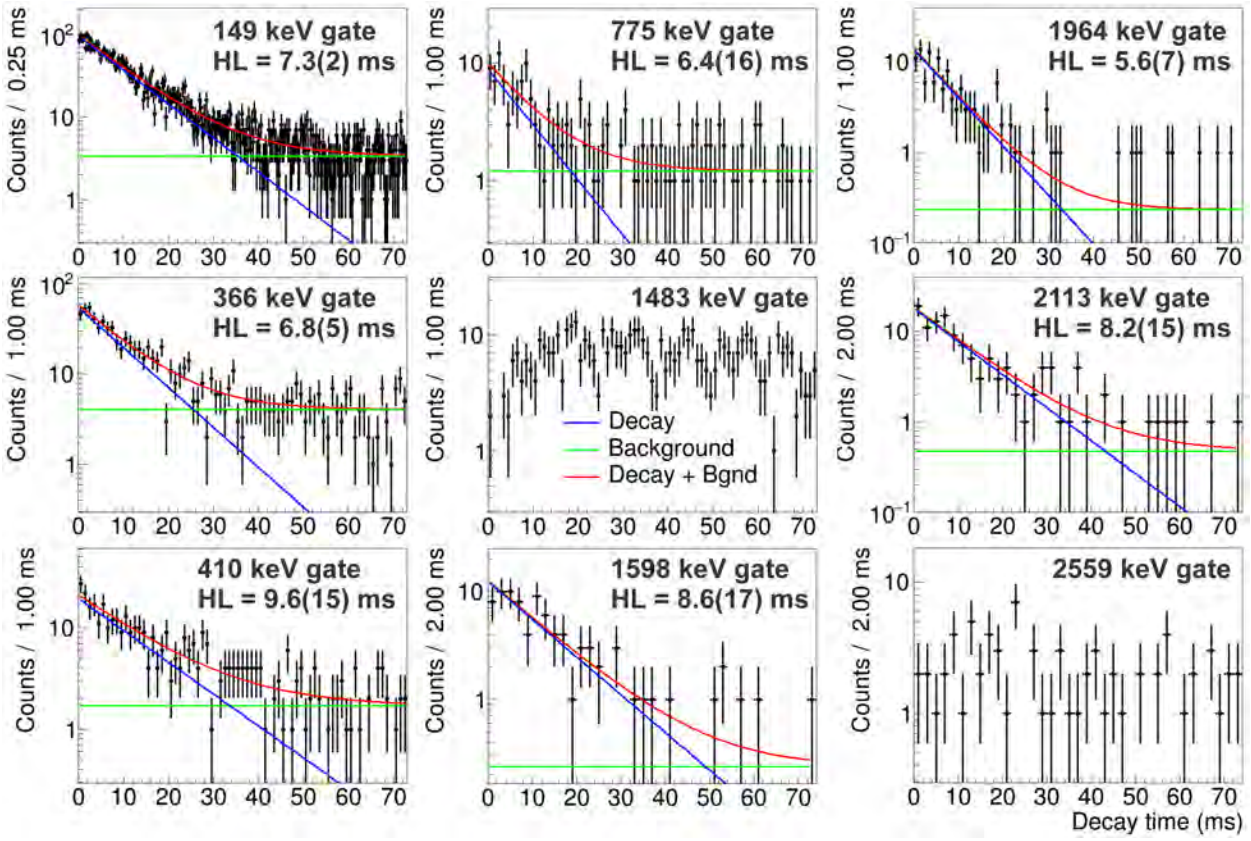

Figure 4.6 Decay time, gated on ^{30}Ne decays and shown for several different γ-ray gates. Peaks associated with the parent decay are overlaid with fit functions (red), where the exponential parent decay component is shown in blue and the constant background shown is in green.

is observed via the presence of very small amounts of ^{18}O and ^{20}O γ rays. It is noted that, compared to the unsubtracted spectrum, the sizes of these peaks are greatly reduced, affirming the present assignment of these peaks to randomly-correlated background. For the assigned grandchild γ rays, the relevant peak energies are given in Table 4.4, and they are sorted by the isotope to which the γ ray belongs.

Most of the descendant γ rays which are observed belong to the ^{30}Mg grandchild. Small amounts of the ^{29,28}Mg grandchild γ rays are observed. Notably, two medium-sized ^{30}Al 4th-generation γ ray peaks are visible, indicating the occurrence of 3rd-generation ^{30}Mg grandchild decays within this time window.

As was described in Section 2.1.1, the amounts of grandchild γ rays present can be used to determine exact values (rather than lower limits) for 1- and 2-neutron emission probabilities,

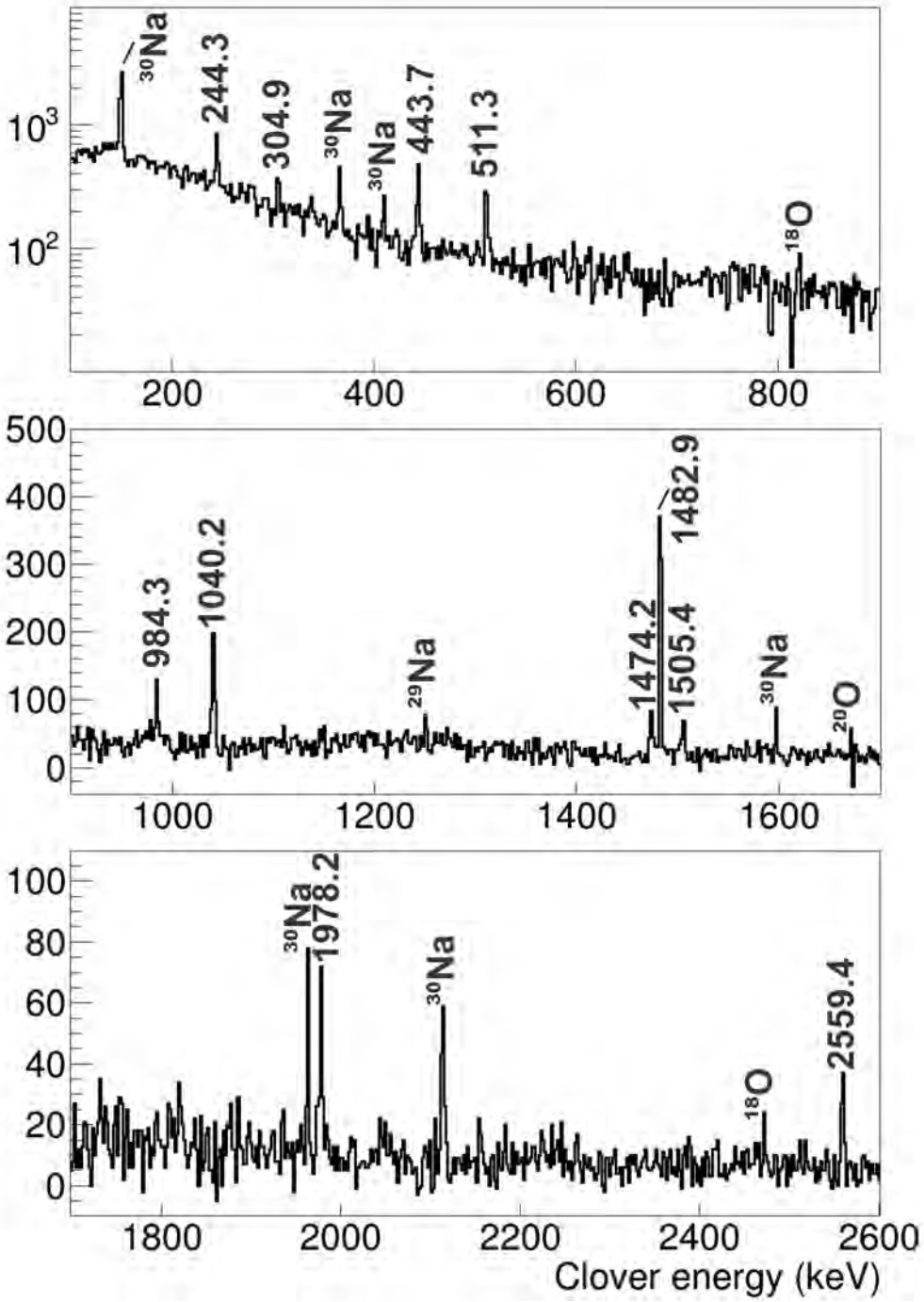

Figure 4.7 Background subtracted γ-ray spectrum in coincidence with identified ^{30}Ne β decays. A correlation window of 200 ms was used to optimize the observation of transitions in the grandchildren. γ rays produced following descendant decays are labeled with their energies in keV. γ rays produced following parent decays are labeled with the name of the isotope to which they belong, and several background lines are noted.

Isotope	E_γ (keV)		
	Present work	Prev.	Ref.
^{30}Mg	304.9(9)	305.3(2)	[94] (see [17, 28, 56, 98, 104])
	984.3(9)	985.0(2)	[94] (see [17, 28, 98, 104])
	1482.9(10)	1483.1(2)	[94] (see [17, 28, 98])
	1505.4(13)	1505.9(2)	[94] (see ([17, 98, 104])
	1978.2(12)	1978.2(2)	[94] (see [17, 28, 56, 98, 104])
^{29}Mg	1040.2(15)	1040.0(2)	[97] (see [103, 104])
	2559.4(15)	2560.2(4)	[103]
^{28}Mg	1474.2(14)	1473.5(1)	[116]
^{30}Al	244.3(10)	243.86(8)	[94] (see [28, 98, 117–119])
	443.7(11)	443.70(8)	[94] (see [28, 98, 117–119])

Table 4.4 γ-ray transition energies observed in Figure 4.7. The previous values shown for comparison are taken from ENSDF Adopted Values; where relevant, the individual measurements used to calculate a weighted average are cited as well. For a more complete history of these γ-ray measurements, see the following references: ^{30}Mg: [15–17, 28, 56, 98, 104–113]; ^{29}Mg: [30, 56, 98, 99, 103–105]; ^{28}Mg: [28, 98, 99, 103, 116, 120, 121]; ^{30}Al: [28, 98, 117–119, 122]

assuming the β-delayed γ-ray intensities are known. In order to achieve this, the ^{30}Ne decay curve was recreated with a 200 ms correlation window, the plot was fitted, and the parent component was integrated in order to determine the number of parent decays occurring within this increased 200 ms correlation window. The fitting procedure was identical to that described previously for Figure 4.1. The extracted N_β value is 192,544 ± 5,258 decays, with extracted fit parameters of $A_1(0) = 4488(19)$ counts/0.25 ms and $t_{1/2} = 7.43(3)$ ms. Within 1σ, there is no difference between this N_β value and the value measured with the 50 ms correlation window. This is reasonable, considering that both correlation windows are expected to capture the vast majority of parent decays, with negligible gains expected when increasing the correlation window to 200 ms.

In order to measure P_{1n}, the 2559 keV peak from ^{29}Mg was selected. According to Ref. [104], this γ ray is not populated substantially in ^{30}Na β_{1n} decay, making it a suitable candidate. After fitting the 2559 keV peak with a Gaussian plus constant background peak shape, an area of 67(16) was extracted. From the efficiency calibration discussed in Section 3.6, a γ-ray detection efficiency of 1.00(6)% is extracted. Finally, a branching ratio of 36(7) γ-ray counts / 100 ^{29}Na decays is taken from Ref. [103]. Combining these quantities results in a neutron emission probability for ^{30}Ne of $P_{1n} = 10(3)\%$. This is in good agreement with previous measurements: $9^{+17}_{-9}\%$ [2], 9(17)% [50],

and 12.6(35)% [3].

Unfortunately, the measurement of P_{2n} was not possible. While the ^{28}Mg 1474 keV peak is visible in the data, according to Ref. [103], the 1474 keV γ ray is substantially produced through the ^{29}Na β_{1n} branch. This would contaminate the measurement and could result in an overestimation of ^{30}Ne P_{2n}. The only γ ray which could be attributed uniquely to the ^{28}Na$\rightarrow^{28}$Mg decay path was observed in incredibly small amounts, so much so that its definitive identification was unreliable, and a converging fit of its shape was not possible.

4.2 β-decay of ^{32}Ne

The next decay studied in this analysis is the decay of the ^{32}Ne parent. This decay is not as well studied as the decay of ^{30}Ne; its half-life has been measured only twice (3.5(9) ms [49] and $4.5(4)_{\text{stat}}(6)_{\text{sys}}$ ms [51]), and the decay scheme of the ^{32}Na child has never been studied through β-delayed γ-ray spectroscopy. Moreover, what little is known about the ^{32}Na decay scheme leaves many questions unanswered (see Section 1.5).

As with the decay of ^{30}Ne, the temporal correlation window was chosen based on the parent and child half-lives. The chosen correlation window is 32 ms, approximately 7 times the parent half-life as measured in Ref. [51]. Over 99% of parent isotopes will have decayed in this time period. Compared to the case of ^{30}Ne, the child half-lives are a bit more disparate — 13.2(4) ms [52], 17.0(4) ms [123], and 45.4(11) ms [94] for ^{32,31,30}Na, respectively — so it is difficult to choose a correlation window that equally suppresses population of all child nuclei. Expected values of approximately 72%, 63%, and 32% of ^{32,31,30}Na children will have decayed in this time window. While a slightly smaller correlation window may have suppressed child activity a bit more, near-complete collection of parent activity is prioritized.

Figure 4.8 shows the decay curve of all identified ^{32}Ne β decays. It is fit with a sum of Bateman equations (Equations 2.5, 2.6, and 2.7). Three generations of β_{xn} decays were considered, but only the contributions expected to be populated in large amounts and with sufficiently short half-lives were included. The isotopes that are included in the fit are: ^{32}Ne, ^{32}Na, ^{31}Na, ^{30}Na, ^{32}Mg, ^{31}Mg, ^{30}Mg. Note that, with large P_{xn} values, certain grandchildren can often be populated through

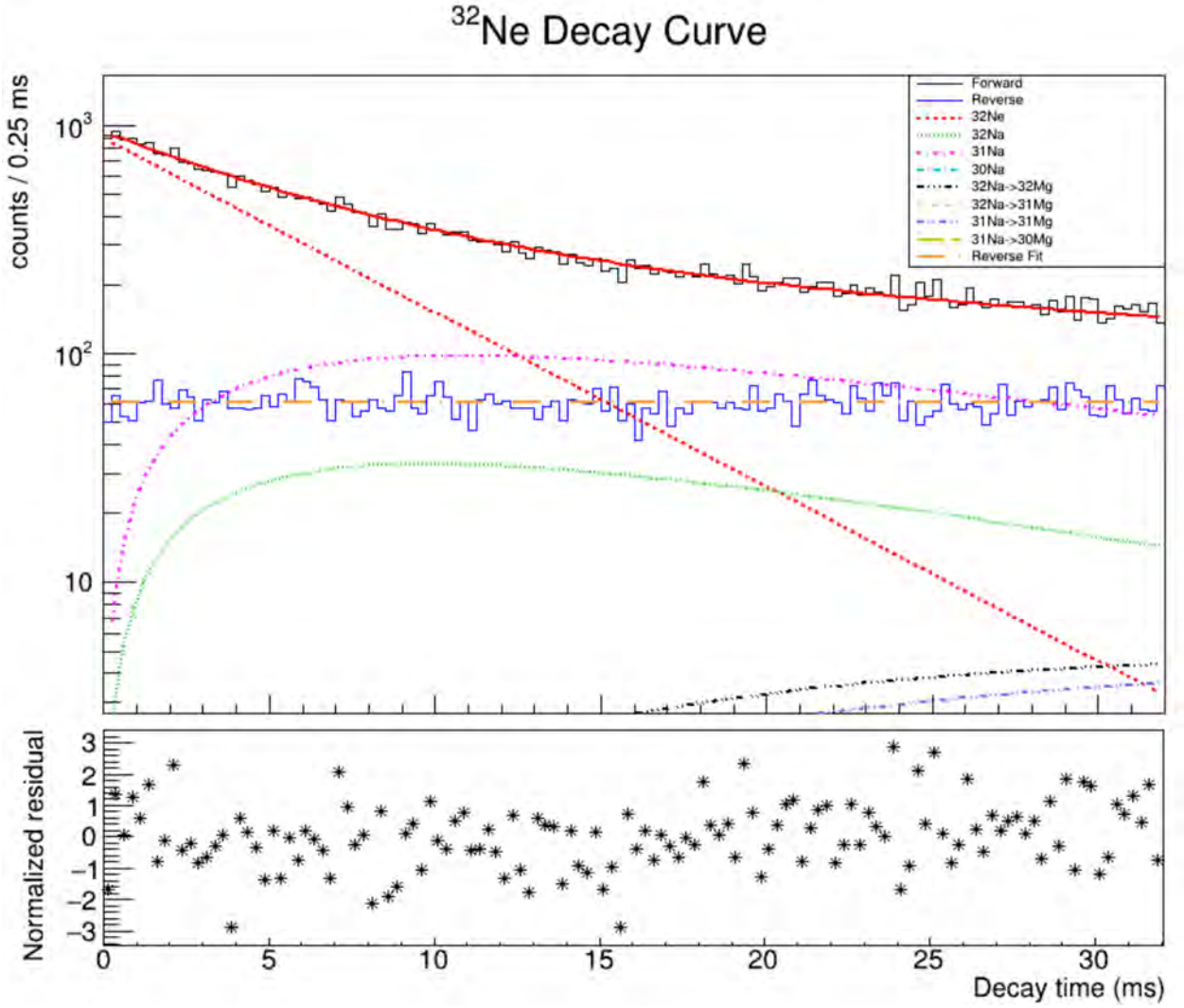

Figure 4.8 Decay time for all identified ^{32}Ne decays, fitted to a sum of Bateman equations. The black histogram represents the forward-correlated decay curve, and the blue histogram represents the reverse-correlated decay curve. The total fit is shown in solid red, the parent contribution is shown in dotted red, and the background fit is shown in dash-dot orange. The remaining fit contributions are descendant contributions which are labeled in the figure. Several components are out of frame, as their contributions to the fit are nominal. The bottom panel shows normalized residuals of the fit. See text for full description of fitting process.

multiple channels. In this case, two decay channels are included which lead to the decay of ^{31}Mg, one involving β decay of ^{31}Na and another involving β_{1n} decay of ^{32}Na.

The parent half-life and the initial parent activity are the only parameters varied in the fit. The constant background is fixed to the value given by the fit of the reverse-correlated decay curve, and the child and grandchild half lives, as well as all P_{xn} values, are fixed to literature values. Table

Contribution	Half-life	P_{1n} (%)	P_{2n} (%)
^{32}Ne	varied	75^{b} [124]	4^{b} [124]
^{32}Na	13.2(4) ms [52]	24(7) [56]	8.3(21)^{a} [56]
^{31}Na	17.0(4) ms [123]	39(5) [123]	0.7(1)^{a} [123]
^{30}Na	45.4(11) ms [94]	30(5) [96]	1.27(25)^{a} [96]
^{32}Mg	80.4(4) ms [125]		
^{31}Mg	270(2) ms [125]		
^{30}Mg	319(6) ms [94]		

Table 4.5 Decay data used to perform fit of the histogram in Figure 4.8. Grandchild P_{xn} values are not listed because future generations are not included in the fit. See the Appendix for a more detailed compilation of previous measurements of these values. ^{a}: Decay pathway neglected in fit. ^{b}: Calculated value.

4.5 shows the values which were adopted for the fit. P_{1n} and P_{2n} have never been measured for ^{32}Ne, so these values are fixed to calculated values given in Ref. [124]. In Section 4.2.2, P_{1n} and P_{2n} are calculated from the present data. For the purpose of examining systematic errors on the decay curve fit results caused by fixing P_{1n} and P_{2n} to calculated values, the present measurements of P_{1n} and P_{2n} are taken into account when choosing what range to vary the quantities within. Uncertainties due to the use of fit parameters fixed to literature values will also be discussed.

The resulting fit shown in Figure 4.8 gives a parent half-life of 3.95(5) ms and an initial parent activity of 875(11) counts / 0.25 ms, with a χ^2/NDF value of 1.2. As it was for the ^{30}Ne case (see Section 4.1), the error in the fit parameter is only inclusive of fitting errors, as the final value for the half-life will be taken from γ-gated decay curves. However, the rough agreement of this extracted half-life with previously measured half-lives (3.5(9) ms [49] and $4.5(4)_{\mathrm{stat}}(6)_{\mathrm{sys}}$ ms [51]) indicates that the fit is reliable.

Again, the most important quantity extracted from this fit is the integral of the parent component, which gives the number of parent β decays observed within the correlation window. The extracted value is $19{,}894 \pm 141_{\mathrm{stat}} \pm 343_{\mathrm{fit}} \pm 1{,}768_{\mathrm{sys}}$. Combining the errors in quadrature, this gives a final value of 19,894 ± 1,806 decays. The systematic error is more significant than it was for the ^{30}Ne fit due to the ^{32}Ne P_{xn} values being unknown and fixed to calculations. To calculate systematic errors, the P_{1n} value was varied to an upper limit of the calculated value plus 10% (relative) and to a lower limit of the presently measured value minus 1σ. This amounts to a massive range of 16%–82.5%,

thus resulting in a large systematic error from this source. The P_{2n} value was varied similarly; its lower limit was the calculated value minus 10% (relative), and its upper limit was the presently measured γ-ray intensity of the β_{2n}-delayed 149 keV γ ray plus 1σ. This corresponds to a range of 3.6%–18%, also resulting in a large systematic uncertainty. Finally, the systematic uncertainty due to the fixed constant background also contributed a comparable amount of uncertainty to the final measurement.

The correlation efficiency is extracted for ^{32}Ne, as $N_\beta/N_{\text{implants}}$. This value is 58(5)%. While the uncertainty is larger, this value is similar to the correlation efficiency of 55.2(18)% for ^{30}Ne.

4.2.1 γ-ray transitions in ^{32}Na

Again, a γ-ray spectrum is drawn for all identified ^{32}Ne β-decay events. It is drawn using both a forward correlation and a reverse correlation in Figure 4.9. The same timing condition is applied as was used in the ^{30}Ne case, such that only γ rays which appear promptly following the β decay are shown. The expected isomeric transitions will be investigated in a separate search with this condition removed.

Multiple newly observed transitions are present (marked with an asterisk), which have, in the present work, been assigned to ^{32}Na. These peak assignments will be discussed in the following text. Overall, moderate-sized peaks from both ^{32,31}Na as well as a small ^{30}Na peak are present in the spectrum, signaling significant P_{xn} branching ratios. These P_{xn} values will be discussed in detail in Section 4.2.2. Peaks from all three Mg grandchild isotopes are visible as well, although their population is slightly suppressed with the chosen correlation window.

The presence of a neutron-induced (n, n') peak, shown in Figure 4.9, also alludes to larger amounts of neutrons being emitted. The peak has a wide energy spread, consistent with neutron-induced interactions. Moreover, a similar structure near this energy is present throughout the dataset in different isotopic gates.

Compared to the ^{30}Ne β-delayed γ-ray spectrum (see Figure 4.2), there are no discernible randomly correlated background peaks. This is likely due to the roughly one order of magnitude difference in statistics between the two ion gates; as discussed in Section 3.2, there were 340,958

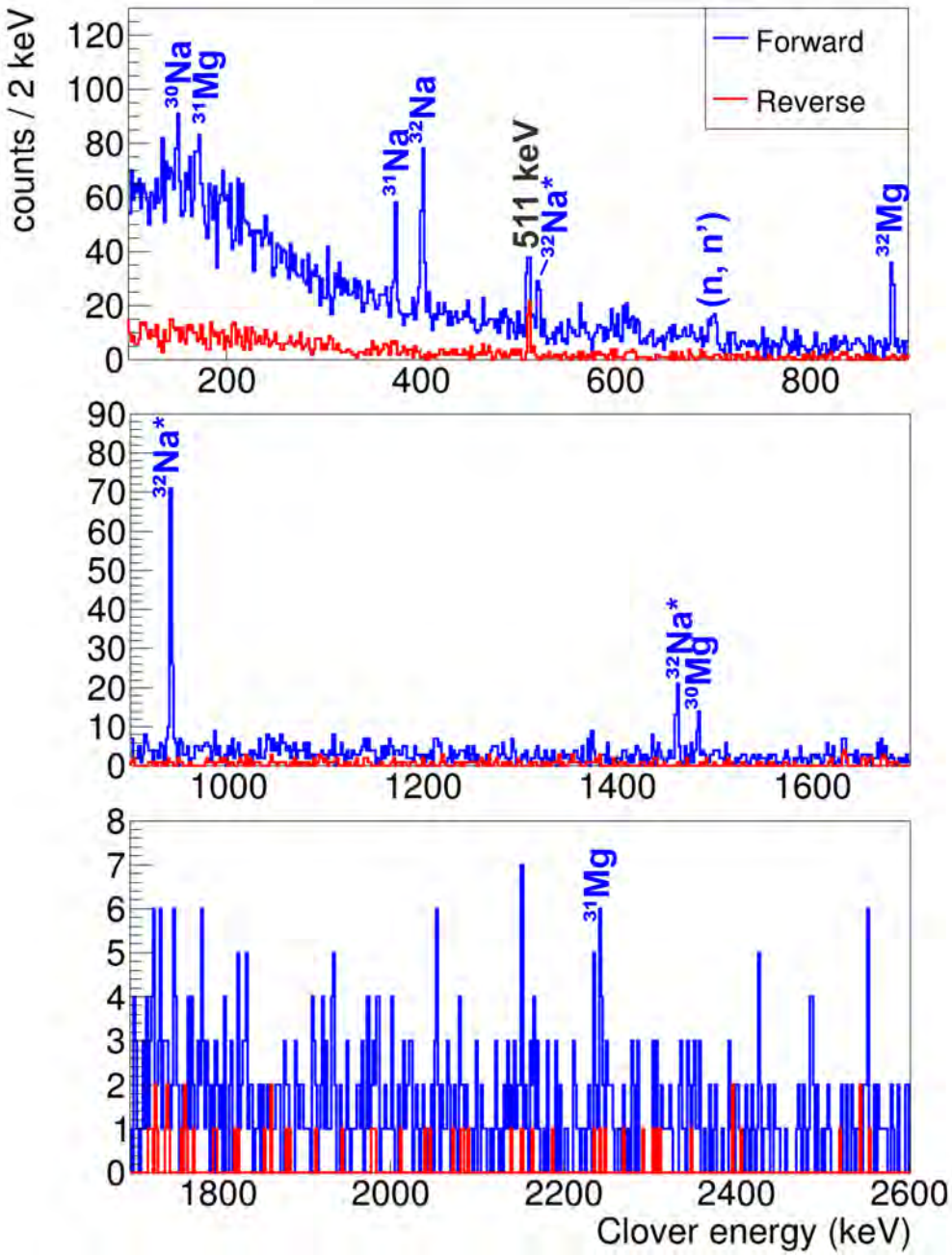

Figure 4.9 γ-ray spectrum in coincidence with identified ^{32}Ne β-decays. A correlation window of 32 ms was used to optimize the observation of transitions in the ^{32}Na child. Peaks are labeled with the name of the isotope to which the transition belongs. The forward correlation is shown in blue, and the reverse correlation is shown in red. Transitions newly observed in this work are marked with an asterisk (*).

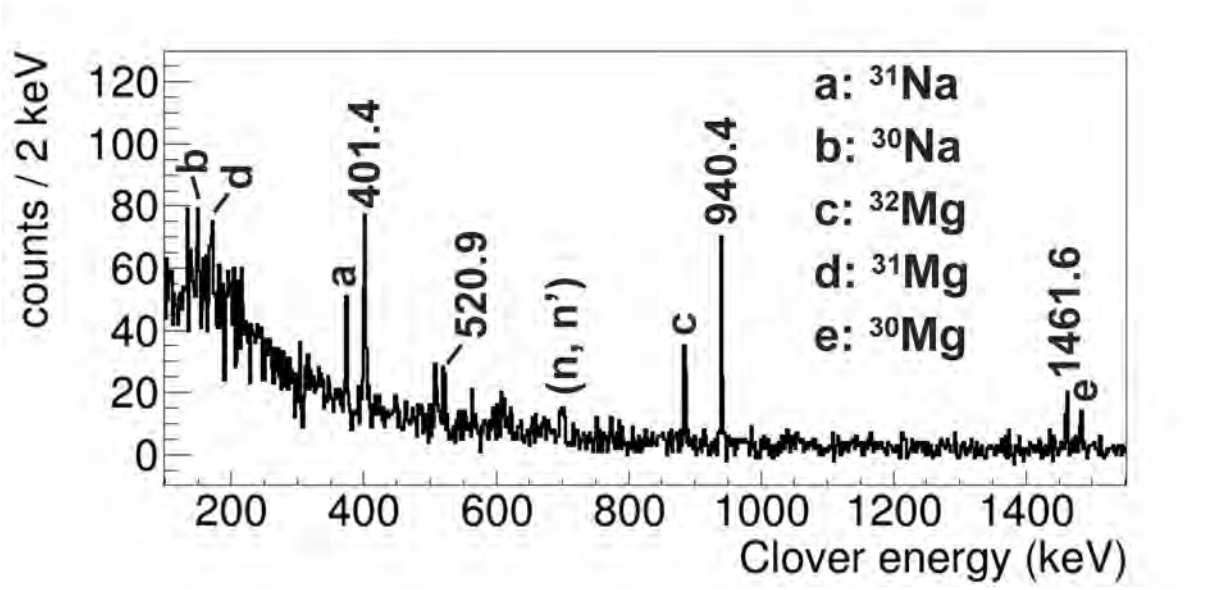

Figure 4.10 γ-ray spectrum in coincidence with identified ^{32}Ne β decays, with an ion–β correlation window of 32 ms. The spectrum is obtained by subtracting the reverse-correlated spectrum from the forward-correlated spectrum (see Figure 4.9). a: Transitions in the ^{31}Na child. b: Transitions in the ^{30}Na child. c: Transitions in the ^{32}Mg grandchild. d: Transitions in the ^{31}Mg grandchild. e: Transitions in the ^{30}Mg grandchild.

^{30}Ne implants compared to 34,547 ^{32}Ne implants. Nevertheless, a background subtraction is performed for the sake of consistency with the ^{30}Ne analysis. This background-subtracted γ-ray spectrum is shown in Figure 4.10.

As mentioned previously, there are three transitions present which, prior to this work, had never been observed: 520.9(8), 940.4(9), and 1461.6(11). The 940 keV peak is quite large, and the 521 keV peak is smaller but nevertheless evident. Of particular interest is the 1462 keV peak. Due to the proximity of the 1460 keV ^{40}K background peak, it is tempting to label this peak as background. However, in the ^{30}Ne analysis, no background 1460 keV peak is observed, primarily due to the application of the prompt γ-ray timing condition. As the 1460 keV background transition is randomly observed, the amount of the background γ ray present in the ^{30}Ne and ^{32}Ne gates should scale with the number of implanted ions. Again, as no 1460 keV background peak is observed in the ^{30}Ne gate, there is no reason that any 1460 keV background peak should be observed in the ^{32}Ne gate. No other environmental background peaks are observed with either ion gate, including the 1435 keV peak which, in ungated spectra, is observed at approximately the same rate as the

1460 keV background peak.

Keeping in mind the newly discovered millisecond isomeric state at 117.6(64) keV [6], energy summing relations immediately suggest the structure of the level scheme. 520.9(8) keV – 401.4(13) keV = 119.5(15) keV, approximately equal to and within 1σ of the energy of the isomeric state. This suggests a level at 520.9(8) keV which decays to the ground state by a γ ray of the same energy and to the 119.5(15) keV level by a 401.4(13) keV γ ray. Next, 520.9(8) + 940.4(9) = 1461.3(12), approximately equal to the energy of the γ ray at 1461.6(11) keV. This suggests a level at 1461.6(11) keV which decays to the ground state by a γ ray of the same energy and to the 520.9(8) keV state by a γ ray of 940.4(9) keV. Thus, from energy summing relations, all observed γ rays can be placed within a level scheme. This level scheme is shown in Figure 4.11.

It is important to investigate whether the deduced level scheme can be confirmed with γ–γ coincidences. However, noting the statistics of the ^{30}Ne coincidence plots given in Figure 4.4, and noting the order of magnitude difference in implantation statistics between ^{30}Ne and ^{32}Ne, it is unlikely that much can be extracted from these coincidence plots. Nevertheless, γ–γ coincidence plots are drawn for several different γ-ray gates and shown in Figure 4.12. In order to enhance statistics and thus enhance likelihood of observing a γ–γ coincidence peak, the spatial correlation window is extended to three pixels for γ–γ coincidence analysis only.

As expected, no strong γ–γ coincidences exist within the ^{32}Ne ion gate. Several smaller peaks that moderately stand out against background are labeled in Figure 4.12. Most of these peaks are not observed in Figure 4.3 and are quite small, so they cannot be definitively labeled as coincident γ-ray transitions. They are noted here but neglected for the rest of the analysis. A small (3 count) coincidence relationship is observed between the 401 keV and 940 keV γ rays, as would be expected based on the level scheme suggested by energy summing relations. Equation 4.3 gives the expected number of coincidence counts observed for a given cascade, based on the area of the higher-lying γ-ray peak in the singles spectrum, the efficiency of the lower lying transition, and the branching ratio for the intermediate state to emit the lower-lying γ ray (denoted as BR_{low}). Based on this calculation, in this dataset, one would expect to see 2.0(10) coincidence counts between the 401

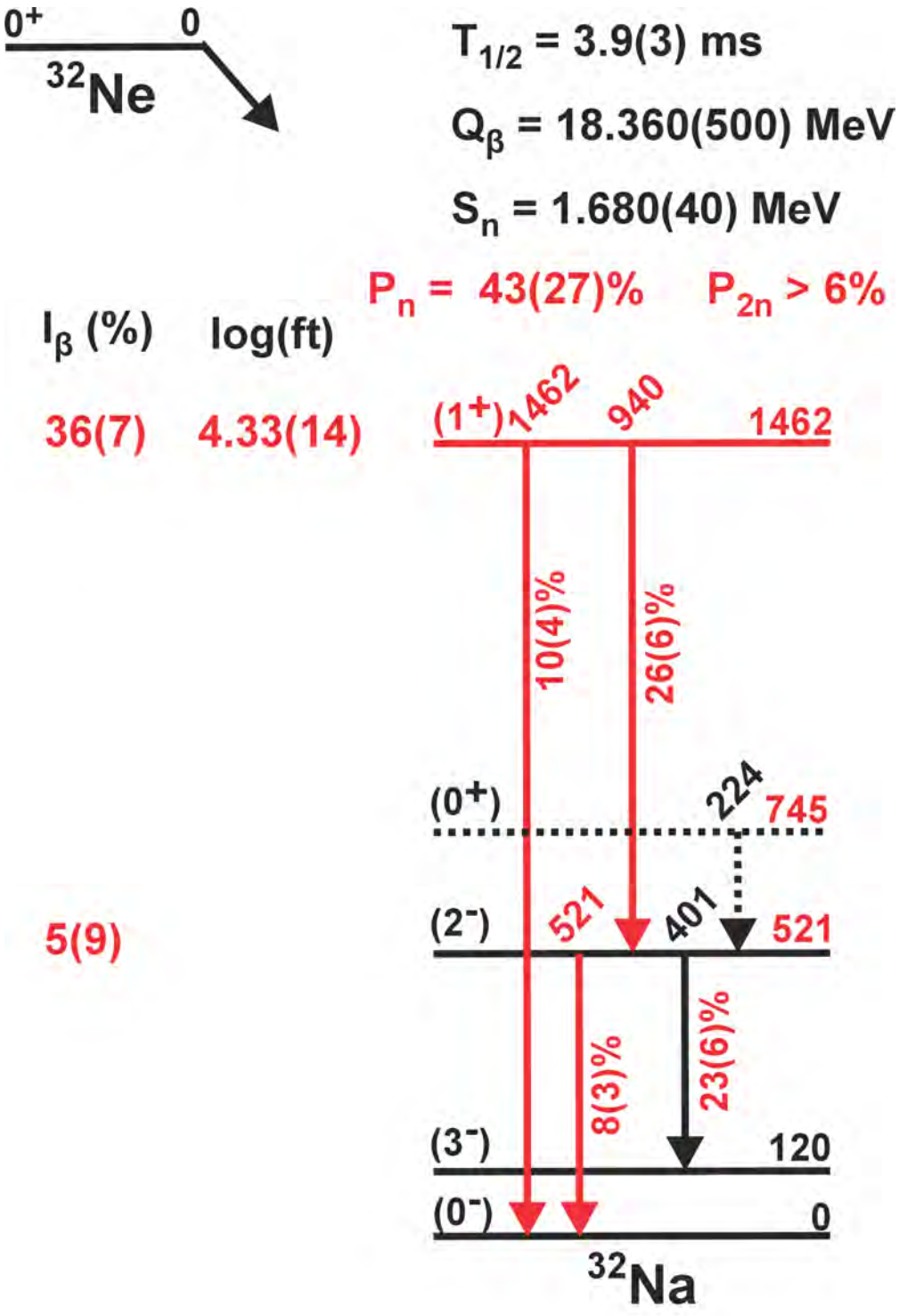

Figure 4.11 Level scheme of ^{32}Na inferred from the present work. Text and lines noted in red are newly measured or calculated in this work. See full text for discussion of calculations cited in this diagram. Q_β and S_n from [53].

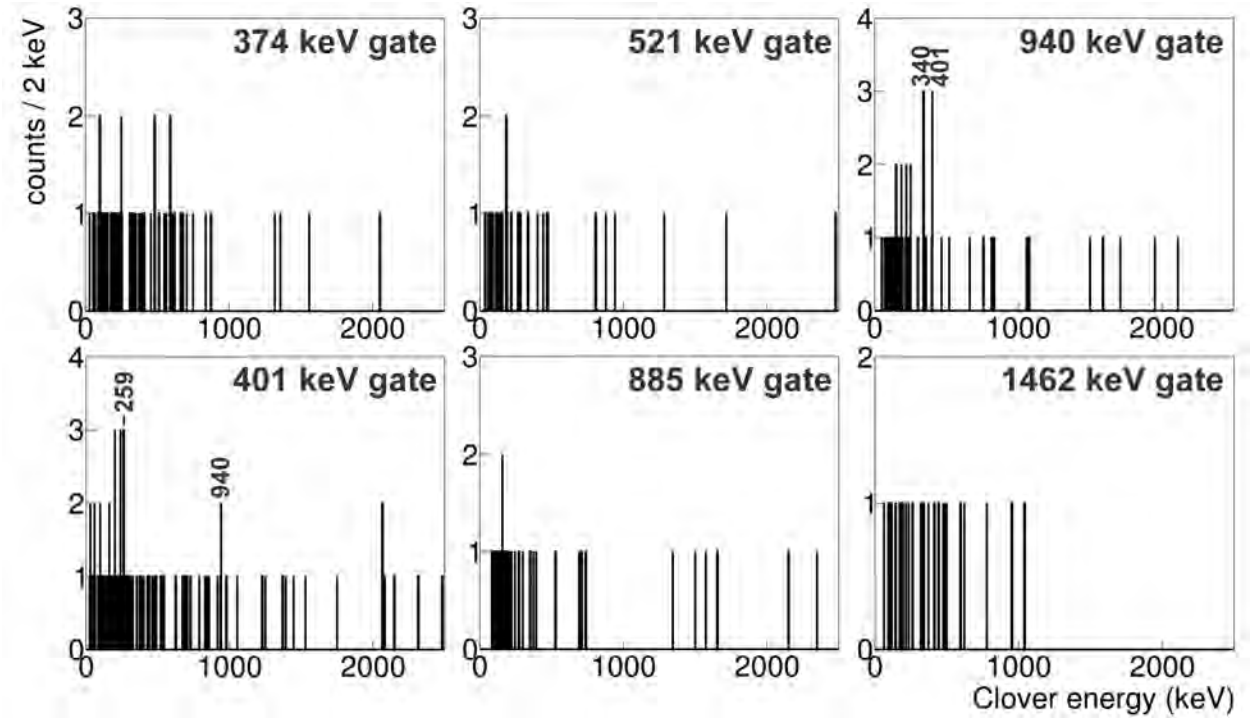

Figure 4.12 γ-ray spectrum in coincidence with identified ^{32}Ne β-decays, shown for several different γ-ray coincidence gates.

keV and 940 keV γ rays. While a larger, more definitive coincidence peak would be ideal to affirm the placements of these transitions within the level scheme, the calculations show that the observed small size of the coincidence peak is not inconsistent with the current placements.

$$N_{\text{coinc}} = [\text{Area}]_{\text{high}} \times \varepsilon_{\text{low}} \times \text{BR}_{\text{low}} \tag{4.3}$$

The energy centroids of the γ-ray transition peaks observed in Figure 4.10 are given in Table 4.6, along with the absolute intensities of these γ rays as a percentage of the number of observed parent decays. Table 4.7 gives the deduced excitation energies of the states shown in Figure 4.11, along with their associated β-decay feeding percentages and log(ft) values (calculated using LogFT [58]). The β-decay feeding into the 521 keV state is consistent with zero, indicating that only one state in the ^{32}Na child experiences significant direct feeding. No ground state feeding is assumed, given that the parity change between the ^{32}Ne ground state and the ^{32}Na ground state would require a forbidden transition. Note that several suggestions for the spin-parity of the ^{32}Na ground state

Isotope	E_γ (keV)			I_γ (%)
	Present work	Prev.	Ref.	
^{32}Na	401.4(13)	401	[5]	23(6)
	520.9(8)			8(3)
	940.4(9)			26(6)
	1461.6(11)			10(4)
^{31}Na	373.5(7)	375.1(7)	[42] (see [41, 54, 126])	8(3)
^{30}Na	149.6(13)	150.6(2)	[2] (see [3, 47])	12(6)

Table 4.6 Child γ-ray transition energies observed in Figure 4.10 along with their intensities as a percentage of the number of observed parent decays.

E_x (keV)	I_β (%)	log(ft)
119.5(15)		
520.9(8)	5(9)	
1461.6(11)	36(7)	4.33(14)

Table 4.7 Excitation energies of inferred states in ^{32}Na, along with their β-decay feeding intensities and calculated log(ft) values.

have been made (3^- or 4^- from Ref. [56]; 0^-, 3^-, or 4^- from Ref. [55]; and 0^- or 3^- from Ref. [5]), but none of these suggested spin-parity assignments would lead to population of the ^{32}Na ground state in allowed β decay. Furthermore, no de-excitations of the millisecond isomeric state were observed (see Section 4.3.2), so calculation of the feeding into this state was impossible. No feeding was assumed to the millisecond isomer, again based on spin-parity mismatch with the ^{32}Ne 0^+ ground state. The present assignments of the ^{32}Na ground state to (0^-) and millisecond isomeric state to (3^-) will be discussed in Section 5.1.

Again, by drawing Figure 4.8 with an additional applied γ-ray gate, a measurement of the ^{32}Ne half-life that is subject to less systematic error can be achieved. The correlation window is increased to 45 ms for increased fitting accuracy. γ-gated decay curves are shown in Figure 4.13 for several different γ-ray gates. For the γ rays associated with parent decays, exponential plus constant background fits are superimposed over the decay curve. Two decay curves gated on γ rays associated with child decays are shown for the sake of comparison: 885 keV (^{32}Mg) and 1483 keV (^{30}Mg). The adopted value from this work is 3.9(3) ms, calculated as the average values of the half-lives deduced from the high-statistics 940 keV and 401 keV γ-ray gates. The adopted value of

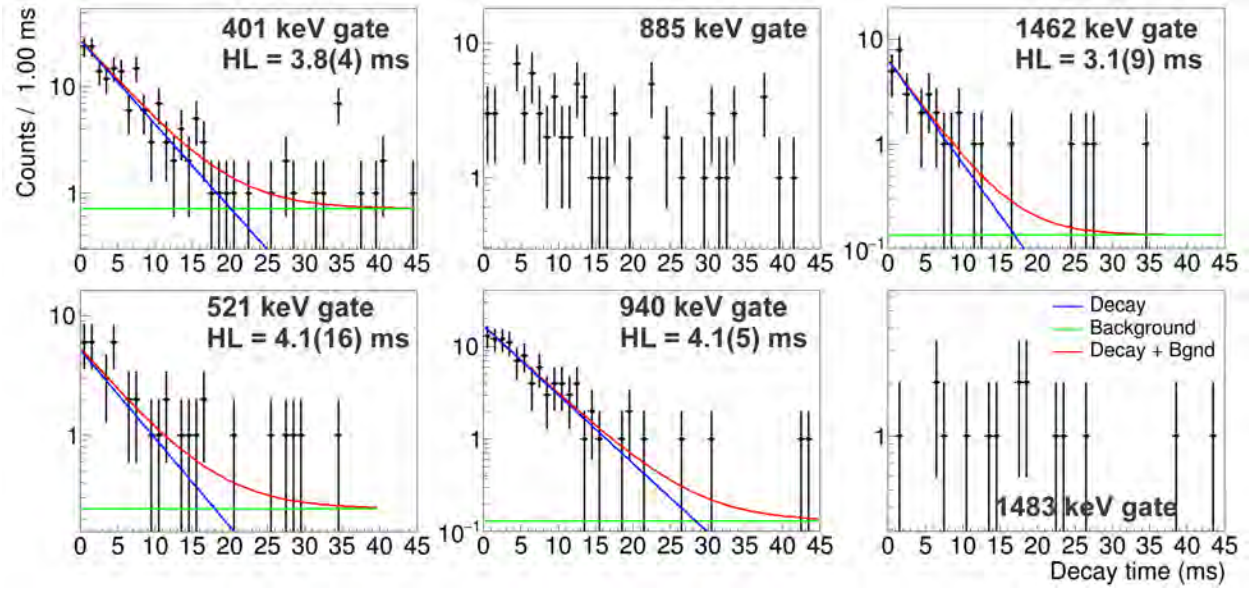

Figure 4.13 Decay time, gated on ^{32}Ne decays and shown for several different γ-ray gates. Peaks associated with the parent decay are overlaid with fit functions (red), where the exponential parent decay component is shown in blue and the constant background is shown in green.

3.9(3) ms shows great agreement with previous measurements of 3.5(9) ms [49] and $4.5(4)_{\text{stat}}(6)_{\text{sys}}$ ms [51].

4.2.2 Descendant decays and delayed neutron emission

In order to examine the presence of β-delayed γ rays associated with child decays, the temporal correlation window was increased to 80 ms. In this time window, over 99.9% of parent decays would be observed, and 93-97% of ^{32,31}Na child decays would be observed. The ^{30}Na child half-life (45.4(11) ms [94], see Appendix) is much longer compared to the ^{32,31}Na child half-lives (13.2(4) ms [52] and 17.0(4) [123], respectively; see Appendix), and only about 65% of ^{30}Na decays would be captured in this window. A longer correlation window — 170 ms, perhaps — may be more suitable for the measurement of the ^{30}Na child decays. However, upon inspection, the gains in ^{30}Mg γ ray counts with this longer correlation window were not worth the excess background accumulated around less intense peaks, such as the 2244 keV peak from ^{31}Mg which will be used to constrain ^{32}Ne P_{1n}. In addition, no visible peak from ^{30}Mg could be identified that could be traced uniquely to the ^{32}Ne$\rightarrow^{30}$Na$\rightarrow^{30}$Mg decay path, even with a longer correlation window. All visible ^{30}Mg γ rays could be attributed substantially to either ^{32}Ne$\rightarrow^{31}$Na$\rightarrow^{30}$Mg or ^{32}Ne$\rightarrow^{32}$Na$\rightarrow^{30}$Mg

Isotope	E_γ (keV)		
	Present work	Prev.	Ref.
^{32}Mg	885.0(11)	885.30(10)	[52] (see [106, 110, 127–130])
	1782.5(7)	1782.7(9)	[52] (see [98, 111])
	2151.6(5)	2152.4(1)	[127]
	2551.4(4)	2550.8(5)	[52] (see [110, 127])
^{31}Mg	171.2(11)	171.1(1)	[123] (see [42, 98, 110, 111, 127, 131])
	2243.5(10)	2243.6(1)	[131]
^{30}Mg	1483.3(9)	1483.1(2)	[94] (see [17, 28, 98])
^{30}Al	244.4(10)	243.86(8)	[94] (see [28, 98, 117–119])

Table 4.8 Grandchild γ-ray transition energies observed in Figure 4.14. For more details on previous spectroscopic studies of these isotopes, see the following references: ^{32}Mg: [20, 42, 56, 98, 107, 110, 111, 127–130, 132–137]; ^{31}Mg: [30, 42, 56, 98, 109–111, 127, 131, 138–140]; ^{30}Mg: [15–17, 28, 56, 98, 104–113]; ^{30}Al: [28, 98, 117–119, 122].

decay paths, making a clean, exact measurement of the ^{32}Ne P_{2n} value impossible. Therefore, clean measurement of the ^{31}Mg grandchild γ rays are prioritized, and the correlation window is set to optimize detection of those.

The γ-ray energy centroids observed in Figure 4.14 are listed in Table 4.8, compared to previously-measured energies of these transitions. Most of these grandchild γ-ray transition peaks are quite small. The 885 keV transition from ^{32}Mg and the 1483 keV transition from ^{30}Mg are the largest observed γ-ray transition peaks from the grandchildren. It is noted here that three small peaks could not be identified, at energies of 102.8(7) keV, 1374.3(6) keV, and 2426.3(9) keV. These peaks, to some degree, are visible in the spectrum drawn with a 32 ms correlation window, but are more apparent with the extended correlation window. While these peaks are intriguing, their sizes are quite small, so there is not much useful information that can be extracted beyond their energies. Summing relationships do not suggest placements for these transitions.

There are two candidate peaks from ^{31}Mg which can be used to calculate ^{32}Ne P_{1n}: 171 keV and 2244 keV. Both are quite small. While the 171 keV peak may appear slightly larger, according to Refs. [56, 98, 110, 111], this 171 keV γ ray is produced substantially through the ^{32}Na β_{1n} process. This would contaminate the ^{32}Ne P_{1n} measurement. The 2244 keV γ ray, on the other hand, is not reported to be produced in ^{32}Na β_{1n} decay by any of Refs. [56, 98, 110, 111], making

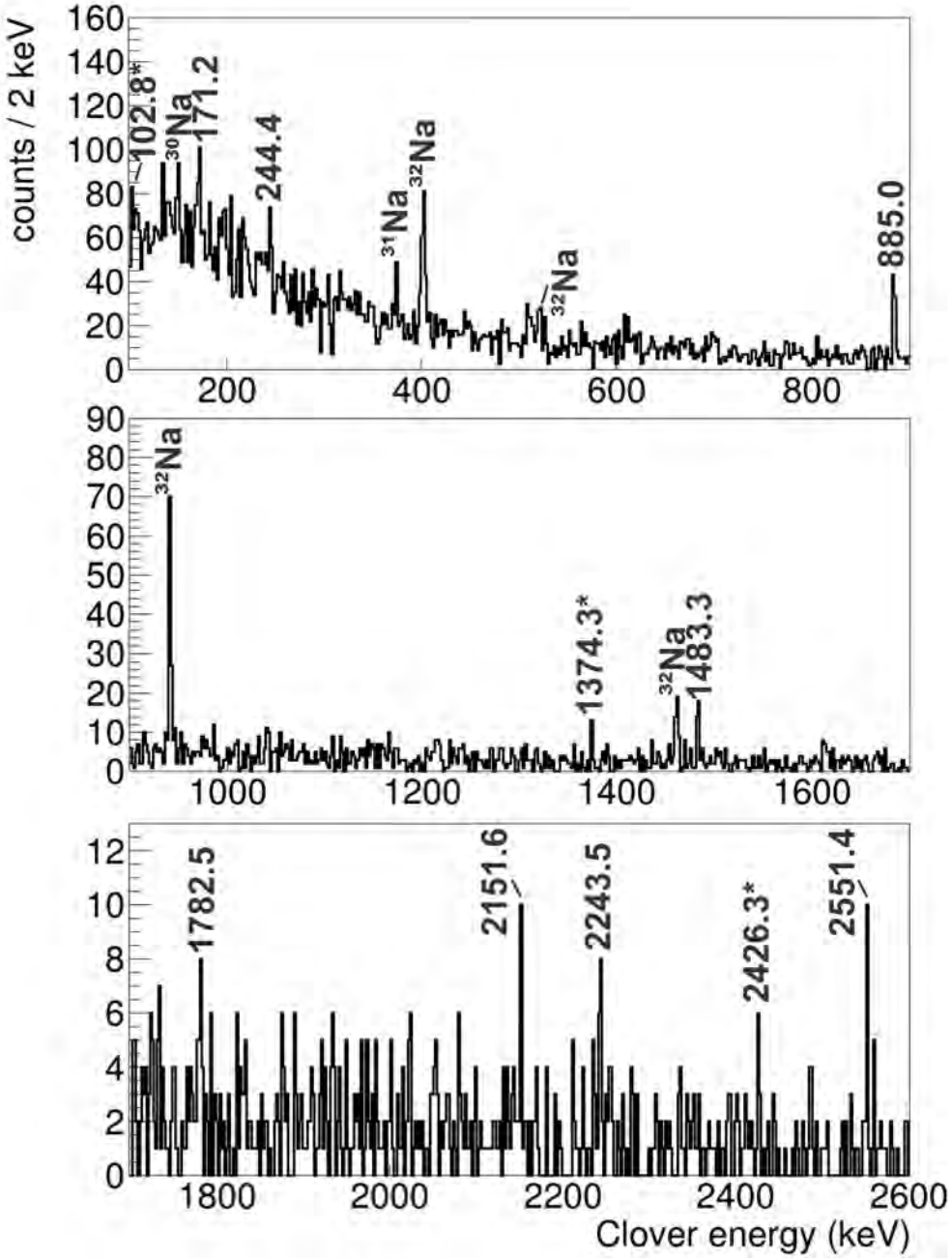

Figure 4.14 Background subtracted γ-ray spectrum in coincidence with identified ^{32}Ne β-decays. A correlation window of 80 ms was used to optimize the observation of transitions in the ^{32,31}Mg grandchildren. Grandchild γ-rays are labeled with their energy in keV, and child γ rays are labeled by the name of the isotope to which the transition belongs. Three γ rays are marked with asterisks (*), indicating that the isotope to which these transitions belong could not be identified.

it a good candidate for this measurement. The area of this peak is 12(7) counts, with the error coming from the quadrature sum of a statistical error and an error from the peak fitting routine. This results in over 50% error on the peak size.

The decay curve shown in Figure 4.8 was recreated with an 80 ms correlation window in order to determine the number of parent decays observed within this extended correlation window, the determined result being $N_\beta = 20,400 \pm 2,130$. To calculate P_{1n}, the efficiency of γ-ray detection at 2244 keV was determined to be 1.11(6)%. Finally, the absolute intensity of production of this γ ray following ^{31}Na β decay is 12.2(19)% [123] (see [56, 98, 131]). This results in a P_{1n} value of 43(27)%, with the largest source of error being the small size of the 2244 keV peak itself.

According to information from Refs. [17, 28, 56, 98, 104, 109–111], no γ ray present in Figure 4.14 could be attributed solely to ^{30}Na β decay without substantial contamination from ^{31}Na β_{1n} decay or ^{32}Na β_{2n} decay. Therefore, it is not possible to calculate an exact value for ^{32}Ne P_{2n}. However, it is noted that, in Figure 4.10, the ^{30}Na 149 keV γ ray is present, unambiguously indicating the occurrence of ^{32}Ne β_{2n} decay. The size of this peak can be used to place a lower limit on the ^{32}Ne P_{2n} value. This value can be considered only a lower limit as it considers only the β_{2n} feeding into the 149 keV state, neglecting both feeding into the ground state of ^{30}Na as well as any potential unobserved feeding into higher-lying states that do not eventually decay to the 149 keV state. There is no way to correct for this by the inclusion of a branching ratio, as it is not known how often the 149 keV γ ray is produced compared to the total number of ^{32}Ne β_{2n} decays only.

The intensity of production of the 149 keV γ ray following ^{32}Ne β decay is 12(6)%, as given in Table 4.6. Taking the lower limit of the error into account, the lower limit for P_{2n} is thus taken to be $P_{2n} > 6\%$. Considering that $P_{1n} = 43(27)\%$ and $I_\beta(1462\text{ keV}) = 36(7)\%$, the majority of β decay feeding seems to be accounted for, albeit with large error bars and allowing for some amount of unobserved feeding through the β_{2n} branch.

4.3 Search for isomeric decays in ^{32}Na

As discussed in Section 1.5, there have been two isomers recently discovered in the ^{32}Na level scheme [5, 6]. It is unclear whether these isomers should be directly populated in β decay of

^{32}Ne. Of course, based on the level scheme in Figure 4.11, the 119.5(15) keV isomer appears to be indirectly populated following the γ decay of higher lying states populated in β decay. Based on the expected long ($\gtrapprox$ ms) half-life of this state, it is unlikely that a γ ray depopulating this state would have been observed in Figure 4.10, as this plot requires that an observed γ ray is observed promptly following a ^{32}Ne β-decay signal. Thus, as is observed, no γ ray depopulating this state should be recorded in Figure 4.10, whether the state is directly fed through β decay or only indirectly fed through γ-ray cascades.

It is also unclear whether the 745 keV isomer should be directly populated in β decay of ^{32}Ne. As it stands, the 224 keV isomeric transition was not observed in Figure 4.10. This is not unexpected; a timing condition was applied to this plot such that only γ decays which occur promptly following the β decay are plotted. With a half-life of 24(2) μs [5], the majority of counts of this γ ray would be measured outside of the prompt peak, were the isomer populated following ^{32}Ne β decay. It is important to determine whether any evidence of this γ-ray transition following ^{32}Ne β decay can be seen in the data. As was discussed in Section 1.5, the spin and parity of this isomer is expected to be either 0^+ or 6^-. If the 0^+ spin-parity assignment is correct, there is a chance this isomer could be populated either directly or through γ-ray cascades following β decay of ^{32}Ne, as the initial spin-parity of the ^{32}Ne ground state is 0^+. On the other hand, it is unlikely that a 6^- isomeric state would be accessible following the parent decay, either directly or indirectly, due to its high spin. Therefore, observation or non-observation of this 224 keV γ ray may favor one spin-parity scenario over the other.

In order to search for the isomeric decays, a correlation procedure was designed as discussed in Section 3.4. The temporal ion–β correlation window was reduced to 14 ms, while the spatial ion–β correlation window was held at 2 pixels. The reduction in the temporal correlation window should not decrease the number of properly correlated parent decays by a lot; about 91% of ^{32}Ne decays should be captured within the reduced temporal correlation window. Overall, this reduction reduces background while retaining a fairly high level of statistics. This background reduction is important for this measurement in particular. As the β–γ correlation window is increased, this allows for a

higher level of background in the γ spectra. The isomeric decay signals in DEGAi are expected to be small (on the order of 50 counts in a spectrum with no γ-ray gate). For the microsecond isomer, the impact of the expanded β–γ correlation window on the background will likely be small, as the β–γ correlation window is not increased by a large amount. For the millisecond isomer, the β–γ correlation window will be increased by 3 orders of magnitude, allowing for a much more substantial accumulation of background. While the reduction in the ion–β correlation window will not reduce all sources of background, it will reduce the one source of background which can be easily controlled.

4.3.1 745 keV isomer

To search for the 224 keV isomeric transition, the β–γ correlation window was increased to 72 μs, approximately three times the half-life of the 745 keV isomer. The choice to increase the β–γ correlation window up to only three half-lives was made in order to keep background as low as possible. As the majority of these γ-ray counts should be delayed, an off-prompt gate was applied to reduce contributions from the prompt distribution, giving a greater chance of a 224 keV γ-ray peak on the order of 80 counts standing out against background. Figure 4.15 shows the resulting γ-ray spectrum. The approximate location of the 224 keV bin is noted in this spectrum. No peak appears here in the spectrum.

It is important to note that there is some ambiguity regarding how many counts of the 224 keV γ ray would be expected in this spectrum, as the I_β(745 keV) value is unknown. Assuming I_β(745 keV) = 15%, the resulting 224 keV peak is expected to be approximately 86 counts. 15% is chosen as this is the maximum amount of β-decay feeding unobserved, assuming P_{2n} is exactly 6% and there is no feeding to any other states except the 1462 keV state and the 745 keV state. An 86 count peak would be clearly visible in Figure 4.15. Even assuming I_β(745 keV) = 5% would result in a peak of approximately 29 counts, which would likely be discernible in Figure 4.15. The discussion remains approximate, and no firm upper limit for I_β(745 keV) is deduced. However, it is clear from this plot that any direct β-decay feeding into the 745 keV state is quite small. Moreover, no prompt 717 keV γ ray connecting the 1462 keV and 745 keV states is observed

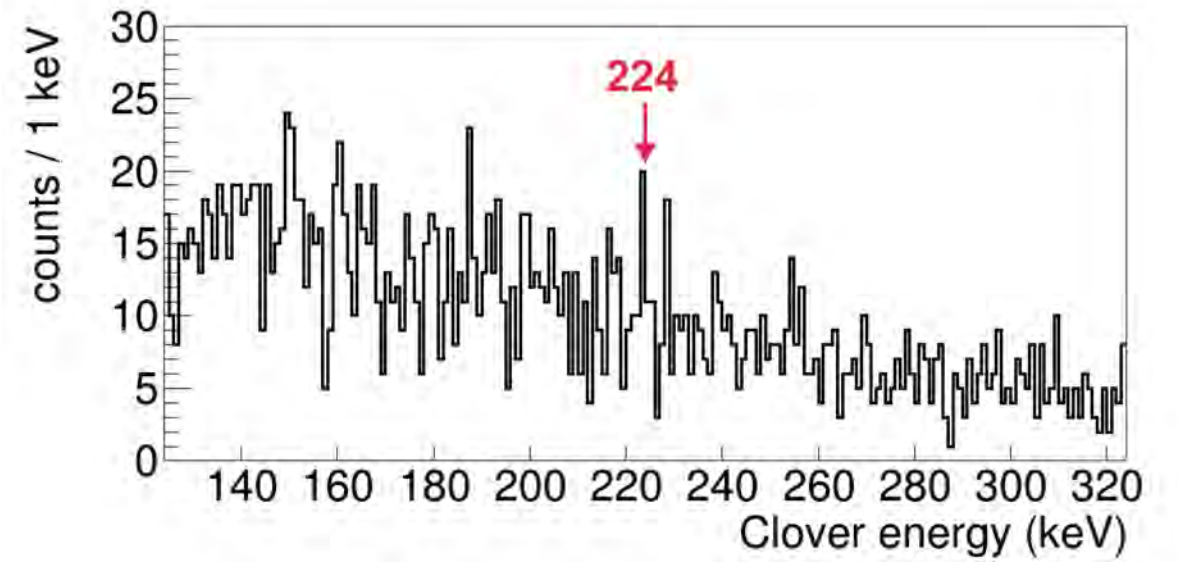

Figure 4.15 Spectrum of γ rays recorded within 72 μs of an identified ^{32}Ne β decay. Prompt γ rays are excluded. A 14 ms ion-β correlation window was chosen to reduce randomly correlated background. The approximate location of the 224 keV bin is noted to guide the eye.

in Figure 4.10, indicating that the isomer is not populated indirectly through a γ decay from the observed higher-lying state. The implications of this non-observation will be discussed in Chapter 5.

4.3.2 120 keV isomer

In order to search for a γ-ray decay from the 119.5(15) keV isomer, the β–γ correlation window is increased. It is important to note that the half-life of the 120 keV isomer is unknown; all that is known is that it is expected to be at least, approximately, a few milliseconds [6]. Therefore, three β–γ correlation windows will be tested: 10 ms, 25 ms, and 40 ms. This will account for three half-lives of 3.3 ms, 8.3 ms, and 13.3 ms. Figure 4.16 shows the result of this search. Unaccompanied Clover events are correlated to identified ^{32}Ne β-decay events, with an ion–β correlation window of 14 ms and a β–γ correlation window of 10 ms, 25 ms, and 40 ms. The spatial ion–β correlation window remains at 2 pixels. γ rays promptly following the β decay are excluded. Additionally, the panels on the right require that the β decay be followed by a prompt 401 keV γ ray, as the level scheme in Figure 4.11 suggests.

For the panels on the left in Figure 4.16, where no 401 keV γ-ray gate is applied, the expected

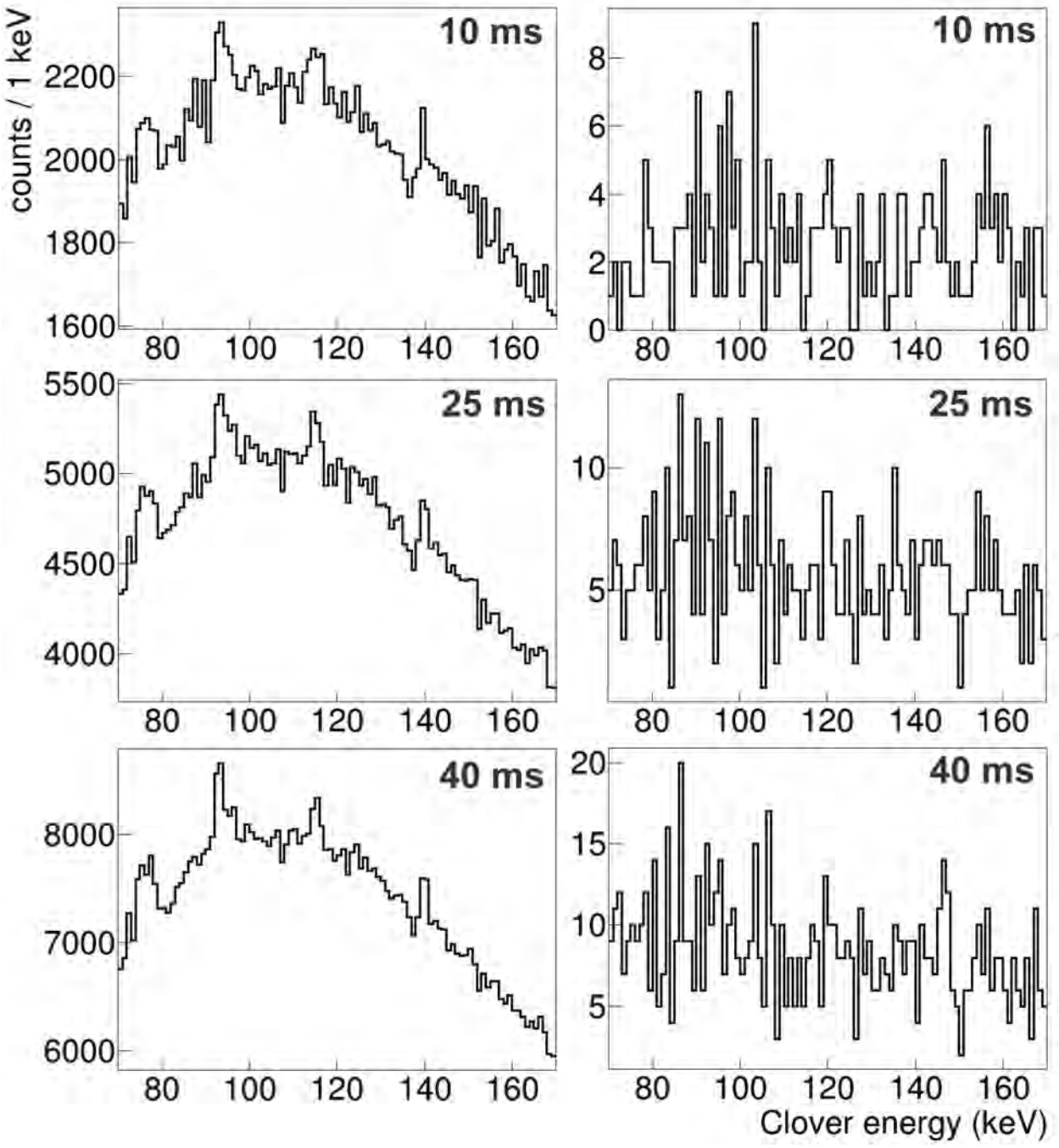

Figure 4.16 Spectrum of γ rays recorded within 10 ms, 25 ms, and 40 ms of an identified ^{32}Ne β decay. Prompt γ rays are excluded. A 14 ms ion-β correlation window was chosen to reduce randomly correlated background. The panels on the right contain an additional condition that the identified β decay be promptly followed by a 401 keV γ ray.

peak size of the 120 keV γ-ray peak would be on the order of 50 counts, based on the number of observed β decays, the γ-ray detection efficiency at 120 keV, and the observed γ-ray intensity feeding into this state. In this estimation, it is assumed that the isomer always decays via γ-ray emission, that there is no direct β-decay feeding into the isomer, and that the β–γ correlation window is sufficiently long to capture all isomeric decays. No peak corresponding to a 120 keV γ ray is observed. Based on the scale of the y-axis of these three plots, it is unlikely that a signal on the order of 50 counts would stand out against background. Note that there is a 115 keV background γ-ray peak directly to the left of where the 120 keV peak would appear, produced following the β decay of ^{18}C [80], which is present in the beam. For comparison, the area of this background peak in the 25 ms spectrum is roughly 300 counts.

In the panels on the right in Figure 4.16, where the 401 keV γ-ray gate is applied, no γ-ray peak at 120 keV is observed. Making the same assumptions as in the previous estimation, based on the number of 401 keV γ rays observed and the γ-ray detection efficiency at 120 keV, only roughly 1–2 counts of the 120 keV γ ray are expected to be observed in these plots. Again, it is unlikely that a signal of this size would stand out against the background.

Notably, any 120 keV photon produced within the YSO scintillator would likely be attenuated quite substantially by the scintillator itself. For a 120 keV photon traveling through 6 mm of YSO, only approximately 33% of photons are expected to be transmitted, with the remainder being absorbed by the YSO, based on γ-ray attenuation calculations completed using the NIST XCOM database [72]. Thus, it is possible that a signal of a 120 keV γ ray was recorded in the YSO, rather than in DEGAi. Its low energy would trigger the high-gain channel of the PSPMT.

The correlation method used to identify a β-delayed γ ray absorbed in the scintillator is slightly different, as the γ-ray signal in the scintillator will be labeled in the correlation code as a β decay. Therefore, one must search for a decay event which is preceded by another decay event, both which are correlated to the same implantation. The high-gain PSPMT dynode spectrum will be plotted for these "second" decay events. In the case where three or more decay events are correlated to the same implant, the second, third, fourth, etc. decay events will all be added to the plot. The search

is carried out as described above; a second search is carried out in which the plotted events consist of all correlated "β-decay-like events" which are preceded by a β-decay which is correlated to the same ^{32}Ne implant and accompanied by a 401 keV γ ray recorded in DEGAi. This is analogous to the first search, with an added γ-ray coincidence condition.

The temporal correlation window within which the initial implant is correlated to both the initial β decay and the secondary isomeric decay is set as a single value, requiring that the parent decay and the isomeric decay must both occur within the same single correlation window. This is different than what was done previously, where there was one correlation window for the ion–β correlation and a secondary window was opened after the β decay for the β–γ correlation. The temporal correlation windows tested are increased to 20 ms, 35 ms, and 50 ms in order to account for the fact that the desired isomeric decay is a second-generation decay. For the sample isomeric half-lives of 3.3 ms, 8.3 ms, and 13.3 ms, these three correlation windows would each collect around 90% of isomeric decays. The spatial correlation window was also fixed to a singular value. The mean free path of a photon traveling through a material of density ρ and mass attenuation coefficient C is given by Equation 4.4 [69]. From this, the mean free path of a 120 keV photon traveling through YSO is approximately 5.4 mm, which is a bit shorter than 3 pixels. Therefore, a 3 pixel correlation window is used. As shown in Section 3.4, when applied to the ion–β correlation, this expanded correlation window should not increase randomly correlated background to an unreasonable level.

$$\lambda = \frac{1}{\rho C} \tag{4.4}$$

The energy of the high-gain PSPMT dynode signal was roughly calibrated to understand in which region to look for the 120 keV peak. This rough calibration was completed by drawing the raw high-gain PSPMT dynode energy in coincidence with 1173 keV γ rays recorded in DEGAi for the ^{60}Co source data. The Compton edge of the 1332 keV coincident γ ray (calculated to be at roughly 1118 keV [69]) was clearly visible, and this was used to generate an approximate calibration. This approximate calibration indicated that a 120 keV γ-ray would be recorded between channels 2600 and 3100. As a cross check, the raw ^{152}Eu source spectrum measured in the high-gain PSPMT

dynode was also generated. A peak corresponding to the known 121.8 keV γ ray [77] was clearly visible, with a centroid at approximately channel 2800 (consistent with the rough calibration) and with a FWHM of roughly 800 channels.

The results of the search for a 120 keV isomeric γ-ray decay in the YSO are shown in Figure 4.17. The raw high-gain PSPMT dynode energy spectra are zoomed in around the region where the 120 keV peak is expected to appear. The panels on the left do not require a γ-ray coincidence, whereas the panels on the right require a 401 keV γ-ray coincidence with the first identified β decay. Spectra are shown for all three chosen temporal correlation windows. No peaks are visible in any of the spectra in the region of interest.

Considering the number of parent β decays identified in this analysis, the branching ratio for production of the feeding 401 keV transition, and an estimated detection efficiency of 80% for the 120 keV γ ray in the YSO, approximately 3300 counts of the isomeric decay are expected in the middle-left panel of Figure 4.17. In this estimation, no direct β-decay feeding into the isomeric state is assumed. It is also assumed that the correlation window is sufficiently long to capture all isomeric decays, and that the isomer always decays via γ-ray emission. The γ-ray detection efficiency in the YSO is estimated from GEANT4. Moving over to the middle-right panel of Figure 4.17, the expected number of counts of the isomeric decay is simply based on the number of 401 keV γ rays observed and the efficiency of 120 keV γ-ray detection in the YSO. The same assumptions as described above are made, resulting in an expected peak area of around 100 counts.

It is worth noting that there may be some "correlation efficiency" effects unaccounted for, as the efficiency for correlating a γ decay recorded in the YSO to an implant event within some spatial correlation window is unknown. This correlation efficiency is not expected to be small enough to drastically change these estimations, as the ion–β correlation efficiency is around 50%. The most significant difference between correlating an ion with a β decay versus a γ ray in the YSO may be in the mean free path of the particle through the detector, but this has been calculated, and is expected to be smaller than the spatial correlation window.

While this discussion is approximate, it seems quite unlikely that such large signals are simply

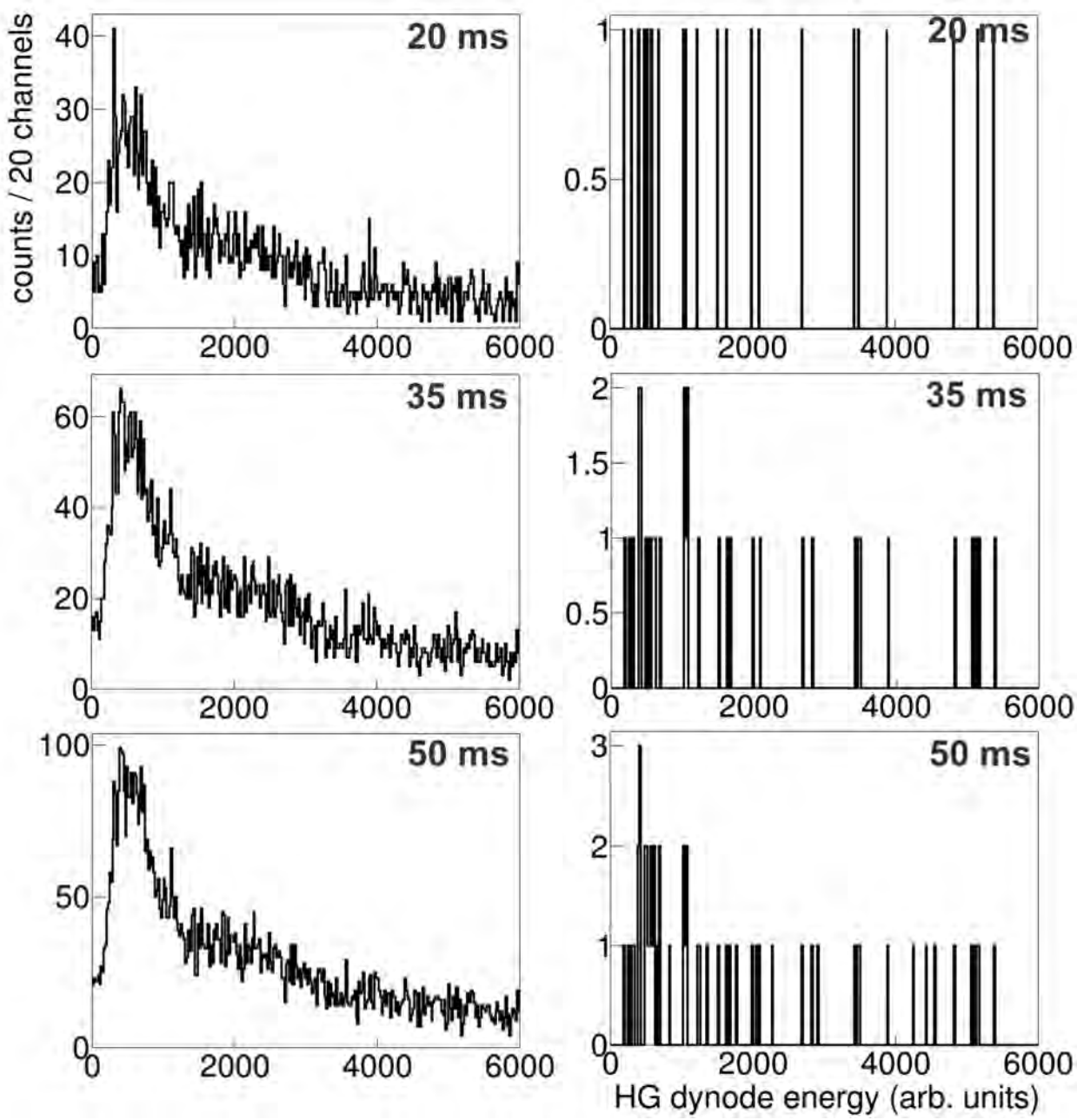

Figure 4.17 High gain PSPMT dynode spectrum of all but the first "β-decay-like" event energies for ^{32}Ne implants which have been correlated to more than one decay. Top: Correlation window of 20 ms. Middle: Correlation window of 35 ms. Bottom: Correlation window of 50 ms. The panels on the right contain an additional condition that the first identified β decay be promptly followed by a 401 keV γ ray measured in DEGAi. See text for full description.

washed out by background. Thus, it seems likely that the isomeric decay does not proceed through γ-ray emission. The implications of this finding will be discussed in Section 5.2.

CHAPTER 5

DISCUSSION

5.1 Spin-parity assignments of excited states in ^{32}Na

Four states were inferred from the present study of the ^{32}Na level scheme, including the ground state. A fifth state — the isomer at 745 keV — was not observed to be populated. As mentioned in Section 1.5, this nonobservation may be used to infer the properties of the state, based on the predictions of Ref. [5]. Thus, there are five states which may be treated in this work, all with unknown spins and parities.

A natural starting point for this discussion is the highest-lying state at 1462 keV. As is evident in the level scheme presented in Figure 4.11, this is the only state observed to have significant, direct β-decay feeding. With a determined log(ft) value of 4.33(14) for the decay to this state, it can be reasonably assumed that this state is populated in allowed β decay (see Figure 2.1, Refs. [59, 60], and the discussion in Section 2.1). The ^{32}Ne ground state has a firm spin-parity assignment of 0^+, as it is an even-even nucleus [10]. This leaves two options for the spin-parity of the 1462 keV state: 0^+ or 1^+. As was discussed in Section 2.1, $0^+ \rightarrow 0^+$ β decays do occur; however, they tend to have log(ft) values in the range of either 3.1–3.6 or >6.4, depending on the isospin change from the initial to the final state. The calculated log(ft) value for this decay is safely outside of this range, leaving $0^+ \rightarrow 1^+$ as the most likely option. Assigning this decay as $0^+ \rightarrow 1^+$ based on the log(ft) value of 4.33(14) is in great agreement with the log(ft) systematics presented in Figure 2.1, as well as the guidelines suggested by Refs. [59, 60]. Thus, the spin-parity of the 1462 keV state is (1^+). It is noted that the assignment is given in parentheses to indicate that it is a tentative value, as it is deduced based on selection rules, rather than concrete measurements which are sensitive to spin or parity.

The next state of interest is the state at 521 keV. This state was first inferred from the isomer decay measurement of Ref. [5], albeit with an ambiguous excitation energy assignment. It is noted that Ref. [5] suggests a spin-parity for this state of either 4^- or 2^- (see Figure 1.12, Ref. [5], and the discussion in Section 1.5). The present data deduces a strong, prompt γ-decay transition from the

(1^+) state at 1462 keV to the state at 521 keV. This is the 940 keV transition; the state at 1462 keV emits this γ ray with a branching ratio of 72(33)%. Based on a final state spin parity of $(2^-, 4^-)$ and an initial state spin-parity of (1^+), the 940 keV decay is either an E1 decay or an E3 decay. Lower multipolarity decays are favored where possible (see Figure 2.3, Figure 2.4 and Section 2.2), so E1 is more likely than E3. Therefore, the 521 keV state is assigned a (2^-) spin-parity. Again, this is a tentative assignment. Another way to examine the spin-parity assignment of the 521 keV state is through the reduced transition strength of the 940 keV transition. Equation 2.9 gives the relationship between the transition probability (which can be related to half-life) and the reduced transition strength. Ref. [63] suggests a Recommended Upper Limit of B(E3) = 50 W.u. for an E3 transition in a low-mass nucleus ($5 \leq A \leq 44$) based on systematic review of experimentally observed E3 transitions. For the 940 keV transition, B(E3) = 50 W.u. corresponds to a half-life of 616 ns. Any smaller transition strength would result in a larger half-life. Thus, if the 940 keV transition were an E3 transition, it would most likely have a half life of at least 616 ns, which the current experimental setup would have been sensitive to. Based on the experimental data, a half-life of this magnitude is not possible for the 1462 keV state. In contrast, the Recommended Upper Limits for E1 isovector and isoscalar transitions from Ref. [63] correspond to half-life lower limits on the order of femtoseconds, which is well below the range of what the current experimental setup would be sensitive to.

The spin-parity assignment of the 521 keV state as (2^-) favors the second scenario suggested by Ref. [5] (see Figure 1.12). As these scenarios cannot be mixed (i.e., one spin-parity is taken from the first scenario and another is taken from the second), all spin-parities from the second scenario can hence be adopted. This suggests a spin-parity of (0^+) for the unobserved 745 keV isomer. The implications of this assignment will be discussed in Section 5.4.

From the selection of the second scenario of Ref. [5], there are two low-lying states with spins and parities of 0^- and 3^-. These are the presently-deduced ground state and isomeric state at 120 keV. The question is, which state has which spin-parity? The spin-parity of the 521 keV state was selected by minimizing the multipolarity of the strong, prompt 940 keV transition which populates

this state. Similar arguments are used to assign the 120 keV isomer as the (3^-) state and the ground state as the (0^-) state. A prompt 1462 keV transition between the (1^+) state and the ground state is observed. As the final (ground state) spin-parity is either 0^- or 3^-, the 1462 keV transition is either E1 or M2. As lower multipolarity electric transitions are preferred, E1 is chosen over M2, suggesting a (0^-) spin parity for the ground state and, thus, a (3^-) spin parity for the isomeric state. The (2^-) state has decay branches to both the ground state and the low-lying isomer; these branches must be M1 and E2. The lower multipolarity (M1) branch proceeds via the stronger 401 keV transition to the (3^-) isomer, and the higher multipolarity (E2) transition goes via the weaker 521 keV transition to the ground state. This is consistent with the previously chosen spin-parity assignments of (0^-) for the ground state and (3^-) for the isomer.

While these spins and parities are are all tentative, as they were assigned based on decay selection rules rather than experimental measurements, even tentative assignments provide a good starting point for comparison with theoretical models. It is quite fortunate, therefore, that all four inferred states as well as the unobserved isomeric state, now have unambiguous spin-parity suggestions. The implications of these assignments will be discussed further in the rest of this chapter.

5.2 Nonobservation of γ decay from the 120 keV isomer

As was discussed in Section 4.3.2, no γ decay was observed to depopulate the 120 keV isomer. Several dedicated searches were carried out, all of which revealed no trace of any γ-ray peak. Based on the number of counts of the 401 keV γ ray which populates the isomer, the observation of a 120 keV γ-ray peak could have been obscured by background in the Clover search, but it seems unlikely that this is the case in the YSO search.

There are two possible explanations for this non-observation. The first option is that the temporal correlation windows used to search for this γ decay were not sufficiently long. The sample isomeric half-lives chosen to search for this decay were 3.3 ms, 8.3 ms, and 13.3 ms. Sample correlation windows were chosen to capture around 90% of isomeric decays within the chosen window, assuming each of the three sample isomeric half-lives. For reference, the ground state half-life of ^{32}Na is 13.2(4) ms [52] (see Appendix), so the search was carried out for isomeric

half-lives approaching an upper limit of approximately the ground state half-life.

The second explanation is that γ decay from this state is so hindered that β decay becomes a competing process. β-decaying isomers are seen across the Chart of Nuclides. The 1^+ isomer in ^{26}F is an example of an isomer which exhibits competition between the two decay processes; the isomer decays via an internal γ-ray transition 82(11)% of the time, with the rest of the decays proceeding through the β and β_{1n} channels. For comparison, the ground state half-life is 7.8(6) ms, and the isomeric half-life is 2.2(1) ms [141]. Another example is the 1^+ isomer in ^{34}Al. An internal transition branch has not been measured for this isomer, and it is thought to decay nearly exclusively through the β and β-n decay channels. The ground state half-life is 53.73(13) ms, and the isomeric half-life is 22.1(2) ms [32] (see also [31, 65, 125]).

The only determination which can be made is that the isomer does not γ decay with a half-life on the order of or shorter than the ground state half-life. A firm determination of the characteristics of the isomeric decay must be identified via a dedicated measurement. This could be done through ^{32}Na β-decay measurements, perhaps isolating the isomer decay and ground state decay via delayed γ-ray gates.

Using the equations given in Section 2.2, an expected partial half-life for the γ decay from the (3^-) state to the ground state can be calculated. The Recommended Upper Limit for the B(M3) value of 10 W.u. is taken from Ref. [63]. It is worth noting that this recommended upper limit is determined based on four observed M3 isovector transitions in the mass region of interest; while it would be preferable to have more observed cases of M3 decay to compare to, this upper limit should give a rough idea of the magnitude of typical B(M3) values. For $A = 32$ and $E_\gamma = 120$ keV, this corresponds to a half-life lower limit of 183 s. Hence, β decay from this isomeric state seems quite likely.

Several previous studies of ^{32}Na β decay have been published, although the existence of the 120 keV isomeric state was not known at the time of these studies. The studies of interest are: Détraz et al. (1979) [28], Guillemaud-Mueller et al. (1984) [98], Klotz et al. (1993) [56], Mattoon et al. (2007) [110], and Tripathi et al. (2008) [111]. These studies will be referred to by their reference

numbers throughout the follow paragraphs. Retrospective comparison of these studies may provide insight into the potential existence of a β-decaying isomer in the ^{32}Na isotope.

The first study, Ref. [28], will be neglected. The second study, Ref. [98], was published by the same group, and the authors state that the results of Ref. [98] are much more reliable than the results of Ref. [28], as Ref. [28] suffered some experimental errors which were resolved in the work of Ref. [98].

For the remaining four studies, measured β-delayed γ-ray intensities are given in Table 5.1. While good agreement within 2σ is observed for most of these transition intensities, for seven of the transitions, discrepancies greater than 2σ are observed between two or more studies. Only these discrepancies greater than 2σ are discussed here. Ref. [56] notes several discrepancies between their work and the earlier work of Ref. [98] (see the 171 keV and 240 keV γ-ray intensities), but does not offer any explanation for these discrepancies. Ref. [110] notes discrepancies between their work and the earlier work of Ref. [56] (see the 171 and 1973 keV γ-ray intensities) and suggests systematic errors in the efficiency calibration of Ref. [56]. Ref. [110] also notes the presence of a contaminant γ ray at 1973 keV in the work of Ref. [56]. The authors offer no explanation for the discrepancy in the γ-ray intensity of the 240 keV between their work and the work of Ref. [98]. Finally, the work of Ref. [111] did not explain discrepancies in γ ray intensities between their work and all three previous works (see the 171 keV, 221 keV, 240 keV, 486 keV, 1232 keV, 1483 keV γ rays).

It is therefore observed that several discrepancies greater than 2σ exist among previous measurements of ^{32}Na β-delayed γ rays, many of which remain unexplained. The most notable is the 240 keV γ ray; among all four measurements, the measurement of [56] agrees with the measurement of Ref. [110], but all other pairs of measurements are discrepant outside of 2σ. This could be explained by the existence of a β-decaying isomer in ^{32}Na.

All four studies used different methods of populating initial states in ^{32}Na (fragmentation of Ir target by 10 GeV protons in Ref. [98], fragmentation of U target by 600 MeV protons in Ref. [56], fragmentation of Ta target by 500 MeV protons in Ref. [110], and fragmentation of ^{48}Ca by

E_γ (keV)	I_γ [relative] (%)			
	Guillemaud-Mueller et al. [98]	Klotz et al. [56]	Mattoon et al. [110]	Tripathi et al. [111]
171[a,*]	9.0(25)	21.9(35)	9.6(6)	14(1)
221[a,*]	4.4(14)	8.9(18)	3.9(4)	9(1)
240[a,*]	27.6(32)	9.7(11)	9.5(6)	16(1)
486[*]			1.3(3)	6(1)
694	3.8(16)			6(1)
885	100	100	100	100
895[a]	4.3(10)	5.1(26)	4.1(5)	3(1)
1232[*]	4.9(14)	4.8(17)	3.8(5)	10(2)
1436	10.2(20)	9.8(25)	9.8(7)	15(2)
1483[b,*]	2.0(17)	4.9(22)	4.2(5)	12(2)
1666			2.4(4)	2(1)
1782	8.3(20)			10(2)
1973[*]	14.3(25)	19.7(25)	11.6(8)	13(2)
2152	52.6(60)	48.5(37)	47.0(17)	47(4)
2268			2.5(3)	4(1)
2551	9.1(20)	10.2(25)	6.4(6)	8(2)
3935	13.3(30)	18.3(37)	12.0(8)	18(4)

Table 5.1 ^{32}Na β-delayed γ-ray intensities measured in four different works. γ-ray energies are approximated values. Some transitions have been omitted. [a]: Produced following β-delayed neutron emission into ^{31}Mg. [b]: Produced following β-delayed neutron emission into ^{30}Mg. [*]: Discrepancies between one or more pairs of measurements exceeds 2σ.

a Be target in Ref. [111]). It is possible that these population methods produced different beam compositions (i.e., the proportion of the isomeric state compared to the ground state in the beam was not the same from one study to the next). As the present work proposes a (3^-) isomeric state and a (0^-) ground state, the final states populated by a potential isomer β decay compared to the ground state decay could be quite different, as β decay is very selective in the final state spin-parity. Varying beam composition paired with different sets of final states for the isomer and ground state decays could result in different studies measuring different intensities of certain γ rays.

This discussion is speculative in nature, and it is emphasized that few firm conclusions regarding the nature of the isomer can be made without additional measurements. While it may seem more likely that the isomer β decays with a half-life on the order of or shorter than the ground state half-life, there are no data measured in this work which allow definitive exclusion of scenarios

involving isomeric β or γ decays with longer half-lives. It is clear, at the very least, that the isomer does not γ decay with a half-life on the order of or shorter than the ground state half-life.

5.3 Model calculations of ^{32}Na level scheme

In order to interpret the present experimental results on a more fundamental level, theoretical models can be utilized. In a theoretical shell model code, different configurations of nucleons can be arranged, and the excitation energy, spin, parity, and decay paths of the resulting state can be predicted. Good agreement between theory calculations and experimental results can indicate that the underlying configuration used in the calculation is a good representation of the state. In this way, model calculations can provide insight into fundamental aspects of nuclear states such as shell model configuration and shape, which are not directly measured in the current experiment. It is important to note that these comparisons are, by nature, model dependent, and different models can interpret a state in different ways. It is therefore important to choose models which have shown high levels of success in reproducing observables across many nuclei in a given region of the nuclear chart. It can also be helpful to choose multiple different models and compare their predictions.

5.3.1 FSU interaction

A calculation of the β decay of ^{32}Ne into the ^{32}Na level scheme was produced using the FSU interaction [142]. The FSU interaction is an empirical shell model interaction, fit using the energies of 270 states in a wide range of nuclei surrounding the $N = 20$ and $N = 28$ shell closures, including isotopes as light as ^{13}C and as heavy as ^{51}Ti. It is important to note that the basis space that was used to fit the model was restricted to a maximum of 1p1h excitations. When the resulting interaction is applied in the $N = 20$ island of inversion, excellent reproduction of experimental data is observed, including the inversion of 0p0h and 2p2h configurations in the ^{30}Ne and ^{32}Mg isotopes [142].

Figure 5.1 shows the results of the theoretical calculations compared to the experimentally-derived level scheme of ^{32}Na. Included in the calculations are excitation energies, spins and parities, and log(ft) values.

First, note the log(ft) values given in Figure 5.1. The predicted log(ft) value of 4.38 for the the lowest excited 1^+ state at 727 keV agrees well with what is observed experimentally: a log(ft) value

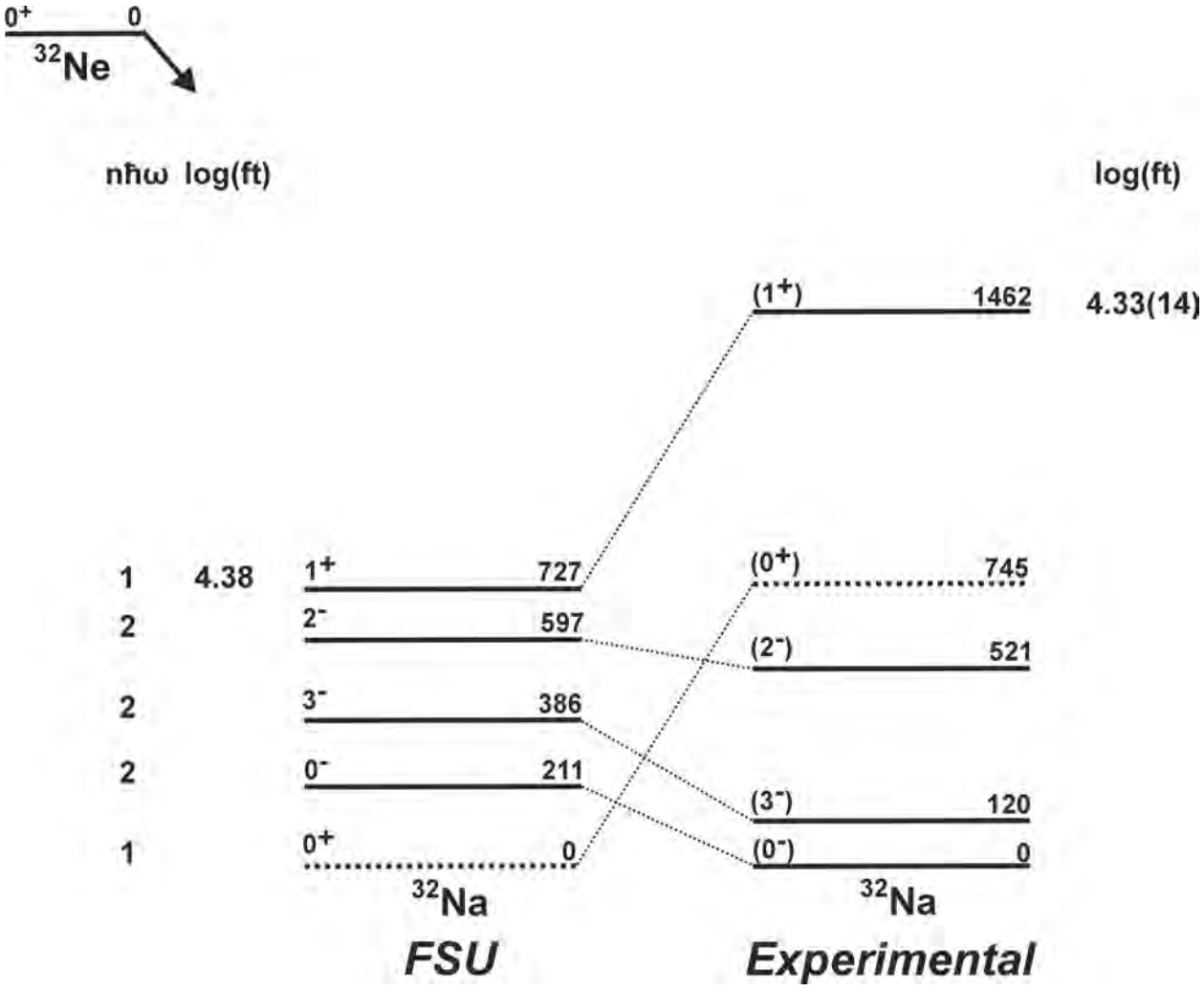

Figure 5.1 Comparison between level scheme calculated with the FSU interaction (left) and experimental level scheme (right). Theory details from A. Volya.

of 4.33(14) for the first excited 1^+ state at 1462 keV. Thus, the β-decay feeding is well reproduced by the calculations. It is noted that the FSU model predicts the ^{32}Ne ground state to have mixed $0\hbar\omega/2\hbar\omega$ character.

In terms of excitation energies, the model's reproduction of experimental values is fair. The negative parity states are all predicted to lie slightly higher in energy, but, in general, they are well reproduced, with a maximum discrepancy of only 266 keV. The positive parity states each lie roughly 700 keV too low in energy, with the 0^+ isomer predicted as the ground state. While a 700 keV discrepancy is worth noting, it could be addressed in a number of trivial ways. One such way would be to reduce the shell gap used in the calculations. Furthermore, the comparison

of experimental data to states calculated with the original FSU interaction (which has been shown to work well for a broad range of nuclei in this region [142]) is more broadly relevant than the comparison of experimental data to states calculated with a custom-tuned interaction based on the FSU interaction. In general, the reproduction of the level scheme is fairly close, and the FSU interaction can still be used to interpret the structures of the observed states.

Figure 5.1 also shows the major $n\hbar\omega$ configurations underlying each calculated state. As a note on notation, $n\hbar\omega$ represents the number of particles excited across a major shell gap — in this case, the $N = 20$ shell gap. This is similar to the np-nh notation. From the calculations, it is seen that all deduced states have significant intruder character. Both positive parity states are predicted to have $1\hbar\omega$ intruder character. The low-lying negative-parity states are all calculated to be of $2\hbar\omega$ intruder character. Overall, this presents a picture of ^{32}Na in which the low-lying level scheme is dominated by states of intruder character, with no traces of the normal $0\hbar\omega$ configuration remaining at low energy. The lowest-lying $0\hbar\omega$ state is predicted around 2.5 MeV.

5.3.2 SDPF-M interaction

A second set of model calculations was performed using the Monte Carlo Shell Model SDPF-M interaction [143]. The valence space of this interaction involves the sd shell as well as the $0f_{7/2}$ and $1p_{3/2}$ orbitals. This model has exhibited satisfactory reproduction of experimental data in the region of interest [143].

Selected calculated levels are shown in Figure 5.2, compared to the experimentally deduced levels. In general, good reproduction of the experimental level energies is seen. Here, the ordering of the three long-lived states is reproduced, and the energy of the 0^+ isomer is reproduced. In general, all excited state energies are well reproduced. In the β-decay calculations, 90% of β-decay feeding populates two 1^+ states below the neutron separation energy. In the calculations, 84% of β-decay feeding populates a 1^+ state at 1183 keV; however, there is another 1^+ state predicted to be fed in small amounts at 1113 keV. For the sake of comparison, the observed 1^+ state is assumed to correspond to the higher-lying calculated 1^+ state. It is difficult to say whether the additional lower-lying 1^+ state might exist near the predicted energy based on current data. To explore this,

J^π	E_x (keV)	% $0\hbar\omega$	% $1\hbar\omega$	% $2\hbar\omega$	% $3\hbar\omega$	% $4\hbar\omega$
0^-	0	0	0	98	0	0
3^-	20	0	0	98	0	0
2^-	322	1	0	98	0	0
0^+	745	0	81	0	18	0
1^+	1113	0	52	0	47	0
1^+	1183	0	34	0	65	0

Table 5.2 For selected states calculated with the SDPF-M interaction, the composition of the states in terms of $n\hbar\omega$ configurations. Theory details from B. A. Brown.

the following assumptions are made: the ratio of the β decay feeding intensities of this proposed 1^+ state and the observed 1^+ state is 6/84, as the model suggests; the γ decay from this proposed 1^+ state proceeds similarly to the γ decay of the observed 1^+ state, populating the 2^- and 0^- states with a similar branching split; and the proposed 1^+ state lies close in energy to the observed 1^+ state. In this scenario, it is unlikely that either of the two depopulating transitions would appear above background. A higher-statistics study would likely be required in order to definitively identify weaker β-decay branches such as this.

Keeping in mind the currently measured neutron emission branches of $P_n = 43(27)\%$ and $P_{2n} > 6\%$, as well as the only deduced I_β value of 36(7)%, the feeding into the 1183 keV 1^+ state ($I_\beta = 84\%$) is overestimated. The corresponding log(ft) value is predicted to be 4.02, which is slightly lower than the presently-deduced value of 4.33(14), again suggesting a moderate overestimation of the β-decay feeding into this 1^+ state. Despite this small discrepancy, overall reproduction of the level scheme is satisfactory.

Table 5.2 shows the composition of the selected states in terms of their $n\hbar\omega$ components. Both 1^+ states are expected to be significantly mixed between $1\hbar\omega$ and $3\hbar\omega$ configurations, with the higher-lying 1^+ state more strongly favoring the more highly deformed $3\hbar\omega$ configuration. The three lowest-lying negative parity states are all predicted to be effectively pure $2\hbar\omega$ configurations.

One remarkable feature of these calculations is that, again, very small $0\hbar\omega$ components are predicted. For the selected states, effectively no $0\hbar\omega$ components are present. In fact, among the 37 states predicted up to 6.895 MeV, only one state has a $0\hbar\omega$ component over 10%. This is a 2^- state

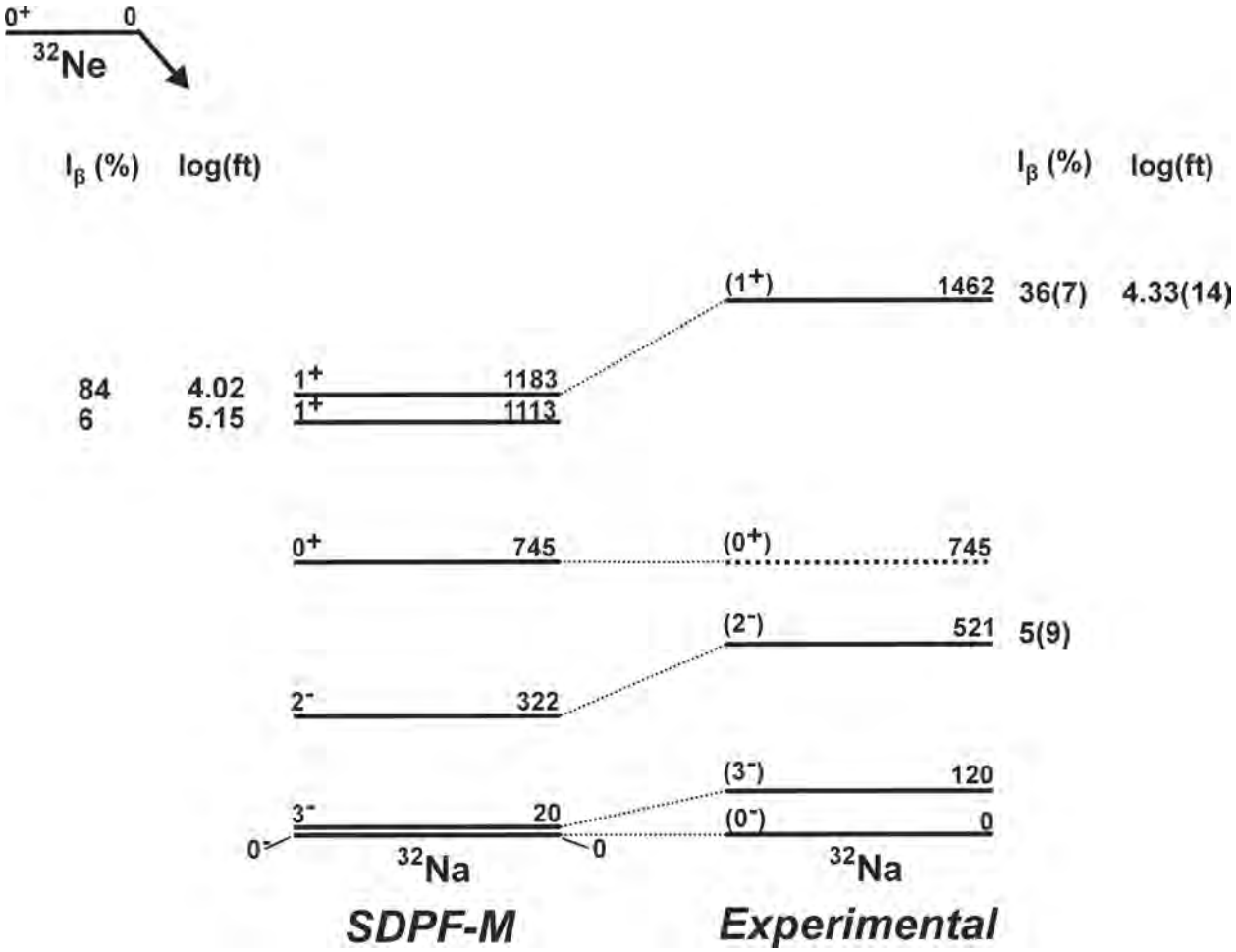

Figure 5.2 Comparison between level scheme calculated with the SDPF-M interaction (left) and experimental level scheme (right). Theory details from B. A. Brown.

at 2.294 MeV with only 13% $0\hbar\omega$ contributions. Therefore, the SDPF-M interaction predicts the normal, spherical configurations to completely disappear from the level scheme, even up to almost 7 MeV.

5.3.3 Nilsson model interpretation

It is possible to interpret the observed states qualitatively in terms of the Nilsson model. Table 5.3 shows a variety of different Nilsson model neutron configurations which are possible for states in ^{32}Na. The assumed ^{32}Ne ground state configuration is shown on the right for comparison. Based on results from Ref. [144], it is taken to have a $2\hbar\omega$ character. D is the number of neutrons excited across the sd-fp shell gap; this is identical to the $n\hbar\omega$ notation. The shell gap lies between the $k_n = 3/2^+$ and $k_n = 1/2^-$ orbitals; for several D values, multiple configurations are possible,

	^{32}Na					^{32}Ne	
k_n	D=1	D=1′	D=2	D=2′	D=3	D=2	D=2′
$3/2^-$		xx	x	xx	xx	xx	xx
$1/2^-$	xx		xx	x	xx	xx	xx
$3/2^+$	x	xx					xx
$1/2^+$	xx	x	xx	xx	x	xx	
$K_{\min}$	0^+	1^+	0^-	1^-	1^+	0^+	
$K_{\max}$	3^+	2^+	3^-	2^-	2^+		

Table 5.3 Different available neutron configurations for states in ^{32}Na and the K^π values available per configuration. The ^{32}Ne ground state neutron configuration is shown on the right for comparison. k_n is the unpaired neutron orbital K value. D is the number of neutrons excited from the sd shell to the fp shell, with ′ symbols indicating alternate ways to make the same D configuration. $k_n = 1/2^+$ and $3/2^+$ are sd shell orbitals, and $k_n = 1/2^-$ and $3/2^-$ are fp shell orbitals. x marks indicate how many neutrons are in each k_n orbital (e.g. xx is two neutrons and x is one neutron). $K_{\min}$ and $K_{\max}$ indicate the minimum and maximum total K values that result from the coupling of k_n to an unpaired proton with $k_p = 3/2^+$. Credit: B. A. Brown

indicated by the ′ symbol. k_n indicates the K value of the neutron orbital. Only the uppermost orbitals are depicted, and fully filled orbitals are assumed below. $K_{\min}$ and $K_{\max}$ indicate the two possible K values that the nucleus can occupy in a given configuration, considering coupling of the unpaired neutron to an unpaired proton with $k_p = 3/2^+$, which is the highest occupied proton orbital.

As Table 5.3 depicts, this interpretation starts with a ^{32}Ne ground state that is dominated by a D=2 configuration, as suggested in Ref. [144]. In ^{32}Na, two 1^+ states are expected: one of D=1 character, and another of D=3 character. Comparing the D=3 configuration to the sample ^{32}Ne ground state configuration, the β decay into this state can be easily understood as a single-particle transition. A $k_n = 1/2^+$ sd shell neutron decays into a $k_p = 3/2^+$ proton, filling the lowest available proton orbital and leaving the neutron configuration unchanged, save for the loss of the β-decaying $1/2^+$ neutron. Thus, decay from a 0^+ D=2 state into a 1^+ D=3 state, qualitatively speaking, can well-describe the ^{32}Ne β decay. This agrees well with the previously-discussed SDPF-M calculations, which predicts the same dominant $3\hbar\omega$ configuration for the observed (1^+) state.

Alternatively, a D=0 ^{32}Ne ground state decay to a D=1 1^+ state in ^{32}Na could be well understood as a single-particle transition from a $k_n = 1/2^+$ neutron into a $k_p = 3/2+$ proton. This interpretation

agrees well with the FSU prediction of the 1^+ state being dominated by $1\hbar\omega$ character, although the subsequent γ-decay transitions are no longer well-described in terms of single-particle transitions. For this reason, the SDPF-M description of a D=3 1^+ state is slightly favored.

The D=3 1^+ state can be understood to primarily γ decay into the D=2 0^- and D=2′ 2^- states. Again, these strong decays only indicate a small change in the neutron configuration, with one neutron dropping down from either the $3/2^-$ or $1/2^-$ orbitals to occupy the $1/2^+$ orbital.

The 0^+ isomer likely comes from the D=1 configuration. Low overlap between the ^{32}Ne D=2 0^+ ground state and the ^{32}Na D=1 0^+ isomer explains the non-observation of the $0^+ \rightarrow 0^+$ β decay. There is also low overlap between the ^{32}Na D=3 1^+ state and the D=1 0^+ isomer, explaining the non-observation of an M1 transition connecting the two states. With this interpretation, the non-observation of the 0^+ isomer decay is, therefore, not surprising.

5.4 Combined model interpretation of the ^{32}Na level scheme

When comparing the FSU interaction calculations to the SDPF-M interaction calculations, both exhibit fair agreement with experimental data, albeit some small discrepancies. The Nilsson interpretation of the results aligns fairly well with the shell model predictions, particularly those of the SDPF-M interaction.

Starting with the 1^+ state that is directly fed in β decay, the models leave some remaining questions. The FSU interaction well reproduces the feeding into this state and interprets the state as resulting from a $1\hbar\omega$ configuration. The SDPF-M model well reproduces the energy of the state, but it greatly overpredicts the feeding into this state, thus implying less delayed neutron emission than was deduced experimentally. Further, the SDPF-M model predicts a highly mixed ($1\hbar\omega$/$3\hbar\omega$) 1^+ state, with significant $3\hbar\omega$ components beyond what the FSU model suggests. Thus, it is clear that the observed 1^+ state is of intruder character, with some $1\hbar\omega$ components. The extent of $3\hbar\omega$ components is a point of discrepancy between these two models. The Nilsson interpretation of this state supports strong $3\hbar\omega$ components for the 1^+ state.

The FSU interaction and the SDPF-M interaction agree that the lowest three negative parity states are effectively pure $2\hbar\omega$ states. The Nilsson interpretation also supports this conclusion. It is

interesting that, in the configuration picture, the low-lying 3^- isomer is quite similar to the ground state. Thus, it seems unlikely that a configuration mismatch has any impact on the isomerism of the state. As discussed previously, the M3 γ transition between the isomer and the ground state is expected to be quite slow, with a partial half-life on the order of hundreds of seconds, implying that the isomerism is likely the result of the combination of a large spin difference and a low γ-ray transition energy.

The 0^+ isomer is predicted by both sets of model calculations to be of $1\hbar\omega$ character. One possibility for the interpretation of this isomer, presented in Ref. [5], suggested that the isomer is a deformed spin isomer. The 224 keV transition represented a transition of a neutron from the $d_{3/2}$ orbital into the $f_{7/2}$ orbital. This agrees well with the present model calculations, which suggest a transition from $1\hbar\omega$ configurations in the isomeric state to $2\hbar\omega$ configurations in the 2^- state (i.e., one additional neutron excited across the shell gap). Thus, the present results support the assignment of the microsecond isomer as a deformed spin isomer. The nonobservation of the isomer in the present work is consistent with the SDPF-M calculations and can be well-described by in a Nilsson model framework, in which the ^{32}Ne ground state has $2\hbar\omega$ character and the ^{32}Na 1^+ excited state has $3\hbar\omega$ character, both which would not easily decay via a single-particle transition into the $1\hbar\omega$ 0^+ isomer. The FSU calculations, which suggest slightly different characteristics for the ^{32}Ne ground state and the ^{32}Na 1^+ excited state, do not necessarily disagree with the present nonobservation of the 0^+ isomer, but, overall, the ^{32}Na γ-decay scheme is better understood in terms of single-particle transitions in a Nilsson model framework if the 1^+ state is of $3\hbar\omega$ character.

CHAPTER 6

CONCLUSIONS AND OUTLOOK

6.1 Conclusions

In the present study, the β decays of ^{30,32}Ne have been utilized to explore the level schemes of the child ^{30,32}Na isotopes. The ^{30}Ne β decay is well understood from previous studies [2–4]; present results well reproduced previously published results, providing a high level of confidence in the present methodology.

The ^{32}Ne decay was not well studied prior to the current study; in fact, many questions remained regarding the nature of the ^{32}Na level scheme. Four states had been identified, two of which were isomeric and three of which had ambiguous excitation energies. For the lower-lying isomer at 120 keV, both the decay mode and half-life were unknown. Finally, ambiguous spin-parity assignments for all states, including the higher-lying microsecond isomer, prevented meaningful interpretation of the observed phenomena.

In the present study, several γ rays were identified following the β decay of ^{32}Ne. These transitions included the previously-known 401 keV transition [5], as well as new transitions at 521, 940, and 1462 keV. With the knowledge of a low-lying isomer around 120 keV [6], energy summing relationships allowed construction of a level scheme for ^{32}Na that significantly expanded upon what had been known previously. Neither isomeric decay was observed, but the low-lying isomer was inferred to be populated based on γ-ray energy summing relationships. Several new quantities were calculated from the experimental data, including neutron emission probabilities, γ-decay intensities, and β-decay intensities.

Informed by β-decay and γ-decay selection rules, as well as theoretical considerations presented in Ref. [5], spin-parities were tentatively assigned for five states, including the ground state, two short-lived excited states, and both isomeric states. It was hence determined that the higher-lying isomer is a deformed spin isomer; based on the underlying configurations of states determined by model calculations, the non-observation of the higher-lying isomer following β decay was found to be unsurprising.

The lower-lying isomer presented a different challenge, as its population was suggested by the observed γ-ray energies, but a γ decay from this state was not observed. While it seems likely that this isomer β decays, thus explaining the non-observation of a γ decay depopulating this state, the only determination which can be made from the present data is that the isomer does not decay via γ decay with a half-life on the order of the ground state half-life or shorter. It is emphasized that other scenarios involving longer half-lives cannot be excluded, and neither the decay mode nor the half-life can be constrained from the present study.

As aforementioned, several models were compared to the experimental data. Calculations were completed using the FSU interaction [142] and the SDPF-M model [143], and a qualitative interpretation based on the Nilsson model was also explored. Good reproduction of experimental data was observed, affirming the accuracy of the theoretical descriptions employed in the model calculations. All models emphasized the importance of neutron excitations across the $N = 20$ shell gap; no trace of the normal configuration was seen in the calculated low-lying level scheme. This affirms the current understanding of ^{32}Na as a quintessential island of inversion isotope.

6.2 Outlook

^{32}Na was one of the first isotopes whose measurements signaled the unique shell evolution occurring near the $N = 20$ island of inversion [1]. Despite the early indication of exotic phenomena in this isotope, five decades later, spectroscopic study of ^{32}Na still leaves many questions. The present study has made progress in finding answers to some of these questions, but questions still remain.

One of the biggest drawbacks of the present study was statistical in natural. Several measurements, such as the neutron emission measurements, have large errors, primarily due to the low count rates of delayed γ rays. A higher-statistics study of ^{32}Ne β decay could reduce some of these errors, and perhaps even identify additional delayed γ-ray transitions which are only weakly produced. The non-observation of the 0^+ isomer decay in the current work was found to be unsurprising, but quantification of how weak this branch is may be of interest.

Of course, β-decay studies are naturally selective in the spin-parity of the final states populated.

Exploratory studies of ^{32}Na using different population methods could identify new states not seen in any of the previous studies.

Most critically, very little is known about the recently discovered 120 keV isomer. It would be useful to revisit the β decay of ^{32}Na, with the idea in mind that a β-decaying isomer could be present. From this angle, a new measurement of the ^{32}Na ground state half-life may be necessary, utilizing delayed γ-ray gates which would isolate the ground state decay from the isomer decay. The same method could be used to determine the isomeric half-life in isolation from the ground state decay branch. Determination of the levels populated by the ground state β decay compared to the potential isomeric β decay could potentially present a challenging measurement. More firm spin-parity measurements of states in ^{32}Mg, made independent of ^{32}Na β decay studies, could facilitate a better understanding of which states are populated following which decay.

The present study has significantly expanded the experimental knowledge of ^{32}Na, indicating a low-lying level scheme completely dominated by deformed intruder states. New spectroscopic information paves the way for improvements in systematic comparison of odd-odd nuclei near the island of inversion. More questions remain unanswered, and future study of this isotope, though challenging, will certainly yield critical structural information. In order to fully understand the forces which drive shape and shell evolution in this region of the nuclear chart, continued study, not only of ^{32}Na but also of other neutron-rich $N \sim 20$ nuclei approaching the neutron dripline, is of paramount importance.

REFERENCES

[1] C. Thibault, R. Klapisch, C. Rigaud, A. M. Poskanzer, R. Prieels, L. Lessard, and W. Reisdorf, Phys. Rev. C **12**, 644 (1975).

[2] A. T. Reed, O. Tarasov, R. D. Page, D. Guillemaud-Mueller, Y. E. Penionzhkevich, R. G. Allatt, J. C. Angélique, R. Anne, C. Borcea, V. Burjan, W. N. Catford, Z. Dlouhý, C. Donzaud, S. Grévy, M. Lewitowicz, S. M. Lukyanov, F. M. Marqués, G. Martinez, A. C. Mueller, P. J. Nolan, J. Novák, N. A. Orr, F. Pougheon, P. H. Regan, M. G. Saint-Laurent, T. Siiskonen, E. Sokol, O. Sorlin, J. Suhonen, W. Trinder, and S. M. Vincent, Phys. Rev. C **60**, 024311 (1999).

[3] V. Tripathi, S. L. Tabor, P. F. Mantica, Y. Utsuno, P. Bender, J. Cook, C. R. Hoffman, S. Lee, T. Otsuka, J. Pereira, M. Perry, K. Pepper, J. S. Pinter, J. Stoker, A. Volya, and D. Weisshaar, Phys. Rev. C **76**, 021301(R) (2007).

[4] K. Steiger, S. Nishimura, Z. Li, R. Gernhäuser, Y. Utsuno, R. Chen, T. Faestermann, C. Hinke, R. Krücken, M. Kurata-Nishimura, G. Lorusso, Y. Miyashita, N. Shimizu, K. Sugimoto, T. Sumikama, H. Watanabe, and K. Yoshinaga, European Physical Journal A **51**, 117 (2015).

[5] T. J. Gray, J. M. Allmond, Z. Xu, T. T. King, R. S. Lubna, H. L. Crawford, V. Tripathi, B. P. Crider, R. Grzywacz, S. N. Liddick, A. O. Macchiavelli, T. Miyagi, A. Poves, A. Andalib, E. Argo, C. Benetti, S. Bhattacharya, C. M. Campbell, M. P. Carpenter, J. Chan, A. Chester, J. Christie, B. R. Clark, I. Cox, A. A. Doetsch, J. Dopfer, J. G. Duarte, P. Fallon, A. Frotscher, T. Gaballah, J. T. Harke, J. Heideman, H. Huegen, J. D. Holt, R. Jain, N. Kitamura, K. Kolos, F. G. Kondev, A. Laminack, B. Longfellow, S. Luitel, M. Madurga, R. Mahajan, M. J. Mogannam, C. Morse, S. Neupane, A. Nowicki, T. H. Ogunbeku, W.-J. Ong, C. Porzio, C. J. Prokop, B. C. Rasco, E. K. Ronning, E. Rubino, T. J. Ruland, K. P. Rykaczewski, L. Schaedig, D. Seweryniak, K. Siegl, M. Singh, A. E. Stuchbery, S. L. Tabor, T. L. Tang, T. Wheeler, J. A. Winger, and J. L. Wood, Phys. Rev. Lett. **130**, 242501 (2023).

[6] E. M. Lykiardopoulou, C. Walls, J. Bergmann, M. Brodeur, C. Brown, J. Cardona, A. Czihaly, T. Dickel, T. Duguet, J.-P. Ebran, M. Frosini, Z. Hockenbery, J. D. Holt, A. Jacobs, S. Kakkar, B. Kootte, T. Miyagi, A. Mollaebrahimi, T. Murboeck, P. Navratil, T. Otsuka, W. R. Plaß, S. Paul, W. S. Porter, M. P. Reiter, A. Scalesi, C. Scheidenberger, V. Somà, N. Shimizu, Y. Wang, D. Lunney, J. Dilling, and A. A. Kwiatkowski, Phys. Rev. Lett. **134**, 052503 (2025).

[7] B. A. Brown, *Lecture Notes in Nuclear Structure Physics* (Michigan State University, East Lansing, Michigan, 2021).

[8] A. Obertelli and H. Sagawa, *Modern Nuclear Physics: From Fundamentals to Fronteirs* (Springer Nature, Singapore, 2021).

[9] T. Otsuka, A. Gade, O. Sorlin, T. Suzuki, and Y. Utsuno, Rev. Mod. Phys. **92**, 015002 (2020).

[10] R. F. Casten, *Nuclear Structure from a Simple Perspective* (Oxford University Press, Inc., New York, New York, 1990).

[11] M. G. Mayer, Phys. Rev. **75**, 1969 (1949).

[12] O. Haxel, J. H. D. Jensen, and H. E. Suess, Phys. Rev. **75**, 1766 (1949).

[13] K. Heyde and J. L. Wood, Rev. Mod. Phys. **83**, 1467 (2011).

[14] NuDat 3.0, https://www.nndc.bnl.gov/nudat3/.

[15] W. Schwerdtfeger, P. G. Thirolf, K. Wimmer, D. Habs, H. Mach, T. R. Rodriguez, V. Bildstein, J. L. Egido, L. M. Fraile, R. Gernhäuser, R. Hertenberger, K. Heyde, P. Hoff, H. Hübel, U. Köster, T. Kröll, R. Krücken, R. Lutter, T. Morgan, and P. Ring, Phys. Rev. Lett. **103**, 012501 (2009).

[16] N. Kitamura, K. Wimmer, N. Shimizu, V. M. Bader, C. Bancroft, D. Barofsky, T. Baugher, D. Bazin, J. S. Berryman, V. Bildstein, A. Gade, N. Imai, T. Kröll, C. Langer, J. Lloyd, E. Lunderberg, G. Perdikakis, F. Recchia, T. Redpath, S. Saenz, D. Smalley, S. R. Stroberg, J. A. Tostevin, N. Tsunoda, Y. Utsuno, D. Weisshaar, and A. Westerberg, Phys. Rev. C **102**, 054318 (2020).

[17] H. Nishibata, K. Tajiri, T. Shimoda, A. Odahara, S. Morimoto, S. Kanaya, A. Yagi, H. Kanaoka, M. R. Pearson, C. D. P. Levy, M. Kimura, N. Tsunoda, and T. Otsuka, Phys. Rev. C **102**, 054327 (2020).

[18] H. Iwasaki, T. Motobayashi, H. Akiyoshi, Y. Ando, N. Fukuda, H. Fujiwara, Z. Fülöp, K. Hahn, Y. Higurashi, M. Hirai, I. Hisanaga, N. Iwasa, T. Kijima, T. Minemura, T. Nakamura, M. Notani, S. Ozawa, H. Sakurai, S. Shimoura, S. Takeuchi, T. Teranishi, Y. Yanagisawa, and M. Ishihara, Physics Letters B **481**, 7 (2000).

[19] H. Iwasaki, A. Dewald, C. Fransen, A. Gelberg, M. Hackstein, J. Jolie, P. Petkov, T. Pissulla, W. Rother, and K. O. Zell, Phys. Rev. Lett. **102**, 202502 (2009).

[20] T. Motobayashi, Y. Ikeda, K. Ieki, M. Inoue, N. Iwasa, T. Kikuchi, M. Kurokawa, S. Moriya, S. Ogawa, H. Murakami, S. Shimoura, Y. Yanagisawa, T. Nakamura, Y. Watanabe, M. Ishihara, T. Teranishi, H. Okuno, and R. Casten, Physics Letters B **346**, 9 (1995).

[21] B. Bastin, S. Grévy, D. Sohler, O. Sorlin, Z. Dombrádi, N. L. Achouri, J. C. Angélique, F. Azaiez, D. Baiborodin, R. Borcea, C. Bourgeois, A. Buta, A. Bürger, R. Chapman, J. C. Dalouzy, Z. Dlouhy, A. Drouard, Z. Elekes, S. Franchoo, S. Iacob, B. Laurent, M. Lazar, X. Liang, E. Liénard, J. Mrazek, L. Nalpas, F. Negoita, N. A. Orr, Y. Penionzhkevich, Z. Podolyák, F. Pougheon, P. Roussel-Chomaz, M. G. Saint-Laurent, M. Stanoiu, I. Stefan, F. Nowacki, and A. Poves, Phys. Rev. Lett. **99**, 022503 (2007).

[22] C. Force, S. Grévy, L. Gaudefroy, O. Sorlin, L. Cáceres, F. Rotaru, J. Mrazek, N. L. Achouri, J. C. Angélique, F. Azaiez, B. Bastin, R. Borcea, A. Buta, J. M. Daugas, Z. Dlouhy, Z. Dombrádi, F. De Oliveira, F. Negoita, Y. Penionzhkevich, M. G. Saint-Laurent, D. Sohler, M. Stanoiu, I. Stefan, C. Stodel, and F. Nowacki, Phys. Rev. Lett. **105**, 102501 (2010).

[23] O. Sorlin, C. Donzaud, F. Nowacki, J. Angélique, F. Azaiez, C. Bourgeois, V. Chiste, Z. Dlouhy, S. Grévy, D. Guillemaud-Mueller, F. Ibrahim, K.-L. Kratz, M. Lewitowicz, S. Lukyanov, J. Mrasek, Y.-E. Penionzhkevich, F. de Oliveira Santos, B. Pfeiffer, F. Pougheon, A. Poves, M. Saint-Laurent, and M. Stanoiu, European Physical Journal A **16**, 55 (2003).

[24] H. L. Crawford, R. M. Clark, P. Fallon, A. O. Macchiavelli, T. Baugher, D. Bazin, C. W. Beausang, J. S. Berryman, D. L. Bleuel, C. M. Campbell, M. Cromaz, G. de Angelis, A. Gade, R. O. Hughes, I. Y. Lee, S. M. Lenzi, F. Nowacki, S. Paschalis, M. Petri, A. Poves, A. Ratkiewicz, T. J. Ross, E. Sahin, D. Weisshaar, K. Wimmer, and R. Winkler, Phys. Rev. Lett. **110**, 242701 (2013).

[25] E. K. Warburton, J. A. Becker, and B. A. Brown, Phys. Rev. C **41**, 1147 (1990).

[26] C. Santamaria, C. Louchart, A. Obertelli, V. Werner, P. Doornenbal, F. Nowacki, G. Authelet, H. Baba, D. Calvet, F. Château, A. Corsi, A. Delbart, J.-M. Gheller, A. Gillibert, T. Isobe, V. Lapoux, M. Matsushita, S. Momiyama, T. Motobayashi, M. Niikura, H. Otsu, C. Péron, A. Peyaud, E. C. Pollacco, J.-Y. Roussé, H. Sakurai, M. Sasano, Y. Shiga, S. Takeuchi, R. Taniuchi, T. Uesaka, H. Wang, K. Yoneda, F. Browne, L. X. Chung, Z. Dombradi, S. Franchoo, F. Giacoppo, A. Gottardo, K. Hadynska-Klek, Z. Korkulu, S. Koyama, Y. Kubota, J. Lee, M. Lettmann, R. Lozeva, K. Matsui, T. Miyazaki, S. Nishimura, L. Olivier, S. Ota, Z. Patel, N. Pietralla, E. Sahin, C. Shand, P.-A. Söderström, I. Stefan, D. Steppenbeck, T. Sumikama, D. Suzuki, Z. Vajta, J. Wu, and Z. Xu, Phys. Rev. Lett. **115**, 192501 (2015).

[27] J. Li, Physics Letters B **840**, 137893 (2023).

[28] C. Détraz, D. Guillemaud, G. Huber, R. Klapisch, M. Langevin, F. Naulin, C. Thibault, L. C. Carraz, and F. Touchard, Phys. Rev. C **19**, 164 (1979).

[29] Evaluated Nuclear Structure Data Files, https://www.nndc.bnl.gov/ensdf/.

[30] J. R. Terry, B. A. Brown, C. M. Campbell, J. M. Cook, A. D. Davies, D.-C. Dinca, A. Gade, T. Glasmacher, P. G. Hansen, B. M. Sherrill, H. Zwahlen, D. Bazin, K. Yoneda, J. A. Tostevin, T. Otsuka, Y. Utsuno, and B. Pritychenko, Phys. Rev. C **77**, 014316 (2008).

[31] F. Rotaru, F. Negoita, S. Grévy, J. Mrazek, S. Lukyanov, F. Nowacki, A. Poves, O. Sorlin, C. Borcea, R. Borcea, A. Buta, L. Cáceres, S. Calinescu, R. Chevrier, Z. Dombrádi, J. M. Daugas, D. Lebhertz, Y. Penionzhkevich, C. Petrone, D. Sohler, M. Stanoiu, and J. C. Thomas, Phys. Rev. Lett. **109**, 092503 (2012).

[32] R. Lică, F. Rotaru, M. J. G. Borge, S. Grévy, F. Negoiţă, A. Poves, O. Sorlin, A. N. Andreyev, R. Borcea, C. Costache, H. De Witte, L. M. Fraile, P. T. Greenlees, M. Huyse, A. Ionescu, S. Kisyov, J. Konki, I. Lazarus, M. Madurga, N. Mărginean, R. Mărginean, C. Mihai, R. E. Mihai, A. Negret, F. Nowacki, R. D. Page, J. Pakarinen, V. Pucknell, P. Rahkila, E. Rapisarda, A. Şerban, C. O. Sotty, L. Stan, M. Stănoiu, O. Tengblad, A. Turturică, P. Van Duppen, N. Warr, P. Dessagne, T. Stora, C. Borcea, S. Călinescu, J. M. Daugas, D. Filipescu, I. Kuti, S. Franchoo, I. Gheorghe, P. Morfouace, P. Morel, J. Mrazek, D. Pietreanu, D. Sohler, I. Stefan, R. Şuvăilă, S. Toma, and C. A. Ur (IDS Collaboration), Phys. Rev. C **100**, 034306 (2019).

[33] R. S. Lubna, A. B. Garnsworthy, V. Tripathi, G. C. Ball, C. R. Natzke, M. Rocchini, C. Andreoiu, S. S. Bhattacharjee, I. Dillmann, F. H. Garcia, S. A. Gillespie, G. Hackman, C. J. Griffin, G. Leckenby, T. Miyagi, B. Olaizola, C. Porzio, M. M. Rajabali, Y. Saito, P. Spagnoletti, S. L. Tabor, R. Umashankar, V. Vedia, A. Volya, J. Williams, and D. Yates, Phys. Rev. C **109**, 014309 (2024).

[34] P. Doornenbal, H. Scheit, S. Takeuchi, Y. Utsuno, N. Aoi, K. Li, M. Matsushita, D. Steppenbeck, H. Wang, H. Baba, E. Ideguchi, N. Kobayashi, Y. Kondo, J. Lee, S. Michimasa, T. Motobayashi, T. Otsuka, H. Sakurai, M. Takechi, Y. Togano, and K. Yoneda, Phys. Rev. C **95**, 041301(R) (2017).

[35] J. Kahlbow, T. Aumann, O. Sorlin, Y. Kondo, T. Nakamura, F. Nowacki, A. Revel, N. L. Achouri, H. Al Falou, L. Atar, H. Baba, K. Boretzky, C. Caesar, D. Calvet, H. Chae, N. Chiga, A. Corsi, F. Delaunay, A. Delbart, Q. Deshayes, Z. Dombrádi, C. A. Douma, Z. Elekes, I. Gašparić, J.-M. Gheller, J. Gibelin, A. Gillibert, M. N. Harakeh, A. Hirayama, M. Holl, A. Horvat, A. Horváth, J. W. Hwang, T. Isobe, N. Kalantar-Nayestanaki, S. Kawase, S. Kim, K. Kisamori, T. Kobayashi, D. Körper, S. Koyama, I. Kuti, V. Lapoux, S. Lindberg, F. M. Marqués, S. Masuoka, J. Mayer, K. Miki, T. Murakami, M. Najafi, K. Nakano, N. Nakatsuka, T. Nilsson, A. Obertelli, N. A. Orr, H. Otsu, T. Ozaki, V. Panin, S. Paschalis, D. M. Rossi, A. T. Saito, T. Saito, M. Sasano, H. Sato, Y. Satou, H. Scheit, F. Schindler, P. Schrock, M. Shikata, K. Shimada, Y. Shimizu, H. Simon, D. Sohler, L. Stuhl, S. Takeuchi, M. Tanaka, M. Thoennessen, H. Törnqvist, Y. Togano, T. Tomai, J. Tscheuschner, J. Tsubota, T. Uesaka, H. Wang, Z. Yang, M. Yasuda, and K. Yoneda (SAMURAI21-NeuLAND Collaboration), Phys. Rev. Lett. **133**, 082501 (2024).

[36] P. Doornenbal, H. Scheit, S. Takeuchi, N. Aoi, K. Li, M. Matsushita, D. Steppenbeck, H. Wang, H. Baba, H. Crawford, C. R. Hoffman, R. Hughes, E. Ideguchi, N. Kobayashi, Y. Kondo, J. Lee, S. Michimasa, T. Motobayashi, H. Sakurai, M. Takechi, Y. Togano, R. Winkler, and K. Yoneda, Phys. Rev. Lett. **111**, 212502 (2013).

[37] M. Madurga, J. M. Christie, Z. Xu, R. Grzywacz, A. Poves, T. King, J. M. Allmond, A. Chester, I. Cox, J. Farr, I. Fletcher, J. Heideman, D. Hoskins, A. Laminack, S. Liddick, S. Neupane, A. L. Richard, N. Shimizu, P. Shuai, K. Siegl, Y. Utsuno, P. Wagenknecht, and R. Yokoyama, Phys. Rev. C **109**, L061301 (2024).

[38] E. Caurier, F. Nowacki, and A. Poves, Phys. Rev. C **90**, 014302 (2014).

[39] A. O. Macchiavelli, H. L. Crawford, C. M. Campbell, R. M. Clark, M. Cromaz, P. Fallon, M. D. Jones, I. Y. Lee, M. Salathe, B. A. Brown, and A. Poves, Phys. Rev. C **94**, 051303(R) (2016).

[40] I. Murray, M. MacCormick, D. Bazin, P. Doornenbal, N. Aoi, H. Baba, H. Crawford, P. Fallon, K. Li, J. Lee, M. Matsushita, T. Motobayashi, T. Otsuka, H. Sakurai, H. Scheit, D. Steppenbeck, S. Takeuchi, J. A. Tostevin, N. Tsunoda, Y. Utsuno, H. Wang, and K. Yoneda, Phys. Rev. C **99**, 011302(R) (2019).

[41] Z. Elekes, Z. Dombrádi, A. Saito, N. Aoi, H. Baba, K. Demichi, Z. Fülöp, J. Gibelin, T. Gomi, H. Hasegawa, N. Imai, M. Ishihara, H. Iwasaki, S. Kanno, S. Kawai, T. Kishida, T. Kubo, K. Kurita, Y. Matsuyama, S. Michimasa, T. Minemura, T. Motobayashi, M. Notani, T. Ohnishi, H. J. Ong, S. Ota, A. Ozawa, H. K. Sakai, H. Sakurai, S. Shimoura, E. Takeshita, S. Takeuchi, M. Tamaki, Y. Togano, K. Yamada, Y. Yanagisawa, and K. Yoneda, Phys. Rev. C **73**, 044314 (2006).

[42] T. Fukui, S. Ota, S. Shimoura, N. Aoi, E. Takeshita, S. Takeuchi, H. Suzuki, H. Baba, T. Fukuchi, Y. Hashimoto, E. Ideguchi, K. Ieki, N. Iwasa, H. Iwasaki, S. Kanno, Y. Kondo, T. Kubo, K. Kurita, T. Minemura, S. Mitimasa, T. Motobayashi, T. Murakami, T. Nakabayashi, T. Nakamura, M. Niikura, T. Okumura, T. K. Onishi, H. Sakurai, M. Shinohara, D. Suzuki, M. K. Suzuki, M. Tamaki, K. Tanaka, Y. Togano, Y. Wakabayashi, and K. Yamada, CNS Annual Report **69**, 19 (2006).

[43] R. Salinas, H. Iwasaki, A. Revel, B. A. Brown, J. Ash, D. Bazin, J. Chen, R. Elder, P. Farris, A. Gade, M. Grinder, N. Kobayashi, J. Li, B. Longfellow, T. Mijatović, J. Pereira, A. Sanchez, M. Spieker, Y. Utsuno, D. Weisshaar, and J. Wu, Phys. Rev. C **113**, 014330 (2026).

[44] B. V. Pritychenko, T. Glasmacher, P. D. Cottle, R. W. Ibbotson, K. W. Kemper, K. L. Miller, L. A. Riley, and H. Scheit, Phys. Rev. C **66**, 024325 (2002).

[45] S. Ettenauer, H. Zwahlen, P. Adrich, D. Bazin, C. M. Campbell, J. M. Cook, A. D. Davies, D.-C. Dinca, A. Gade, T. Glasmacher, J.-L. Lecouey, W. F. Mueller, T. Otsuka, R. R. Reynolds, L. A. Riley, J. R. Terry, Y. Utsuno, and K. Yoneda, Phys. Rev. C **78**, 017302 (2008).

[46] M. Seidlitz, P. Reiter, R. Altenkirch, B. Bastin, C. Bauer, A. Blazhev, N. Bree, B. Bruyneel, P. A. Butler, J. Cederkäll, T. Davinson, H. De Witte, D. D. DiJulio, J. Diriken, L. P. Gaffney, K. Geibel, G. Georgiev, R. Gernhäuser, M. Huyse, N. Kesteloot, T. Kröll, R. Krücken, R. Lutter, J. Pakarinen, F. Radeck, M. Scheck, D. Schneiders, B. Siebeck, C. Sotty, T. Steinbach, J. Taprogge, P. Van Duppen, J. Van de Walle, D. Voulot, N. Warr, F. Wenander, K. Wimmer, P. J. Woods, and K. Wrzosek-Lipska, Phys. Rev. C **89**, 024309 (2014).

[47] M. Petri, P. Fallon, A. Macchiavelli, S. Heil, E. Rodriguez-Vieitez, D. Bazin, C. Campbell, R. Clark, M. Cromaz, A. Gade, T. Glasmacher, I. Lee, S. Malbrunot-Ettenauer, S. Paschalis,

A. Ratkiewicz, J. Terry, D. Weisshaar, and M. Wiedeking, Physics Letters B **748**, 173 (2015).

[48] O. Tarasov, R. Allatt, J. Angélique, R. Anne, C. Borcea, Z. Dlouhy, C. Donzaud, S. Grévy, D. Guillemaud-Mueller, M. Lewitowicz, S. Lukyanov, A. Mueller, F. Nowacki, Y. Oganessian, N. Orr, A. Ostrowski, R. Page, Y. Penionzhkevich, F. Pougheon, A. Reed, M. Saint-Laurent, W. Schwab, E. Sokol, O. Sorlin, W. Trinder, and J. Winfield, Physics Letters B **409**, 64 (1997).

[49] M. Notani, N. Aoi, N. Fukuda, E. Ideguchi, M. Ishihara, H. Iwasaki, H. Ogawa, T. Kubo, S. M. Lukyanov, T. Nakamura, Y. E. Penionzhkevich, H. Sakurai, T. Teranishi, Y. X. Watanabe, K. Yoneda, and A. Yoshida, RIKEN Accelerator Progress Report **31**, 74 (1998).

[50] Z. Dlouhý, Y. Penionzhkevich, R. Anne, D. Baiborodin, C. Borcea, A. Fomichev, D. Guillemaud-Mueller, R. Kalpakchieva, M. Lewitowicz, S. Lukyanov, A. C. Mueller, Y. Oganessian, R. D. Page, A. Reed, M. G. Saint-Laurent, E. Sokol, N. Skobelev, O. Sorlin, O. Tarasov, V. Toneev, and W. Trinder, Journal of Physics G: Nuclear and Particle Physics **25**, 859 (1999).

[51] H. L. Crawford, V. Tripathi, J. M. Allmond, B. P. Crider, R. Grzywacz, S. N. Liddick, A. Andalib, E. Argo, C. Benetti, S. Bhattacharya, C. M. Campbell, M. P. Carpenter, J. Chan, A. Chester, J. Christie, B. R. Clark, I. Cox, A. A. Doetsch, J. Dopfer, J. G. Duarte, P. Fallon, A. Frotscher, T. Gaballah, T. J. Gray, J. T. Harke, J. Heideman, H. Heugen, R. Jain, T. T. King, N. Kitamura, K. Kolos, F. G. Kondev, A. Laminack, B. Longfellow, R. S. Lubna, S. Luitel, M. Madurga, R. Mahajan, M. J. Mogannam, C. Morse, S. Neupane, A. Nowicki, T. H. Ogunbeku, W.-J. Ong, C. Porzio, C. J. Prokop, B. C. Rasco, E. K. Ronning, E. Rubino, T. J. Ruland, K. P. Rykaczewski, L. Schaedig, D. Seweryniak, K. Siegl, M. Singh, S. L. Tabor, T. L. Tang, T. Wheeler, J. A. Winger, and Z. Xu, Phys. Rev. Lett. **129**, 212501 (2022).

[52] J. Chen, Nuclear Data Sheets **201**, 1 (2025).

[53] M. Wang, W. Huang, F. Kondev, G. Audi, and S. Naimi, Chinese Physics C **45**, 030003 (2021).

[54] P. Doornenbal, H. Scheit, N. Kobayashi, N. Aoi, S. Takeuchi, K. Li, E. Takeshita, Y. Togano, H. Wang, S. Deguchi, Y. Kawada, Y. Kondo, T. Motobayashi, T. Nakamura, Y. Satou, K. N. Tanaka, and H. Sakurai, Phys. Rev. C **81**, 041305(R) (2010).

[55] A. Poves and J. Retamosa, Nuclear Physics A **571**, 221 (1994).

[56] G. Klotz, P. Baumann, M. Bounajma, A. Huck, A. Knipper, G. Walter, G. Marguier, C. Richard-Serre, A. Poves, and J. Retamosa, Phys. Rev. C **47**, 2502 (1993).

[57] N. Gove and M. Martin, Atomic Data and Nuclear Data Tables **10**, 205 (1971).

[58] LogFT, https://www.nndc.bnl.gov/logft/ (2025).

[59] S. Raman and N. B. Gove, Phys. Rev. C **7**, 1995 (1973).

[60] B. Singh, J. Rodriguez, S. Wong, and J. Tuli, Nuclear Data Sheets **84**, 487 (1998).

[61] H. Bateman, Proceedings of the Cambridge Philosophical Society, Mathematical and Physical Sciences **15**, 423 (1910).

[62] W. D. Loveland, D. J. Morrissey, and G. T. Seaborg, *Modern Nuclear Chemistry* (John Wiley & Sons, Inc., Hoboken, New Jersey, 2006).

[63] P. Endt, Atomic Data and Nuclear Data Tables **55**, 171 (1993).

[64] J. Williams, G. Hackman, K. Starosta, R. S. Lubna, P. Choudhary, P. C. Srivastava, C. Andreoiu, D. Annen, H. Asch, M. D. H. K. G. Badanage, G. C. Ball, M. Beuschlein, H. Bidaman, V. Bildstein, R. Coleman, A. B. Garnsworthy, B. Greaves, G. Leckenby, V. Karayonchev, M. S. Martin, C. Natzke, C. M. Petrache, A. Radich, E. Raleigh-Smith, D. Rhodes, R. Russell, M. Satrazani, P. Spagnoletti, C. E. Svensson, D. Tam, F. Wu, D. Yates, and Z. Yu, Phys. Rev. C **108**, L051305 (2023).

[65] R. Lică, F. Rotaru, M. J. G. Borge, S. Grévy, F. Negoiţă, A. Poves, O. Sorlin, A. N. Andreyev, R. Borcea, C. Costache, H. De Witte, L. M. Fraile, P. T. Greenlees, M. Huyse, A. Ionescu, S. Kisyov, J. Konki, I. Lazarus, M. Madurga, N. Mărginean, R. Mărginean, C. Mihai, R. E. Mihai, A. Negret, R. D. Page, J. Pakarinen, S. Pascu, V. Pucknell, P. Rahkila, E. Rapisarda, A. Şerban, C. O. Sotty, L. Stan, M. Stănoiu, O. Tengblad, A. Turturică, P. Van Duppen, R. Wadsworth, and N. Warr (IDS Collaboration), Phys. Rev. C **95**, 021301(R) (2017).

[66] M. Portillo, B. Sherrill, Y. Choi, M. Cortesi, K. Fukushima, M. Hausmann, E. Kwan, S. Lidia, P. Ostroumov, R. Ringle, M. Smith, M. Steiner, O. Tarasov, A. Villari, and T. Zhang, Nuclear Instruments and Methods in Physics Research Section B: Beam Interactions with Materials and Atoms **540**, 151 (2023).

[67] Fdsi proposal, https://fds.ornl.gov/wp-content/uploads/2020/09/fdsi-proposal-may2020.pdf (2020).

[68] Fdsi website, https://fds.ornl.gov/initiator/ (2026).

[69] G. F. Knoll, *Radiation Detection and Measurement* (John Wiley & Sons, Inc., New York, New York, 2000).

[70] H. O. Anger, Review of Scientific Instruments **29**, 27 (1958).

[71] R. Yokoyama, M. Singh, R. Grzywacz, A. Keeler, T. King, J. Agramunt, N. Brewer, S. Go, J. Heideman, J. Liu, S. Nishimura, P. Parkhurst, V. Phong, M. Rajabali, B. Rasco, K. Rykaczewski, D. Stracener, J. Tain, A. Tolosa-Delgado, K. Vaigneur, and M. Wolińska-Cichocka, Nuclear Instruments and Methods in Physics Research Section A: Accelerators,

Spectrometers, Detectors and Associated Equipment **937**, 93 (2019).

[72] M. Berger, J. Hubbell, S. Seltzer, J. Chang, J. Coursey, R. Sukumar, D. Zucker, and K. Olsen, XCOM: Photon Cross Sections Database, https://www.nist.gov/pml/xcom-photon-cross-sections-database (2010).

[73] R. Helmer, Nuclear Instruments and Methods **164**, 355 (1979).

[74] P. J. Mohr, D. B. Newell, B. N. Taylor, and E. Tiesinga, Rev. Mod. Phys. **97**, 025002 (2025).

[75] J. Chen, Nuclear Data Sheets **140**, 1 (2017).

[76] R. Helmer, R. Gehrke, and R. Greenwood, Nuclear Instruments and Methods **166**, 547 (1979).

[77] R. Helmer and C. van der Leun, Nuclear Instruments and Methods in Physics Research Section A: Accelerators, Spectrometers, Detectors and Associated Equipment **450**, 35 (2000).

[78] TSpectrum Class Reference, https://root.cern.ch/doc/v636/classTSpectrum.html (2026).

[79] R. Spitzer and J. H. Kelley, Evaluated Nuclear Structure Data Files (2021).

[80] M. Pravikoff, F. Hubert, R. Del Moral, J.-P. Dufour, A. Fleury, D. Jean, A. Mueller, K.-H. Schmidt, K. Sümmerer, E. Hanelt, J. Fréhaut, M. Beau, G. Giraudet, and B. Brown, Nuclear Physics A **528**, 225 (1991).

[81] M. Wiedeking, P. Fallon, A. O. Macchiavelli, L. A. Bernstein, J. Gibelin, L. Phair, J. T. Harke, D. L. Bleuel, R. M. Clark, M.-A. Deleplanque, S. Gros, R. Hatarik, H. B. Jeppesen, I.-Y. Lee, B. F. Lyles, M. A. McMahan, L. G. Moretto, J. Pavan, E. Rodriguez-Vieitez, and A. Volya, Phys. Rev. C **77**, 054305 (2008).

[82] S. Ziliani, Il Nuovo Cimento **43C**, 107 (2020).

[83] D. Tilley, H. Weller, C. Cheves, and R. Chasteler, Nuclear Physics A **595**, 1 (1995).

[84] F. Quarati, P. Dorenbos, and X. Mougeot, Applied Radiation and Isotopes **108**, 30 (2016).

[85] D. Tilley, C. Cheves, J. Kelley, S. Raman, and H. Weller, Nuclear Physics A **636**, 249 (1998).

[86] M. J. Martin, Nuclear Data Sheets **114**, 1497 (2013).

[87] E. Browne and J. K. Tuli, Nuclear Data Sheets **114**, 1849 (2013).

[88] S. Agostinelli, J. Allison, K. Amako, J. Apostolakis, H. Araujo, P. Arce, M. Asai, D. Axen, S. Banerjee, G. Barrand, F. Behner, L. Bellagamba, J. Boudreau, L. Broglia, A. Brunengo,

H. Burkhardt, S. Chauvie, J. Chuma, R. Chytracek, G. Cooperman, G. Cosmo, P. Degtyarenko, A. Dell'Acqua, G. Depaola, D. Dietrich, R. Enami, A. Feliciello, C. Ferguson, H. Fesefeldt, G. Folger, F. Foppiano, A. Forti, S. Garelli, S. Giani, R. Giannitrapani, D. Gibin, J. Gómez Cadenas, I. González, G. Gracia Abril, G. Greeniaus, W. Greiner, V. Grichine, A. Grossheim, S. Guatelli, P. Gumplinger, R. Hamatsu, K. Hashimoto, H. Hasui, A. Heikkinen, A. Howard, V. Ivanchenko, A. Johnson, F. Jones, J. Kallenbach, N. Kanaya, M. Kawabata, Y. Kawabata, M. Kawaguti, S. Kelner, P. Kent, A. Kimura, T. Kodama, R. Kokoulin, M. Kossov, H. Kurashige, E. Lamanna, T. Lampén, V. Lara, V. Lefebure, F. Lei, M. Liendl, W. Lockman, F. Longo, S. Magni, M. Maire, E. Medernach, K. Minamimoto, P. Mora de Freitas, Y. Morita, K. Murakami, M. Nagamatu, R. Nartallo, P. Nieminen, T. Nishimura, K. Ohtsubo, M. Okamura, S. O'Neale, Y. Oohata, K. Paech, J. Perl, A. Pfeiffer, M. Pia, F. Ranjard, A. Rybin, S. Sadilov, E. Di Salvo, G. Santin, T. Sasaki, N. Savvas, Y. Sawada, S. Scherer, S. Sei, V. Sirotenko, D. Smith, N. Starkov, H. Stoecker, J. Sulkimo, M. Takahata, S. Tanaka, E. Tcherniaev, E. Safai Tehrani, M. Tropeano, P. Truscott, H. Uno, L. Urban, P. Urban, M. Verderi, A. Walkden, W. Wander, H. Weber, J. Wellisch, T. Wenaus, D. Williams, D. Wright, T. Yamada, H. Yoshida, and D. Zschiesche, Nuclear Instruments and Methods in Physics Research Section A: Accelerators, Spectrometers, Detectors and Associated Equipment **506**, 250 (2003).

[89] J. Allison, K. Amako, J. Apostolakis, H. Araujo, P. Arce Dubois, M. Asai, G. Barrand, R. Capra, S. Chauvie, R. Chytracek, G. Cirrone, G. Cooperman, G. Cosmo, G. Cuttone, G. Daquino, M. Donszelmann, M. Dressel, G. Folger, F. Foppiano, J. Generowicz, V. Grichine, S. Guatelli, P. Gumplinger, A. Heikkinen, I. Hrivnacova, A. Howard, S. Incerti, V. Ivanchenko, T. Johnson, F. Jones, T. Koi, R. Kokoulin, M. Kossov, H. Kurashige, V. Lara, S. Larsson, F. Lei, O. Link, F. Longo, M. Maire, A. Mantero, B. Mascialino, I. McLaren, P. Mendez Lorenzo, K. Minamimoto, K. Murakami, P. Nieminen, L. Pandola, S. Parlati, L. Peralta, J. Perl, A. Pfeiffer, M. Pia, A. Ribon, P. Rodrigues, G. Russo, S. Sadilov, G. Santin, T. Sasaki, D. Smith, N. Starkov, S. Tanaka, E. Tcherniaev, B. Tome, A. Trindade, P. Truscott, L. Urban, M. Verderi, A. Walkden, J. Wellisch, D. Williams, D. Wright, and H. Yoshida, IEEE Transactions on Nuclear Science **53**, 270 (2006).

[90] J. Allison, K. Amako, J. Apostolakis, P. Arce, M. Asai, T. Aso, E. Bagli, A. Bagulya, S. Banerjee, G. Barrand, B. Beck, A. Bogdanov, D. Brandt, J. Brown, H. Burkhardt, P. Canal, D. Cano-Ott, S. Chauvie, K. Cho, G. Cirrone, G. Cooperman, M. Cortés-Giraldo, G. Cosmo, G. Cuttone, G. Depaola, L. Desorgher, X. Dong, A. Dotti, V. Elvira, G. Folger, Z. Francis, A. Galoyan, L. Garnier, M. Gayer, K. Genser, V. Grichine, S. Guatelli, P. Guèye, P. Gumplinger, A. Howard, I. Hřivnáčová, S. Hwang, S. Incerti, A. Ivanchenko, V. Ivanchenko, F. Jones, S. Jun, P. Kaitaniemi, N. Karakatsanis, M. Karamitros, M. Kelsey, A. Kimura, T. Koi, H. Kurashige, A. Lechner, S. Lee, F. Longo, M. Maire, D. Mancusi, A. Mantero, E. Mendoza, B. Morgan, K. Murakami, T. Nikitina, L. Pandola, P. Paprocki, J. Perl, I. Petrović, M. Pia, W. Pokorski, J. Quesada, M. Raine, M. Reis, A. Ribon, A. Ristić Fira, F. Romano, G. Russo, G. Santin, T. Sasaki, D. Sawkey, J. Shin, I. Strakovsky, A. Taborda, S. Tanaka, B. Tomé, T. Toshito, H. Tran, P. Truscott, L. Urban, V. Uzhinsky, J. Verbeke, M. Verderi, B. Wendt, H. Wenzel, D. Wright, D. Wright, T. Yamashita, J. Yarba, and H. Yoshida, Nuclear Instruments and Methods in Physics Research Section A:

Accelerators, Spectrometers, Detectors and Associated Equipment **835**, 186 (2016).

[91] L. Riley, D. Weisshaar, H. Crawford, M. Agiorgousis, C. Campbell, M. Cromaz, P. Fallon, A. Gade, S. Gregory, E. Haldeman, L. Jarvis, E. Lawson-John, B. Roberts, B. Sadler, and C. Stine, Nuclear Instruments and Methods in Physics Research Section A: Accelerators, Spectrometers, Detectors and Associated Equipment **1003**, 165305 (2021).

[92] Hamamatsu Photonics K. K., Flat panel type multianode PMT assembly H12700 series / H14220 series, https://www.hamamatsu.com/content/dam/hamamatsu-photonics/sites/documents/99_SALES_LIBRARY/etd/H12700_H14220_TPMH1379E.pdf (2025).

[93] Yu. E. Penionzhkevich, Physics of Atomic Nuclei **64**, 1121 (2001).

[94] M. S. Basunia and A. Chakraborty, Nuclear Data Sheets **197**, 1 (2024).

[95] Z. I. Kolar, J. A. van der Velden, R. C. Vollinga, P. Zandbergen, and J. J. M. de Goeij, Radiochimica Acta **54**, 167 (1991).

[96] M. Birch, B. Singh, I. Dillmann, D. Abriola, T. Johnson, E. McCutchan, and A. Sonzogni, Nuclear Data Sheets **128**, 131 (2015).

[97] M. Shamuzzoha Basunia, Nuclear Data Sheets **113**, 909 (2012).

[98] D. Guillemaud-Mueller, C. Detraz, M. Langevin, F. Naulin, M. de Saint-Simon, C. Thibault, F. Touchard, and M. Epherre, Nuclear Physics A **426**, 37 (1984).

[99] E. Roeckl, P. F. Dittner, C. Détraz, R. Klapisch, C. Thibault, and C. Rigaud, Phys. Rev. C **10**, 1181 (1974).

[100] B. Singh and J. Chen, Nuclear Data Sheets **126**, 1 (2015).

[101] V. Tripathi, S. L. Tabor, C. R. Hoffman, M. Wiedeking, A. Volya, P. F. Mantica, A. D. Davies, S. N. Liddick, W. F. Mueller, A. Stolz, B. E. Tomlin, T. Otsuka, and Y. Utsuno, Phys. Rev. C **73**, 054303 (2006).

[102] A. Hurst, C. Wu, J. Becker, M. Stoyer, C. Pearson, G. Hackman, M. Schumaker, C. Svensson, R. Austin, G. Ball, D. Bandyopadhyay, C. Barton, A. Boston, H. Boston, R. Churchman, D. Cline, S. Colosimo, D. Cross, G. Demand, M. Djongolov, T. Drake, P. Garrett, C. Gray-Jones, K. Green, A. Grint, A. Hayes, K. Leach, W. Kulp, G. Lee, S. Lloyd, R. Maharaj, J.-P. Martin, B. Millar, S. Mythili, L. Nelson, P. Nolan, D. Oxley, E. Padilla-Rodal, A. Phillips, M. Porter-Peden, S. Rigby, F. Sarazin, C. Sumithrarachchi, S. Triambak, P. Walker, S. Williams, J. Wong, and J. Wood, Physics Letters B **674**, 168 (2009).

[103] P. Baumann, P. Dessagne, A. Huck, G. Klotz, A. Knipper, G. Marguier, C. Miehé, M. Ram-

dane, C. Richard-Serre, G. Walter, and B. H. Wildenthal, Phys. Rev. C **36**, 765 (1987).

[104] P. Baumann, P. Dessagne, A. Huck, G. Klotz, A. Knipper, C. Miehé, M. Ramdane, G. Walter, G. Marguier, H. Gabelmann, C. Richard-Serre, K. Schlösser, and A. Poves, Phys. Rev. C **39**, 626 (1989).

[105] H. Scheit, O. Niedermaier, M. Pantea, F. Aksouh, C. Alvarez, F. Ames, T. Behrens, V. Bildstein, H. Boie, P. Butler, J. Cederkäll, T. Davinson, P. Delahaye, P. Van Duppen, J. Eberth, S. Emhofer, J. Fitting, S. Franchoo, R. Gernhäuser, G. Gersch, D. Habs, R. Hahn, H. Hess, A. Hurst, M. Huyse, O. Ivanov, J. Iwanicki, O. Kester, F. Köck, T. Kröll, R. Krücken, M. Lauer, R. Lutter, P. Mayet, M. Münch, U. Pal, M. Pasini, P. Reiter, A. Richter, A. Scherillo, G. Schrieder, D. Schwalm, T. Sieber, H. Simon, O. Thelen, P. Thirolf, J. van de Walle, N. Warr, and D. Weißhaar, Nuclear Physics A **746**, 96 (2004), proceedings of the Sixth International Conference on Radioactive Nuclear Beams (RNB6).

[106] B. Pritychenko, T. Glasmacher, P. Cottle, M. Fauerbach, R. Ibbotson, K. Kemper, V. Maddalena, A. Navin, R. Ronningen, A. Sakharuk, H. Scheit, and V. Zelevinsky, Physics Letters B **461**, 322 (1999).

[107] V. Chisté, A. Gillibert, A. Lépine-Szily, N. Alamanos, F. Auger, J. Barrette, F. Braga, M. Cortina-Gil, Z. Dlouhy, V. Lapoux, M. Lewitowicz, R. Lichtenthäler, R. Neto, S. Lukyanov, M. MacCormick, F. Marie, W. Mittig, F. de Oliveira Santos, N. Orr, A. Ostrowski, S. Ottini, A. Pakou, Y. Penionzhkevich, P. Roussel-Chomaz, and J. Sida, Physics Letters B **514**, 233 (2001).

[108] O. Niedermaier, H. Scheit, V. Bildstein, H. Boie, J. Fitting, R. von Hahn, F. Köck, M. Lauer, U. K. Pal, H. Podlech, R. Repnow, D. Schwalm, C. Alvarez, F. Ames, G. Bollen, S. Emhofer, D. Habs, O. Kester, R. Lutter, K. Rudolph, M. Pasini, P. G. Thirolf, B. H. Wolf, J. Eberth, G. Gersch, H. Hess, P. Reiter, O. Thelen, N. Warr, D. Weisshaar, F. Aksouh, P. Van den Bergh, P. Van Duppen, M. Huyse, O. Ivanov, P. Mayet, J. Van de Walle, J. Äystö, P. A. Butler, J. Cederkäll, P. Delahaye, H. O. U. Fynbo, L. M. Fraile, O. Forstner, S. Franchoo, U. Köster, T. Nilsson, M. Oinonen, T. Sieber, F. Wenander, M. Pantea, A. Richter, G. Schrieder, H. Simon, T. Behrens, R. Gernhäuser, T. Kröll, R. Krücken, M. Münch, T. Davinson, J. Gerl, G. Huber, A. Hurst, J. Iwanicki, B. Jonson, P. Lieb, L. Liljeby, A. Schempp, A. Scherillo, P. Schmidt, and G. Walter, Phys. Rev. Lett. **94**, 172501 (2005).

[109] H. Mach, L. M. Fraile, O. Tengblad, R. Boutami, C. Jollet, W. A. Płóciennik, D. T. Yordanov, M. Stanoiu, M. J. G. Borge, P. A. Butler, J. Cederkäll, P. Dessagne, B. Fogelberg, H. Fynbo, P. Hoff, A. Jokinen, A. Korgul, U. Köster, W. Kurcewicz, F. Marechal, T. Motobayashi, J. Mrazek, G. Neyens, T. Nilsson, S. Pedersen, A. Poves, B. Rubio, E. Ruchowska, and I. Collaboration, European Physical Journal A **25**, 105 (2005).

[110] C. M. Mattoon, F. Sarazin, G. Hackman, E. S. Cunningham, R. A. E. Austin, G. C. Ball, R. S. Chakrawarthy, P. Finlay, P. E. Garrett, G. F. Grinyer, B. Hyland, K. A. Koopmans, J. R. Leslie, A. A. Phillips, M. A. Schumaker, H. C. Scraggs, J. Schwarzenberg, M. B. Smith,

C. E. Svensson, J. C. Waddington, P. M. Walker, B. Washbrook, and E. Zganjar, Phys. Rev. C **75**, 017302 (2007).

[111] V. Tripathi, S. L. Tabor, P. Bender, C. R. Hoffman, S. Lee, K. Pepper, M. Perry, P. F. Mantica, J. M. Cook, J. Pereira, J. S. Pinter, J. B. Stoker, D. Weisshaar, Y. Utsuno, and T. Otsuka, Phys. Rev. C **77**, 034310 (2008).

[112] A. N. Deacon, J. F. Smith, S. J. Freeman, R. V. F. Janssens, M. P. Carpenter, B. Hadinia, C. R. Hoffman, B. P. Kay, T. Lauritsen, C. J. Lister, D. O'Donnell, J. Ollier, T. Otsuka, D. Seweryniak, K.-M. Spohr, D. Steppenbeck, S. L. Tabor, V. Tripathi, Y. Utsuno, P. T. Wady, and S. Zhu, Phys. Rev. C **82**, 034305 (2010).

[113] B. Fernández-Domínguez, B. Pietras, W. Catford, N. Orr, M. Petri, M. Chartier, S. Paschalis, N. Patterson, J. Thomas, M. Caamaño, T. Otsuka, A. Poves, N. Tsunoda, N. Achouri, J.-C. Angélique, N. Ashwood, A. Banu, B. Bastin, R. Borcea, J. Brown, F. Delaunay, S. Franchoo, M. Freer, L. Gaudefroy, S. Heil, M. Labiche, B. Laurent, R. Lemmon, A. Macchiavelli, F. Negoita, E. Paul, C. Rodríguez-Tajes, P. Roussel-Chomaz, M. Staniou, M. Taylor, L. Trache, and G. Wilson, Physics Letters B **779**, 124 (2018).

[114] G. Huber, F. Touchard, S. Büttgenbach, C. Thibault, R. Klapisch, H. T. Duong, S. Liberman, J. Pinard, J. L. Vialle, P. Juncar, and P. Jacquinot, Phys. Rev. C **18**, 2342 (1978).

[115] V. Tripathi, S. L. Tabor, P. F. Mantica, C. R. Hoffman, M. Wiedeking, A. D. Davies, S. N. Liddick, W. F. Mueller, T. Otsuka, A. Stolz, B. E. Tomlin, Y. Utsuno, and A. Volya, Phys. Rev. Lett. **94**, 162501 (2005).

[116] K. Kura, K. Tajiri, T. Shimoda, A. Odahara, T. Hori, M. Kazato, T. Masue, M. Suga, A. Takashima, T. Suzuki, T. Fukuchi, Y. Hirayama, N. Imai, H. Miyatake, M. Pearson, C. D. P. Levy, and K. P. Jackson, Phys. Rev. C **85**, 034310 (2012).

[117] R. L. Kozub, C. B. Chitwood, D. J. Fields, C. J. Lister, J. W. Olness, and E. K. Warburton, Phys. Rev. C **28**, 2343 (1983).

[118] T. A. Hinners, V. Tripathi, S. L. Tabor, A. Volya, P. C. Bender, C. R. Hoffman, S. Lee, M. Perry, P. F. Mantica, A. D. Davies, S. N. Liddick, W. F. Mueller, A. Stolz, and B. E. Tomlin, Phys. Rev. C **77**, 034305 (2008).

[119] B. Olaizola, H. Mach, L. M. Fraile, J. Benito, M. J. G. Borge, R. Boutami, P. A. Butler, Z. Dlouhy, H. O. U. Fynbo, P. Hoff, S. Hyldegaard, H. B. Jeppesen, A. Jokinen, C. Jollet, A. Korgul, U. Köster, T. Kröll, W. Kurcewicz, F. Marechal, J. Mrazek, T. Nilsson, W. A. Płóciennik, E. Ruchowska, R. Schuber, W. Schwerdtfeger, M. Sewtz, G. S. Simpson, M. Stanoiu, O. Tengblad, P. G. Thirolf, and D. T. Yordanov, Phys. Rev. C **94**, 054318 (2016).

[120] T. R. Fisher, T. T. Bardin, J. A. Becker, L. F. Chase, D. Kohler, R. E. McDonald, A. R. Poletti, and J. G. Pronko, Phys. Rev. C **7**, 1878 (1973).

[121] K. L. Keyes, A. Papenberg, R. Chapman, J. Ollier, X. Liang, M. J. Burns, M. Labiche, K. M. Spohr, N. Amzal, C. Beck, P. Bednarczyk, F. Haas, G. Duchêne, P. Papka, B. Gebauer, T. Kokalova, S. Thummerer, W. von Oertzen, and C. Wheldon, Journal of Physics G: Nuclear and Particle Physics **31**, S1903 (2005).

[122] D. Steppenbeck, A. Deacon, S. Freeman, R. Janssens, M. Carpenter, C. Hoffman, B. Kay, T. Lauritsen, C. Lister, D. O'Donnell, J. Ollier, D. Seweryniak, J. Smith, K.-M. Spohr, S. Tabor, V. Tripathi, P. Wady, and S. Zhu, Nuclear Physics A **847**, 149 (2010).

[123] J. Chen and B. Singh, Nuclear Data Sheets **184**, 29 (2022).

[124] P. Möller, M. Mumpower, T. Kawano, and W. Myers, Atomic Data and Nuclear Data Tables **125**, 1 (2019).

[125] R. Han, X. Li, W. Jiang, Z. Li, H. Hua, S. Zhang, C. Yuan, D. Jiang, Y. Ye, J. Li, Z. Li, F. Xu, Q. Chen, J. Meng, J. Wang, C. Xu, Y. Sun, C. Wang, H. Wu, C. Niu, C. Li, C. He, W. Jiang, P. Li, H. Zang, J. Feng, S. Chen, Q. Liu, X. Chen, H. Xu, Z. Hu, Y. Yang, P. Ma, J. Ma, S. Jin, Z. Bai, M. Huang, Y. Zhou, W. Ma, Y. Li, X. Zhou, Y. Zhang, G. Xiao, and W. Zhan, Physics Letters B **772**, 529 (2017).

[126] B. V. Pritychenko, T. Glasmacher, B. A. Brown, P. D. Cottle, R. W. Ibbotson, K. W. Kemper, L. A. Riley, and H. Scheit, Phys. Rev. C **63**, 011305(R) (2000).

[127] S. Nummela, F. Nowacki, P. Baumann, E. Caurier, J. Cederkäll, S. Courtin, P. Dessagne, A. Jokinen, A. Knipper, G. Le Scornet, L. G. Lyapin, C. Miehé, M. Oinonen, E. Poirier, Z. Radivojevic, M. Ramdhane, W. H. Trzaska, G. Walter, J. Äystö, and I. Collaboration, Phys. Rev. C **64**, 054313 (2001).

[128] F. Azaiez, M. Belleguic, D. Sohler, M. Stanoiu, Z. Dombrádi, O. Sorlin, J. Timár, F. Amorini, D. Baiborodin, A. Bauchet, F. Becker, C. Borcea, C. Bourgeois, Z. Dlouhy, C. Donzaud, J. Duprat, D. Guillemaud-Mueller, F. Ibrahim, M. Lopez, R. Lucas, S. Lukyanov, V. Maslov, J. Mrazek, C. Moore, F. Nowacki, B. Nyakó, Y.-E. Penionzhkevich, M. Saint-Laurent, F. Sarazin, J. Scarpaci, G. Sletten, C. Stodel, M. Taylor, C. Theisen, and G. Voltolini, European Physical Journal A **15**, 93 (2002).

[129] S. Takeuchi, N. Aoi, T. Motobayashi, S. Ota, E. Takeshita, H. Suzuki, H. Baba, T. Fukui, Y. Hashimoto, K. Ieki, N. Imai, H. Iwasaki, S. Kanno, Y. Kondo, T. Kubo, K. Kurita, T. Minemura, T. Nakabayashi, T. Nakamura, T. Okumura, T. K. Onishi, H. Sakurai, S. Shimoura, R. Sugou, D. Suzuki, M. K. Suzuki, M. Takashina, M. Tamaki, K. Tanaka, Y. Togano, and K. Yamada, Phys. Rev. C **79**, 054319 (2009).

[130] H. L. Crawford, P. Fallon, A. O. Macchiavelli, A. Poves, V. M. Bader, D. Bazin, M. Bowry, C. M. Campbell, M. P. Carpenter, R. M. Clark, M. Cromaz, A. Gade, E. Ideguchi, H. Iwasaki, C. Langer, I. Y. Lee, C. Loelius, E. Lunderberg, C. Morse, A. L. Richard, J. Rissanen, D. Smalley, S. R. Stroberg, D. Weisshaar, K. Whitmore, A. Wiens, S. J. Williams, K. Wim-

mer, and T. Yamamato, Phys. Rev. C **93**, 031303(R) (2016).

[131] H. Nishibata, S. Kanaya, T. Shimoda, A. Odahara, S. Morimoto, A. Yagi, H. Kanaoka, M. R. Pearson, C. D. P. Levy, M. Kimura, N. Tsunoda, and T. Otsuka, Phys. Rev. C **99**, 024322 (2019).

[132] W. Mittig, H. Savajols, D. Baiborodin, J. Casandjian, C. Demonchy, P. Roussel-Chomaz, F. Sarazin, Z. Dlouhý, J. Mrazek, A. Belozyorov, S. Lukyanov, Y. Penionzhkevich, N. Alamanos, A. Drouart, A. Gillibert, C. Jouanne, V. Lapoux, E. Pollacco, A. Korichi, and J. Scarpaci, European Physical Journal A **15**, 157 (2002).

[133] D. Bazin, B. A. Brown, C. M. Campbell, J. A. Church, D. C. Dinca, J. Enders, A. Gade, T. Glasmacher, P. G. Hansen, W. F. Mueller, H. Olliver, B. C. Perry, B. M. Sherrill, J. R. Terry, and J. A. Tostevin, Phys. Rev. Lett. **91**, 012501 (2003).

[134] K. Wimmer, T. Kröll, R. Krücken, V. Bildstein, R. Gernhäuser, B. Bastin, N. Bree, J. Diriken, P. Van Duppen, M. Huyse, N. Patronis, P. Vermaelen, D. Voulot, J. Van de Walle, F. Wenander, L. M. Fraile, R. Chapman, B. Hadinia, R. Orlandi, J. F. Smith, R. Lutter, P. G. Thirolf, M. Labiche, A. Blazhev, M. Kalkühler, P. Reiter, M. Seidlitz, N. Warr, A. O. Macchiavelli, H. B. Jeppesen, E. Fiori, G. Georgiev, G. Schrieder, S. Das Gupta, G. Lo Bianco, S. Nardelli, J. Butterworth, J. Johansen, and K. Riisager, Phys. Rev. Lett. **105**, 252501 (2010).

[135] S. Michimasa, Y. Yanagisawa, K. Inafuku, N. Aoi, Z. Elekes, Z. Fülöp, Y. Ichikawa, N. Iwasa, K. Kurita, M. Kurokawa, T. Machida, T. Motobayashi, T. Nakamura, T. Nakabayashi, M. Notani, H. J. Ong, T. K. Onishi, H. Otsu, H. Sakurai, M. Shinohara, T. Sumikama, S. Takeuchi, K. Tanaka, Y. Togano, K. Yamada, M. Yamaguchi, and K. Yoneda, Phys. Rev. C **89**, 054307 (2014).

[136] K. Li, Y. Ye, T. Motobayashi, H. Scheit, P. Doornenbal, S. Takeuchi, N. Aoi, M. Matsushita, E. Takeshita, D. Pang, and H. Sakurai, Phys. Rev. C **92**, 014608 (2015).

[137] R. Elder, H. Iwasaki, J. Ash, D. Bazin, P. C. Bender, T. Braunroth, C. M. Campbell, H. L. Crawford, B. Elman, A. Gade, M. Grinder, N. Kobayashi, B. Longfellow, T. Mijatović, J. Pereira, A. Revel, D. Rhodes, and D. Weisshaar, Phys. Rev. C **104**, 024307 (2021).

[138] H. Scheit, O. Niedermaier, V. Bildstein, H. Boie, J. Fitting, R. von Hahn, F. Köck, M. Lauer, U. Pal, H. Podlech, R. Repnow, D. Schwalm, C. Alvarez, F. Ames, G. Bollen, S. Emhofer, D. Habs, O. Kester, R. Lutter, K. Rudolph, M. Pasini, P. Thirolf, B. Wolf, J. Eberth, G. Gersch, H. Hess, P. Reiter, O. Thelen, N. Warr, D. Weisshaar, F. Aksouh, P. V. den Bergh, P. V. Duppen, M. Huyse, O. Ivanov, P. Mayet, J. V. de Walle, J. Äystö, P. Butler, J. Cederkäll, P. Delahaye, H. Fynbo, L. Fraile, O. Forstner, S. Franchoo, U. Köster, T. Nilsson, M. Oinonen, T. Sieber, F. Wenander, M. Pantea, A. Richter, G. Schrieder, H. Simon, T. Behrens, R. Gernhäuser, T. Kröll, R. Krücken, M. Münch, T. Davinson, J. Gerl, G. Huber, A. Hurst, J. Iwanicki, B. Jonson, P. Lieb, L. Liljeby, A. Schempp, A. Scherillo, P. Schmidt, and G. Walter, European Physical Journal A **25**, 397 (2005).

[139] D. Miller, P. Adrich, B. A. Brown, V. Moeller, A. Ratkiewicz, W. Rother, K. Starosta, J. A. Tostevin, C. Vaman, and P. Voss, Phys. Rev. C **79**, 054306 (2009).

[140] M. Seidlitz, D. Mücher, P. Reiter, V. Bildstein, A. Blazhev, N. Bree, B. Bruyneel, J. Cederkäll, E. Clement, T. Davinson, P. Van Duppen, A. Ekström, F. Finke, L. Fraile, K. Geibel, R. Gernhäuser, H. Hess, A. Holler, M. Huyse, O. Ivanov, J. Jolie, M. Kalkühler, T. Kotthaus, R. Krücken, R. Lutter, E. Piselli, H. Scheit, I. Stefanescu, J. Van de Walle, D. Voulot, N. Warr, F. Wenander, and A. Wiens, Physics Letters B **700**, 181 (2011).

[141] A. Lepailleur, O. Sorlin, L. Caceres, B. Bastin, C. Borcea, R. Borcea, B. A. Brown, L. Gaudefroy, S. Grévy, G. F. Grinyer, G. Hagen, M. Hjorth-Jensen, G. R. Jansen, O. Llidoo, F. Negoita, F. de Oliveira, M.-G. Porquet, F. Rotaru, M.-G. Saint-Laurent, D. Sohler, M. Stanoiu, and J. C. Thomas, Phys. Rev. Lett. **110**, 082502 (2013).

[142] R. S. Lubna, K. Kravvaris, S. L. Tabor, V. Tripathi, E. Rubino, and A. Volya, Phys. Rev. Res. **2**, 043342 (2020).

[143] Y. Utsuno, T. Otsuka, T. Mizusaki, and M. Honma, Phys. Rev. C **60**, 054315 (1999).

[144] P. Doornenbal, H. Scheit, N. Aoi, S. Takeuchi, K. Li, E. Takeshita, H. Wang, H. Baba, S. Deguchi, N. Fukuda, H. Geissel, R. Gernhäuser, J. Gibelin, I. Hachiuma, Y. Hara, C. Hinke, N. Inabe, K. Itahashi, S. Itoh, D. Kameda, S. Kanno, Y. Kawada, N. Kobayashi, Y. Kondo, R. Krücken, T. Kubo, T. Kuboki, K. Kusaka, M. Lantz, S. Michimasa, T. Motobayashi, T. Nakamura, T. Nakao, K. Namihira, S. Nishimura, T. Ohnishi, M. Ohtake, N. A. Orr, H. Otsu, K. Ozeki, Y. Satou, S. Shimoura, T. Sumikama, M. Takechi, H. Takeda, K. N. Tanaka, K. Tanaka, Y. Togano, M. Winkler, Y. Yanagisawa, K. Yoneda, A. Yoshida, K. Yoshida, and H. Sakurai, Phys. Rev. Lett. **103**, 032501 (2009).

[145] R. Klapisch, C. Thibault-Philippe, C. Detraz, J. Chaumont, R. Bernas, and E. Beck, Phys. Rev. Lett. **23**, 652 (1969).

[146] R. Klapisch, C. Thibault, A. M. Poskanzer, R. Prieels, C. Rigaud, and E. Roeckl, Phys. Rev. Lett. **29**, 1254 (1972).

[147] C. Thibault, M. Epherre, G. Audi, G. Huber, R. Klapisch, F. Touchard, D. Guillemaud, and F. Naulin, Proceedings of the International Conference on Nuclei Far from Stability, Helsingor, Denmark **2**, 365 (1981).

[148] M. Langevin, C. Détraz, D. Guillemaud-Mueller, A. Mueller, C. Thibault, F. Touchard, and M. Epherre, Nuclear Physics A **414**, 151 (1984).

[149] C. Detraz, M. Epherre, D. Guillemaud, P. Hansen, B. Jonson, R. Klapisch, M. Langevin, S. Mattsson, F. Naulin, G. Nyman, A. Poskanzer, H. Ravn, M. de Saint-Simon, K. Takahashi, C. Thibault, and F. Touchard, Physics Letters B **94**, 307 (1980).

[150] E. Iwersen, W. S. Koski, and F. Rasetti, Phys. Rev. **91**, 1229 (1953).

[151] M. Lindner, Phys. Rev. **91**, 642 (1953).

[152] L. Marquez, Phys. Rev. **90**, 330 (1953).

[153] R. K. Sheline and N. R. Johnson, Phys. Rev. **90**, 325 (1953).

[154] A. H. Wapstra and A. L. Veenendaal, Phys. Rev. **91**, 426 (1953).

[155] A. Weiss and M. Hillman, The International Journal of Applied Radiation and Isotopes **14**, 628 (1963).

[156] M. Mori, R. Chiba, A. Tani, H. Aikawa, and N. Kawai, The International Journal of Applied Radiation and Isotopes **18**, 579 (1967).

[157] S. J. Rothman, N. L. Peterson, W. K. Chen, J. J. Hines, R. Bastar, L. C. Robinson, L. J. Nowicki, and J. B. Anderson, Phys. Rev. C **9**, 2272 (1974).

[158] D. R. Goosman, C. N. Davids, and D. E. Alburger, Phys. Rev. C **8**, 1331 (1973).

[159] M. J. Murphy, T. J. M. Symons, G. D. Westfall, and H. J. Crawford, Phys. Rev. Lett. **49**, 455 (1982).

[160] J. P. Dufour, R. D. Moral, A. Fleury, F. Hubert, D. Jean, M. S. Pravikoff, H. Delagrange, H. Geissel, and K.-H. Schmidt, Zeitschrift für Physik A Atomic Nuclei **324**, 487 (1986).

[161] J. Dufour, R. Del Moral, H. Emmermann, F. Hubert, D. Jean, C. Poinot, M. Pravikoff, A. Fleury, H. Delagrange, and K.-H. Schmidt, Nuclear Instruments and Methods in Physics Research Section A: Accelerators, Spectrometers, Detectors and Associated Equipment **248**, 267 (1986).

[162] F. Maréchal, D. L. Balabanski, D. Borremans, J.-M. Daugas, F. d. O. Santos, P. Dessagne, G. Georgiev, J. Giovinazzo, S. Grévy, P. Himpe, C. Jollet, I. Matea, G. Neyens, F. Perrot, E. Poirier, O. Roig, M. Stanoiu, C. Stodel, J.-C. Thomas, K. Turzó, D. Yordanov, E. Caurier, F. Nowacki, and A. Poves, Phys. Rev. C **72**, 044314 (2005).

[163] S. Grévy, S. Pietri, L. Achouri, J. Angélique, P. Baumann, C. Borcea, A. Buta, W. Catford, S. Courtin, J. Daugas, F. De Oliveira, P. Dessagne, Z. Dlouhy, D. G. Mueller, R. Hadeler, A. Knipper, F. Lecolley, J. Lecouey, M. Lewitowicz, E. Liénard, C. Miehe, J. Mrazek, F. Negoita, N. Orr, Y. Penionzhkevich, J. Peter, E. Poirier, M. Stanoiu, O. Tarasov, C. Timis, and G. Walter, Nuclear Physics A **734**, 369 (2004).

[164] R. Overstreet, L. Jacobson, and P. R. Stout, Phys. Rev. **75**, 231 (1949).

[165] G. Andersson, The London, Edinburgh, and Dublin Philosophical Magazine and Journal of Science **45**, 621 (1954).

[166] W. E. Nervik and G. T. Seaborg, Phys. Rev. **97**, 1092 (1955).

[167] S. Hontzeas and L. Yaffe, Canadian Journal of Chemistry **41**, 2194 (1963).

[168] H. W. Taylor, J. D. King, H. Ing, and R. J. Cox, Canadian Journal of Physics **47**, 1539 (1969).

[169] S. L. Waters, Radiochimica Acta **17**, 63 (1972).

[170] J. F. Emery, S. A. Reynolds, and E. I. Wyatt, Nuclear Science and Engineering **48**, 319 (1972).

APPENDIX

A Decay data for isotopes of interest

Some of the isotopes which have contributed to this study — mainly children and grandchildren of the isotopes of interest — have been studied themselves numerous times. In this Appendix, previous measurements of ground state properties of interest are cataloged for the sake of completeness.

The National Nuclear Data Center (NNDC) is the preeminent authority on nuclear data in the United States. Many nuclear scientists rely upon data compiled in the NNDC's databases, such as the Evaluated Nuclear Structure Data Files (ENSDF) database. The purpose of ENSDF is to compile past measurements of quantities such as half-lives, P_{xn} values, and γ-ray energies. For these quantities, adopted values are recommended, sometimes based on weighted averages of multiple measurements. When nuclear data is required for this study (e.g. for the fixed fit parameters in Sections 4.1 and 4.2), the adopted values are typically chosen in accordance with the ENSDF adopted values.

For each measurement recorded in the following table, the quantity in bold is chosen as the adopted value for the purpose of this study. Weighted averages (abbreviated as W. A.) from secondary sources such as ENSDF or other evaluations are clearly labeled in the table. In the rare case where experimental data do not exist, model calculations may be used, and they are also labeled clearly in the table.

Isotope	Half-life	P_n (%)	P_{2n} (%)	Source	Notes
^{30}Ne	7(2) ms			[48]	
	5.8(2) ms			[49]	
	7(2) ms	9^{+17}_{-9}		[2]	
	7.5(15) ms	9(17)		[50]	
	7.3(3) ms	**12.6(35)**	**8.9(23)**	[3]	
	7.18(22) ms			[4]	
^{32}Ne	3.5(9) ms			[49]	
		75	**4**	[124]	Calculated

Isotope	Half-life	P_n (%)	P_{2n} (%)	Source	Notes
	$4.5(4)_{stat}(6)_{sys}$ ms			[51]	
	4.1(7) ms			[52]	ENSDF W. A.
^{28}Na	34(1) ms			[145]	
	35.7(1) ms			[146]	
	30.5(4) ms	**0.58(12)**		[99]	
	30.5(4) ms			[28]	
	34.1(6) ms			[147]	
	34.1(6) ms			[98]	
	34.6(10)			[125]	
^{29}Na	47(3) ms			[145]	
	48.6(2) ms			[146]	
	44.9(12) ms			[147]	
	44(1) ms	**21.5(30)**		[148]	
	44.9(12) ms			[98]	
	42.9(15) ms			[99]	
	42.8(5) ms			[125]	
	44.1(9) ms			[97]	ENSDF W. A.
^{30}Na	55(3) ms			[145]	
	55(3) ms			[146]	
	53.0(30) ms			[99]	
		26(4)		[28]	
			1.30(25), 1.15(25)	[149]	
	50(3) ms			[147]	
	48(2) ms	30(6)	1.4(3)	[148]	
	50(3) ms	30(4)	1.15(25)	[98]	P_{1n} is a W. A.
	48(5) ms			[48]	

Isotope	Half-life	P_n (%)	P_{2n} (%)	Source	Notes
	50(4) ms			[50]	
	50(4) ms			[93]	
	49.4(20) ms	**30(5)**	**1.27(25)**	[96]	Evaluation
	44.1(8) ms			[125]	
	45.4(11) ms			[94]	ENSDF W. A.
^{31}Na	16.5(4) ms			[145]	
	17.7(1) ms			[146]	
	16.9(7) ms			[99]	
			0.70(25)	[149]	
	17.7(5) ms			[147]	
	17.0(4) ms	36(6)		[148]	
	17.0(4) ms	37.3(54)	0.87(24)	[98]	P_{1n} is a W. A.
	18(2) ms			[48]	
	19(4) ms			[49]	
	16.9(15) ms			[50]	
	18(2) ms			[93]	
	16.6(4) ms			[125]	
		40(5)	0.7(1)	[131]	
	17.0(4) ms	**39(5)**	**0.7(1)**	[123]	ENSDF W. A.
^{32}Na	14.5(3)			[146]	
	13.5(5)			[99]	
		10(4)	5.0(19), 5.5(25)	[149]	
	14.0(5)			[147]	
	13.2(4)	21(8)	9.4(25)	[148]	
	14.0(5)	**23.9(68)**	**8.3(21)**	[98]	$P_{1n,2n}$ are W.A.
	11.5(8) ms			[49]	

Isotope	Half-life	P_n (%)	P_{2n} (%)	Source	Notes
	13.2(4) ms			[52]	ENSDF W. A.
^{28}Mg	21.8 ± 0.32 h			[150]	
	21.2(2) h			[151]	
	20.8(5) h			[152]	
	1278 min			[153]	
	21.4(6) h			[154]	
	20.88(6) h			[155]	
	21.3(2) h			[156]	
	20.93(4) h			[157]	
	20.915(9) h			[95]	
^{29}Mg	1.20(13) s			[158]	
	1470(90) ms			[99]	
	1090(120) ms			[28]	
	1.30(12) s			[97]	ENSDF W. A.
^{30}Mg	1200(500) ms			[99]	
	325(30) ms			[28]	
	270(135) ms			[159]	
	340(20) ms			[160]	
	335(40) ms			[161]	
	314(5) ms			[118]	
	335(10) ms			[119]	
	3111(8) ms			[125]	
	319(6) ms			[94]	ENSDF W. A.
^{31}Mg	259(30) ms			[28]	
	230(20) ms			[148]	
	237(25) ms			[162]	

Isotope	Half-life	P_n (%)	P_{2n} (%)	Source	Notes
	270(2) ms			[125]	
^{32}Mg	120(20) ms			[148]	
	86(5) ms			[163]	
	80.4(4) ms			[125]	
^{43}K	22.4 h			[164]	
	22.4 h			[165]	
	22.4 h			[166]	
	21.75(5) h			[167]	
	22 h			[168]	
	22.6(2) h			[169]	
	22.2(1) h			[170]	
	22.3(1) h			[100]	ENSDF W. A.

Table A.1 Ground state properties for several nuclei of interest in this study. Note that P_{xn} values are omitted for the Mg isotopic chain, as these quantities were irrelevant to the current study.